GENETIC FEATURES CONTRIBUTING TO EYE DEVELOPMENT AND DISEASE

EDITED BY: Ling Zhao, Qingjiong Zhang, Youjin Hu and Jie Zhu
PUBLISHED IN: Frontiers in Cell and Developmental Biology

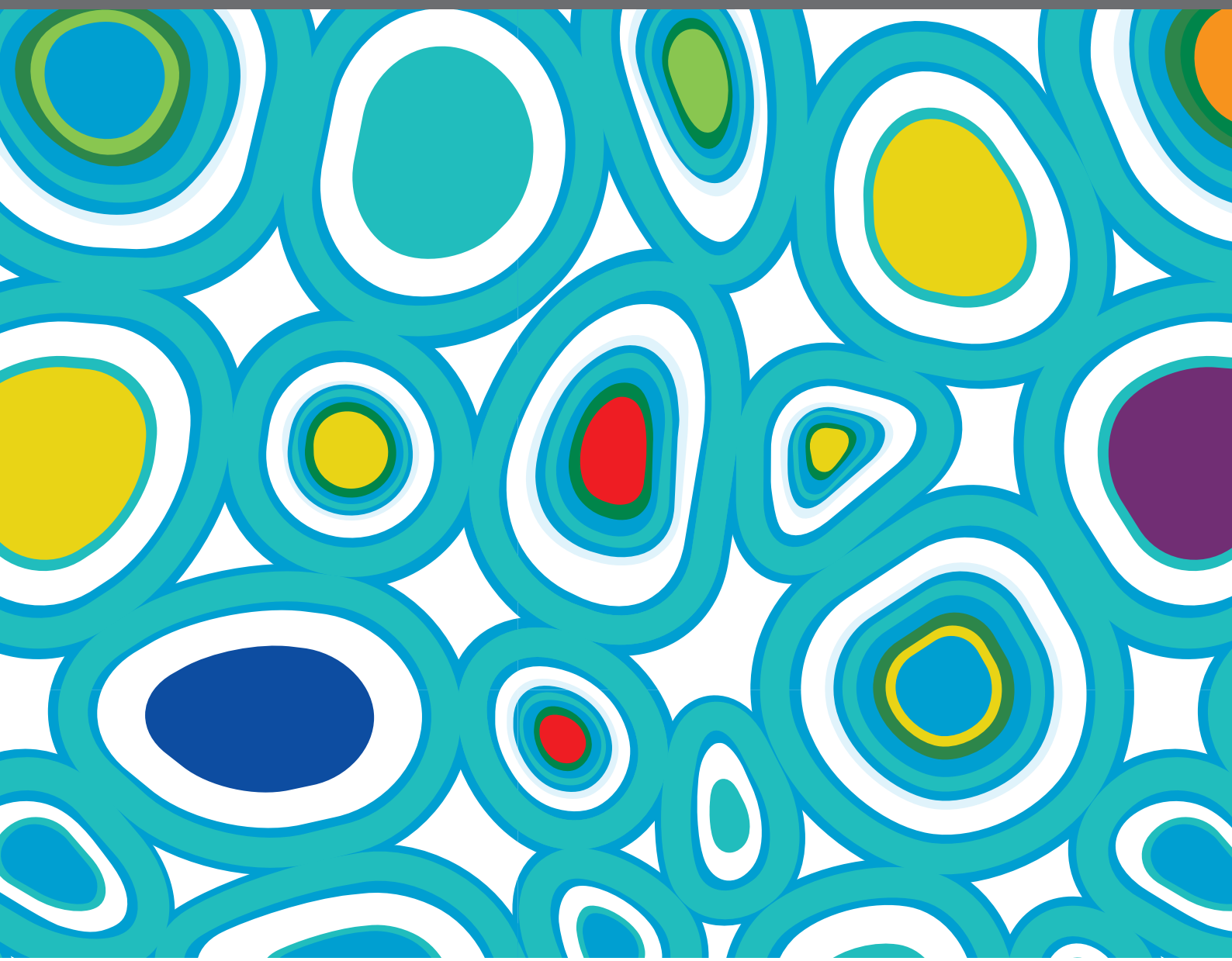

frontiers Research Topics

frontiers

Frontiers eBook Copyright Statement

The copyright in the text of individual articles in this eBook is the property of their respective authors or their respective institutions or funders. The copyright in graphics and images within each article may be subject to copyright of other parties. In both cases this is subject to a license granted to Frontiers.

The compilation of articles constituting this eBook is the property of Frontiers.

Each article within this eBook, and the eBook itself, are published under the most recent version of the Creative Commons CC-BY licence. The version current at the date of publication of this eBook is CC-BY 4.0. If the CC-BY licence is updated, the licence granted by Frontiers is automatically updated to the new version.

When exercising any right under the CC-BY licence, Frontiers must be attributed as the original publisher of the article or eBook, as applicable.

Authors have the responsibility of ensuring that any graphics or other materials which are the property of others may be included in the CC-BY licence, but this should be checked before relying on the CC-BY licence to reproduce those materials. Any copyright notices relating to those materials must be complied with.

Copyright and source acknowledgement notices may not be removed and must be displayed in any copy, derivative work or partial copy which includes the elements in question.

All copyright, and all rights therein, are protected by national and international copyright laws. The above represents a summary only. For further information please read Frontiers' Conditions for Website Use and Copyright Statement, and the applicable CC-BY licence.

ISSN 1664-8714
ISBN 978-2-83250-294-5
DOI 10.3389/978-2-83250-294-5

About Frontiers

Frontiers is more than just an open-access publisher of scholarly articles: it is a pioneering approach to the world of academia, radically improving the way scholarly research is managed. The grand vision of Frontiers is a world where all people have an equal opportunity to seek, share and generate knowledge. Frontiers provides immediate and permanent online open access to all its publications, but this alone is not enough to realize our grand goals.

Frontiers Journal Series

The Frontiers Journal Series is a multi-tier and interdisciplinary set of open-access, online journals, promising a paradigm shift from the current review, selection and dissemination processes in academic publishing. All Frontiers journals are driven by researchers for researchers; therefore, they constitute a service to the scholarly community. At the same time, the Frontiers Journal Series operates on a revolutionary invention, the tiered publishing system, initially addressing specific communities of scholars, and gradually climbing up to broader public understanding, thus serving the interests of the lay society, too.

Dedication to Quality

Each Frontiers article is a landmark of the highest quality, thanks to genuinely collaborative interactions between authors and review editors, who include some of the world's best academicians. Research must be certified by peers before entering a stream of knowledge that may eventually reach the public - and shape society; therefore, Frontiers only applies the most rigorous and unbiased reviews.
Frontiers revolutionizes research publishing by freely delivering the most outstanding research, evaluated with no bias from both the academic and social point of view. By applying the most advanced information technologies, Frontiers is catapulting scholarly publishing into a new generation.

What are Frontiers Research Topics?

Frontiers Research Topics are very popular trademarks of the Frontiers Journals Series: they are collections of at least ten articles, all centered on a particular subject. With their unique mix of varied contributions from Original Research to Review Articles, Frontiers Research Topics unify the most influential researchers, the latest key findings and historical advances in a hot research area! Find out more on how to host your own Frontiers Research Topic or contribute to one as an author by contacting the Frontiers Editorial Office: frontiersin.org/about/contact

GENETIC FEATURES CONTRIBUTING TO EYE DEVELOPMENT AND DISEASE

Topic Editors:
Ling Zhao, Sun Yat-sen University, China
Qingjiong Zhang, Sun Yat-sen University, China
Youjin Hu, Sun Yat-sen University, China
Jie Zhu, Guangzhou Medical University, China

Citation: Zhao, L., Zhang, Q., Hu, Y., Zhu, J., eds. (2022). Genetic Features Contributing to Eye Development and Disease. Lausanne: Frontiers Media SA. doi: 10.3389/978-2-83250-294-5

Table of Contents

frontiers | Frontiers in Cell and Developmental Biology

TYPE Editorial
PUBLISHED 09 September 2022
DOI 10.3389/fcell.2022.1008907

Check for updates

OPEN ACCESS

EDITED AND REVIEWED BY
Ramani Ramchandran,
Medical College of Wisconsin,
United States

*CORRESPONDENCE
Ling Zhao,
zhaoling6@mail.sysu.edu.cn

SPECIALTY SECTION
This article was submitted to Molecular and Cellular Pathology, a section of the journal Frontiers in Cell and Developmental Biology

RECEIVED 01 August 2022
ACCEPTED 22 August 2022
PUBLISHED 09 September 2022

CITATION
Xu W, Liu X, Han W and Zhao L (2022), Editorial: Genetic features contributing to eye development and disease. *Front. Cell Dev. Biol.* 10:1008907. doi: 10.3389/fcell.2022.1008907

COPYRIGHT
© 2022 Xu, Liu, Han and Zhao. This is an open-access article distributed under the terms of the Creative Commons Attribution License (CC BY). The use, distribution or reproduction in other forums is permitted, provided the original author(s) and the copyright owner(s) are credited and that the original publication in this journal is cited, in accordance with accepted academic practice. No use, distribution or reproduction is permitted which does not comply with these terms.

Editorial: Genetic features contributing to eye development and disease

Wenchang Xu[1], Xinqi Liu[1,2], Wenjuan Han[1] and Ling Zhao[1]*

[1]State Key Laboratory of Ophthalmology, Zhongshan Ophthalmic Center, Sun Yat-sen University, Guangdong Provincial Key Laboratory of Ophthalmology and Visual Science, Guangzhou, China, [2]Guangdong Province Key Laboratory of Brain Function and Disease, Zhongshan School of Medicine, Sun Yat-sen University, Guangzhou, China

KEYWORDS

eye diseases, eye development, causal genes, susceptibility genes, genetic mechanisms

Editorial on the Research Topic
Genetic features contributing to eye development and disease

Growing evidence has shown that genetic factors play crucial roles in the disorder of eye development and the progression of ocular diseases (Singh and Tyagi, 2018). Ocular disorders with complex inheritance are responsible for most blindness, however, there are currently no cures for many of these conditions (Singh and Tyagi, 2018; Chen et al., 2021). A better understanding of the genetic underpinnings of ocular diseases could facilitate the accurate diagnosis, counseling and treatment of these diseases.

The eye consists of three main types of tissues: 1) refracting tissues that focus incoming light onto light-sensitive tissues (including the pupil, iris, lens, ciliary muscle, cornea, vitreous and aqueous fluid), 2) light-sensitive tissues that convert detected light into electrical signals and transmit them to the brain (including the retina and optic nerve), and 3) support tissues that provide the architectural support for the shape of the eyeball (including the sclera, conjunctiva and uvea) (Rocher, 2010). These parts in the eyes must work together to produce a clear vision.

This topic summarizes ten original research articles that explored the genetic effects and mechanisms of genetic factors contributing to eye development and disease from diverse aspects, providing new insights into treating eye diseases (Table 1). According to the research object, these studies can be divided into three categories: novel causal and susceptibility genes in eye diseases, genetically engineered animal models for eye diseases, and novel concepts or innovative approaches for eye development and diseases.

Novel causal and susceptibility genes in eye diseases

Inherited eye diseases affect approximately one in 1,000 people worldwide, but the molecular mechanisms underlying most of them remain unclear (Mejecase et al., 2020).

TABLE 1 Genes studied in the article collection.

Gene name	Eye development or diseases	Article
OPA1	Ethambutol-induced optic neuropathy	Wei et al.
BMP4	Syndromic microphthalmia and pathologic myopia	Zhang et al.
GJA8	Congenital hereditary cataract	Jin et al.
FBN1	Congenital ectopia lentis	Jiang et al.
MDM2	Epimacular membranes	Luo et al.
LSS	Congenital hereditary cataract	Zhao et al.
KCNJ13	Snowflake Vitreoretinal Degeneration and Leber congenital amaurosis	Hejtmancik et al.
ASRGL1	Retinitis pigmentosa	Zhu et al.
Atoh7 and Brn3b	*In vivo* regeneration of functional RGCs	Xiang et al.
Transcriptome atlas of the hRPE	Human retinal disease	Hou et al.

Identifying novel causal and susceptibility genes allows a better understanding of the disorders and offers new clues for better-targeted disease management.

Wei et al. identified mitochondrial mutations (*OPA1* and LHON-mtDNA) in nearly half of patients with ethambutol-induced optic neuropathy (EON), a well-recognized ocular complication associated with ethambutol treatment in tuberculosis patients. Since some patients with EON have severe and permanent visual loss even without the known risk factors, their findings that mitochondrial genetic variations are major predisposing factors for the development of EON provided a better understanding of EON and additional support for genetic counseling.

Zhang et al. found variants in *BMP4* contribute to a novel phenotype of pathologic myopia rather than syndromic microphthalmia that have been reported in a previous study (Reis et al., 2011). The observations that mutations in the same gene could cause both syndromic microphthalmia and pathologic myopia suggested bidirectional roles of *BMP4* in early ocular development and provided new insight into the disease mechanism.

Jin et al. identified a novel connexin 50 mutation P88L in patients with congenital cataract and analyzed the function of this mutation. Congenital hereditary cataract is a heterogeneous disorder and the most common cause of childhood blindness (Berry et al., 2020). Their findings expand the spectrum of pathogenic connexin 50 mutations in congenital cataract and provide additional support for clinical diagnosis and genetic counseling.

Congenital ectopia lentis (CEL), the second leading cause of pediatric lens surgery after congenital cataracts, could be caused by mutations in cbEGF-like domains of fibrillin-1 (*FBN1*) (Faivre et al., 2008). However, the correlations between genotype and phenotype of cbEGF-like mutations remain unknown. Jiang et al. focused on clinical manifestations of CEL in patients with different mutations in cbEGF-like domains of *FBN1*. And they clarified the correlations between genotype and phenotype for cbEGF-like mutations. Their work increases our knowledge of CEL and offers new clues for the targeted treatment of the disease.

Luo et al. presented work on the role of the *mouse double minute 2* (*MDM2*) gene single nucleotide polymorphism (SNP) T309G in the development of epimacular membranes (EMMs), relatively common sight-threatening conditions characterized by fibrocellular proliferation along the surface of the internal limiting membrane (ILM) of the retina. They first reported that the *MDM2* SNP309 G allele was a risk allele for EMM in a Chinese population. Their observation provides new insights into the molecular mechanism underlying these pathologies.

Genetically engineered animal models for eye diseases

Since the experimental studies of many inherited eye disorders in human beings are limited, the availability of genetically engineered animal models is very valuable for exploring the pathogenic mechanisms of these conditions and developing translational therapies.

Zhao et al. generated a knock-in mouse model with lanosterol synthase (Lss) G589S mutation, which can recapitulate human congenital cataract resulting from G588S mutation in human LSS. Mice with homozygous Lss G589S mutation exhibited disrupted lens fiber differentiation at early-stage of lens development and down-regulated cholesterol synthesis signaling pathways. Their findings elucidate the important roles of LSS in lens development, contributing to a better understanding of LSS defects and disturbed sterol signaling in cataractogenesis and the development of therapies for cataracts.

Mutations in KCNJ13 are responsible for both snowflake vitreoretinal degeneration (SVD) and Leber congenital amaurosis (LCA) (Hejtmancik et al., 2008; Sergouniotis et al., 2011). Existing animal models have not been able to well verify causality and dissect the mechanisms and pathogenesis of these diseases. Hejtmancik

et al. generated and characterized the Kcnj13 knockout mouse and RPE-specific conditional Kcnj13 knockout mice. Their work provides a potential mouse model system for elucidating the pathology of these diseases and developing gene therapy trials.

G178R in asparaginase and isoaspartyl peptidase 1 (*ASRGL1*) has been reported as a causing mutation for retinitis pigmentosa (RP), an inherited retinal degenerative disease for which there is currently no cure (Biswas et al., 2016). Since the pathological and molecular mechanisms of *ASRGL1* in causing RP remains unknown, Zhu et al. developed *Asrgl1* knockout mice and explored the function of *Asrgl1* in the mammalian retina. Their findings provide a knockout mouse model for improving the understanding of RP disease mechanisms.

Novel concepts or innovative approaches for eye development and diseases

Novel concepts or innovative approaches could provide new insights into understanding the mechanism of eye development and diseases, and developing new diagnostic and treatment strategies.

Glaucoma is the most common cause of irreversible blindness worldwide and irreversible degeneration of retinal ganglion cells (RGCs) and the optic nerve are the common features shared by all forms of glaucoma (Jonas et al., 2017). *In vivo* RGC regeneration would be an ideal therapy but mammalian retinas are thought to lack regenerative capacity. Xiang et al. demonstrated that endogenous mouse Müller glia (MG) could be reprogramed into functional retinal ganglion cells (RGCs) *in vivo* by Math5 and Brn3b together, two crucial transcription factors (TFs) involved in retinal ganglion cell (RGC) generation and differentiation (Yang et al., 2003; Pan et al., 2008). Their study provides a promising new therapeutic approach for visual restoration in patients with glaucoma and other optic neuropathies.

Hou et al. profiled a single-cell transcriptome atlas of human RPE (hRPE) cells and provided a map of disease-related genes in the hRPE. They found two subpopulations, the macular RPE and peripheral RPE clusters which exhibited substantial differences in gene expression patterns and functions, play crucial roles in the potential treatment of retinal diseases. Their work provides important information for understanding the cellular mechanisms and treating pathological conditions of the hRPE associated with ocular diseases.

Conclusion

These research articles on the topic show that elucidating the genetic underpinnings of ocular disorders leads to a better understanding of these diseases, which will contribute to clinical diagnosis, genetic counseling, early intervention and targeted treatment. The application and advancement of integrated multi-omics will further improve our knowledge of complex traits and provide new insights into the pathogenesis of ocular diseases. New genetic methodologies based on automated methods are expected to be developed for accurate and routine diagnosis of eye diseases that have highly diverse genetic causes and are difficult to identify. And gene and cell therapies will open new doors for the treatment of currently incurable eye disorders.

Author contributions

WX, XL and WH prepared the manuscript. LZ revised the manuscript and provided financial support. All authors read and approved the final manuscript.

Funding

This study was supported by funding from the National Natural Science Foundation of China (NSFC: 82000915; 81670894; 81721003), National Key Research and Development Program of China (2020YFA0112701), the Open Research Funds of the State Key Laboratory of Ophthalmology (2022KF04).

Acknowledgments

We would like to thank the support from the State Key Laboratory of Ophthalmology, Zhongshan Ophthalmic Center.

Conflict of interest

The authors declare that the research was conducted in the absence of any commercial or financial relationships that could be construed as a potential conflict of interest.

Publisher's note

All claims expressed in this article are solely those of the authors and do not necessarily represent those of their affiliated organizations, or those of the publisher, the editors and the reviewers. Any product that may be evaluated in this article, or claim that may be made by its manufacturer, is not guaranteed or endorsed by the publisher.

References

Berry, V., Georgiou, M., Fujinami, K., Quinlan, R., Moore, A., and Michaelides, M. (2020). Inherited cataracts: Molecular genetics, clinical features, disease mechanisms, and novel therapeutic approaches. *Br. J. Ophthalmol.* 104, 1331–1337. doi:10.1136/bjophthalmol-2019-315282

Biswas, P., Chavali, V. R., Agnello, G., Stone, E., Chakarova, C., Duncan, J. L., et al. (2016). A missense mutation in ASRGL1 is involved in causing autosomal recessive retinal degeneration. *Hum. Mol. Genet.* 25, 2483–2497. doi:10.1093/hmg/ddw113

Chen, H. Y., Lehmann, O. J., and Swaroop, A. (2021). Genetics and therapy for pediatric eye diseases. *EBioMedicine* 67, 103360. doi:10.1016/j.ebiom.2021.103360

Faivre, L., Collod-Beroud, G., Child, A., Callewaert, B., Loeys, B. L., Binquet, C., et al. (2008). Contribution of molecular analyses in diagnosing marfan syndrome and type I fibrillinopathies: An international study of 1009 probands. *J. Med. Genet.* 45, 384–390. doi:10.1136/jmg.2007.056382

Hejtmancik, J. F., Jiao, X., Li, A., Sergeev, Y. V., Ding, X., Sharma, A. K., et al. (2008). Mutations in KCNJ13 cause autosomal-dominant snowflake vitreoretinal degeneration. *Am. J. Hum. Genet.* 82, 174–180. doi:10.1016/j.ajhg.2007.08.002

Jonas, J. B., Aung, T., Bourne, R. R., Bron, A. M., Ritch, R., and Panda-Jonas, S. (2017). Glaucoma. *Lancet* 390, 2183–2193. doi:10.1016/S0140-6736(17)31469-1

Mejecase, C., Malka, S., Guan, Z., Slater, A., Arno, G., and Moosajee, M. (2020). Practical guide to genetic screening for inherited eye diseases. *Ther. Adv. Ophthalmol.* 12, 2515841420954592. doi:10.1177/2515841420954592

Pan, L., Deng, M., Xie, X., and Gan, L. (2008). ISL1 and BRN3B co-regulate the differentiation of murine retinal ganglion cells. *Development* 135, 1981–1990. doi:10.1242/dev.010751

Reis, L. M., Tyler, R. C., Schilter, K. F., Abdul-Rahman, O., Innis, J. W., Kozel, B. A., et al. (2011). BMP4 loss-of-function mutations in developmental eye disorders including SHORT syndrome. *Hum. Genet.* 130, 495–504. doi:10.1007/s00439-011-0968-y

Rocher, N. (2010). Anatomy and physiology of the human eye. *Soins.* 38, 30–31.

Sergouniotis, P. I., Davidson, A. E., Mackay, D. S., Li, Z., Yang, X., Plagnol, V., et al. (2011). Recessive mutations in KCNJ13, encoding an inwardly rectifying potassium channel subunit, cause leber congenital amaurosis. *Am. J. Hum. Genet.* 89, 183–190. doi:10.1016/j.ajhg.2011.06.002

Singh, M., and Tyagi, S. C. (2018). Genes and genetics in eye diseases: A genomic medicine approach for investigating hereditary and inflammatory ocular disorders. *Int. J. Ophthalmol.* 11, 117–134. doi:10.18240/ijo.2018.01.20

Yang, Z., Ding, K., Pan, L., Deng, M., and Gan, L. (2003). Math5 determines the competence state of retinal ganglion cell progenitors. *Dev. Biol.* 264, 240–254. doi:10.1016/j.ydbio.2003.08.005

frontiers in Cell and Developmental Biology

ORIGINAL RESEARCH
published: 04 October 2021
doi: 10.3389/fcell.2021.755544

In vivo Regeneration of Ganglion Cells for Vision Restoration in Mammalian Retinas

Dongchang Xiao[1†], Kangxin Jin[1†], Suo Qiu[1], Qiannan Lei[1], Wanjing Huang[1], Haiqiao Chen[1], Jing Su[1], Qiang Xu[1], Zihui Xu[1], Bin Gou[1], Xiaoxiu Tie[1], Feng Liu[1], Sheng Liu[1], Yizhi Liu[1]* and Mengqing Xiang[1,2]**

[1] State Key Laboratory of Ophthalmology, Zhongshan Ophthalmic Center, Sun Yat-sen University, Guangzhou, China, [2] Guangdong Provincial Key Laboratory of Brain Function and Disease, Zhongshan School of Medicine, Sun Yat-sen University, Guangzhou, China

OPEN ACCESS

Edited by:
Jie Zhu,
Guangzhou Medical University, China

Reviewed by:
Jingxue Zhang,
Capital Medical University, China
Haisong Jiang,
Sichuan Academy of Medical Sciences, Sichuan Provincial People's Hospital, China

***Correspondence:**
Mengqing Xiang
xiangmq3@mail.sysu.edu.cn
Yizhi Liu
yzliu62@yahoo.com
Sheng Liu
liush87@mail.sysu.edu.cn

[†] These authors have contributed equally to this work

Specialty section:
This article was submitted to Molecular and Cellular Pathology, a section of the journal Frontiers in Cell and Developmental Biology

Received: 09 August 2021
Accepted: 14 September 2021
Published: 04 October 2021

Citation:
Xiao D, Jin K, Qiu S, Lei Q, Huang W, Chen H, Su J, Xu Q, Xu Z, Gou B, Tie X, Liu F, Liu S, Liu Y and Xiang M (2021) In vivo Regeneration of Ganglion Cells for Vision Restoration in Mammalian Retinas. Front. Cell Dev. Biol. 9:755544. doi: 10.3389/fcell.2021.755544

Glaucoma and other optic neuropathies affect millions of people worldwide, ultimately causing progressive and irreversible degeneration of retinal ganglion cells (RGCs) and blindness. Previous research into cell replacement therapy of these neurodegenerative diseases has been stalled due to the incapability for grafted RGCs to integrate into the retina and project properly along the long visual pathway. *In vivo* RGC regeneration would be a promising alternative approach but mammalian retinas lack regenerative capacity. It therefore has long been a great challenge to regenerate functional and properly projecting RGCs for vision restoration in mammals. Here we show that the transcription factors (TFs) Math5 and Brn3b together are able to reprogram mature mouse Müller glia (MG) into RGCs. The reprogrammed RGCs extend long axons that make appropriate intra-retinal and extra-retinal projections through the entire visual pathway to innervate both image-forming and non-image-forming brain targets. They exhibit typical neuronal electrophysiological properties and improve visual responses in RGC loss mouse models. Together, our data provide evidence that mammalian MG can be reprogrammed by defined TFs to achieve *in vivo* regeneration of functional RGCs as well as a promising new therapeutic approach to restore vision to patients with glaucoma and other optic neuropathies.

Keywords: retinal ganglion cell, cell reprogramming, retinal ganglion cell regeneration, glaucoma, transcription factor

INTRODUCTION

Glaucoma is a neurodegenerative disorder characterized by progressive and irreversible degeneration of retinal ganglion cells (RGCs) and the optic nerve, and is the second leading cause of blindness worldwide (Quigley and Broman, 2006; Quigley, 2011). Despite its discovery almost a century and half ago (Grewe, 1986), there is currently still no cure for glaucoma and other optic neuropathies. RGCs project their axons along a long visual pathway through the optic nerve, optic chiasm and optic tract to connect to their appropriate central targets in the brain (McLaughlin and O'Leary, 2005; Petros et al., 2008; Crair and Mason, 2016; Herrera et al., 2019). They are the only output neurons in the retina that transmit visual signals from the retina to the brain, and as such,

are critical for sight. During development, RGCs are guided by a variety of neurotrophic factors and guidance cues to successfully navigate the complex visual pathway (Oster et al., 2004; McLaughlin and O'Leary, 2005; Petros et al., 2008; Crair and Mason, 2016; Herrera et al., 2019). However, adult RGCs lose their ability to respond to the guidance cues perhaps due to the downregulation in expression of the corresponding receptors and signaling molecules and other intrinsic changes (Chen et al., 1995; Crair and Mason, 2016; Benowitz et al., 2017). Because of the numerous guidance barriers needed to overcome by transplanted RGCs to reach the brain targets (Crair and Mason, 2016; Benowitz et al., 2017), cell transplantation therapies using donor RGCs or iPSC-derived RGCs to treat RGC degenerative diseases have been unsuccessful even in mammalian animal models. For instance, intra-retinally directing grafted RGCs to extend axons toward the optic disk has proven to be a major challenge since grafted RGCs usually grow axons in random directions (Kador et al., 2013). The use of a scaffold may improve transplantation therapies but major progress has yet to be made to realize its potential (Kador et al., 2013, 2014; Li et al., 2017).

Apart from cell transplantation treatments, *in vivo* RGC regeneration would be an ideal therapy but mammalian retinas are thought to lack regenerative capacity. In spite of this, the Müller glia (MG) have been shown to serve as retinal stem cells to repair injured retinas in cold-blood vertebrates such as zebrafish (Bernardos et al., 2007; Goldman, 2014; Lenkowski and Raymond, 2014). Similarly, mammalian MG display stem cell-like/late retinal progenitor features, e.g., having a molecular signature similar to that of the late retinal progenitors (Roesch et al., 2008; Jadhav et al., 2009; Dvoriantchikova et al., 2019), exhibiting limited proliferative and neurogenic capacity in damaged retinas (Ooto et al., 2004; Karl et al., 2008; Ueki et al., 2015; Wilken and Reh, 2016; Jorstad et al., 2017), and transdifferentiating into rods by a combination of β-catenin and transcription factors (TFs) (Yao et al., 2018). Thus, a fundamental question that remains to be answered is whether MG can be induced to efficiently regenerate functional and properly projecting RGCs for vision restoration in mammals. We sought to harness the stem cell-like property of MG to regenerate RGCs *in vivo* by TF-directed reprogramming. During murine retinogenesis, the bHLH TF Math5/Atoh7 is transiently expressed in a subset of retinal progenitors and required for conferring them with the competence of RGC generation (Brown et al., 2001; Wang et al., 2001; Yang et al., 2003; Xiang, 2013). Previously, we and others have demonstrated the expression of the POU-domain transcription factor Brn3b/Pou4f2 in RGC precursors and its crucial function in RGC specification and differentiation (Xiang et al., 1993; Erkman et al., 1996; Gan et al., 1996; Xiang, 1998, 2013; Qiu et al., 2008). We thus investigated the ability of the Math5 and Brn3b TF combination to reprogram adult mouse MG into RGCs. Remarkably, we were able to show that without stimulating proliferation, Math5 together with Brn3b reprogrammed mature mouse MG into RGCs while either alone had no or limited capacity. The reprogrammed RGCs were functional, extended long axons through the entire visual pathway to innervate both image-forming and non-image-forming targets in the brain, and improved visual responses in two RGC loss mouse models: *Brn3b* null mutant mice and mice with the optic nerve crushed (ONC).

RESULTS

Reprogramming of Müller Glia Into Retinal Ganglion Cells by Math5 and Brn3b

To regenerate RGCs *in vivo*, MG-specific expression of TFs was achieved by a GFAP promoter in the adeno-associated viruses (AAVs, serotype 9 or ShH10) injected subretinally into the adult mouse eyes (**Figure 1A**). Two weeks after infection with the GFAP-GFP AAVs, numerous MG located in the inner nuclear layer (INL) of the retina were seen to express GFP and display a typical Müller cell morphology with processes spanning both the inner and outer retinal layers (**Figures 2B,C**). The GFP+ cells were immunoreactive only for the MG marker Sox9 in the INL but not for the astrocyte markers Pax2, Sox9, GFAP, or S100β in the ganglion cell layer (GCL), nor were they immunoreactive for RGC markers Rbpms or Brn3a in the GCL (**Figures 2A,D–M**). Thus, the GFAP promoter we used in this study was highly specific to MG without driving reporter expression in astrocytes and RGCs. Consistent with this, we found that GFAP-Brn3b-GFP and GFAP-Math5-Brn3b-GFP AAVs mediated Brn3b expression in MG only (**Figures 1A**, **2N–P**). Moreover, at 3.5 days following infection, GFAP-Math5-Brn3b-GFP AAVs did not drive GFP expression in either Sox9-immunoreactive astrocytes or RGCs immunoreactive for Rbpms and Brn3a (**Figures 2Q–T**).

By 2 weeks after viral infection, compared to MG infected with control GFAP-GFP AAVs, we found that many MG infected with GFAP-Math5-Brn3b-GFP AAVs changed their morphology, lost MG processes and migrated into the GCL (**Figure 1B**). They were immunoreactive for RGC markers Rbpms and Brn3a or for the amacrine cell marker Tfap2a/2b, but not for the Müller cell marker Sox9 (**Figures 1B,C**). Quantification of immunoreactive cells revealed that the Math5 and Brn3b combination reprogrammed infected MG into 25.0% Rbpms+ RGCs, 16.2% Brn3a+ RGCs, and 6.1% Tfap2a/2b+ amacrine cells with 67.9% remained as Sox9+ Müller cells, whereas MG infected with control GFP AAVs remained as 100% Sox9+ Müller cells (**Figures 1B,D**). Single Brn3b factor did not exert any reprogramming effect although single Math5 TF converted infected MG into 10.9% Rbpms+ RGCs, 8.0% Brn3a+ RGCs, and 12.7% Tfap2a/2b+ amacrine cells (**Figures 1B,D**). These results indicate that Math5 together with Brn3b are able to reprogram mature MG into RGCs whereas either TF alone has no or weaker capacity. The reprogrammed RGCs included some cells that expressed melanopsin, Eomes or peripherin, which are protein markers for ipRGCs (Mao et al., 2014), some that expressed Foxp2 and Brn3c, which are markers for F- and F-midi^{ON} RGCs, respectively (Rousso et al., 2016), as well as those expressing Satb2, a maker for three RGC subtypes: On-Off DSGC, Off DSGC, and Off-sustained RGC (Dhande et al., 2019; **Supplementary Figure 1**). Thus, MG appear to be converted into different RGC subtypes by Math5 and Brn3b.

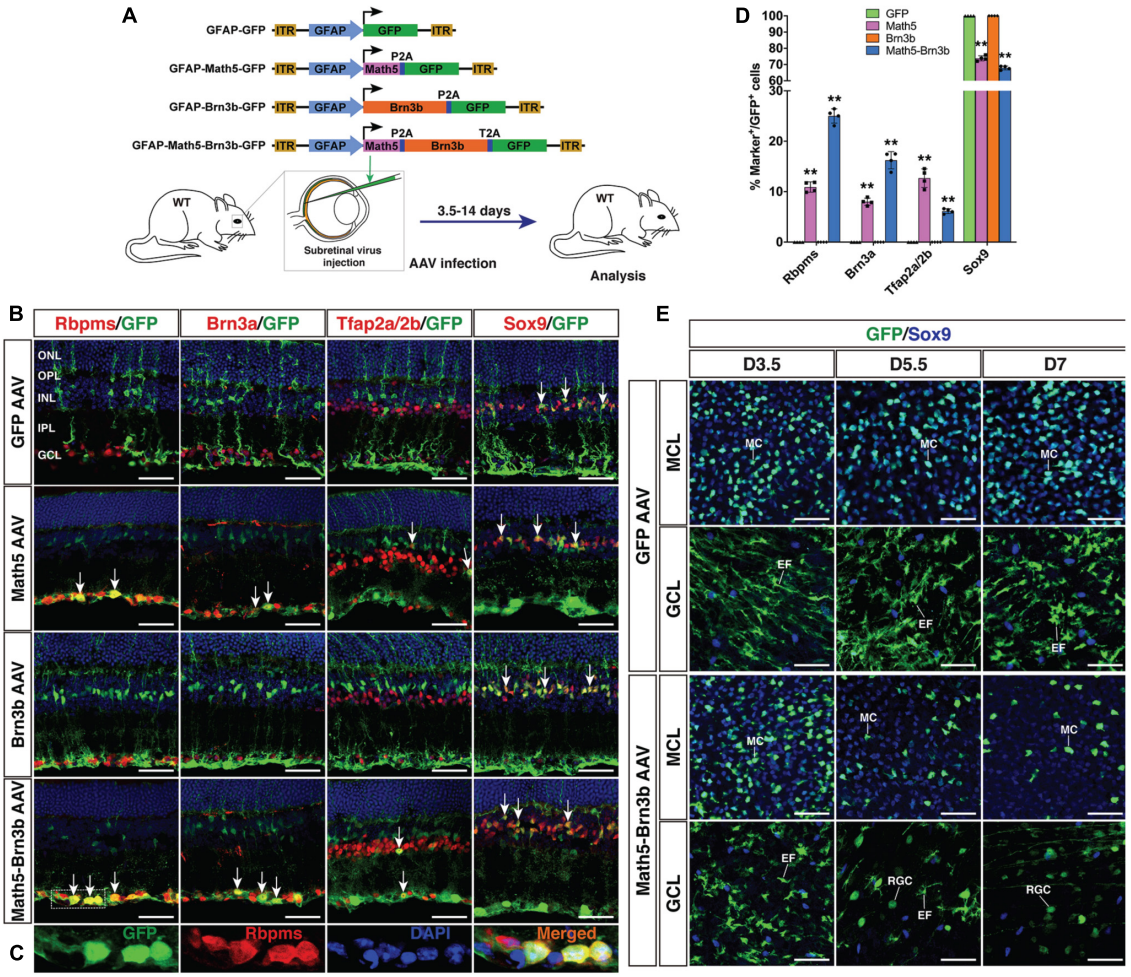

FIGURE 1 | Generation of RGCs by TF-mediated reprogramming of adult mouse MG. **(A)** Schematic of the AAV constructs and infection procedure to generate RGCs in adult wild-type (WT) mice. **(B,C)** Two weeks after infection with GFAP-GFP, GFAP-Math5-GFP, GFAP-Brn3b-GFP or GFAP-Math5-Brn3b-GFP AAVs, sections from infected retinas were double-immunolabeled with the indicated antibodies and counterstained with nuclear DAPI. Arrows point to representative co-labeled cells. Shown in **(C)** are higher magnification single-plane confocal images of the outlined region in **(B)**. **(D)** Quantitation of GFP+ cells that become immunoreactive for Rbpms, Brn3a, Tfap2a/2b or Sox9 in retinas infected with GFAP-GFP, GFAP-Math5-GFP, GFAP-Brn3b-GFP, or GFAP-Math5-Brn3b-GFP AAVs. Data are presented as mean ± SD (n = 4). Asterisks indicate significance in two-way ANOVA test with Bonferroni's correction: $^{**}p < 0.0001$. **(E)** At 3.5 (D3.5), 5.5 and 7 days after viral infection, flat-mounts of adult mouse retinas infected with GFAP-GFP or GFAP-Math5-Brn3b-GFP AAVs were immunostained for both GFP and Sox9. The confocal images are focused on the Müller cell layer (MCL) or ganglion cell layer (GCL). EF, MG endfoot; GCL, ganglion cell layer; INL, inner nuclear layer; IPL, inner plexiform layer; MC, Müller cell; MCL, Müller cell layer; ONL, outer nuclear layer; OPL, outer plexiform layer; RGC, retinal ganglion cell. Scale bars = 40 μm **(B,E)**.

To confirm that RGCs were indeed reprogrammed from MG by Math5 and Brn3b, we performed cell lineage-tracing analysis using the FLEX Cre-Switch system (**Figure 3A**). In wild-type retinas infected with both CAG-FLEX-Math5-Brn3b-GFP and GFAP-tdTomato-Cre AAVs, there were many Rbpms+ RGCs that were also immunoreactive for tdTomato and GFP; whereas essentially all GFP+/tdTomato+ cells were restricted to the INL and immunoreactive for Sox9 in retinas infected with both CAG-FLEX-GFP and GFAP-tdTomato-Cre AAVs (**Figures 3B–E**). Moreover, GFP+/tdTomato+ cells were not seen in retinas infected with both CAG-FLEX-Math5-Brn3b-GFP and GFAP-tdTomato AAVs (**Figure 3B**). These results suggest that the newly generated RGCs arose from tdTomato-marked MG in cell lineage. To more stringently trace reprogrammed RGCs, we further utilized the tamoxifen-inducible Glast-CreER transgenic line (Heng et al., 2019; **Figure 3F**). These mice were infected with CAG-FLEX-Math5-Brn3b-GFP or CAG-FLEX-GFP AAVs, immediately followed by 4 daily tamoxifen administrations, and analyzed at 21 days post virus-injection. In retinas infected with control CAG-FLEX-GFP AAVs, GFP+ cells were found only in the INL, which were co-labeled for Cre and Sox9 (**Figure 3G**), confirming the MG-specificity of Cre expression in the Glast-CreER animals. By contrast, in retinas infected with CAG-FLEX-Math5-Brn3b-GFP AAVs, there were not only GFP+ cells that were immunoreactive for Sox9 in the INL but also many GFP+

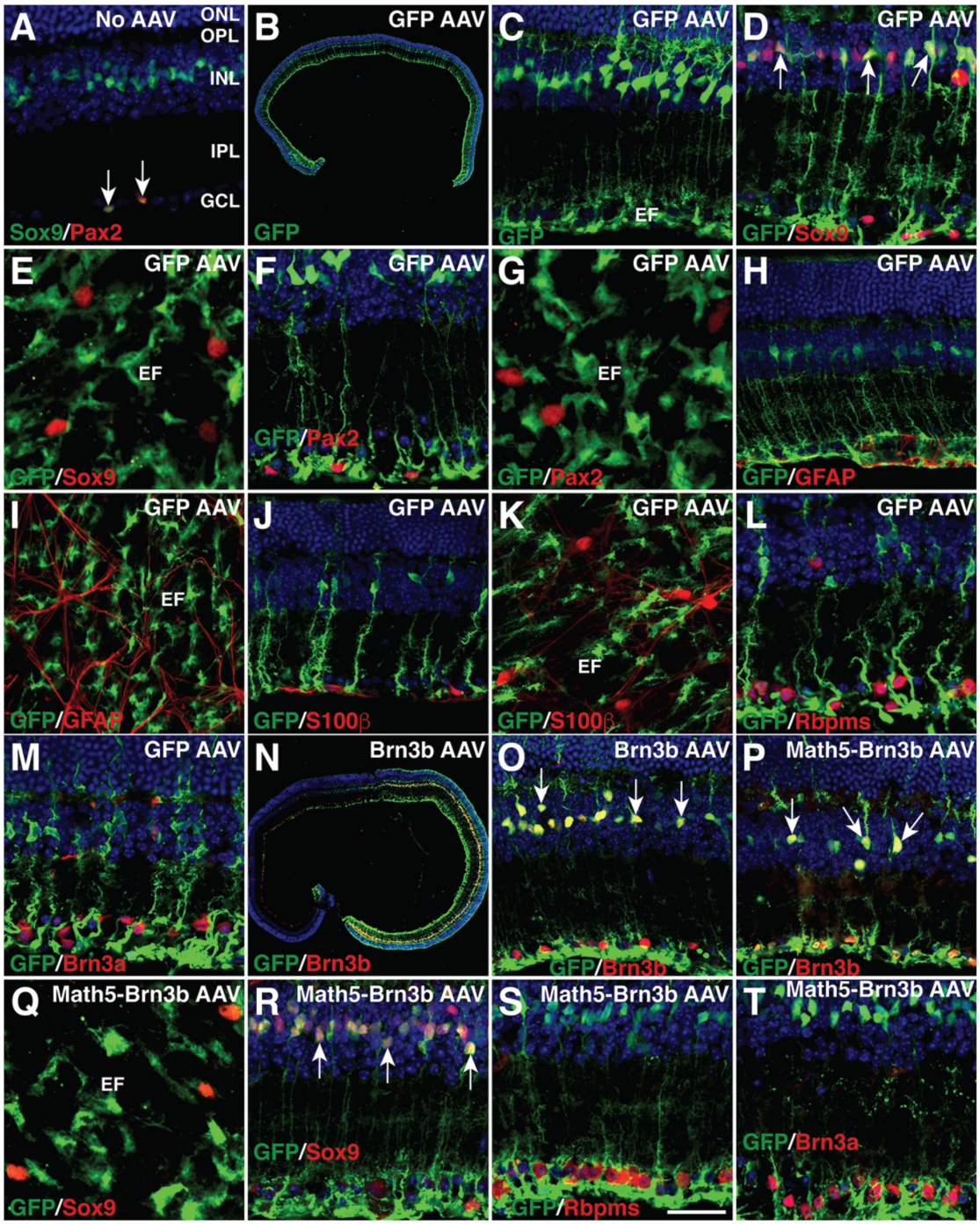

FIGURE 2 | MG-specificity of the GFAP promoter in adult mouse retinas. **(A)** Sections from retinas without AAV infection were double-immunolabeled with antibodies against Sox9 and Pax2 and counterstained with nuclear DAPI. Arrows point to co-labeled cells. Sox9 and Pax2 are completely co-localized in astrocytes within the GCL. **(B–M)** Two weeks after infection with GFAP-GFP AAVs, sections **(B–D,F,H,J,L,M)** or flat-mounts **(E,G,I,K)** from infected retinas were immunolabeled with the indicated antibodies. Sections were also counterstained with nuclear DAPI. Arrows point to representative co-labeled cells. The GFP+ cells are not immunoreactive for Sox9, Pax2, GFAP, or S100β in the GCL **(D–K)**, nor are they immunoreactive for Rbpms or Brn3a **(L,M)**. **(N,O)** Two weeks after infection with GFAP-Brn3b-GFP AAVs, sections from infected retinas were immunolabeled with antibodies against GFP and Brn3b and counterstained with nuclear DAPI. Arrows point to representative co-labeled cells. **(P–T)** At 3.5 **(Q–T)** and 5.5 **(P)** days after infection with GFAP-Math5-Brn3b-GFP AAVs, sections **(P,R–T)** or flat-mount **(Q)** from infected retinas were immunolabeled with the indicated antibodies. Sections were also counterstained with nuclear DAPI. Arrows point to representative co-labeled cells. At day 3.5, the GFP+ cells are not immunoreactive for Sox9 in the GCL **(Q,R)**, nor are they immunoreactive for Rbpms or Brn3a **(S,T)**. EF, MG endfoot; GCL, ganglion cell layer; INL, inner nuclear layer; IPL, inner plexiform layer; ONL, outer nuclear layer; OPL, outer plexiform layer. Scale bar: 640 μm **(B)**, 457 μm **(N)**, 40 μm **(C,H–K,O,P)**, 30 μm **(A,D,F,L,M,R–T)**, 20 μm **(E,G,Q)**.

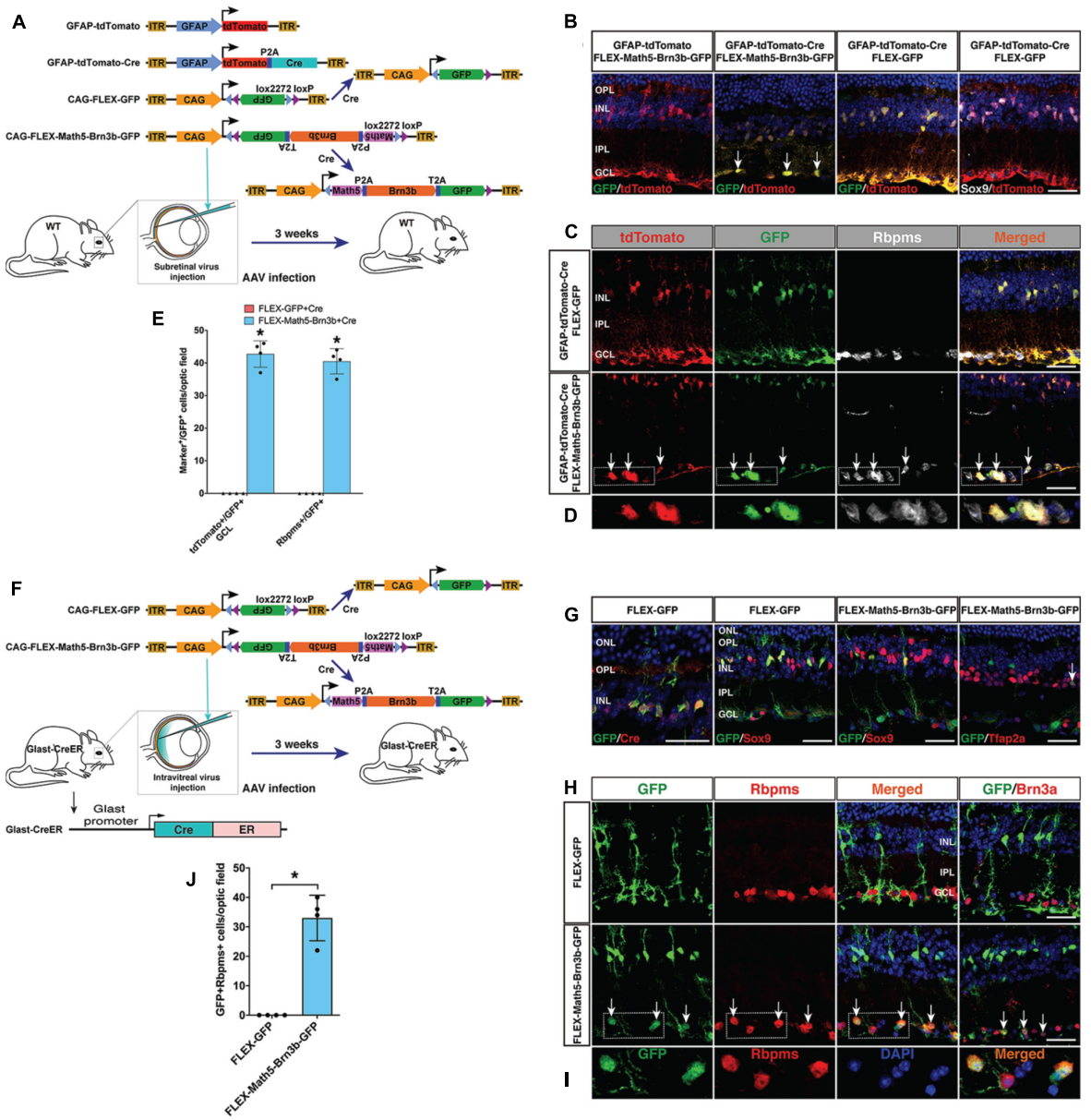

FIGURE 3 | Lineage tracing analysis of MG-derived RGCs. **(A)** Schematic of the AAV constructs and infection procedure as well as the resulting FLEX AAV constructs in the presence of Cre. **(B)** Three weeks after injection of the indicated AAVs, sections from infected retinas were double-immunolabeled with the indicated antibodies and counterstained with DAPI. Arrows point to representative double-positive cells located within the GCL. **(C,D)** Three weeks after injection of the indicated AAVs, sections from infected retinas were triple-immunolabeled with the indicated antibodies and counterstained with DAPI. Arrows point to representative triple-positive cells located within the GCL. Shown in **(D)** are higher magnification single-plane confocal images of the outlined region in **(C)**. **(E)** Quantitation of tdTomato+/GFP+ cells in the GCL as well as Rbpms+/GFP+ cells. Data are presented as mean ± SD ($n = 4$). Asterisks indicate significance in unpaired two-tailed Student's t-test: $^*p < 0.0001$. **(F)** Schematic of the FLEX AAV constructs, resulting FLEX AAV constructs in the presence of Cre, infection procedure, and the Glast-CreER mice. **(G)** Three weeks after injection of the indicated AAVs, sections from infected retinas were double-immunolabeled with the indicated antibodies and counterstained with DAPI. The arrow points to a double-positive cell located within the INL. **(H,I)** Three weeks after injection of the indicated AAVs, sections from infected retinas were double-immunolabeled with the indicated antibodies and counterstained with DAPI. Arrows point to representative double-positive cells located within the GCL. Shown in **(I)** are higher magnification single-plane confocal images of the outlined region in **(H)**. **(J)** Quantitation of GFP+/Rbpms+ double-positive RGCs. Data are presented as mean ± SD ($n = 4$). Asterisks indicate significance in unpaired two-tailed Student's t-test: $^*p < 0.0005$. GCL, ganglion cell layer; INL, inner nuclear layer; IPL, inner plexiform layer; OPL, outer plexiform layer. Scale bars = 30 μm **(B,C,G,H)**.

cells that were positive for Rbpms or Brn3a in the GCL and some GFP+ cells positive for Tfap2a (**Figures 3G–I**). In fact, we found GFP+/Rbpms+ double-positive RGCs only in retinas infected with CAG-FLEX-Math5-Brn3b-GFP AAVs but not in those infected with CAG-FLEX-GFP AAVs (**Figures 3H–J**), demonstrating that the reprogrammed RGCs were derived from

MG and that *Math5* and *Brn3b* DNA sequences do not affect the AAV tropism or expression specificity.

Temporal, Morphological, and Molecular Changes During Müller Glia Transdifferentiation

To determine the onset time during which Math5/Brn3b-mediated MG transdifferentiation occurs, we immunolabeled retinal flat-mounts of 3.5, 5.5, and 7 days post-infection with antibodies against GFP and Sox9 (**Figure 1E**). Infection by GFAP-Math5-Brn3b-GFP AAVs resulted in numerous GFP+/Sox9+ double-positive MG in the Müller cell layer at day 3.5, which were decreased by days 5.5 and 7 (**Figure 1E**). The AAVs did not drive reporter gene expression in RGCs by day 3.5 as evidenced by the lack of GFP+ RGCs within the GCL, but some round GFP+ RGCs began to emerge in the GCL by day 5.5 and they became more numerous by day 7 (**Figure 1E**). In contrast, the number of MG infected by control GFAP-GFP AAVs did not display any obvious change from day 3.5 to 7, and even by day 7, there were no GFP+ RGCs visible in the GCL of retinas infected with control AAVs (**Figure 1E**). The dynamic cellular changes induced by Math5 and Brn3b thus suggest that during the MG reprogramming process, the transdifferentiation events take place 3.5 days after viral infection.

To further monitor the MG reprogramming process, we generated a Brn3b-GFP reporter mouse line in which GFP was simultaneously expressed with Brn3b to specifically mark both immature and mature RGCs (**Figures 4A,D**). Thus, most MG-derived RGCs in this line would be labeled by the GFP reporter whenever the expression of the endogenous *Brn3b* was turned on. Indeed, by 2–3 weeks post-infection, within the GCL of retinas infected with GFAP-Math5-Brn3b-tdTomato AAVs, the majority of tdTomato-positive cells were also immunoreactive for GFP as well as Rbpms, whereas in control retinas, tdTomato-positive cells remained immunoreactive only for Sox9 but negative for either GFP or Rbpms (**Figure 4B**). Quantification of immunoreactive cells showed that there were 16.6% of GFP+ cells in all tdTomato+ cells within retinas infected with GFAP-Math5-Brn3b-tdTomato AAVs (**Figure 4C**).

As described above, the terminal stage of MG transdifferentiation induced by Math5 and Brn3b is represented by the differentiated RGCs located in the GCL. Based on the determined onset time of MG reprogramming (**Figure 1E**), we next searched for the initial and intermediate states of MG transdifferentiation in the Brn3b-GFP reporter mouse line at 4–6 days following infection with GFAP-Math5-Brn3b-tdTomato AAVs. As expected, in this time window, many MG-like cells within the INL were seen to express both tdTomato and various levels of GFP, representing the initial stage of MG transdifferentiation (**Figures 4E–J**). By GFP labeling, some of the cells with high GFP expression exhibited a MG-like morphology and co-expressed Sox9 but not the mature RGC marker Rbpms (**Figures 4E–J,N,O**), whereas in retinas without AAV infection, GFP, as a RGC-specific marker expressed from the endogenous *Brn3b* gene locus, was never found in the MG (**Figure 4D**). We have shown previously that Brn3b is the earliest known RGC marker with an onset expression in RGC precursors (Gan et al., 1996; Xiang, 1998). So the cells at the initial transdifferentiation stage may represent those competent for RGC generation (**Figure 4S**). In addition, we found GFP+/tdTomato+ double-positive cells located at the inner edge of the INL or in the inner plexiform layer, with larger cell bodies and short processes, representing a migratory intermediate state between the initial and terminal stages of MG transdifferentiation (**Figures 4K–M,P–R**). These cells gradually lost the MG morphology, did not express Sox9 but instead expressed more mature RGC markers Rbpms and Brn3a (**Figures 4P–R**), indicating that their fate was already specified/determined as RGCs (**Figure 4S**). Therefore, Math5 and Brn3b rather quickly induce temporal, morphological, and molecular changes in MG to direct them toward the RGC differentiation pathway during reprogramming.

To further confirm the existence of intermediate stages during the reprogramming process, we enriched GFP+ cells in wild-type retinas 5.5 days post-infection with GFAP-Math5-Brn3b-GFP AAVs, and subjected them to scRNA-seq analysis. Among 23238 sequenced cells, 1214 cells were GFP+. Because the cells at intermediate stages are expected to be GFP+, we subjected these GFP+ cells to pseudotime trajectory analysis, which yielded several states along which the expression of the RGC marker genes *Tubb3* (*Tuj1*), *Gap43* and *Sncg* gradually increases while the expression of the MG marker genes *Sox2* and *Sox9* progressively decreases (**Supplementary Figures 2A,B**). Moreover, there are many cells that express both *Sox9* and *Rbpms, Gap43* or *Syt4* (synaptotagmin IV) (**Supplementary Figures 2C–F**), indicating the presence of intermediate cells expressing both MG and RGC marker genes. UMAP visualization of all 23238 sequenced cells revealed a group of related cell populations expressing *Rbpms*, *Sox2* or both (**Supplementary Figure 2H**), which was re-analyzed by UMAP. This analysis clearly demonstrates trajectories reflecting the transition process from MG to intermediate stage RGCs where *Sox2*, *Sox9,* and *Slc1a3* (*Glast*) are mostly expressed at high levels in MG but at low levels in intermediate stage RGCs, while the opposite is true for *Rbpms*, *Sox4* and *Stmn2* (**Supplementary Figures 2H–M**). Other more mature RGC marker genes *Sncg*, *Ebf1,* and *Irx3* display a later onset expression during the process (**Supplementary Figures 2N–P**). Notably, *Sox4* has recently been identified as a marker for developmentally nascent RGCs (Wu et al., 2021). Thus, MG-to-RGC reprogramming undergoes intermediate states and corresponding molecular changes.

To determine if proliferation is required for MG-to-RGC reprogramming, we investigated whether MG proliferation was stimulated by Math5 and Brn3b. The retinas were labeled by EdU injection at day 2.5 or 4.5 following infection with GFAP-Math5-Brn3b-GFP AAVs, and harvested 1 or 4.5 days later; or labeled by EdU at day 7, 14, 21, and 28 and harvested at day 30 (**Supplementary Figure 3A**). In all cases, essentially no EdU-positive MG or other cells were observed (**Supplementary Figure 3**), suggesting that Math5 together with Brn3b are

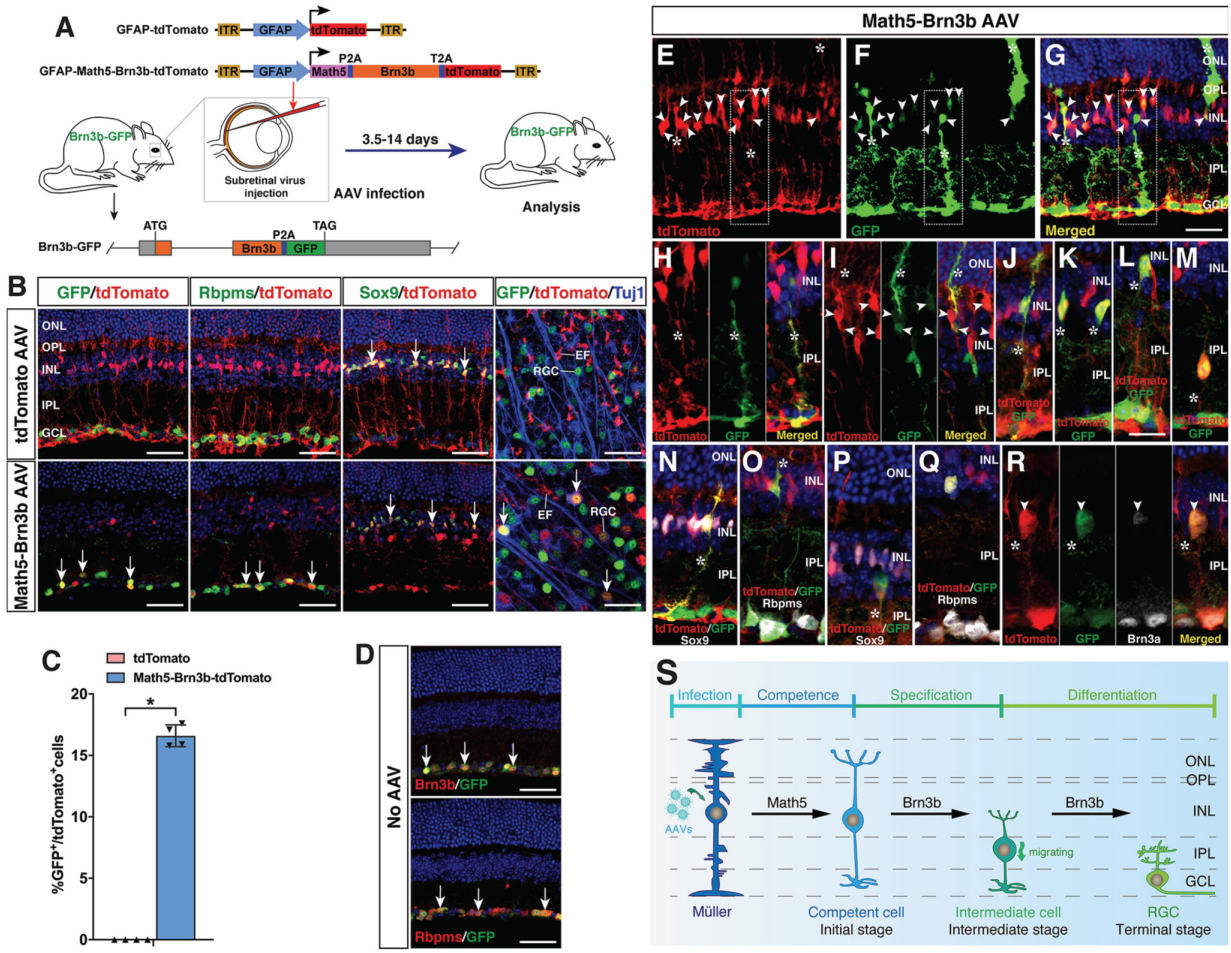

FIGURE 4 | Initial, intermediate and terminal stages of MG transdifferentiation induced by Math5 and Brn3b. **(A)** Schematic of the AAV constructs and infection procedure to generate RGCs in Brn3b-GFP reporter mice. **(B)** Two weeks after infection with the indicated AAVs, sections or flat-mounts from infected retinas were double-immunolabeled with the indicated antibodies. Sections were also counterstained with DAPI. Note that fluorescent staining for Rbpms and Sox9 is in manually assigned false green color. Arrows point to representative co-labeled cells. **(C)** Quantitation of tdTomato+ cells that become immunoreactive for GFP 3 weeks following infection with GFAP-Math5-Brn3b-tdTomato AAVs. Data are presented as mean ± SD (n = 4). Asterisks indicate significance in unpaired two-tailed Student's t-test: $^*p < 0.0001$. **(D)** Sections from retinas of Brn3b-GFP reporter mice without AAV infection were double-immunolabeled with the indicated antibodies and counterstained with DAPI. Arrows point to representative co-labeled cells. **(E–R)** At day 4–6 post-infection with GFAP-Math5-Brn3b-tdTomato AAVs, sections from infected retinas were double- or triple-immunolabeled with the indicated antibodies and counterstained with DAPI. Shown in **(H)** is a higher magnification view of the region outlined in **(E–G)**. **(I,J)** show more representative images of the initial-stage cells that co-express tdTomato and GFP. **(K–M)** show intermediate-stage cells located at the inner edge of the INL and in the IPL with the MG morphology lost. Note that the MG-like cells at the initial stage were labeled by tdTomato, GFP and Sox9 but not by Rbpms **(N,O)**, whereas the bigger cells at the intermediate stage were labeled by tdTomato, GFP, Rbpms, and Brn3a but not by Sox9 **(P–R)**. Arrowheads point to representative co-labeled cells. Asterisks indicate co-labeled MG-like and other cellular processes. **(S)** Proposed changes and mechanism during the MG-to-RGC transdifferentiation process. AAV-mediated Math5 expression may confer RGC competence to MG, on which Brn3b may subsequently act to drive RGC specification and differentiation. During reprogramming, MG undergo morphological and molecular changes including losing MG processes and marker expression while gaining RGC morphology and marker expression. EF, MG endfoot; GCL, ganglion cell layer; INL, inner nuclear layer; IPL, inner plexiform layer; ONL, outer nuclear layer; OPL, outer plexiform layer; RGC, retinal ganglion cell. Scale bars = 40 μm **(B,D)**, 30 μm **(E–G)**, 20 μm **(H–R)**.

able to reprogram mature MG into RGCs without triggering their proliferation.

Proper Projection of Müller Glia-Derived Retinal Ganglion Cells in the Visual Pathway

Endogenous RGC axons project along a stereotypic visual pathway to connect to their appropriate central targets in the brain (Petros et al., 2008; Crair and Mason, 2016; Herrera et al., 2019). We investigated whether *in vivo* regenerated RGCs had the ability to overcome the guidance obstacles to make correct projection along the same pathway. At 3–4 weeks following infection of the adult retina by GFAP-Math5-Brn3b-tdTomato AAVs, numerous tdTomato-immunoreactive RGCs were observed on the vitreous surface of the retina, which extended axons that were fasciculated into many thick axon bundles immunoreactive for Tuj1 (**Figures 5A–E**). Remarkably,

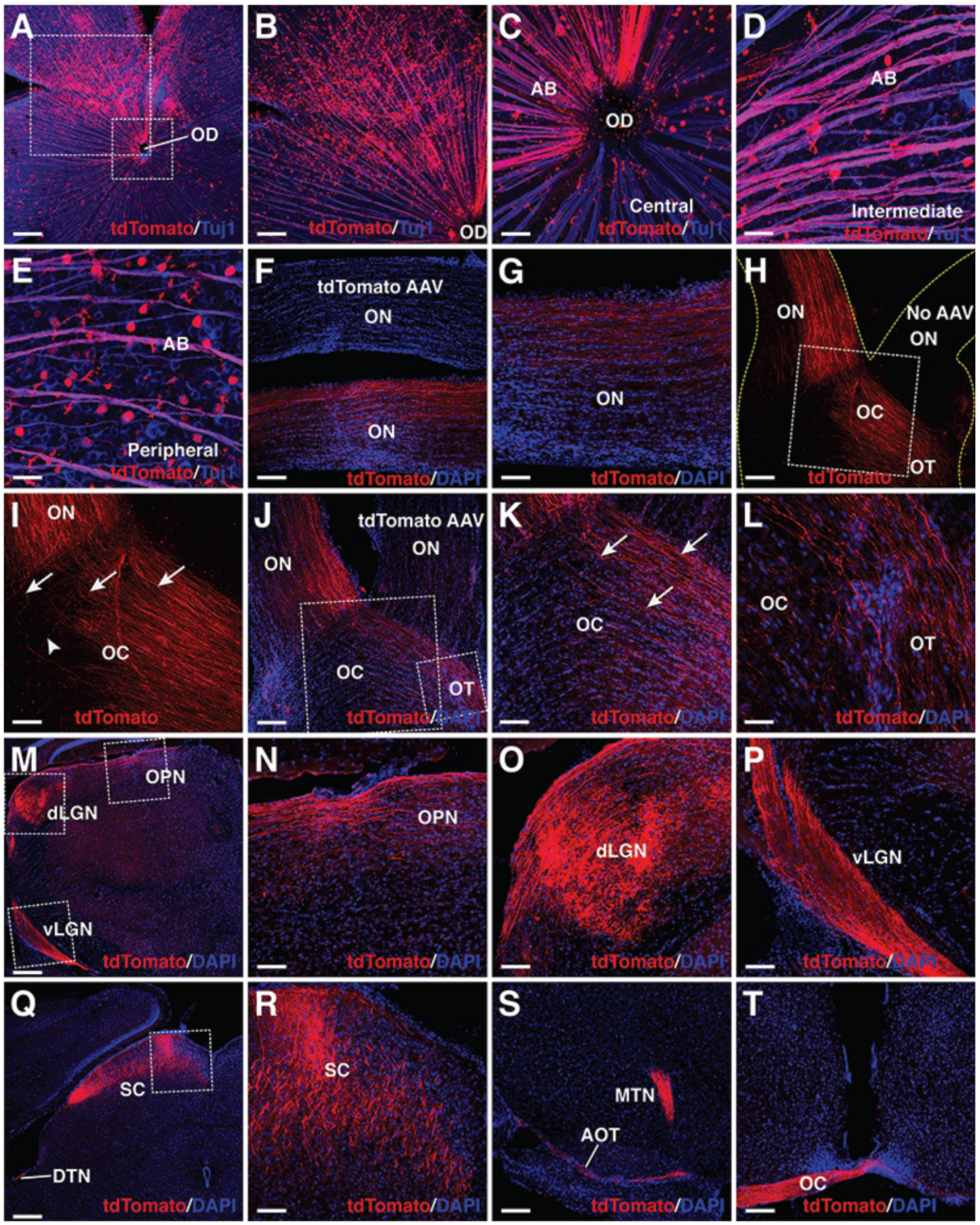

FIGURE 5 | MG-derived RGCs recapitulate the visual projection pathway of endogenous RGCs. **(A–E)** Flat-mounts of wild-type adult mouse retinas treated with GFAP-Math5-Brn3b-tdTomato AAVs were double-immunolabeled with anti-tdTomato and anti-Tuj1 antibodies. The two areas outlined by the large and small squares in **(A)** are shown at a higher magnification in **(B,C)**, respectively. Shown in **(C–E)** are representative images from the central, intermediate and peripheral retinas, respectively. **(F,G)** The optic nerves of mice treated with GFAP-Math5-Brn3b-tdTomato or GFAP-tdTomato (tdTomato AAV) AAVs were immunolabeled with an anti-tdTomato antibody and counterstained with DAPI. **(H,I)** Mono-ocular treatment of adult mice with GFAP-Math5-Brn3b-tdTomato AAVs revealed that tdTomato-immunoreactive axons projected predominantly into the contralateral optic tract. The yellow dashed lines in **(H)** outline the optic nerve and chiasm regions. The optic nerve from the uninjected eye (No AAV) is indicated. Shown in **(I)** is a higher magnification view of the region outlined in **(H)**. Arrows in **(I)** point to axons crossing the midline of the optic chiasm while the arrowhead indicates a non-crossing axon. **(J–L)** The optic nerves, optic chiasms and optic tracts of mice treated with GFAP-Math5-Brn3b-tdTomato AAVs in one eye and GFAP-tdTomato AAVs in the other were immunolabeled with an anti-tdTomato antibody and counterstained with DAPI. The two areas outlined by the large and small squares in **(J)** are shown at a higher magnification in **(K)** and **(L)**, respectively. Arrows in **(K)** point to axons crossing the midline of the optic chiasm. **(M–T)** Brain areas innervated by MG-derived RGCs in mice treated with GFAP-Math5-Brn3b-tdTomato AAVs. Shown in **(N–P)** are higher magnification views of the corresponding outlined regions in **(M)** and shown in **(R)** is a higher magnification view of the region outlined in **(Q)**. AB, axon bundle; AOT, accessory optic tract; dLGN, dorsal lateral geniculate nucleus; DTN, dorsal terminal nucleus; EF, MG endfoot; MTN, medial terminal nucleus; OC, optic chiasm; OD, optic disk; ON, optic nerve; OPN, olivary pretectal nucleus; OT, optic tract; RGC, retinal ganglion cell; SC, superior colliculus; vLGN, ventral lateral geniculate nucleus. Scale bars = 320 μm **(A,M,Q)**, 160 μm **(B,F,H,J,S,T)**, 80 μm **(G,I,K,N,O,P,R)**, 40 μm **(C–E,L)**.

these bundles extended all the way from the periphery through intermediate and central retinal areas to enter the optic disk (**Figures 5A–E**). Once exiting the optic disk, these RGC axons continued to navigate through the optic nerve (**Figures 5F,G**). The great majority of them crossed over the midline of the optic chiasm to continue their projection in the contralateral optic tract while a small number continued their projection in the ipsilateral optic tract (**Figures 5H–L**). The predominant contralateral axon projection was confirmed by treating one eye with GFAP-Math5-Brn3b-tdTomato AAVs and the other with control GFAP-tdTomato AAVs or no AAVs, which unambiguously showed that the great majority of axons from MG-derived RGCs crossed the midline of the optic chiasm (**Figures 5H,J**). In the brain, there were plenty of tdTomato+ axons from MG-derived RGCs that reached and innervated various central targets responsible for both image-forming and non-image forming vision: the lateral geniculate nucleus, superior colliculus, olivary pretectal nucleus, terminal nucleus, accessory optic tract, and the above-mentioned optic chiasm (**Figures 5M–T**). Therefore, MG-derived RGCs are able to extend long axons capable of navigating the entire visual pathway to innervate proper central targets. By contrast, adult eyes without treatment or treated with control GFAP-tdTomato AAVs did not project tdTomato+ axons into the optic nerve (**Figures 5F,H,J** and **Supplementary Figures 5B–E**).

We further confirmed by rabies-virus *trans*-synaptic tracing that MG-derived RGCs innervate neurons of the lateral geniculate nucleus that project to the primary visual cortex (V1). In this experiment, RGCs were converted from MG by GFAP-Math5-Brn3b-tdTomato AAVs and the ΔG-RABV-GFP rabies viruses were injected into the V1 area of visual cortex. As expected, we observed a fraction of RGCs that were immunoreactive for both tdTomato and GFP (**Supplementary Figure 4**). In addition, we investigated the onset and temporal progression of MG-derived RGC projections. By 3.5 days post-infection with the GFAP-Math5-Brn3b-tdTomato AAVs, no tdTomato+ axons were seen in the optic nerve (**Supplementary Figure 5F**), in agreement with the observation that there were no RGCs reprogrammed from MG by this time (**Figure 1E**). Half a day later, however, tdTomato+ axons entered the optic nerve and traveled a small distance (**Supplementary Figure 5G**). By day 5.5, there were some tdTomato+ axons that traversed the entire optic nerve to reach the optic chiasm but few appeared to cross over it (**Supplementary Figures 5H,I**). By day 7, however, there were abundant tdTomato+ axons that reached the optic chiasm and crossed its midline (**Supplementary Figures 5J,K**). Thus, the onset and progression patterns of MG-derived RGC axons closely follow the temporal window of MG transdifferentiation (**Figure 1E**).

Retinal Ganglion Cell Regeneration in Young and Aged *Brn3b* Null Mutant Mice

To evaluate the functionality of regenerated RGCs, we attempted to reprogram MG into RGCs in $Brn3b^{AP/AP}$ knockout mutant mice (1 month old) where 70–80% of RGCs are lost (Gan et al., 1996, 1999; **Figure 6**). On the vitreous surface of mutant retinas infected with GFAP-tdTomato AAVs, except for numerous tdTomato-positive MG endfeet, there were no RGCs and axon bundles labeled by tdTomato (**Figures 6B,C**). By contrast, in mutant retinas infected with GFAP-Math5-Brn3b-tdTomato AAVs, many tdTomato-immunoreactive RGCs were present and these regenerated RGCs extended numerous tdTomato-positive axon bundles that exhibited proper projection to the optic disk (**Figures 6D–G**). Moreover, these nerve fibers navigated all the way through the optic nerve, optic chiasm and optic tract whereas no tdTomato-positive axons were seen in the control optic nerve (**Figures 6H–K**). Overall, there was two to three-fold increase of RGCs in the central, intermediate and peripheral regions in retinas infected with GFAP-Math5-Brn3b-tdTomato AAVs (**Figures 6L,M** and **Supplementary Figure 6A**). Thus, similar to in wild-type retinas, RGCs can be efficiently reprogrammed from MG in $Brn3b^{AP/AP}$ null mutant retinas as well. Consistent with this, transmission electron microscopy revealed an increase of axon density as well as axons with thick myelin sheath in optic nerves of $Brn3b^{AP/AP}$ mice treated with GFAP-Math5-Brn3b-tdTomato AAVs, compared to those treated with GFAP-tdTomato AAVs (**Supplementary Figure 6B**).

We investigated age-dependency of this TF-mediated *in vivo* RGC regeneration by performing similar experiments in 8-month-old $Brn3b^{AP/AP}$ mice (**Supplementary Figure 7**). In these animals treated with GFAP-Math5-Brn3b-tdTomato AAVs, RGCs were also increased by approximately two-fold and the regenerated RGCs extended axons all the way from the retina to the optic tract and displayed predominant contralateral projection at the optic chiasm (**Supplementary Figure 7**). Therefore, MG can be reprogrammed to regenerate RGCs even in aged animals.

Regenerated Retinal Ganglion Cells Improve Visual Function in Mouse Models of Retinal Ganglion Cell Loss

To determine whether we reprogrammed MG into functional RGC neurons, we infected adult wild-type and Brn3b-GFP reporter mouse retinas with GFAP-Math5-Brn3b-tdTomato AAVs. Three weeks after viral infection, patch-clamp recording was carried out for the MG-derived RGCs that were located in the GCL and displayed the tdTomato red fluorescence (**Figure 7A**). We included the green fluorophore Alexa Fluor 488 in the internal solution to confirm that the recorded cells were also labeled by tdTomato and found that the well-filled cells extended a long visible axon (**Figure 7A**). The great majority of recorded neurons (17 out of 18) had multiple action potential responses (**Figures 7B–E**). To investigate the synaptic mechanism of the reprogrammed RGCs, we recorded spontaneous postsynaptic currents (sPSCs) (**Figures 7F–J**). We found that D-AP5, an NMDA receptor antagonist, slightly decreased the amplitude of the sPSCs (**Figures 7G,H**), while CNQX, a competitive AMPA/kainate receptor antagonist, blocked almost all the events (**Figure 7I**), and the effect could be abolished by washing out the drug (**Figure 7J**). Moreover, patch-clamp recording showed that the light responses of reprogrammed RGCs were similar to those of unlabeled endogenous RGCs (**Figure 7K**). These results thus suggest that RGCs reprogrammed from MG are able to

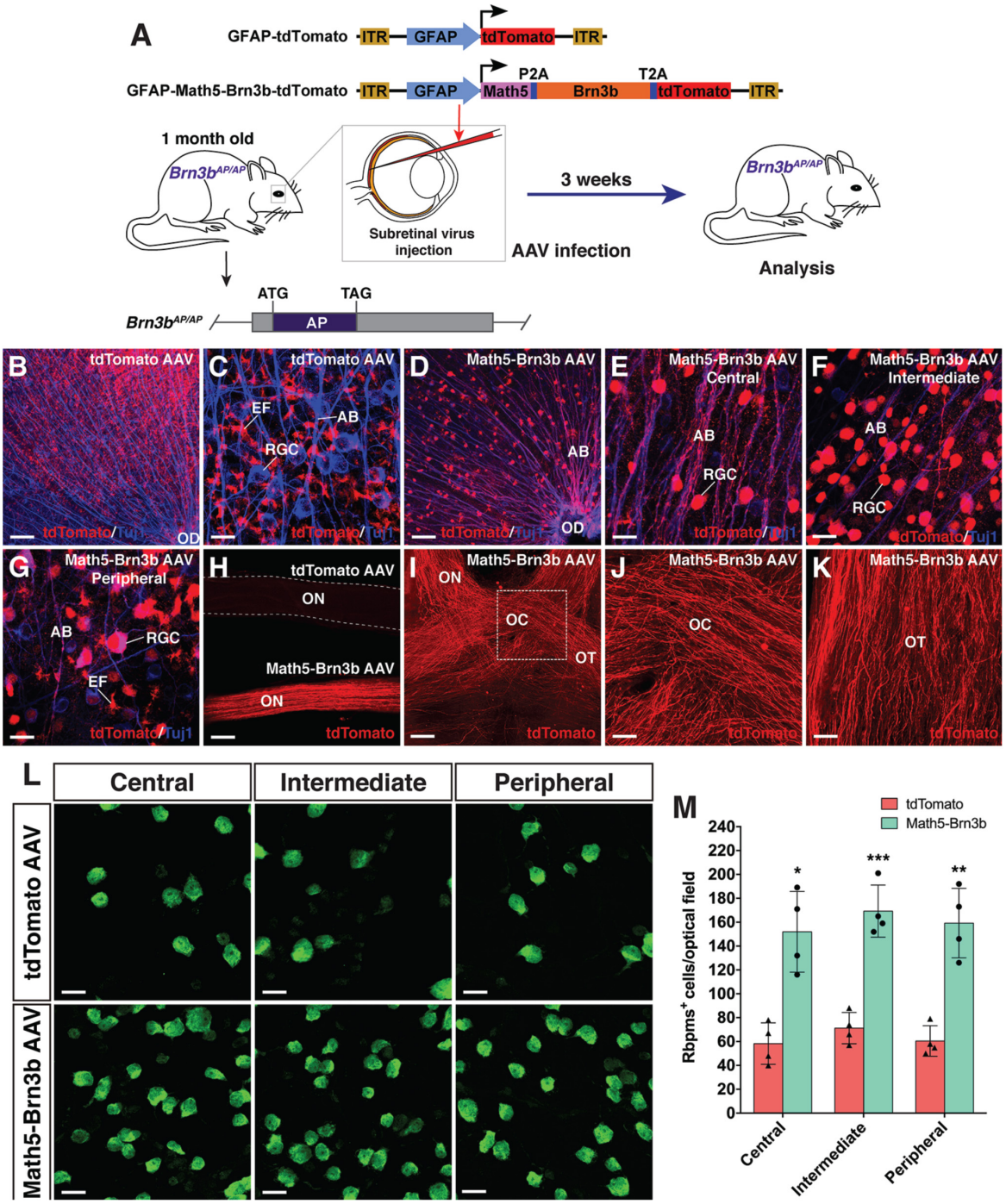

FIGURE 6 | RGC regeneration in *Brn3b*$^{AP/AP}$ mice. **(A)** Schematic of the AAV constructs and infection procedure to regenerate RGCs in *Brn3b*$^{AP/AP}$ mice at 1 month of age. **(B,C)** Flat-mounts of *Brn3b*$^{AP/AP}$ retinas treated with GFAP-tdTomato AAVs were double-immunolabeled with anti-tdTomato and anti-Tuj1 antibodies. **(D–G)** Flat-mounts of *Brn3b*$^{AP/AP}$ retinas treated with GFAP-Math5-Brn3b-tdTomato AAVs were double-immunolabeled with anti-tdTomato and anti-Tuj1 antibodies. Shown in **(E–G)** are representative images from the central, intermediate and peripheral retinas, respectively. **(H)** The optic nerves from *Brn3b*$^{AP/AP}$ mice treated with GFAP-Math5-Brn3b-tdTomato AAVs were immunoreactive for tdTomato whereas those from *Brn3b*$^{AP/AP}$ mice treated with GFAP-tdTomato AAVs were not. **(I–K)** The optic nerves, optic chiasms and optic tracts from *Brn3b*$^{AP/AP}$ mice treated with GFAP-Math5-Brn3b-tdTomato AAVs were immunoreactive for tdTomato. Shown in **(J)** is a higher magnification view of the region outlined in **(I)**. **(L)** Flat-mounts of central, intermediate and peripheral *Brn3b*$^{AP/AP}$ retinas treated with GFAP-tdTomato or GFAP-Math5-Brn3b-tdTomato AAVs were immunostained with an anti-Rbpms antibody. **(M)** Quantification of Rbpms+ cells in central, intermediate and peripheral *Brn3b*$^{AP/AP}$ retinas treated with GFAP-tdTomato or GFAP-Math5-Brn3b-tdTomato AAVs. Data are presented as mean ± SD ($n = 4$). Asterisks indicate significance in unpaired two-tailed Student's *t*-test: $^{*}p < 0.005$, $^{**}p < 0.001$, $^{***}p < 0.0005$. AB, axon bundle; EF, MG endfoot; OC, optic chiasm; OD, optic disk; ON, optic nerve; OT, optic tract; RGC, retinal ganglion cell. Scale bars = 114 μm **(I)**, 80 μm **(B,D,H)**, 40 μm **(J,K)**, 20 μm **(C,E–G,L)**.

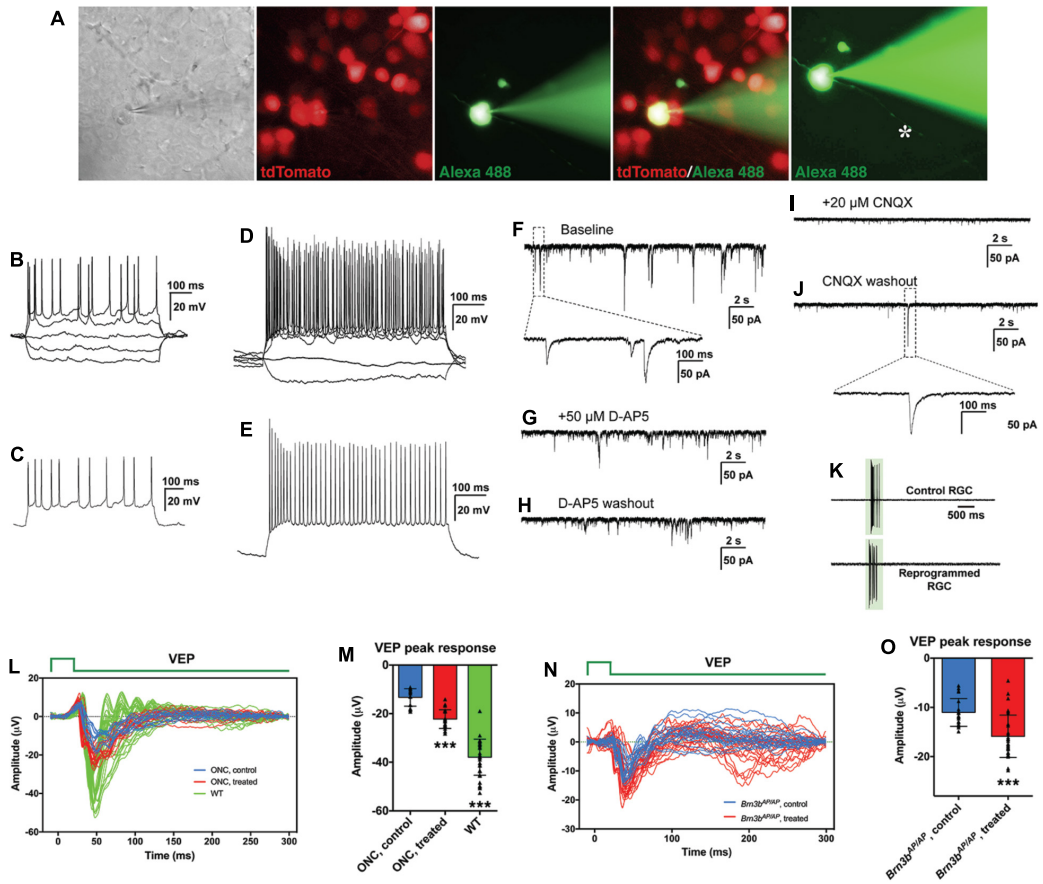

FIGURE 7 | MG-derived RGCs improve visual function of RGC loss mouse models. **(A–J)** Patch-clamp recordings of reprogrammed RGCs in mouse retinas at 3 weeks after treatment with GFAP-Math5-Brn3b-tdTomato AAVs. **(A)** An MG-derived RGC marked by tdTomato (red) was chosen for patch-clamp recording. Alexa Fluor 488 hydrazide was used to confirm the recorded cell and visualize the axon (indicated by the asterisk). **(B,D)** Current-clamp recordings revealed action potential responses of the MG-derived RGCs under current injection. **(C,E)** Action potentials were induced after depolarization of the patched cells. **(F–J)** Representative traces of spontaneous excitatory postsynaptic currents (sEPSCs) of an MG-derived RGC. Voltage clamp was performed and responses were recorded under baseline condition **(F)**, D-AP5 application **(G)**, D-AP5 washout **(H)**, CNQX application **(I)**, and CNQX washout **(J)**. **(K)** Light-evoked spikes of control and reprogrammed RGCs were obtained with current-clamp recording. The duration of light stimulus is indicated by the green rectangle. **(L,M)** Visual evoked responses (VEPs) to a flash light in the visual cortex of ONC mouse models in right eyes (WT, without optic nerve crush, $n = 7$) and in left eyes (optic nerve crushed) treated with GFAP-Math5-Brn3b-GFP AAVs (ONC, treated, $n = 4$) or GFAP-GFP AAVs (ONC, control, $n = 3$). VEP recordings were performed at 6 weeks after AAV treatment. Shown in **(L)** are responses from all trials and five trials were performed for each eye. Shown in **(M)** are amplitudes of the VEP response peaks for control, treated and WT eye groups. Points represent single trials. Data are presented as mean ± SD. Asterisks indicate significance in one-way ANOVA test with Bonferroni's correction: $^{***}p < 0.0001$. **(N,O)** VEPs to a flash light in the visual cortex of *Brn3b*$^{AP/AP}$ mice treated with GFAP-Math5-Brn3b-tdTomato AAVs (*Brn3b*$^{AP/AP}$, treated, $n = 6$ eyes) or GFAP-tdTomato AAVs (*Brn3b*$^{AP/AP}$, control, $n = 4$ eyes). VEP recordings were performed at 4 weeks after AAV treatment. Shown in **(N)** are responses from all trials. Shown in **(O)** are amplitudes of the positive VEP response peaks for control and treated eye groups. Points represent single trials. Data are presented as mean ± SD. Asterisks indicate significance in unpaired two-tailed Student's *t*-test: $^{***}p < 0.0001$.

differentiate into mature functional neurons, develop ionotropic glutamate receptors to receive excitatory inputs, and integrate into the retinal neural circuits.

Given the apparently proper projection of the MG-derived RGCs along the visual pathway, we tested whether they were able to transmit light responses to the primary visual cortex *in vivo*. Six weeks after AAV treatment, visual evoked potentials (VEPs) to a flash light in the primary visual cortex were recorded from well-characterized RGC loss mouse models with the optic nerve crushed (ONC) (**Supplementary Figures 8F,G**). From ONC eyes infected with GFAP-GFP AAVs (control), the light stimulus elicited much smaller VEP responses compared to those from normal wild-type eyes. Infection of the ONC eyes with GFAP-Math5-Brn3b-GFP AAVs (treated) triggered obviously stronger VEP responses than the control treatment (**Figure 7L**). Quantification showed that the amplitudes of the VEP response peaks from the treated eyes were increased by ∼ 67% compared to those from the control eyes (**Figure 7M**). In agreement, in treated ONC animals, many labeled axons extended beyond the injury site of the optic nerve and reached brain targets including the lateral geniculate nucleus and superior colliculus, whereas hardly any axons extended beyond the injury site in control ONC mice (**Supplementary Figure 8**). Additionally, 4 weeks after AAV treatment, we recorded VEPs from *Brn3b*$^{AP/AP}$ mice

infected with GFAP-Math5-Brn3b-tdTomato AAVs (treated) or GFAP-tdTomato AAVs (control). In agreement with the loss of 70–80% RGCs in *Brn3b* knockout animals (Gan et al., 1996), the control mutant eyes gave only small VEP responses (**Figure 7N**). Again, the light stimulus triggered stronger VEP responses from the treated eyes, with the response amplitudes increased by ∼ 44% compared to control eyes (**Figure 7O**), consistent with the observed increase of RGCs in the treated retina (**Figure 6**). However, when VEP recordings were performed at 2 weeks following AAV infection, we did not observe significant difference in VEP response amplitudes between the treated and control groups in either ONC models or *Brn3b* mutant mice (**Supplementary Figure 9**), suggesting that it may take more than 2 weeks for the regenerated RGCs to form functional visual neural circuits.

DISCUSSION

Mammalian Müller Glia Can Be Reprogrammed Into Retinal Ganglion Cells by Defined Transcription Factors

Despite the fact that mammalian MG have little regenerative capacity, our present study demonstrates that mature mouse MG can be reprogrammed by Math5 and Brn3b TFs into functional RGCs that make proper axon projections and have appropriate electrophysiological properties. The result is remarkable and one may wonder whether the reprogrammed RGCs might actually result from infected extant endogenous RGCs that non-specifically express reporters. However, multiple lines of evidence indicate that this is extremely unlikely: (1) We have shown that the GFAP promoter used in this work is completely specific to MG. We did not observe any GFP+ RGCs owing to infection by control GFAP-GFP AAVs; (2) Infection of MG by GFAP-GFP or GFAP-Brn3b-GFP AAVs alone did not produce any GFP+ RGCs. Robust number of GFP+ RGCs appeared only when GFAP-Math5-Brn3b-GFP AAVs were used for infection; (3) By 3.5 days post-infection of retinas with GFAP-Math5-Brn3b-GFP AAVs, many MG but no RGCs were GFP+; only after 5.5 days post-infection were GFP+ RGCs seen, consistent with the time-window of RGC reprogramming and the appearance of intermediate cells (**Figures 1**, **4**). Thus, GFAP-Math5-Brn3b-GFP AAVs have no ability to drive GFP reporter expression in existing RGCs and the resulting GFP+ RGCs must be derived from infected MG; (4) By genetic labeling and single cell transcriptomics, we observed the initial and intermediate states of MG transdifferentiation mediated by Math5 and Brn3b, which were accompanied with temporal, morphological and molecular changes characteristic of RGC reprogramming (**Figure 4** and **Supplementary Figure 2**); (5) Our lineage tracing experiments demonstrated that the reprogrammed GFP+ RGCs were all derived from MG; (6) tdTomato-positive axons were observed only in optic nerves extended from eyes treated with GFAP-Math5-Brn3b-tdTomato AAVs but not in optic nerves from eyes treated with control GFAP-tdTomato AAVs; and (7) Infection with GFAP-Math5-Brn3b-tdTomato AAVs increased RGC density by up to three-fold even in the absence of ∼70–80% of endogenous RGCs in the $Brn3b^{AP/AP}$ retina (**Figure 6** and **Supplementary Figure 7**). This indicates that the newly generated RGCs are reprogrammed rather than AAV-infected extant RGCs because it would be impossible to observe increased RGC density even if all extant RGCs were infected by AAVs and expressed the tdTomato reporter. Therefore, these lines of evidence strongly argue that the RGCs increased by infection with AAVs expressing both Math5 and Brn3b were not extant endogenous RGCs but reprogrammed from MG.

Another possibility to explain our data is that RGCs might be reprogrammed from astrocytes residing in the GCL rather than from MG. However, we can essentially rule out this possibility because following infection by GFAP-GFP AAVs, there were no GFP+ cells present in the GCL that co-localized with either Pax2, Sox9, GFAP, or S100β which are astrocyte markers. Moreover, as shown in this study (**Figure 2**) and by others (Stanke et al., 2010), astrocytes in adult mouse retinas represent a very small cell population, which can hardly explain the numerous reprogrammed RGCs present in the GCL in the absence of cell proliferation.

In this work, we have provided evidence that mature MG are able to be reprogrammed by defined TFs to generate functional RGCs even without activation by injury or proliferation-stimulants. This is in contrast to previous observation of neurogenesis and rod generation by murine MG, which does require prior MG activation (Ooto et al., 2004; Karl et al., 2008; Ueki et al., 2015; Jorstad et al., 2017; Yao et al., 2018), suggesting a possible cell type-specificity of this requirement. In addition, we have shown that the RGC reprogramming efficiency from MG by TFs is similar in both young and aged *Brn3b* null mutant mice, making it feasible to treat not only young but also aged patients with glaucoma and other optic neuropathies by this regeneration strategy.

In vivo Reprogrammed Retinal Ganglion Cells Are Functional and Make Proper Projection in the Visual Pathway

Our study shows that the *in vivo* reprogrammed RGCs migrate into the GCL and make proper intra-retinal and extra-retinal projections through the entire visual pathway to innervate both image-forming and non-image-forming targets in the brain. These results implicate that even in the adult organism, the mammalian visual system may still maintain a relatively intact and permissive environment for regenerated RGC axons to outgrow and navigate to appropriate brain targets, and that unlike postnatal endogenous RGCs which lose their ability to extend (Chen et al., 1995), *in vivo* regenerated RGCs retain the ability to project axons along the visual pathway, similar to embryonically born RGCs (Chen et al., 1995). Although the obstacles to regenerate mammalian RGCs with appropriate central projections once appeared to be insurmountable due to countless guidance barriers present along the long visual pathway (Crair and Mason, 2016), evidence is accumulating that RGC axons regenerated *in vivo* or derived from transplanted donor cells do have the ability to properly navigate the adult visual

pathway. For instance, in mice, a combinatorial treatment of *Pten* deletion and injection with Zymosan and CPT-cAMP stimulated regeneration of RGC axons that traversed the entire visual pathway to reach correct brain target zones including the lateral geniculate nucleus, superior colliculus, olivary pretectal nucleus, and terminal nucleus (de Lima et al., 2012). Similarly, combining neural activity with mTOR activation led to regeneration of RGC axons that projected to the correct brain visual targets (Lim et al., 2016). A very recent study reports that RGCs converted from MG by *Ptbp1* knockdown project properly to the central targets (Zhou et al., 2020). Apart from regenerated RGC axons, axons extended from transplanted early postnatal RGCs also had a limited capability of correct intra-retinal projection and navigation across the optic chiasm to reach the dorsal and ventral lateral geniculate nucleus and superior colliculus (Venugopalan et al., 2016). Therefore, adult mammalian visual system most likely still maintains a permissive environment to allow for normal or properly regenerated RGCs to make correct projections and establish accurate neural circuit connections.

During visual system development, RGCs newly generated from RPCs express a series of attractive and repulsive guidance molecules and TFs such as Ephrins, Neuropilin 1, Slits, DCC, DSCAM, Vax1, and Zic2, to ensure their accurate axon pathfinding through the visual pathway to innervate the correct brain processing centers (Oster et al., 2004; McLaughlin and O'Leary, 2005; Erskine and Herrera, 2007; Petros et al., 2008; Crair and Mason, 2016; Herrera et al., 2019). Because MG are similar to late retinal progenitors (Roesch et al., 2008; Jadhav et al., 2009; Dvoriantchikova et al., 2019), it is likely that the RGCs newly reprogrammed from MG by Math5 and Brn3b express a similar repertoire of guidance cues such that they are also able to readily navigate the complex visual pathway. Adult RGCs may downregulate expression of these critical guidance molecules and undergo unfavorable intrinsic changes while ES/iPSC-derived RGCs may fail to express the complete repertoire of guidance receptors and signaling molecules due to the lack of proper developmental milieu. Thus, when transplanted, adult RGCs and ES/iPSC-derived RGCs may have great difficulty to navigate the visual pathway due to their inability to respond to the guidance cues. Given the many desirable feats of regenerated RGCs never achieved by transplanted retinal stem cells or *in vitro* differentiated RGCs, *in vivo* regeneration of RGCs by MG through directed reprogramming provides a promising new therapeutic approach to restore vision to patients with glaucoma and related optic neuropathies.

The RGCs reprogrammed from MG had action potential responses and excitatory postsynaptic potentials typical of functional neurons and responded to lights. These electrophysiological properties combined with their ability to project to and innervate proper brain visual targets foretold their integration in the visual system and the formation of effective neural circuits. Indeed, after treatment with AAVs expressing both Math5 and Brn3b for 4–6 weeks, we observed a significant increase of VEP responses in both $Brn3b^{AP/AP}$ and ONC mice, indicating that *in vivo* regenerated RGCs are able to improve visual function in RGC loss mouse models. However, no significant difference was seen in VEP responses after treating these model animals for only 2 weeks, suggesting that just like embryonic RGCs, it may take weeks for the reprogrammed RGCs to differentiate and mature properly, navigate the lengthy visual pathway, and make appropriate central connections.

Mechanism of Müller Glia-to-Retinal Ganglion Cell Reprogramming by Transcription Factors

In this study, we used Math5 and Brn3b, two TFs critical for the specification and differentiation of RGCs during development, to efficiently reprogram MG into RGCs in the adult retina, suggesting that MG reprogramming events may largely recapitulate the molecular events that occur in development. Previously, we and others have shown that during retinogenesis, Math5 is required for conferring RPCs with the competence of RGC generation and its overexpression promotes RGC differentiation by RPCs (Brown et al., 2001; Liu et al., 2001; Wang et al., 2001; Yang et al., 2003). Moreover, Brn3b acts downstream of Math5 and plays an essential role in RGC specification and differentiation (Xiang et al., 1993; Erkman et al., 1996; Gan et al., 1996; Xiang, 1998; Liu et al., 2001; Qiu et al., 2008). In particular, we showed that overexpression of Brn3b alone was able to promote RGC differentiation in early RPCs but unable to do so in postnatal mouse RPCs (Liu et al., 2000; Qiu et al., 2008), suggesting that postnatal RPCs lose the competence of generating RGCs. This loss of competence most likely results from the demonstrated downregulation of Math5 expression in postnatal retinas (Brown et al., 1998). Given that mouse MG have a molecular signature similar to that of late postnatal RPCs (Roesch et al., 2008; Jadhav et al., 2009; Dvoriantchikova et al., 2019), it is no wonder that MG do not have any competence of RGC generation. However, in our reprogramming scheme, with the replenishment of Math5 by AAV-mediated expression, MG may gain the competence of RGC generation. Overexpressed Brn3b may then act on the competent MG to promote RGC generation and differentiation (**Figure 4S**), hence making it possible to regenerate RGCs *in vivo* from mammalian MG.

The fact that Math5 alone was able to convert 10.9% MG into RGCs suggests that it indeed has the ability to make MG competent for RGC generation. But because Math5 is not a RGC determination factor (Yang et al., 2003), it also reprogrammed MG into 12.7% amacrine cells. The addition of Brn3b increased the fraction of reprogrammed RGCs but reduced that of reprogrammed amacrine cells, in agreement with our previous finding that Brn3b promotes the RGC fate while inhibiting amacrine cell development (Qiu et al., 2008). Apart from Math5 and Brn3b, there are other TFs such as Isl1 and Sox factors involved in RGC specification and differentiation (Mu et al., 2008; Pan et al., 2008; Jiang et al., 2013; Xiang, 2013; Wu et al., 2015; Chang et al., 2017; Kuwajima et al., 2017). It will be interesting to determine whether these TFs also have an activity in reprogramming MG into RGCs.

In summary, to search for RGC regeneration strategies for potential therapy and vision restoration in damaged and diseased retinas, we made a remarkable discovery that the mammalian MG can be reprogrammed by developmentally

pertinent TFs Math5 and Brn3 into functional RGCs. The MG-to-RGC transdifferentiation occurs in the absence of cell proliferation. The reprogrammed RGCs extend long axons that traverse the optic nerve and project predominantly into the contralateral optic tract through the optic chiasm to innervate both image-forming and non-image-forming brain targets such as lateral geniculate nucleus and superior colliculus. They display typical neuronal electrophysiological features and improve vision in RGC loss mouse models. With the great difficulties RGC transplantation therapy is currently facing, our work of successful *in vivo* RGC regeneration may provide a powerful approach leading to therapeutics for glaucoma, optic dystrophy, diabetic retinopathy and other optic neuropathies.

MATERIALS AND METHODS

Animals

All experiments on mice were performed according to the Institutional Animal Care and Use Committee (IACUC) standards, and approved by Sun Yat-sen University and Zhongshan Ophthalmic Center. The *Brn3b*$^{AP/AP}$ knockin mutant mice were previously generated and maintained in our laboratory (Gan et al., 1999). The Brn3b-GFP reporter mouse line was created by CRISPR/Cas9 gene editing, in which the *Brn3b* open reading frame was tethered to the GFP reporter gene by a P2A self-cleaving peptide sequence (Xiao et al., 2020). More related results about this line will be published elsewhere. The Glast-CreER mice (Heng et al., 2019) (stock number: 012586) were purchased from The Jackson Laboratory (Bar Harbor, ME, United States). The C57BL6 and CD1 mice were purchased from the Vital River Laboratories (Beijing, China). All genotypes were determined by PCR.

Construction of Viral Plasmids and Adeno-Associated Virus Production and Injection

The control GFAP-GFP AAV vector containing an approximately 700 bp GFAP promoter (Kuzmanovic et al., 2003) was a gift from Bryan Roth (pAAV-GFAP-EGFP, Addgene plasmid #50473). The full-length open reading frames (ORFs) of murine Math5 and Brn3b alone or in combination via P2A or T2A were subcloned into this vector to construct desired AAV viral plasmids. By replacing GFP, we also used this vector as a backbone to construct the AAV plasmids expressing tdTomato or Cre. For construction of the FLEX Cre-Switch plasmid, the fusion ORF of Math5-P2A-Brn3b-T2A was amplified using a high fidelity DNA polymerase (Takara, R051S), and cloned into the *Kpn*I site of the CAG-FLEX-GFP vector (Addgene, #28304) by homologous recombination.

Adeno-associated virus production was performed as described previously with modification (Grieger et al., 2006). In brief, 20–24 h before transfection, AAV-293 cells (Sangon Biotech Co., Ltd., Shanghai, China) were cultured in 10 150-mm plates. For each plate, they were transfected with 6 μg of AAV vector DNA, 6 μg of AAV Rep/Cap plasmid DNA and 18 μg of adenovirus helper plasmid DNA using the Polyethylenimine (PEI) transfection method. After 60–72 h, the transfected cells were collected and resuspended in lysis buffer (150 mM NaCl, 20 mM Tris–HCl, pH8.0), then for three times frozen in dry ice/ethanol bath and thawed completely in 55°C water bath. The cell lysate was digested with Benzonase (50 U/ml) for 1 h at 37°C, and centrifuged to remove the cell debris. For purification, the virus-containing supernatant was applied to discontinuous iodixanol gradients followed by ultracentrifugation. The virus band was collected from the 40–60% interface using a syringe with a 21-gauge needle. The iodixanol solution was exchanged to 1x DPBS (Dulbecco's phosphate-buffered saline) using the Amicon Ultra-15 centrifugal filter units from Millipore and the viruses were further concentrated by shrinking the volume. Virus titers were determined by qRT-PCR using linearized plasmid standards and primers against the ITR. AAVs were injected subretinally or intravitreally into adult mouse eyes using a microsyringe with a 33-gauge needle as described (Mo et al., 2004; Yao et al., 2018).

Rabies-Virus *Trans*-Synaptic Tracing

For *trans*-synaptic tracing of the MG-derived RGCs→dLGN→V1 pathway, 0.6 μl of helper viruses containing a mixture of 0.2 μl each AAV9-hSyn-Cre, AAV9-EF1α-DIO-RVG, and AAV9-EF1α-DIO-BFP-T2A-TVA viruses (titer: 2–4 × 10^{12} particles/ml, BrainVTA, China) was injected into the dLGN of 2-month-old mice [AP (anterior-posterior: posterior to bregma): 2.2 mm; ML (midline to lateral): ±2.3 mm; DV (dorsoventral): 2.6 mm]. In addition, 2 μl of GFAP-Math5-Brn3b-tdTomato AAVs (titer: 2–4 × 10^{12} particles/ml) were injected subretinally into the eye. Three weeks later, 0.4 μl of ΔG-RABV-GFP rabies viruses (RV-ENVA-ΔG-EGFP, titer: 2 × 10^{8} particles/ml, BrainVTA, China) was injected into the V1 region (primary visual cortex) [AP (anterior to Lambda): 0.2–0.5 mm, ML: ±2.5 mm, DV: 0.15–0.5 mm]. Seven days after infection of rabies viruses, tissues were harvested and analyzed as described previously (Xiao et al., 2018).

Tamoxifen Administration

100 mg of tamoxifen (T5648, Sigma) was first dissolved in 1 ml of ethanol and then 4 ml of corn oil was added to a final concentration of 20 mg/ml. Glast-CreER mice were administered with tamoxifen intraperitoneally at a daily dose of 200 mg/kg body weight for four consecutive days.

Electrophysiology

Three weeks following infection of the eyes of adult wild-type and Brn3b-GFP reporter mice by GFAP-Math5-Brn3b-tdTomato AAVs, the retina was dissected out from the eyeball and its edge was removed to allow the tissue to lie flat. It was transferred to a recording chamber and bathed in external solution containing the Ames' medium (Sigma-Aldrich). The chamber was mounted on a microscope equipped with a 40× water immersion objective. The cells and recording pipettes were viewed on a monitor that was coupled to a camera (Scientifica SciCam Pro, Canada). Oxygenated external solution was continuously perfused into the recording chamber at a flow rate of 1.5–2 ml/min. tdTomato-positive cells were identified with a mercury lamp (TH4-200,

Olympus, Japan). Then, patch-clamp recordings were performed with a 700B amplifier (Molecular Devices, United States) and digitized at 10 kHz with a Digidata 1550B (Molecular Devices, United States). Alexa Fluor 488 hydrazide was used to label the patched cells. The action potentials of the cells were recorded under current clamp mode, with 6–9 MΩ resistance pipettes that were filled with an internal solution consisting of the following: 123 mM K-gluconate, 12 mM KCl, 10 mM HEPES, 0.2 mM EGTA, 4 mM Mg-ATP, 0.3 mM Na-GTP, 10 mM Na_2-phosphocreatine, and 20 μg/ml glycogen (the pH value was adjusted to 7.25 with 0.5 M KOH). For current-clamp recording, we set the initial resting membrane potential (V-rest) to −55 mV using a small, constant holding current and applied current pulses with a step size of 20 pA to test the ability to generate action potentials. The cells were held at −55 mV under voltage clamp mode to record sPSCs, and the patch pipettes (6–9 MΩ) were filled with an internal solution containing: 40 mM CsCl, 90 mM K-gluconate, 1.8 mM NaCl, 1.7 mM $MgCl_2$, 3.5 mM KCl, 0.05 mM EGTA, 10 mM HEPES, 2 mM Mg-ATP, 0.4 mM Na_2-GTP, and 10 mM Na_2-phosphocreatine (the pH value was adjusted to 7.25 with 0.1 M CsOH). To block responses mediated by ionotropic glutamate receptors, D-AP5 (50 μM) or CNQX (20 μM) was added to the external solution and perfused into the recording chamber.

For light response recordings, the dark-adapted mouse retina was isolated under far-red light and incubated in oxygenated Ames' medium (Sigma, A1420) with constant bubbling (95% O_2, 5% CO_2) at room temperature. Four sections were made to flat-mount the retina with RGCs facing up in a superfusion chamber on the stage of a custom-built upright fluorescence microscope. The recording chamber was perfused with Ames solution at 31–33°C and RGC bodies were visualized and recognized using upright IR light and green fluorescence. Light-evoked spikes of labeled RGCs were obtained with whole-cell current-clamp recording (Heka patch system) using patch pipettes, which had an impedance of 3–4 MΩ and were filled with high potassium internal solution (116 mM K^+ glucose, 12 mM KCl, 10 mM HEPES, 10 mM EGTA, 4 mM Mg-ATP, 0.3 mM Na-GTP, 0.3 mM $CaCl_2$, 0.5 mM $MgCl_2$). Light stimuli were delivered from a modified mercury bulb (Olympus) with band-pass filtering (530–550 nm, green), and focused onto the RGC side of the retina through a 40X water immersion objective. Intensities of green and blue light were equal and measured ($\log_{10}$ 7 photons/s/μm^2) using the calibrated photometer (Thorlabs, PM100D, S170C). Data were analyzed using MATLAB (MathWorks).

Optic Nerve Crush Injury

Mice were anesthetized by intraperitoneal injection of 4% chloral hydrate and one drop of 0.4% oxybuprocaine hydrochloride was administered for local anesthesia. ONC was performed as described (Li et al., 1999). Briefly, a small incision was made with scissors in the conjunctiva of the left eye located at the 3–9 o'clock of eyeball. The exposed optic nerve was grasped approximately 1 mm from the eyeball with forceps for 10 s. It was then released to allow the eyeball to rotate back into place. Three days following ONC, the left eye of each animal was infected with AAVs by subretinal injection.

Visual Evoked Potential Test

Two to six weeks after AAV injection, the ONC and *Brn3b*$^{AP/AP}$ mice were dark-adapted overnight, prior to being prepared for the experiments. They were anesthetized by intraperitoneal injection of 4% chloral hydrate and their pupils were dilated with a drop of tropicamide. One drop of 0.4% oxybuprocaine hydrochloride was administered for local anesthesia of the cornea.

During VEP recordings which were carried out using the Celeris ERG system (Diagnosys LLC, Lowell, MA, United States), the animals were placed on a heated platform to keep warm. Needle electrodes placed subcutaneously at the base of the tail and at the snout served as ground and reference electrodes, respectively. The active electrode was inserted subcutaneously at the midline at the back of the head. Two contact-lens light-emitting diodes (LEDs) were placed over the two eyes of the animal to serve as light stimulators. Each eye was separately exposed to white light flashes of 0.05 cd.s/m^2, swept 100 times per trial. For each mouse, we performed five trials. Analyses were performed using GraphPad Prism 8.

Immunohistochemistry

Immunostaining of retinal sections, retinal flat-mounts and optic nerves were carried out as previously described (Xiang et al., 1995; Li et al., 2004). Mouse brain tissues were immunostained as free floating sections also as previously described (Xiao et al., 2018). In brief, for section labeling, retinas were fixed in 4% paraformaldehyde (PFA) in PBS for 30 min at 4°C and sectioned at 14 μm. Sample sections were washed three times with 0.1% Tween in PBS (PBST) for 5 min each before being incubated in 5% normal donkey serum in PBST for 1 h at room temperature (RT). Then primary antibodies in 2% normal donkey serum in PBST were added for overnight incubation at 4°C. After washing with PBST, the sections were incubated with secondary antibodies and DAPI in PBST for 1 h at RT. Images were captured by a laser scanning confocal microscope (Carl Zeiss, LSM700).

The following primary antibodies were used: GFP (Abcam, ab6673, 1:2000), GFP (MBL, 598, 1:2000), RFP (Rockland antibodies and assays, 40657, 1:1000), tdTomato (Kerafast, EST203, 1:2000), Rbpms (Novus, NBP2-20112, 1:1000), Brn3a (Millipore, MAB1585, 1:500), Brn3b (Santa Cruz, SC-390780, 1:1000), Brn3c (Proteintech, 21509-1-AP, 1:1000), Sox9 (Millipore, ab5535, 1:1000), Sox9 (Abnova, H00006662-M02, 1:2000), Tfap2a and b (Abcam, ab11828, 1:1000), Pax2 (R&D Systems, AF3364, 1:1000), GFAP (DAKO, Z0334, 1:2000), S100β (Abcam, ab52642, 1:2000), Tuj1 (Covance, MMS-435P, 1:1000), melanopsin (Thermo Fisher Scientific, PA1-781, 1:100), Eomes (Abcam, ab23345, 1:2000), peripherin (Millipore, ab1530, 1:1000), Foxp2 (Abcam, ab16046, 1:4000), and Satb2 (Abcam, ab51501, 1:4000).

Single-Cell RNA Sequencing Analysis

Single-cell RNA sequencing (scRNA)-seq analysis was carried out as previously described (Xiao et al., 2020). In brief, 5.5 days after infection of adult mouse retinas with GFAP-Math5-Brn3b-GFP AAVs, two retinas were quickly dissected and dissociated

using papain with DNase I at 37°C for 5 min. Then isometric amount of DPBS containing 10% FBS was added and retinas were triturated by soft pipetting for dissociation. The dissociated cells were filtered using a 40-μm cell strainer. Filtered cells were centrifuged and resuspended with 2 ml DPBS containing 5% FBS. GFP^+ retinal cells were then enriched by fluorescence-activated cell sorting (FACS) using the FACSAria Fusion cell sorter (BD Biosciences). Single-cell libraries were generated from the enriched GFP+ cells and sequenced on the Illumina X Ten platform (Berry Genomics, China). Further analyses were performed using Seurat and Monocle (Xiao et al., 2020).

EdU Labeling and Detection

Following infection of adult mouse retinas with GFAP-Math5-Brn3b-GFP AAVs, 2 μl of EdU solution (1 mg/ml) was injected into the vitreous chamber of each eye at different time points. For sample collection, under deep anesthesia induced with intraperitoneal injection of chloral hydrate (4.5 μg/g body weight), mice were intracardially perfused with cold PBS for 5 min, followed by 4% cold PFA in PBS for 15 min. The eyeballs were isolated and post-fixed in 4% PFA for 1 h at 4°C. The retinas were dissected out and the vitreous was completely removed. They were shaped into a "petal" by 4–5 radial incisions, flattened in a 48-well plate, and permeabilized with 0.3% Triton-100 in PBST for 15 min at RT. After incubation in 10% normal donkey serum in PBST for 2 h at RT, the retinas were incubated in primary antibodies against Sox9 and GFP diluted in 2% normal donkey serum in PBST for 2 days at 4°C. Retinas were washed with PBST and incubated with secondary antibodies for 2 h. After three washes with PBS, the retinas were stained for EdU with the Click-iT EdU Kit (Invitrogen). Images were captured by a laser scanning confocal microscope (Carl Zeiss, LSM700).

Transmission Electron Microscopy

One month following infection of adult mouse retinas with GFAP-Math5-Brn3b-tdTomato AAVs or GFAP-tdTomato AAVs, electron microscopy of corresponding optic nerves was performed as previously described (Gan et al., 1996; Liu et al., 2020).

Statistics

Statistical analysis was performed using the GraphPad Prism 8 and Microsoft Excel computer programs. The results are expressed as mean ± SD for experiments conducted at least in triplicates. Unpaired two-tailed Student's *t*-test and one-way or two-way ANOVA with Bonferroni's correction were used to test for significance, and a value of $P < 0.05$ was considered statistically significant.

DATA AVAILABILITY STATEMENT

The datasets presented in this study can be found in online repositories. The names of the repository/repositories and accession number(s) can be found below: NCBI (accession: PRJNA648671).

ETHICS STATEMENT

The animal study was reviewed and approved by the Institutional Animal Care and Use Committee (IACUC), Zhongshan Ophthalmic Center, Sun Yat-sen University.

AUTHOR CONTRIBUTIONS

DX, KJ, SL, YL, and MX conceived and designed the research. DX, KJ, SQ, QL, WH, HC, BG, ZX, XT, FL, QX, MX, and JS performed the experiments and analyzed the data. DX, KJ, and MX interpreted the data and wrote the manuscript. All authors contributed to critical reading of the manuscript.

FUNDING

This work was supported in part by the National Natural Science Foundation of China (81670862, 81970794, 81721003, 81530028, 31871497, and 81870682), National Key R&D Program of China (2017YFA0104100), Local Innovative and Research Teams Project of Guangdong Pearl River Talents Program, Science and Technology Planning Projects of Guangzhou City (201904020036, 201904010358, and 2019A1515012033), China Postdoctoral Science Foundation (2019M650223), and Fundamental Research Funds of the State Key Laboratory of Ophthalmology, Sun Yat-sen University.

ACKNOWLEDGMENTS

We are grateful to William Klein (MD Anderson Cancer Center) for providing the *Brn3b*$^{AP/+}$ mice.

SUPPLEMENTARY MATERIAL

The Supplementary Material for this article can be found online at: https://www.frontiersin.org/articles/10.3389/fcell.2021.755544/full#supplementary-material

REFERENCES

Benowitz, L. I., He, Z., and Goldberg, J. L. (2017). Reaching the brain: advances in optic nerve regeneration. *Exp. Neurol.* 287, 365–373. doi: 10.1016/j.expneurol.2015.12.015

Bernardos, R. L., Barthel, L. K., Meyers, J. R., and Raymond, P. A. (2007). Late-stage neuronal progenitors in the retina are radial Müller glia that function as retinal stem cells. *J. Neurosci.* 27, 7028–7040. doi: 10.1523/jneurosci.1624-07.2007

Brown, N. L., Kanekar, S., Vetter, M. L., Tucker, P. K., Gemza, D. L., and Glaser, T. (1998). Math5 encodes a murine basic helix-loop-helix transcription factor expressed during early stages of retinal neurogenesis. *Development* 125, 4821–4833. doi: 10.1242/dev.125.23.4821

Brown, N. L., Patel, S., Brzezinski, J., and Glaser, T. (2001). Math5 is required for retinal ganglion cell and optic nerve formation. *Development* 128, 2497–2508. doi: 10.1242/dev.128.13.2497

Chang, K. C., Hertz, J., Zhang, X., Jin, X. L., Shaw, P., Derosa, B. A., et al. (2017). Novel regulatory mechanisms for the SoxC transcriptional network required for visual pathway development. *J. Neurosci.* 37, 4967–4981. doi: 10.1523/jneurosci.3430-13.2017

Chen, D. F., Jhaveri, S., and Schneider, G. E. (1995). Intrinsic changes in developing retinal neurons result in regenerative failure of their axons. *Proc. Natl. Acad. Sci. U. S. A.* 92, 7287–7291. doi: 10.1073/pnas.92.16.7287

Crair, M. C., and Mason, C. A. (2016). Reconnecting eye to brain. *J. Neurosci.* 36, 10707–10722. doi: 10.1523/jneurosci.1711-16.2016

de Lima, S., Koriyama, Y., Kurimoto, T., Oliveira, J. T., Yin, Y., Li, Y., et al. (2012). Full-length axon regeneration in the adult mouse optic nerve and partial recovery of simple visual behaviors. *Proc. Natl. Acad. Sci. U. S. A.* 109, 9149–9154. doi: 10.1073/pnas.1119449109

Dhande, O. S., Stafford, B. K., Franke, K., El-Danaf, R., Percival, K. A., Phan, A. H., et al. (2019). Molecular fingerprinting of on-off direction-selective retinal ganglion cells across species and relevance to primate visual circuits. *J. Neurosci.* 39, 78–95. doi: 10.1523/jneurosci.1784-18.2018

Dvoriantchikova, G., Seemungal, R. J., and Ivanov, D. (2019). The epigenetic basis for the impaired ability of adult murine retinal pigment epithelium cells to regenerate retinal tissue. *Sci. Rep.* 9:3860.

Erkman, L., McEvilly, R. J., Luo, L., Ryan, A. K., Hooshmand, F., O'Connell, S. M., et al. (1996). Role of transcription factors Brn-3.1 and Brn-3.2 in auditory and visual system development. *Nature* 381, 603–606. doi: 10.1038/381603a0

Erskine, L., and Herrera, E. (2007). The retinal ganglion cell axon's journey: insights into molecular mechanisms of axon guidance. *Dev. Biol.* 308, 1–14. doi: 10.1016/j.ydbio.2007.05.013

Gan, L., Wang, S. W., Huang, Z., and Klein, W. H. (1999). POU domain factor Brn-3b is essential for retinal ganglion cell differentiation and survival but not for initial cell fate specification. *Dev. Biol.* 210, 469–480. doi: 10.1006/dbio.1999.9280

Gan, L., Xiang, M., Zhou, L., Wagner, D. S., Klein, W. H., and Nathans, J. (1996). POU domain factor Brn-3b is required for the development of a large set of retinal ganglion cells. *Proc. Natl. Acad. Sci. U. S. A.* 93, 3920–3925. doi: 10.1073/pnas.93.9.3920

Goldman, D. (2014). Müller glial cell reprogramming and retina regeneration. *Nat. Rev. Neurosci.* 15, 431–442. doi: 10.1038/nrn3723

Grewe, R. (1986). The history of glaucoma. *Klin. Monbl. Augenheilkd.* 188, 167–169.

Grieger, J. C., Choi, V. W., and Samulski, R. J. (2006). Production and characterization of adeno-associated viral vectors. *Nat. Protoc.* 1, 1412–1428.

Heng, J. S., Rattner, A., Stein-O'Brien, G. L., Winer, B. L., Jones, B. W., Vernon, H. J., et al. (2019). Hypoxia tolerance in the Norrin-deficient retina and the chronically hypoxic brain studied at single-cell resolution. *Proc. Natl. Acad. Sci. U. S. A.* 116, 9103–9114. doi: 10.1073/pnas.1821122116

Herrera, E., Erskine, L., and Morenilla-Palao, C. (2019). Guidance of retinal axons in mammals. *Semin. Cell Dev. Biol.* 85, 48–59. doi: 10.1016/j.semcdb.2017.11.027

Jadhav, A. P., Roesch, K., and Cepko, C. L. (2009). Development and neurogenic potential of Müller glial cells in the vertebrate retina. *Prog. Retin Eye Res.* 28, 249–262. doi: 10.1016/j.preteyeres.2009.05.002

Jiang, Y., Ding, Q., Xie, X., Libby, R. T., Lefebvre, V., and Gan, L. (2013). Transcription factors SOX4 and SOX11 function redundantly to regulate the development of mouse retinal ganglion cells. *J. Biol. Chem.* 288, 18429–18438. doi: 10.1074/jbc.m113.478503

Jorstad, N. L., Wilken, M. S., Grimes, W. N., Wohl, S. G., VandenBosch, L. S., Yoshimatsu, T., et al. (2017). Stimulation of functional neuronal regeneration from Müller glia in adult mice. *Nature* 548, 103–107.

Kador, K. E., Alsehli, H. S., Zindell, A. N., Lau, L. W., Andreopoulos, F. M., Watson, B. D., et al. (2014). Retinal ganglion cell polarization using immobilized guidance cues on a tissue-engineered scaffold. *Acta Biomater.* 10, 4939–4946. doi: 10.1016/j.actbio.2014.08.032

Kador, K. E., Montero, R. B., Venugopalan, P., Hertz, J., Zindell, A. N., Valenzuela, D. A., et al. (2013). Tissue engineering the retinal ganglion cell nerve fiber layer. *Biomaterials* 34, 4242–4250.

Karl, M. O., Hayes, S., Nelson, B. R., Tan, K., Buckingham, B., and Reh, T. A. (2008). Stimulation of neural regeneration in the mouse retina. *Proc. Natl. Acad. Sci. U. S. A.* 105, 19508–19513. doi: 10.1073/pnas.0807453105

Kuwajima, T., Soares, C. A., Sitko, A. A., Lefebvre, V., and Mason, C. (2017). SoxC transcription factors promote contralateral retinal ganglion cell differentiation and axon guidance in the mouse visual system. *Neuron* 93, 1110–1125 e5.

Kuzmanovic, M., Dudley, V. J., and Sarthy, V. P. (2003). GFAP promoter drives Müller cell-specific expression in transgenic mice. *Invest. Ophthalmol. Vis. Sci.* 44, 3606–3613. doi: 10.1167/iovs.02-1265

Lenkowski, J. R., and Raymond, P. A. (2014). Müller glia: stem cells for generation and regeneration of retinal neurons in teleost fish. *Prog. Retin Eye Res.* 40, 94–123. doi: 10.1016/j.preteyeres.2013.12.007

Li, K., Zhong, X., Yang, S., Luo, Z., Li, K., Liu, Y., et al. (2017). HiPSC-derived retinal ganglion cells grow dendritic arbors and functional axons on a tissue-engineered scaffold. *Acta Biomater.* 54, 117–127. doi: 10.1016/j.actbio.2017.02.032

Li, S., Mo, Z., Yang, X., Price, S. M., Shen, M. M., and Xiang, M. (2004). Foxn4 controls the genesis of amacrine and horizontal cells by retinal progenitors. *Neuron* 43, 795–807. doi: 10.1016/j.neuron.2004.08.041

Li, Y., Schlamp, C. L., and Nickells, R. W. (1999). Experimental induction of retinal ganglion cell death in adult mice. *Invest. Ophthalmol. Vis. Sci.* 40, 1004–1008.

Lim, J. H., Stafford, B. K., Nguyen, P. L., Lien, B. V., Wang, C., Zukor, K., et al. (2016). Neural activity promotes long-distance, target-specific regeneration of adult retinal axons. *Nat. Neurosci.* 19, 1073–1084. doi: 10.1038/nn.4340

Liu, S., Liu, X., Li, S., Huang, X., Qian, H., Jin, K., et al. (2020). Foxn4 is a temporal identity factor conferring mid/late-early retinal competence and involved in retinal synaptogenesis. *Proc. Natl. Acad. Sci. U. S. A.* 117, 5016–5027. doi: 10.1073/pnas.1918628117

Liu, W., Khare, S. L., Liang, X., Peters, M. A., Liu, X., Cepko, C. L., et al. (2000). All Brn3 genes can promote retinal ganglion cell differentiation in the chick. *Development* 127, 3237–3247. doi: 10.1242/dev.127.15.3237

Liu, W., Mo, Z., and Xiang, M. (2001). The Ath5 proneural genes function upstream of Brn3 POU domain transcription factor genes to promote retinal ganglion cell development. *Proc. Natl. Acad. Sci. U. S. A.* 98, 1649–1654. doi: 10.1073/pnas.98.4.1649

Mao, C. A., Li, H., Zhang, Z., Kiyama, T., Panda, S., Hattar, S., et al. (2014). T-box transcription regulator Tbr2 is essential for the formation and maintenance of Opn4/melanopsin-expressing intrinsically photosensitive retinal ganglion cells. *J. Neurosci.* 34, 13083–13095. doi: 10.1523/jneurosci.1027-14.2014

McLaughlin, T., and O'Leary, D. D. (2005). Molecular gradients and development of retinotopic maps. *Annu. Rev. Neurosci.* 28, 327–355.

Mo, Z., Li, S., Yang, X., and Xiang, M. (2004). Role of the Barhl2 homeobox gene in the specification of glycinergic amacrine cells. *Development* 131, 1607–1618. doi: 10.1242/dev.01071

Mu, X., Fu, X., Beremand, P. D., Thomas, T. L., and Klein, W. H. (2008). Gene regulation logic in retinal ganglion cell development: Isl1 defines a critical branch distinct from but overlapping with Pou4f2. *Proc. Natl. Acad. Sci. U. S. A.* 105, 6942–6947. doi: 10.1073/pnas.0802627105

Ooto, S., Akagi, T., Kageyama, R., Akita, J., Mandai, M., Honda, Y., et al. (2004). Potential for neural regeneration after neurotoxic injury in the adult mammalian retina. *Proc. Natl. Acad. Sci. U. S. A.* 101, 13654–13659. doi: 10.1073/pnas.0402129101

Oster, S. F., Deiner, M., Birgbauer, E., and Sretavan, D. W. (2004). Ganglion cell axon pathfinding in the retina and optic nerve. *Semin. Cell Dev. Biol.* 15, 125–136. doi: 10.1016/j.semcdb.2003.09.006

Pan, L., Deng, M., Xie, X., and Gan, L. (2008). ISL1 and BRN3B co-regulate the differentiation of murine retinal ganglion cells. *Development* 135, 1981–1990. doi: 10.1242/dev.010751

Petros, T. J., Rebsam, A., and Mason, C. A. (2008). Retinal axon growth at the optic chiasm: to cross or not to cross. *Annu. Rev. Neurosci.* 31, 295–315. doi: 10.1146/annurev.neuro.31.060407.125609

Qiu, F., Jiang, H., and Xiang, M. (2008). A comprehensive negative regulatory program controlled by Brn3b to ensure ganglion cell specification from multipotential retinal precursors. *J. Neurosci.* 28, 3392–3403. doi: 10.1523/jneurosci.0043-08.2008

Quigley, H. A. (2011). Glaucoma. *Lancet* 377, 1367–1377.

Quigley, H. A., and Broman, A. T. (2006). The number of people with glaucoma worldwide in 2010 and 2020. *Br. J. Ophthalmol.* 90, 262–267. doi: 10.1136/bjo.2005.081224

Roesch, K., Jadhav, A. P., Trimarchi, J. M., Stadler, M. B., Roska, B., Sun, B. B., et al. (2008). The transcriptome of retinal Müller glial cells. *J. Comp. Neurol.* 509, 225–238.

Rousso, D. L., Qiao, M., Kagan, R. D., Yamagata, M., Palmiter, R. D., and Sanes, J. R. (2016). Two pairs of ON and OFF retinal ganglion cells are defined by intersectional patterns of transcription factor expression. *Cell Rep.* 15, 1930–1944. doi: 10.1016/j.celrep.2016.04.069

Stanke, J., Moose, H. E., El-Hodiri, H. M., and Fischer, A. J. (2010). Comparative study of Pax2 expression in glial cells in the retina and optic nerve of birds and mammals. *J. Comp. Neurol.* 518, 2316–2333. doi: 10.1002/cne.22335

Ueki, Y., Wilken, M. S., Cox, K. E., Chipman, L., Jorstad, N., Sternhagen, K., et al. (2015). Transgenic expression of the proneural transcription factor Ascl1 in Müller glia stimulates retinal regeneration in young mice. *Proc. Natl. Acad. Sci. U. S. A.* 112, 13717–13722. doi: 10.1073/pnas.1510595112

Venugopalan, P., Wang, Y., Nguyen, T., Huang, A., Muller, K. J., and Goldberg, J. L. (2016). Transplanted neurons integrate into adult retinas and respond to light. *Nat. Commun.* 7:10472.

Wang, S. W., Kim, B. S., Ding, K., Wang, H., Sun, D., Johnson, R. L., et al. (2001). Requirement for math5 in the development of retinal ganglion cells. *Genes Dev.* 15, 24–29. doi: 10.1101/gad.855301

Wilken, M. S., and Reh, T. A. (2016). Retinal regeneration in birds and mice. *Curr. Opin. Genet. Dev.* 40, 57–64. doi: 10.1016/j.gde.2016.05.028

Wu, F., Bard, J. E., Kann, J., Yergeau, D., Sapkota, D., Ge, Y., et al. (2021). Single cell transcriptomics reveals lineage trajectory of retinal ganglion cells in wild-type and Atoh7-null retinas. *Nat. Commun.* 12:1465.

Wu, F., Kaczynski, T. J., Sethuramanujam, S., Li, R., Jain, V., Slaughter, M., et al. (2015). Two transcription factors, Pou4f2 and Isl1, are sufficient to specify the retinal ganglion cell fate. *Proc. Natl. Acad. Sci. U. S. A.* 112, E1559–E1568.

Xiang, M. (1998). Requirement for Brn-3b in early differentiation of postmitotic retinal ganglion cell precursors. *Dev. Biol.* 197, 155–169. doi: 10.1006/dbio.1998.8868

Xiang, M. (2013). Intrinsic control of mammalian retinogenesis. *Cell. Mol. Life Sci.* 70, 2519–2532. doi: 10.1007/s00018-012-1183-2

Xiang, M., Zhou, L., Macke, J. P., Yoshioka, T., Hendry, S. H., Eddy, R. L., et al. (1995). The Brn-3 family of POU-domain factors: primary structure, binding specificity, and expression in subsets of retinal ganglion cells and somatosensory neurons. *J. Neurosci.* 15, 4762–4785. doi: 10.1523/jneurosci.15-07-04762.1995

Xiang, M., Zhou, L., Peng, Y. W., Eddy, R. L., Shows, T. B., and Nathans, J. (1993). Brn-3b: a POU domain gene expressed in a subset of retinal ganglion cells. *Neuron* 11, 689–701. doi: 10.1016/0896-6273(93)90079-7

Xiao, D., Deng, Q., Guo, Y., Huang, X., Zou, M., Zhong, J., et al. (2020). Generation of self-organized sensory ganglion organoids and retinal ganglion cells from fibroblasts. *Sci. Adv.* 6:eaaz5858. doi: 10.1126/sciadv.aaz5858

Xiao, D., Liu, X., Zhang, M., Zou, M., Deng, Q., Sun, D., et al. (2018). Direct reprogramming of fibroblasts into neural stem cells by single non-neural progenitor transcription factor Ptf1a. *Nat. Commun.* 9:2865.

Yang, Z., Ding, K., Pan, L., Deng, M., and Gan, L. (2003). Math5 determines the competence state of retinal ganglion cell progenitors. *Dev. Biol.* 264, 240–254. doi: 10.1016/j.ydbio.2003.08.005

Yao, K., Qiu, S., Wang, Y. V., Park, S. J. H., Mohns, E. J., Mehta, B., et al. (2018). Restoration of vision after de novo genesis of rod photoreceptors in mammalian retinas. *Nature* 560, 484–488. doi: 10.1038/s41586-018-0425-3

Zhou, H., Su, J., Hu, X., Zhou, C., Li, H., Chen, Z., et al. (2020). Glia-to-neuron conversion by CRISPR-CasRx alleviates symptoms of neurological disease in mice. *Cell* 181, 590–603e516. , 590-603 e516

Conflict of Interest: The authors declare that the research was conducted in the absence of any commercial or financial relationships that could be construed as a potential conflict of interest.

Publisher's Note: All claims expressed in this article are solely those of the authors and do not necessarily represent those of their affiliated organizations, or those of the publisher, the editors and the reviewers. Any product that may be evaluated in this article, or claim that may be made by its manufacturer, is not guaranteed or endorsed by the publisher.

Copyright © 2021 Xiao, Jin, Qiu, Lei, Huang, Chen, Su, Xu, Xu, Gou, Tie, Liu, Liu, Liu and Xiang. This is an open-access article distributed under the terms of the Creative Commons Attribution License (CC BY). The use, distribution or reproduction in other forums is permitted, provided the original author(s) and the copyright owner(s) are credited and that the original publication in this journal is cited, in accordance with accepted academic practice. No use, distribution or reproduction is permitted which does not comply with these terms.

frontiers in Cell and Developmental Biology

ORIGINAL RESEARCH
published: 05 October 2021
doi: 10.3389/fcell.2021.754676

Mitochondrial Mutations in Ethambutol-Induced Optic Neuropathy

Xiao-Hui Zhang[1,2], Yue Xie[2], Quan-Gang Xu[1], Kai Cao[2], Ke Xu[2], Zi-Bing Jin[2], Yang Li[2]* and Shi-Hui Wei[1]**

[1] Department of Ophthalmology, The Chinese People's Liberation Army General Hospital, The Chinese People's Liberation Army Medical School, Beijing, China, [2] Beijing Ophthalmology and Visual Sciences Key Laboratory, Beijing Institute of Ophthalmology, Beijing Tongren Eye Center, Beijing Tongren Hospital, Capital Medical University, Beijing, China

Background: Ethambutol-induced optic neuropathy (EON) is a well-recognized ocular complication in patients who take ethambutol as a tuberculosis treatment. The aim of the current study was to investigate the presence of mitochondrial mutations, including *OPA1* and Leber's hereditary optic neuropathy (LHON)-mitochondrial DNA (mtDNA), in patients with EON and to determine their effect on clinical features of these patients.

Methods: All 47 patients underwent clinical evaluations, including best-corrected visual acuity, fundus examination, and color fundus photography; 37 patients were then followed up over time. Molecular screening methods, including PCR-based sequencing of the *OPA1* gene and LHON-mtDNA mutations, together with targeted exome sequencing, were used to detect mutations.

Results: We detected 15 *OPA1* mutations in 18 patients and two LHON-mtDNA mutations in four patients, for an overall mutation detection rate of 46.8%. The mean presentation age was significantly younger in the patients with the mitochondrial mutations (27.5 years) than in those without mutations (48 years). Fundus examination revealed a greater prevalence of optic disc hyperemia in the patients with mutations (70.5%) than without mutations (48%). Half of the patients with mutations and 91% of the patients without mutations had improved vision. After adjusting for confounders, the logistic regression revealed that the patients with optic disc pallor on the first visit ($p = 0.004$) or the patients with the mitochondrial mutations ($p < 0.001$) had a poorer vision prognosis.

Conclusion: Our results indicated that carriers with *OPA1* mutations might be more vulnerable for the toxicity of EMB to develop EON.

Keywords: ethambutol, optic neuropathy, *OPA1*, mitochondrial DNA, mutation

OPEN ACCESS

Edited by:
Ling Zhao,
Sun Yat-sen University, China

Reviewed by:
Chunqiao Liu,
Sun Yat-sen University, China
Wenjuan Zhuang,
Ningxia Hui Autonomous Region People's Hospital, China

****Correspondence:***
Zi-Bing Jin
jinzb@mail.eye.ac.cn
Yang Li
yilbio@163.com
Shi-Hui Wei
weishihui706@hotmail.com

Specialty section:
This article was submitted to Molecular and Cellular Pathology, a section of the journal Frontiers in Cell and Developmental Biology

Received: *06 August 2021*
Accepted: *15 September 2021*
Published: *05 October 2021*

Citation:
Zhang XH, Xie Y, Xu QG, Cao K, Xu K, Jin ZB, Li Y and Wei SH (2021) Mitochondrial Mutations in Ethambutol-Induced Optic Neuropathy. Front. Cell Dev. Biol. 9:754676. doi: 10.3389/fcell.2021.754676

INTRODUCTION

Ethambutol (EMB), one of the first-line drugs used to treat tuberculosis, works by inhibiting the arabinosyl transferase of mycobacteria (Belanger et al., 1996). However, its use is associated with a well-recognized ocular complication, ethambutol-induced optic neuropathy (EON), which is characterized by blurring of the vision, dyschromatopsia, and central or cecocentral scotoma

(Carr and Henkind, 1962). The ocular symptoms usually appear after 7 to 8 months of treatment with EMB, and the development of EON is both time- and dose-dependent (Fraunfelder et al., 2006; Lee et al., 2008). The incidence of EON is about 1% in patients prescribed an EMB dose at 15 mg/kg/d (Santaella and Fraunfelder, 2007; Yang et al., 2016). The risk factors for the occurrence of EON include older age, low body weight, and renal dysfunction (Chen et al., 2012). About 30 to 54% of the patients have varying degrees of vision recovery at 3 to 7 months after EMB discontinuation (Lee et al., 2008; Ezer et al., 2013); however, some patients have severe and permanent visual loss, even without the known risk factors. Therefore, other predisposing factors might exist for EON.

At present, the pathophysiology of EON still remains unclear. Several previous studies have indicated that EMB disrupts energy metabolism and the network structure of mitochondria by inducing severe vacuole formation and by decreasing membrane potential (Chung et al., 2009; Guillet et al., 2010). Dotti et al. (1998) first described the m.G11778A mitochondrial DNA (mtDNA) mutation in an EON patient, pointing to a relationship between mitochondrial mutation and the development of EON. Leber's hereditary optic neuropathy (LHON) is caused by mtDNA mutations that disrupt complex I activity of the mitochondrial respiratory chain and ATP synthesis (Zhang et al., 2018). Autosomal dominant optic atrophy (ADOA) is another form of mitochondrial optic neuropathy that is caused by mutations of the *OPA1* gene (Delettre et al., 2000). The *OPA1* gene encodes a dynamin-related GTPase, which is localized at the inner membrane of mitochondria and plays a role in mitochondrial fusion (Kao et al., 2015).

Both LHON and ADOA have a common pathophysiological outcome, which is mitochondrial energy deficiency and retinal ganglion cell apoptosis (Kao et al., 2015; Zhang et al., 2018). The current literature reports 8 patients carrying LHON mtDNA mutations and 2 patients harboring *OPA1* mutations who developed optic neuropathy during the use of EMB (Dotti et al., 1998; De Marinis, 2001; Hwang et al., 2003; Chowdhury et al., 2006; Ikeda et al., 2006; Guillet et al., 2010; Pradhan et al., 2010; Seo et al., 2010). Most of these studies are case reports, and the final clinical diagnosis is controversial for those patients. The relationship between the mitochondrial mutations and the clinical features of EON has not been fully studied.

In the present study, we investigated the presence of mitochondrial mutations (*OPA1* and LHON-mtDNA) in a cohort of 47 patients with EON. We also studied the effects of these mutations on the clinical features of the patients by performing genetic analysis and identified disease-causing gene mutations in 22 patients.

MATERIALS AND METHODS

Patients

This study was approved by the Medical Ethics Committee of Beijing Tongren Hospital. All investigations followed the tenets of the Declaration of Helsinki. Clinical data were retrospectively collected from outpatient and hospitalized patients diagnosed with EON from 2011 to 2018 at the Department of Ophthalmology in Chinese People's Liberation Army General Hospital and at the Genetics Laboratory of the Beijing Institute of Ophthalmology at Beijing Tongren Hospital. Blood was taken at initial presentation for genetic analysis with the patients' or their parents'/guardians' consent. We recruited a total of 47 unrelated patients, and 37 patients were followed up either by revisit evaluation (two patients) or by telephone surveys (35 patients). All patients underwent ophthalmological evaluations, including the best corrected visual acuity (BCVA), slit-lamp biomicroscopy, fundus examination, and color fundus photography. Some patients had color perception tests (Lanthony 15-Hue, Farnsworth D-15, or Ishihara color plates), Octopus or Humphry visual field tests, and spectral domain OCT examinations. We extracted genomic DNA from peripheral blood leukocytes from all patients and from available family members, following the manufacturer's instructions (Vigorous, Beijing, China).

The inclusion criteria for EON were based on previous guidelines (Fraunfelder et al., 2006; Lee et al., 2008). The diagnosis had to satisfy the major criterion and at least two of the minor criteria. The major criterion is vision loss appearing only after taking EMB and within 2 months after discontinuation of the drug. The minor criteria are: (1) abnormal results on color perception tests, and (2) central, paracentral, or cecocentral scotoma or temporal hemianopia on visual field examinations, and (3) optic disc hyperemia or pallor on color fundus photography. Exclusion criteria include optic neuritis, glaucoma, and other retinal diseases.

PCR-Based Sequencing of the *OPA1* Gene and Leber's Hereditary Optic Neuropathy-mtDNA

All coding regions of the *OPA1* gene and 19 primary LHON-mtDNA mutations were amplified by PCR in 36 patients. The primer sequences and the product lengths for amplification were described previously (Chen et al., 2014). The 19 primary LHON-mtDNA mutations included m.11778G > A, m.3460G > A, m.14484T > C, m.3376G > A, m.3635G > A, m.3697G > A, m.3700G > A, m.3733G > A, m.4171C > A, m.10197G > A, m.10663T > C, m.13051G > A, m.13094T > C, m.14459G > A, m.14482C > A, m.14482C > G, m.14495A > G, m.14502T > C, and m.14568C > T [1]. Purified PCR products were sequenced with an ABI PRISM 3730 DNA sequencer (Applied Biosystems, Foster City, CA, United States). Sequencing data were compared with the GenBank sequence for the *OPA1* gene (NM_015560) and mtDNA sequence (AC_000021.2).

Targeted Exome Sequencing

Eleven patients were investigated by TES with a capture panel including 194 known neuro-ophthalmological genes (**Supplementary Table 1**). The Illumina library preparation and capture experiments were performed as previously reported (Sun et al., 2018). Briefly, genomic DNA was fragmented

[1] https://www.mitomap.org

by endonuclease digestion and used to capture the targeted genomic sequences. The amplicon-based enrichment library was sequenced on an Illumina NextSeq 500 (Illumina, Inc., San Diego, CA, United States). After removing the sequencing adapters, low quality reads, and duplicated reads, the high quality reads were aligned with the reference human genome (hg19) using the Burrows-Wheeler Aligner. Single nucleotide polymorphisms and insertions or deletions were called using the Genomic Analysis Toolkit Haplotype Caller.

Bioinformatics Analysis

The potential functional impacts of missense mutations were evaluated with Polyphen-2 [2], Mutation Taster [3], and SIFT[4]. The effect of splicing mutations was analyzed with NetGene2[5] and BDGP [6]. The allele frequency of the variants was confirmed in the 1,000 Genome Project[7] and ExAC[8]. Co-segregation analysis was performed in available family members to verify the suspected mutations. We classified the variants into pathogenic, likely pathogenic, uncertain of significant, likely benign, and benign according to the guidelines published by the American Academy of Medical Genetics and Genomics (ACMG) (Richards et al., 2015).

Statistical Analysis

We converted the Snellen ratios into logarithm of the minimum angle of resolution (logMAR) values for statistical purpose. LogMAR values of 0, 1.0, and 2.0 are equal to a Snellen vision of 1.0, 0.1, and counting fingers, respectively (Holladay, 1997). The Wilcoxon rank sum test and Pearson Chi-square or Fisher's exact test were used to analyze the quantitative and categorical data, respectively. The Kruskal–Wallis test or multivariate logistic regression was used to analyze correlations. We performed all statistical analysis using SPSS version 22 software (IBM Corporation, New York, United States). The statistical significance level was 5%.

RESULTS

Mitochondrial Mutation Detection Rate and Related Mutations

We detected *OPA1* and LHON-mtDNA mutations in 22 of the 47 patients with EON, for an overall mutation detection rate of 46.8%. Mutations in 15 patients were detected by Sanger sequencing and mutations in 7 patients were detected by TES (**Supplementary Table 2**). The average coverage of the TES was 99.8%. The average sequencing depth was 288X. About 99% of the data had a depth of 10X or more.

We identified 15 distinct mutations of the *OPA1* gene in 18 patients (**Supplementary Figure 1**), for a detection rate of 38.3%. According to the ACMG guidelines, 13 mutations were defined as pathogenic and two mutations were defined as likely pathogenic (**Table 1**). Of these mutations, 8 were newly detected in the current study. These mutations included five (33.3%) nonsense, four (26.5%) frameshift indels, three (20%) splicing defects, two (13.3%) missense, and one (7%) large deletion mutation (**Table 1**). The most common mutation was c.2708_2711delTTAG (p.V903Gfs*3), with an allele frequency of 22.2% (4/18); the remaining 14 mutations were detected only once. The eight novel mutations included three frameshift indels, two missense, one splicing effect, one nonsense, and one large deletion. None of these novel mutations were observed in the public databases. The two missense mutations were predicted as disease-causing by three *in silico* analysis programs (**Table 1**).

We detected the m.11778G > A mutation in two patients and the m.14484T > C mutation in two patients. The detection rate of LHON-mtDNA mutations was 8.5%.

Demographics and Clinical Characteristics of All Patients

The 47 patients in the current study included 31 males and 16 females, for a male-to-female ratio of 1.9:1 (**Supplementary Table 2**). Of these patients, seven had a family history of optic neuropathy, two carrying an *OPA1* mutation and four harboring an mtDNA mutation. The mean age of presentation was 39 years (range 16–74 years). The mean daily dose of EMB was 12.9 mg/kg (range 3.8–29.2 mg/kg) and the mean medication duration was 4 months (range 1–24 months). All patients had a major complaint of blurred vision, and 41 (87.2%) of them experienced the visual impairment simultaneously in both eyes. The mean course of the disease, defined as the time interval from the vision loss to the first visit, was 2 months (range 0.5–24 months). Eight patients had a complaint of ocular pain, numbness of a lower extremity, or hearing loss. Their mean BCVA was 1.0 (logMAR; range 0.5–1.3), which was not correlated with their daily EMB dose ($p = 0.646$), their medication duration ($p = 0.099$), or the course of their disease ($p = 0.939$).

Fundus examination revealed a symmetrical fundus appearance in 43 patients (91.5%). Of the 94 eyes, 46 (48.9%) showed optic disc hyperemia and retinal nerve fiber layer (RNFL) swelling, 15 (16.0%) had temporal disc pallor, nine (9.6%) presented with nasal disc hyperemia and temporal disc pallor, four (4.2%) showed total disc pallor, and 20 (21.3%) presented a normal optic disc appearance (**Figure 1**). Unilateral retinal hemorrhage was observed in four patients (**Figure 2**). The result of logistic regression showed that the patients with optic disc pallor had a longer course of disease compared with patients with optic disc hyperemia or with normal optic disc appearance ($p < 0.001$).

Of the 33 patients (61 eyes) who had a color perception test, 23 eyes (37.7%) presented with red/green color vision impairment, 22 eyes (36.1%) showed total color blindness, eight eyes (13.1%) presented with yellow/blue color vision impairment, and eight eyes (13.1%) showed normal color perception. Of the

[2]http://genetics.bwh.harvard.edu/pph2/
[3]http://www.mutationtaster.org/
[4]http://provean.jcvi.org/index.php
[5]http://www.cbs.dtu.dk/services/NetGene2/
[6]http://www.fruitfly.org/seq_tools/splice.html
[7]http://browser.1000genomes.org/index.html
[8]http://exac.broadinstitute.org/

TABLE 1 | Fifteen mutations of the *OPA1* gene identified in this study.

cDNA change	Protein change	Protein domain	Allele number	Polyphen-2	Mutation Taster	SIFT	PROVEAN	NetGene2	BDGP	1000G	ExAC	gnomAD	References	ACMG
c.32 + 1G > C	-	basic	1		DC			donor loss	donor loss	N	N	N	This study	P
c.154C > T	p.R52X	basic	1		DC					N	N	4.02E-06	Ban et al., 2007	P
c.544_545 insT	p.T184Yfs*11	-	1		DC					N	N	N	This study	P
c.934C > T	p.R312X	GTPase	1		DC					N	N	N	Cardaioli et al., 2006	P
exon12-17 deletion	-	GTPase, dynamin	1		-					N	N	N	This study	P
c.1516 + 1G > A	-	GTPase	1		DC			donor loss	donor loss	N	N	N	Santarelli et al., 2015	P
c.1631T > A	p.L544X	dynamin	1		DC					N	N	N	This study	P
c.1847 + 1_ + 4del	-	dynamin	1		DC			donor loss	donor loss	N	N	N	Ferré et al., 2009	P
c.1808A > C	p.D603A	dynamin	1	PD	DC	D	Deleterious	no splice sites change	no splice sites change	N	N	N	This study	LP
c.2111T > A	p.V704D	dynamin	1	PD	DC	D	Deleterious	no splice sites change	no splice sites change	N	N	N	This study	LP
c.2121_2124del	p.S708Lfs*14	dynamin	1		DC					N	N	N	This study	P
c.2131C > T	p.R711X	dynamin	1		DC					N	N	N	Delettre et al., 2001	P
c.2197C > T	p.R733X	dynamin	1		DC					N	N	N	Li et al., 2008	P
c.2246_2247insTTA	p.E749Dfs*2	dynamin	1		DC					N	N	N	This study	P
c.2708_2711delTTAG	p.V903Gfs*3	GTPase effector	4		DC					N	N	N	Delettre et al., 2000	P

PD, probably damaging; DC, disease causing; D, damaging; N, none; P, pathogenic; LP, likely pathogenic.

33 patients (66 eyes) who had a visual field examination, 31 eyes (47%) presented with central scotoma, 23 eyes (34.8%) showed cecocentral scotoma, six eyes (9.1%) presented with paracentral scotoma, and six eyes (9.1%) showed temporal hemianopia.

The 37 patients were followed up over time (range 1–87 months), with a mean follow-up time of 15 months. Patient E005, carrying *OPA1* mutation p.R52X, and patient A3124, without mutations, underwent revisit examinations. After 4 years of follow-up, the BCVA of patient E005 improved from 0.02 in the right eye and 0.04 in the left eye to 0.1 in both eyes. The RNFL thickness at the temporal side of binocular optic discs was below the limits (**Figure 3**). After 11 months of follow-up, the BCVA of patient A3124 improved from 0.05 in the right eye and 0.03 in the left eye to 0.5 and 0.3, respectively. Fundus photography showed the optic disc hyperemia resolved at follow-up in both eyes (**Figure 3**). Of the remaining patients, 26 patients stated their VA had improved, eight patients reported their VA was unchanged, and one patient said his VA had worsened. None of patients with VA improved underwent cataract surgery or other intervention that would affect the assessment of visual outcome. The mean recovery time of the VA was 4 months (range 1–12 months). After adjusting for any confounders, the logistic regression revealed that the patients with optic disc pallor on the first visit ($p = 0.004$) or the patients with the mitochondrial mutations ($p < 0.001$) had a poorer vision prognosis (**Supplementary Table 3**).

Comparison of Patients With Mitochondrial Mutations and Without Mutations

To simplify the description and statistical analysis, we divided the 47 patients into two groups: group 1 consisted of the patients carrying mitochondrial mutations and group 2 included the patients without mitochondrial mutations. We compared the difference in the demographics, EMB medications (**Table 2**), and clinical characteristics (**Table 3**) between the patients in the two groups. The mean visiting age was significantly younger in group 1 (27.5 years) than in group 2 (48 years). The percentage of patients with a family history was statistically higher in group 1 (27%) than in group 2 (4%). The percentage of eyes with optic disc hyperemia was higher in group 1 than in group 2. The visual outcome was better for group 2 than for group 1. Among the nine patients whose VA did not improve, six patients (66.7%) carried *OPA1* mutations and one patient (11.1%) carried the m.G11778A mutation.

DISCUSSION

The current study investigated the mitochondrial mutations in 47 unrelated patients with EON and described the clinical characteristics of the patients. We identified *OPA1* mutations in 18 (38.3%) patients and LHON-mtDNA mutations in four (8.5%) patients. EON is a dose-dependent form of toxic neuropathy related to several other risk factors, such as renal dysfunction and older age (Santaella and Fraunfelder, 2007; Chen et al., 2012; Yang et al., 2016). In the current cohort, 91.5% of the patients with EON had taken low-dose EMB ($\leq$ 15mg/kg/day),

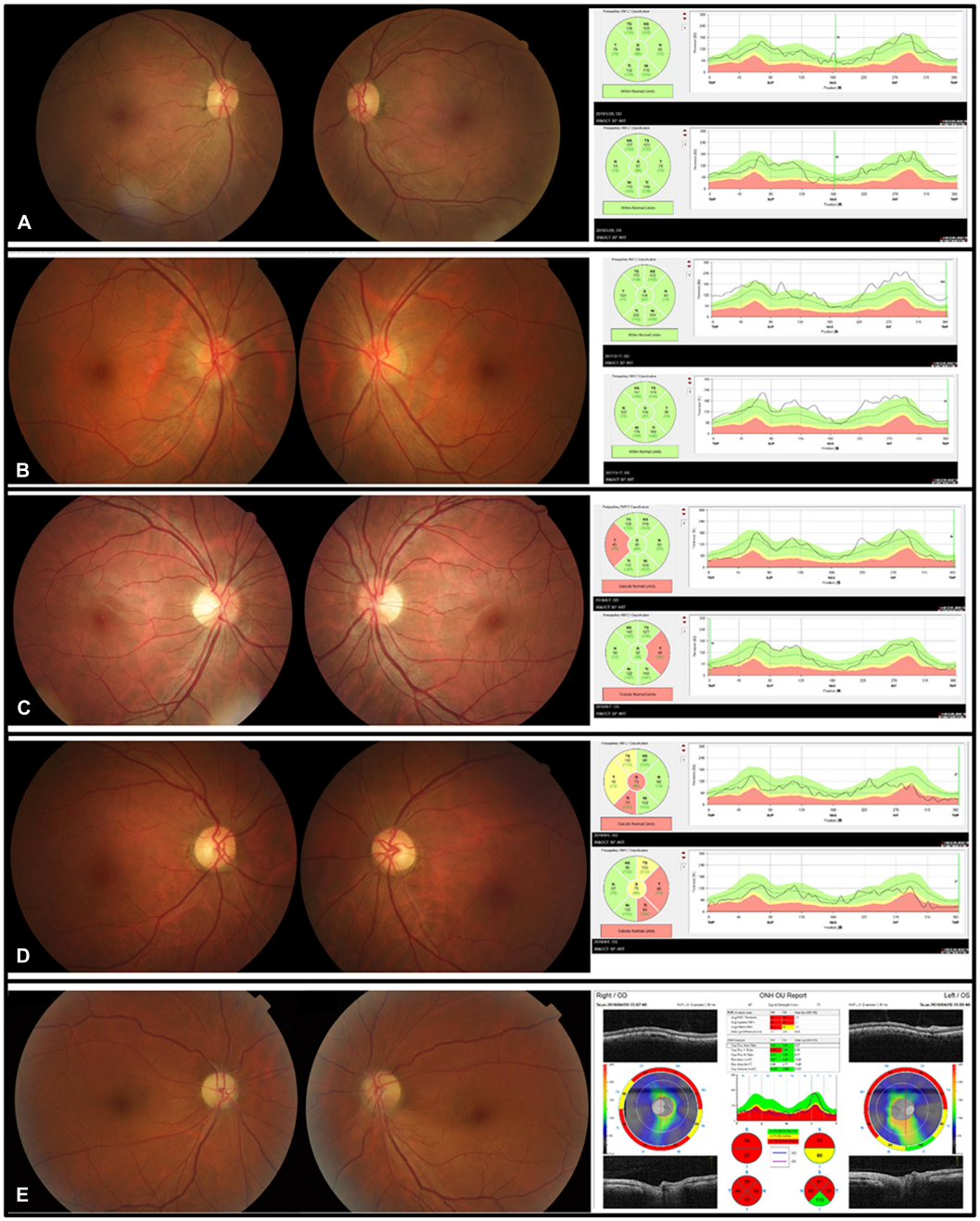

FIGURE 1 | Five kinds of disc appearances and OCT images in five patients with EON. **(A)** The disc appearance and the RNFL thickness were normal. **(B)** The optic discs were hyperemic. The superior, temporal, and inferior RNFL was thickened. **(C)** The border of the nasal discs was blurred and the temporal discs were pale. The temporal RNFL thickness was thinner than normal. **(D)** The temporal discs were pale and the temporal RNFL became thin. **(E)** The optic discs were pale, with the inferior border of the disc blurred in the left eye.

95.7% of the patients had a normal renal function, and 89.4% of the patients were younger than 60 years; therefore, the risk of developing ocular toxicity was relatively low in our cohort. Our results suggested that mitochondrial genetic variations, and especially *OPA1* mutations, are major predisposing factors for the occurrence of toxic optic neuropathy.

Mutations of the *OPA1* gene are responsible for 50–70% of ADOA, (Cohn et al., 2007; Yu-Wai-Man et al., 2010) which is the most common form of inherited optic neuropathy. *OPA1*-related ADOA is usually a mild and slowly progressive disorder (Cohn et al., 2007). Typically, patients suffer an insidious, symmetrical, and progressive visual defect in their childhood; however, the

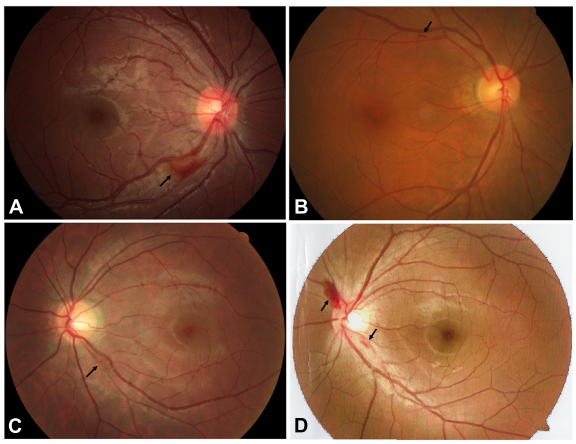

FIGURE 2 | Fundus appearance of 4 patients with retinal hemorrhage (black arrows). **(A)** Retinal hemorrhage located at the inferior temporal side of the optic disc in the right eye of the patient A781. **(B)** Retinal hemorrhage located at the superior temporal side of the optic disc in the right eye of the patient A2579. **(C)** Retinal hemorrhage located at the inferior temporal side of the optic disc in the left eye of the patient A3198. **(D)** Retinal hemorrhages located at the border of the optic disc in the left eye of the patient E004.

severity of visual impairment is highly variable (Cohn et al., 2007). About 10–20% of mutation carriers are "asymptomatic," as they have a normal visual acuity or only a subtle visual disturbance (Cohn et al., 2007; Yu-Wai-Man et al., 2010). In the current cohort, we identified different kinds of mutations of the *OPA1* gene, but the type and location of these mutations were similar to those reported in typical patients with ADOA, (Cohn et al., 2007; Ferré et al., 2009; Yu-Wai-Man et al., 2010; Chen et al., 2014) except for the low frequency (13%, 2/15) of missense mutations. This frequency was only the half rate observed previously in patients with ADOA (approximately 27%) (Chen et al., 2014). Another previous study indicated that vision loss was usually more severe in patients with missense mutations than with null mutations (Yu-Wai-Man et al., 2010). Unlike the typical patients with ADOA, the *OPA1* mutation carriers in the current study all experienced a subacute visual loss while taking EMB therapy, and none of them noticed a visual abnormality before the treatment; therefore, they might be "asymptomatic" cases. In addition, 71% of the *OPA1* mutation carriers presented optic disc hyperemia, which has never been observed in typical patients with ADOA. By contrast, only 20% of those carriers showed temporal disc pallor, which is a prominent optic appearance in patients with ADOA (41–86%) (Cohn et al., 2007; Yu-Wai-Man et al., 2010; Chen et al., 2014). Four patients harboring the most common mutation c.2708_2711delTTAG had different fundus appearance. We speculate that the difference in the fundus performance may be due to the different course of vision loss of patients. In a previous study, Pradhan et al. described a 36-year old man who suffered a bilateral, painless visual loss during his anti-tuberculosis treatment that included EMB

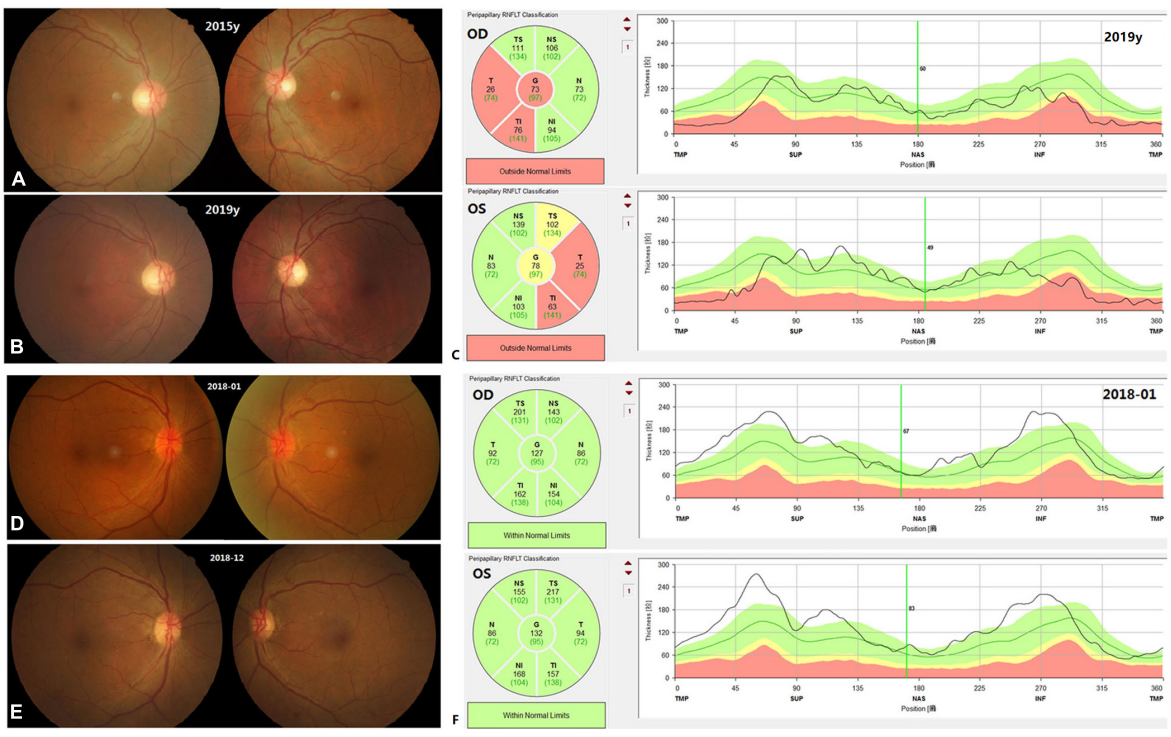

FIGURE 3 | Fundus appearance and OCT images on the first visit and at follow-up for patient E005 **(A–C)** and patient A3124 **(D–F)**. In the patient E005, the fundus appearance did not change. The temporal RNFL in both eyes was below the normal limits at follow-up **(C)**. In the patient A3124, the color and border of the optic discs turned normal. The RNFL was thickened in both eyes on the first visit **(F)**.

TABLE 2 | Comparison of the demographic and the EMB medication of the two groups of patients.

	Group 1	Group 2	*P* value
No. of patients	22	25	–
OPA1 mutant allele, *N* (%)	18 (81.8)	0	–
MtDNA mutant allele, *N* (%)	4 (18.2)	0	–
Male, N (%)	17 (77.27)	14 (56.00)	0.125‡
Mean age at presentation, years (range)	27.50 (16.00–73.00)	48.00 (17.00–74.00)	0.006†
Family history, *N* (%)	6 (27.27)	1 (4.00)	0.025‡
Smoking, *N* (%)	3 (15.00)	2 (8.00)	0.458‡
Renal dysfunction, *N* (%)	0 (0.00)	2 (9.52)	0.179§
Mean daily dose, mg/kg/d (range)	12.90 (3.80–16.90)	12.90 (8.80–29.20)	0.943†
Mean medication time, months (range)	3.75 (1.40–22.00)	5.00 (1.00–24.00)	0.864†

Group 1, patients with mitochondrial mutations; Group 2, patients without mitochondrial mutations; ‡Pearson $\chi 2$ test; † Wilcoxon rank sum test; § Fisher's exact test.

TABLE 3 | Comparison of the clinical characteristic of the two groups of patients.

	Group 1	Group 2	*P* value
Mean LogMAR BCVA (range)	1.22 (0.10–1.70)	1.00 (0.10–2.00)	0.453†
Mean course of the vision loss, months (range)	2.00 (0.50–10.00)	2.00 (0.50–24.00)	0.497†
Disc appearance, eyes (%)	44 (100.00)	50 (100.00)	0.020‡
Normal	4 (9.09)	16 (32.00)	
Hyperemia	31 (70.45)	24 (48.00)	
Pallor	9 (20.46)	10 (20.00)	
Color vision, eyes (%)	24 (100.00)	37 (100.00)	0.607‡
Normal	3 (12.50)	5 (13.51)	
Red/green color vision impairment	7 (29.17)	16 (43.24)	
Yellow/blue color vision impairment	3 (12.50)	5 (13.51)	
Total color blindness	11 (45.83)	11 (29.74)	
Visual field, eyes (%)	34 (100.00)	32 (100.00)	0.059§
Central scotoma	18 (52.94)	13 (40.63)	
Paracentral scotoma	4 (11.76)	2 (6.25)	
Cecocentral scotoma	12 (35.30)	11 (34.38)	
Temporal hemianopia	0 (0.00)	6 (18.74)	
Vision outcomes, patients (%)	14 (100.00)	23 (100.00)	0.016‡
Improved	7 (50.00)	21 (91.30)	
Unchanged	6 (42.86)	2 (8.70)	
Decreased	1 (7.14)	0 (0.00)	
Mean recovery time, months (range)	6.00 (2.00–12.00)	3.00 (1.00–12.00)	0.107†

Group 1, patients with mitochondrial mutations; Group 2, patients without mitochondrial mutations; †Wilcoxon rank sum test; ‡Pearson $\chi 2$ test; §Fisher's exact test.

(Pradhan et al., 2010). This patient also had optic disc hyperemia and peripapillary hemorrhage. After a series of differential diagnoses, the researchers finally identified a nonsense p.R38X *OPA1* mutation in this patient and inferred that the visual loss in that patient had been exacerbated following EMB therapy. We speculate that optic disc hyperemia is an acute response to the toxic effect of EMB; consequently, a concomitant effect of *OPA1* mutations and EMB toxicity renders *OPA1* mutations carriers prone to optic disc hyperemia. This might be the reason why the *OPA1* mutations carriers presented more optic disc hyperemia than was observed in the patients without mutations, even though both groups had a similar disease time course. The mutation rate (38.3%) of *OPA1* mutations in this EON cohort was higher than that (9.6 and 7.6%) reported in a group of Chinese patients with suspected hereditary optic neuropathy (Chen et al., 2014) and other Han Chinese population (Zhang et al., 2017). One reason might be the patients harboring *OPA1* mutations are more sensitive to the toxicity of EMB and present more obvious visual defects as our mentioned above. Another reason might be due to the small number of patients in the current cohort.

In this cohort, we only identified four male patients carrying a LHON-mtDNA mutation, and this rate (8.5%) was much lower than the rate (38.3%) in patients harboring *OPA1* mutations and the rate (33%) in Chinese patients with LHON or suspected with LHON (Ji et al., 2008; Yu et al., 2010). Hwang et al. (2003) screened a cohort of 24 patients with EON for LHON-mtDNA mutations but were unable to identify any LHON-mtDNA mutations. Therefore, the existence of LHON-mtDNA mutations might be uncommon in patients with EON. To date, twelve patients (including our four patients) have been reported to develop optic neuropathy while taking EMB (**Table 4**; Dotti et al., 1998; De Marinis, 2001; Chowdhury et al., 2006; Ikeda et al., 2006; Seo et al., 2010). Ten of these patients carried mutation m.11778G > A, which is the most common primary mutation of LHON (Chen et al., 2014). In the present study, we described two patients carrying the m.14484T > C mutation (the second commonest primary mutation of LHON) who developed LHON while taking EMB (**Table 4**). Unlike the eight previously described cases, the four patients in our cohort had a younger onset age (48 years vs. 21.5 years). In addition, these four patients all had a family history, and three of them showed optic disc hyperemia and RNFL pseudoedema, which is a typical fundus appearance in the acute stage of LHON (Chen et al., 2014). Not all individuals who carry LHON-mtDNA mutations will develop visual symptoms, as the occurrence of LHON usually needs other risk factors, like heavy smoking and alcohol consumption (Sadun et al., 2003). EMB might have been a trigger or an epigenetic factor for the manifestation of LHON in these four patients.

The toxicity of EMB is related to its zinc-chelating effect and its metabolites (Chung et al., 2009). At present, the exact mechanism for the toxic neuropathy induced by EMB remains unclear, but increasing evidence indicates a relationship with mitochondrial dysfunction. In an early study, Heng et al. found that EMB was specifically toxic to retinal ganglion cells and that it caused ganglion cell degeneration by a glutamate excitotoxic pathway

TABLE 4 | Clinical features of reported patients with EMB-induced LHON.

ID	Onset age (years)	Gender	Medication time (months)	BCVA (OD/OS)	Follow-up time (months)	Follow-up BCVA (OD/OS)	Optic disc finding (OD/OS)	Mutation	References
1	50–55	M	8	0.5/0.04	24	0.5/0.04	TEP/TEP	m.G11778A	Dotti et al., 1998
2	50–55	M	11	0.5/0.04	21	1.0/0.7	normal/normal	m.G11778A#	De Marinis, 2001
3	65–70	F	12	0.2/0.05	6	0.3/0.09	–	m.G11778A	Ikeda et al., 2006
4	65–70	F	3	0.03/0.03	12	0.01/0.01	normal/normal	m.G11778A	Ikeda et al., 2006
5	30–35	M	4	0.3/0.15	1	0.06/HM	H/H	m.G11778A	Chowdhury et al., 2006
6	40–45	M	4	0.1/0.1	5	FC/FC	normal/H	m.G11778A	Seo et al., 2010
7	20- 25	M	12	0.6/1.0	15	FC/FC	H/H	m.G11778A	Seo et al., 2010
8	30–35	F	4	FC/FC	-	-	TOP/TOP	m.G11778A	Seo et al., 2010
A2061	15–20	M	12	0.06/0.06	-	-	H/H	m.G11778A	This study
A2290	20–25	M	18	FC/FC	24	FC/FC	TEP/TEP	m.G11778A	This study
A781	15–20	M	12	0.8/0.02	–	–	H*/H	m.T14484C	This study
A1780	25–30	M	7	0.1/0.3	–	–	H/H	m.T14484C	This study

*F, female; M, male; FC, finger counting; HM, hand move; TEP, temporal pallor; H, hyperemia; TOP, total pallor; *hemorrhage; #heteroplasmic.*

(Heng et al., 1999). LHON-mtDNA and *OPA1* mutations also cause damage to the small-caliber papillomacular bundle axons (Barboni et al., 2010) therefore, the clinical features of EON, LHON, and ADOA partially overlap. All three conditions show color vision abnormality and visual field defects. In the current cohort, most patients presented central or cecocentral scotoma, which could be observed in both EON and LHON or ADOA, whereas only three patients in group 2 showed temporal hemianopia, which is a typical visual field defect of EMB-related optic chiasmopathy (Jayanetti et al., 2017). In this cohort, the majority of patients presented with red/green color vision impairment or total color blindness, while only two patients carrying *OPA1* mutations displayed yellow/blue color vision impairment, which is a typical color defect of ADOA (Cohn et al., 2007). Fundus hemorrhage is not common in LHON or ADOA, and three of the four patients with fundus hemorrhage were in group 2, indicating it to be one of the EON clinical features. Our results showed that the mean age was significantly younger in the patients with mitochondrial mutations (27.5 years; group 1) than in the patients without mutations (48 years; group 2), further demonstrating that mitochondrial mutation was an important risk factor for the occurrence of EON, especially in young tuberculosis patients. Patients carrying mitochondrial mutations (*OPA1* or mtDNA) may be more vulnerable to the toxicity of EMB. Of the seven patients with a family history, six patients were mutation carriers; therefore, physicians should carefully question patients with tuberculosis or their family members about ophthalmic problems before EMB is prescribed.

Consistent with the observation by Lee et al. (2008) we found that the visual prognosis was related to the initial fundus appearance of the patients with EON. Up to 79.8% of the patients in our cohort showed normal optic disc appearance or optic disc hyperemia, which suggested they were in the early stage of EON. This might be a reason why our patients had a higher visual recovery rate (75.7%) than the rates described in other EON studies (23.1–47%) (Lee et al., 2008; Ezer et al., 2013). Another reason for this high rate might be due to that the 94.6% VA improvement was reported by patients subjectively; this is one limitation of the current study. Nevertheless, we still observed that the visual outcome was better in the patients in group 2 than in group 1, suggesting that the mitochondrial mutations were a critical factor affecting visual prognosis of patients with EON. Of the eight patients carrying mutation m.11778G > A, only one patient who harbored a heteroplasmic mutation showed VA improvement, (De Marinis, 2001) whereas the other patients all experienced VA decreases or no change during their follow-up (**Table 4**). Another limitation of the current study is that we did not take into account the ocular toxicity of other anti-tuberculosis drugs, such as isoniazid. The third limitation is that since the study was retrospective in nature, the examinations were not standardized.

In conclusion, our results indicated that carriers with *OPA1* mutations might be more vulnerable for the toxicity of EMB to develop EON, whereas the exact effect of these *OPA1* mutations has not been confirmed in future functional assays. Although mitochondrial mutation screening is not possible in all patients prior to anti-tuberculosis medication, genetic analysis should be strongly recommended for patients with a family history of optic neuropathy.

DATA AVAILABILITY STATEMENT

The data presented in the study are deposited in the NCBI GenBank, accession numbers NM_015560 and AC_000021.2.

ETHICS STATEMENT

The studies involving human participants were reviewed and approved by Medical Ethics Committee of Beijing Tongren Hospital. The patients/participants provided their written informed consent to participate in this study.

AUTHOR CONTRIBUTIONS

X-HZ participated in the data collection, data analysis, and manuscript preparation. YX, KX, and KC participated in the data collection and analysis. Q-GX contributed in the study design and data collection. Z-BJ, YL, and S-HW participated in the study design and the manuscript revision. All authors contributed to the article and approved the submitted version.

SUPPLEMENTARY MATERIAL

The Supplementary Material for this article can be found online at: https://www.frontiersin.org/articles/10.3389/fcell.2021.754676/full#supplementary-material

Supplementary Figure 1 | Sanger sequencing electropherograms for 17 identified *OPA1* mutations in the study.

Supplementary Figure 2 | Family pedigrees for seven patients with family history of optic neuropathy.

REFERENCES

Ban, Y., Yoshida, Y., Kawasaki, S., and Mochida, C. (2007). A novel mutation of the OPA1 gene in a Japanese patient with autosomal dominant optic atrophy. *Graefes Arch. Clin. Exp. Ophthalmol.* 245, 1581–1583. doi: 10.1007/s00417-007-0598-1

Barboni, P., Carbonelli, M., Savini, G., Ramos Cdo, V., Carta, A., Berezovsky, A., et al. (2010). Natural history of Leber's hereditary optic neuropathy: longitudinal analysis of the retinal nerve fiber layer by optical coherence tomography. *Ophthalmology* 117, 623–627. doi: 10.1016/j.ophtha.2009.07.026

Belanger, A. E., Besra, G. S., Ford, M. E., Mikusová, K., Belisle, J. T., Brennan, P. J., et al. (1996). The embAB genes of Mycobacterium avium encode an arabinosyl transferase involved in cell wall arabinan biosynthesis that is the target for the antimycobacterial drug ethambutol. *Proc. Natl. Acad. Sci. U. S. A.* 93, 11919–11924. doi: 10.1073/pnas.93.21.11919

Cardaioli, E., Gallus, G. N., Da Pozzo, P., Rufa, A., Franceschini, R., Motolese, E., et al. (2006). A novel mutation producing premature termination codon at the OPA1 gene causes autosomal dominant optic atrophy. *J. Neurol.* 253, 672–673. doi: 10.1007/s00415-005-0057-z

Carr, R. E., and Henkind, P. (1962). Ocular manifestations of ethambutol, Toxic amblyopia after administration of an experimental antituberculous drug. *Arch. Ophthalmol.* 67, 566–571. doi: 10.1001/archopht.1962.00960020566009

Chen, H. Y., Lai, S. W., Muo, C. H., Chen, P. C., and Wang, I. J. (2012). Ethambutol-induced optic neuropathy: a nationwide population-based study from Taiwan. *Br. J. Ophthalmol.* 96, 1368–1371. doi: 10.1136/bjophthalmol-2012-301870

Chen, J., Xu, K., Zhang, X., Jiang, F., Liu, L., Dong, B., et al. (2014). Mutation screening of mitochondrial DNA as well as OPA1 and OPA3 in a Chinese cohort with suspected hereditary optic atrophy. *Invest. Ophthalmol. Vis. Sci.* 55, 6987–6995. doi: 10.1167/iovs.14-14953

Chowdhury, B., Nagpaul, A. K., and Chowdhury, D. (2006). Leber's hereditary optic neuropathy masquerading as ethambutol-induced optic neuropathy in a young male. *Indian J. Ophthalmol.* 54, 218–219. doi: 10.4103/0301-4738.27091

Chung, H., Yoon, Y. H., Hwang, J. J., Cho, K. S., Koh, J. Y., and Kim, J. G. (2009). Ethambutol-induced toxicity is mediated by zinc and lysosomal membrane permeabilization in cultured retinal cells. *Toxicol. Appl. Pharmacol.* 235, 163–170. doi: 10.1016/j.taap.2008.11.006

Cohn, A. C., Toomes, C., Potter, C., Towns, K. V., Hewitt, A. W., Inglehearn, C. F., et al. (2007). Autosomal dominant optic atrophy: penetrance and expressivity in patients with OPA1 mutations. *Am. J. Ophthalmol.* 143, 656–662. doi: 10.1016/j.ajo.2006.12.038

De Marinis, M. (2001). Optic neuropathy after treatment with anti-tuberculous drugs in a subject with Leber's hereditary optic neuropathy mutation. *J. Neurol.* 248, 818–819. doi: 10.1007/s004150170103

Delettre, C., Griffoin, J. M., Kaplan, J., Dollfus, H., Lorenz, B., Faivre, L., et al. (2001). Mutation spectrum and splicing variants in the OPA1 gene. *Hum. Genet.* 109, 584–591. doi: 10.1007/s00439-001-0633-y

Delettre, C., Lenaers, G., Griffoin, J. M., Gigarel, N., Lorenzo, C., Belenguer, P., et al. (2000). Nuclear gene OPA1, encoding a mitochondrial dynamin-related protein, is mutated in dominant optic atrophy. *Nat. Genet.* 26, 207–210. doi: 10.1038/79936

Dotti, M. T., Plewnia, K., Cardaioli, E., Manneschi, L., Rufa, A., Alemà, G., et al. (1998). A case of ethambutol-induced optic neuropathy harbouring the primary mitochondrial LHON mutation at nt 11778. *J. Neurol.* 245, 302–303. doi: 10.1007/s004150050223

Ezer, N., Benedetti, A., Darvish-Zargar, M., and Menzies, D. (2013). Incidence of ethambutol-related visual impairment during treatment of active tuberculosis. *Int. J. Tuberc. Lung Dis.* 17, 447–455. doi: 10.5588/ijtld.11.0766

Ferré, M., Bonneau, D., Milea, D., Chevrollier, A., Verny, C., Dollfus, H., et al. (2009). Molecular screening of 980 cases of suspected hereditary optic neuropathy with a report on 77 novel OPA1 mutations. *Hum. Mutat.* 30, E692–E705.

Fraunfelder, F. W., Sadun, A. A., and Wood, T. (2006). Update on ethambutol optic neuropathy. *Expert Opin. Drug Saf.* 5, 615–618.

Guillet, V., Chevrollier, A., Cassereau, J., Letournel, F., Gueguen, N., Richard, L., et al. (2010). Ethambutol-induced optic neuropathy linked to OPA1 mutation and mitochondrial toxicity. *Mitochondrion* 10, 115–124. doi: 10.1016/j.mito.2009.11.004

Heng, J. E., Vorwerk, C. K., Lessell, E., Zurakowski, D., Levin, L. A., and Dreyer, E. B. (1999). Ethambutol is toxic to retinal ganglion cells via an excitotoxic pathway. *Invest. Ophthalmol. Vis. Sci.* 40, 190–196.

Holladay, J. T. (1997). Proper method for calculating average visual acuity. *J. Refract. Surg.* 13, 388–391. doi: 10.3928/1081-597x-19970701-16

Hwang, J. M., Kim, J., and Park, S. S. (2003). Leber's hereditary optic neuropathy mutations in ethambutol-induced optic neuropathy. *J. Neurol.* 250, 87–89. doi: 10.1007/s00415-003-0960-0

Ikeda, A., Ikeda, T., Ikeda, N., Kawakami, Y., and Mimura, O. (2006). Leber's hereditary optic neuropathy precipitated by ethambutol. *Jpn. J. Ophthalmol.* 50, 280–283. doi: 10.1007/s10384-005-0308-7

Jayanetti, V., Rossiter-Thornton, M., Azar, D., and Fraser, C. L. (2017). Sibling Ethambutol optic chiasmopathy. *Neuroophthalmology* 42, 40–43. doi: 10.1080/01658107.2017.1322616

Ji, Y., Zhang, A. M., Jia, X., Zhang, Y. P., Xiao, X., Li, S., et al. (2008). Mitochondrial DNA haplogroups M7b1'2 and M8a affect clinical expression of leber hereditary optic neuropathy in Chinese families with the m.11778G–>a mutation. *Am. J. Hum. Genet.* 83, 760–768. doi: 10.1016/j.ajhg.2008.11.002

Kao, S. H., Yen, M. Y., Wang, A. G., Yeh, Y. L., and Lin, A. L. (2015). Changes in mitochondrial morphology and bioenergetics in human lymphoblastoid cells with four novel OPA1 mutations. *Invest. Ophthalmol. Vis. Sci.* 56, 2269–2278. doi: 10.1167/iovs.14-16288

Lee, E. J., Kim, S. J., Choung, H. K., Kim, J. H., and Yu, Y. S. (2008). Incidence and clinical features of ethambutol-induced optic neuropathy in Korea. *J. Neuroophthalmol.* 28, 269–277. doi: 10.1097/wno.0b013e31818e3c6b

Li, Y., Deng, T., Tong, Y., Peng, S., Dong, B., He, D., et al. (2008). Identification of two novel OPA1 mutations in Chinese families with autosomal dominant optic atrophy. *Mol. Vis.* 14, 2451–2457.

Pradhan, M., Sharp, D., Best, S., Vincent, A., and Vaphiades, M. (2010). Drug-induced optic neuropathy-TB or not TB. *Surv. Ophthalmol.* 55, 378–385. doi: 10.1016/j.survophthal.2009.10.005

Richards, S., Aziz, N., Bale, S., Bick, D., Das, S., Gastier-Foster, J., et al. (2015). Standards and guidelines for the interpretation of sequence variants: a joint

consensus recommendation of the American College of Medical Genetics and Genomics and the Association for Molecular Pathology. *Genet. Med.* 17, 405–424. doi: 10.1038/gim.2015.30

Sadun, A. A., Carelli, V., Salomao, S. R., Berezovsky, A., Quiros, P. A., Sadun, F., et al. (2003). Extensive investigation of a large Brazilian pedigree of 11778/haplogroup J Leber hereditary optic neuropathy. *Am. J. Ophthalmol.* 136, 231–238. doi: 10.1016/s0002-9394(03)00099-0

Santaella, R. M., and Fraunfelder, F. W. (2007). Ocular adverse effects associated with systemic medications: recognition and management. *Drugs* 67, 75–93. doi: 10.2165/00003495-200767010-00006

Santarelli, R., Rossi, R., Scimemi, P., Cama, E., Valentino, M. L., La Morgia, C., et al. (2015). OPA1-related auditory neuropathy: site of lesion and outcome of cochlear implantation. *Brain* 138, 563–576. doi: 10.1093/brain/awu378

Seo, J. H., Hwang, J. M., and Park, S. S. (2010). Antituberculosis medication as a possible epigenetic factor of Leber's hereditary optic neuropathy. *Clin. Exp. Ophthalmol.* 38, 363–366. doi: 10.1111/j.1442-9071.2010.02240.x

Sun, T., Xu, K., Ren, Y., Xie, Y., Zhang, X., Tian, L., et al. (2018). Comprehensive molecular screening in Chinese Usher syndrome patients. *Invest. Ophthalmol. Vis. Sci.* 59, 1229–1237. doi: 10.1167/iovs.17-23312

Yang, H. K., Park, M. J., Lee, J. H., Lee, C. T., Park, J. S., and Hwang, J. M. (2016). Incidence of toxic optic neuropathy with low dose ethambuol. *Int. J. Tuberc. Lung Dis.* 20, 261–264. doi: 10.5588/ijtld.15.0275

Yu, D., Jia, X., Zhang, A. M., Li, S., Zou, Y., Zhang, Q., et al. (2010). Mitochondrial DNA sequence variation and haplogroup distribution in Chinese patients with LHON and m.14484T>C. *PLoS One* 5:e13426. doi: 10.1371/journal.pone.0013426

Yu-Wai-Man, P., Griffiths, P. G., Burke, A., Sellar, P. W., Clarke, M. P., Gnanaraj, L., et al. (2010). The prevalence and natural history of dominant optic atrophy due to OPA1 mutations. *Ophthalmology* 117, 1538–1546. doi: 10.1016/j.ophtha.2009.12.038

Zhang, A. M., Bi, R., Hu, Q. X., Fan, Y., Zhang, Q., and Yao, Y. G. (2017). The OPA1 gene mutations are frequent in Han Chinese patients with suspected optic neuropathy. *Mol. Neurobiol.* 54, 1622–1630. doi: 10.1007/s12035-016-9771-z

Zhang, J., Ji, Y., Lu, Y., Fu, R., Xu, M., Liu, X., et al. (2018). Leber's hereditary optic neuropathy (LHON)-associated ND5 12338T > C mutation altered the assembly and function of complex I, apoptosis and mitophagy. *Hum. Mol. Genet.* 27, 1999–2011. doi: 10.1093/hmg/ddy107

Conflict of Interest: The authors declare that the research was conducted in the absence of any commercial or financial relationships that could be construed as a potential conflict of interest.

Publisher's Note: All claims expressed in this article are solely those of the authors and do not necessarily represent those of their affiliated organizations, or those of the publisher, the editors and the reviewers. Any product that may be evaluated in this article, or claim that may be made by its manufacturer, is not guaranteed or endorsed by the publisher.

Copyright © 2021 Zhang, Xie, Xu, Cao, Xu, Jin, Li and Wei. This is an open-access article distributed under the terms of the Creative Commons Attribution License (CC BY). The use, distribution or reproduction in other forums is permitted, provided the original author(s) and the copyright owner(s) are credited and that the original publication in this journal is cited, in accordance with accepted academic practice. No use, distribution or reproduction is permitted which does not comply with these terms.

frontiers in Cell and Developmental Biology

ORIGINAL RESEARCH
published: 01 December 2021
doi: 10.3389/fcell.2021.769636

Novel *BMP4* Truncations Resulted in Opposite Ocular Anomalies: Pathologic Myopia Rather Than Microphthalmia

*Yi Jiang[1], Jiamin Ouyang[1], Xueqing Li[1], Yingwei Wang[1], Lin Zhou[1,2], Shiqiang Li[1], Xiaoyun Jia[1], Xueshan Xiao[1], Wenmin Sun[1], Panfeng Wang[1] and Qingjiong Zhang[1]**

[1] State Key Laboratory of Ophthalmology, Zhongshan Ophthalmic Center, Sun Yat-sen University, Guangzhou, China,
[2] Department of Ophthalmology, West China Hospital, Sichuan University, Chengdu, China

OPEN ACCESS

Edited by:
Timothy W. Corson, Indiana University Bloomington, United States

Reviewed by:
Lance Doucette, University of Alberta, Canada
Ruifang Sui, Peking Union Medical College Hospital (CAMS), China

***Correspondence:**
Qingjiong Zhang
zhangqji@mail.sysu.edu.cn;
zhangqingjiong@gzzoc.com

Specialty section:
This article was submitted to Molecular and Cellular Pathology, a section of the journal Frontiers in Cell and Developmental Biology

Received: *02 September 2021*
Accepted: *12 October 2021*
Published: *01 December 2021*

Citation:
Jiang Y, Ouyang J, Li X, Wang Y, Zhou L, Li S, Jia X, Xiao X, Sun W, Wang P and Zhang Q (2021) Novel BMP4 Truncations Resulted in Opposite Ocular Anomalies: Pathologic Myopia Rather Than Microphthalmia. Front. Cell Dev. Biol. 9:769636. doi: 10.3389/fcell.2021.769636

BMP4 variants have been reported to be associated with syndromic microphthalmia (MCOPS6, OMIM 607932). This study aims to describe *BMP4* truncation mutations contributing to a novel phenotype in eight patients from four Chinese families. In this study, *BMP4* variants were collected from a large dataset from in-house exome sequencing. Candidate variants were filtered by multiple *in silico* tools as well as comparison with data from multiple databases. Potential pathogenic variants were further confirmed by Sanger sequencing and cosegregation analysis. Four novel truncation variants in *BMP4* were detected in four out of 7,314 unrelated probands with different eye conditions. These four mutations in the four families solely cosegregated in all eight patients with a specific form of pathologic myopia, characterized by significantly extended axial length, posterior staphyloma, macula patchy, chorioretinal atrophy, myopic optic neuropathy or glaucoma, vitreous opacity, and unique peripheral snow-grain retinopathy. The extreme rarity of the truncations in *BMP4* (classified as intolerant in the gnomAD database, pLI = 0.96), the exclusive presence of these variants in the four families with pathologic myopia, variants fully co-segregated with the same specific phenotypes in eight patients from the four families, and the association of the pathogenicity of truncations with syndromic microphthalmia in previous studies, all support a novel association of *BMP4* truncations with a specific form of pathologic myopia. The data presented in this study demonstrated that heterozygous *BMP4* truncations contributed to a novel phenotype: pathologic myopia rather than microphthalmia. Mutations in the same gene resulting in both high myopia and microphthalmia have been observed for a few other genes like *FZD5* and *PAX6*, suggesting bidirectional roles of these genes in early ocular development. Further studies are expected to elucidate the molecular mechanism of the bidirectional regulation.

Keywords: pathologic myopia, early-onset myopia, *BMP4*, truncation variants, microphthalmia

INTRODUCTION

Pathologic myopia is characterized by posterior staphyloma, fundus degenerative changes, and abnormal corrected visual acuity. Pathologic myopia usually belongs to a subgroup of high myopia, which is defined as an axial length of 26 mm or more (Ohno-Matsui et al., 2016; Sankaridurg et al., 2021; Spaide et al., 2021). The complications associated with pathologic myopia are among the first to third common causes of legal blindness worldwide (Wong et al., 2014; Sankaridurg et al., 2021). Genetic defects play a major role in the development of pathologic myopia or high myopia, and among these defects, at least 28 loci or genes have been reported to contribute to non-syndromic forms, while variants in a number of genes are known to cause syndromic forms. However, the genetic defects for most cases of high myopia or pathologic myopia are still unknown, and the identification of additional implicating genes may enrich our understanding of the pathogenesis and facilitate the prevention and management of these conditions (Zhang, 2021).

Comparative exome sequencing has been used to detect genetic factors contributing to retinitis pigmentosa and glaucoma in our previous studies (Sun et al., 2019; Yi et al., 2020). Using similar strategy, four truncation variants in *BMP4* (OMIM 112262) were detected in four unrelated families with pathologic myopia. These variants were confirmed by Sanger sequencing and cosegregated with pathologic myopia in eight patients from four families but in none of the unaffected individuals or any in-house controls, suggesting that *BMP4* may be an important factor for pathologic myopia. *BMP4* plays a vital regulatory role in embryonic development (Hogan, 1996) and truncations in this gene are extremely rare and intolerant [gnomAD, probability of being loss-of-function intolerant (pLI) = 0.96; Exp. 14.2 with obs. 1]. Previously, truncations in *BMP4* were reported to cause microphthalmia, anophthalmia, and coloboma (MAC) (Reis et al., 2011) and anterior segment dysgenesis (ASGD) (Takenouchi et al., 2013), phenotypes that in contrast to those of pathologic myopia. The identification of a novel and bidirectional ocular abnormality associated with *BMP4* truncations may provide new clues for elucidation of the developmental regulation of ocular size and shape.

MATERIALS AND METHODS

Patient Recruitment and Data Collection

The probands with different eye disorders and their related family members were enrolled through the Pediatric and Genetic Clinic, Zhongshan Ophthalmic Center. Clinical data and peripheral blood samples were collected from these individuals. Prior to collection, all the participants or their guardians voluntarily signed informed content according to the tenets of the Declaration of Helsinki. This study was approved by the Institutional Review Board of Zhongshan Ophthalmic Center. Genomic DNA was extracted from the leukocytes within peripheral venous blood samples by following a previously reported method (Wang et al., 2010).

Each participating individual received a routine ophthalmologic examination. Additional specific ocular examinations were performed when required, including anterior segment photography, fundus photography, optic coherence tomography (OCT), electroretinogram (ERG), and scanning laser opthalmoscopy (SLO).

Variant Detection and Evaluation

Whole-exome sequencing (Li et al., 2015) or target-exome sequencing (Wang et al., 2019) was performed on the genomic DNA from the 7,314 probands including 928 with early onset myopia, and 6,386 with other ocular conditions. After the detection of variants in *BMP4* from the exome sequencing data, the variants were filtered by multiple bioinformatic analytic steps. First, variants with low sequencing quality with a coverage of less than 5 were excluded. Second, synonymous and non-coding variants without effects on splicing site alterations, which were predicted by the Berkeley Drosophila Genome Project,[1] were excluded. Third, through the evaluation of the minor allelic frequencies (MAFs) of variants based on the gnomAD database,[2] variants with an MAF $\geq$ 0.01 were excluded. The remaining variants were evaluated by five *in silico* tools, including SIFT,[3] Polyphen-2,[4] PROVEAN,[5] CADD,[6] and REVEL.[7] Finally, the variants were classified as potential pathogenic variants (PPVs) after comparison with the distribution of variants in our cohort and the gnomAD database.

The variants were further confirmed by Sanger sequencing. The online design program Primer3.0[8] was used for primer design and the primer sequences are listed in **Supplementary Table 1**. Sanger sequencing validation including amplification, sequencing and target sequences analysis was performed following a previously described method (Chen et al., 2013). Then, the cosegregation analysis was conducted based on Sanger sequencing on genomic DNA from family relatives in these families.

Statistical Analysis

IBM SPSS software version 26.0 (Amonk, NY: IBM Corp.) was applied to all statistical analyses in this study. The comparison of the frequency of truncation variants between in-house data related to early onset myopia and data in the gnomAD database was analyzed using the chi-square test or Fisher's exact test. An in-house data comparison between the frequency of these truncation variants in patients with early onset myopia and the frequency of these truncation variants in patients with other eye conditions was also performed using the chi-square test or Fisher's exact test. A *P*-value less than 0.05 was considered as statistically significant.

Immunohistochemical Staining

To examine the BMP4 protein expression in the retinal tissue, immunohistochemical staining was performed on the human

[1]https://www.fruitfly.org/
[2]https://gnomad.broadinstitute.org/
[3]http://sift.jcvi.org/
[4]http://genetics.bwh.harvard.edu/pph2/
[5]http://provean.jcvi.org/seq_submit.php
[6]http://cadd.gs.washington.edu
[7]https://sites.google.com/site/revelgenomics/
[8]http://primer3.ut.ee/

eyes of the donor who died of meningioma. The donor eyes were obtained from the Eye Bank of Guangdong Province. All the procedure was conducted following the Declaration of Helsinki and the written informed content was obtained from the donor before the study. The human eyes were fixed in the 4% paraformaldehyde and then embedded in paraffin. The paraffin-embedded eyes were cut into 4-μm-thick sections. Antigen retrieval was performed on the sections using high temperature (98°C) for 30 min and the sections were blocked with 5% normal goat serum. The primary antibodies, a mouse anti-BMP4 antibody (1:25; sc-12721; Santa Cruz) and a rabbit anti-PKC α antibody (1:500; sc-208; Santa Cruz), were used to incubate the sections. The secondary antibodies were Alexa Fluor 568-conjugated donkey anti-mouse IgG antibody (1:500; ab175472; Abcam) and Alexa Fluor 488-conjugated donkey anti-rabbit IgG antibodies (1:500; ab150073; Abcam) and DAPI (1:3000; 28718-90-3; Sigma-Aldrich) was used for the nuclear labeling. The images of stained sections were taken using the confocal microscope (*Zeiss LSM* 980, Carl Zeiss Microscopy GmbH, Jena, Germany).

RESULTS

Mutation Analysis

Totally, four novel truncation variants in *BMP4* were identified in four out of 7,314 unrelated probands with different eye conditions, including c.43delC:p.(Gln15Lysfs*4), c.97A > T:p.(Lys33*), c.419delT:p.(Phe140Serfs*13), and c.766C > T:p.(Arg256*) (**Figure 1**). These four truncations were novel and potential candidates of disease-causing variants since this type of variants were extremely rare and intolerant based on gnomAD database (pLI = 0.96) (**Figure 2B**). In the current study, interestingly, all the four probands with these *BMP4* truncations had early onset pathologic myopia, accounting for 4 of 928 probands with early onset high myopia, but in none of the 6,386 probands with other eye conditions ($P = 2.58 \times 10^{-4}$, Fisher's exact test) (**Figures 2A,C**). Similarly, the frequency of *BMP4* truncations in probands with early onset high myopia is significantly higher compared with the frequency in gnomAD ($P = 1.23 \times 10^{-7}$, Fisher's exact test) (**Figures 2A–C**). The four truncations in our cohort were

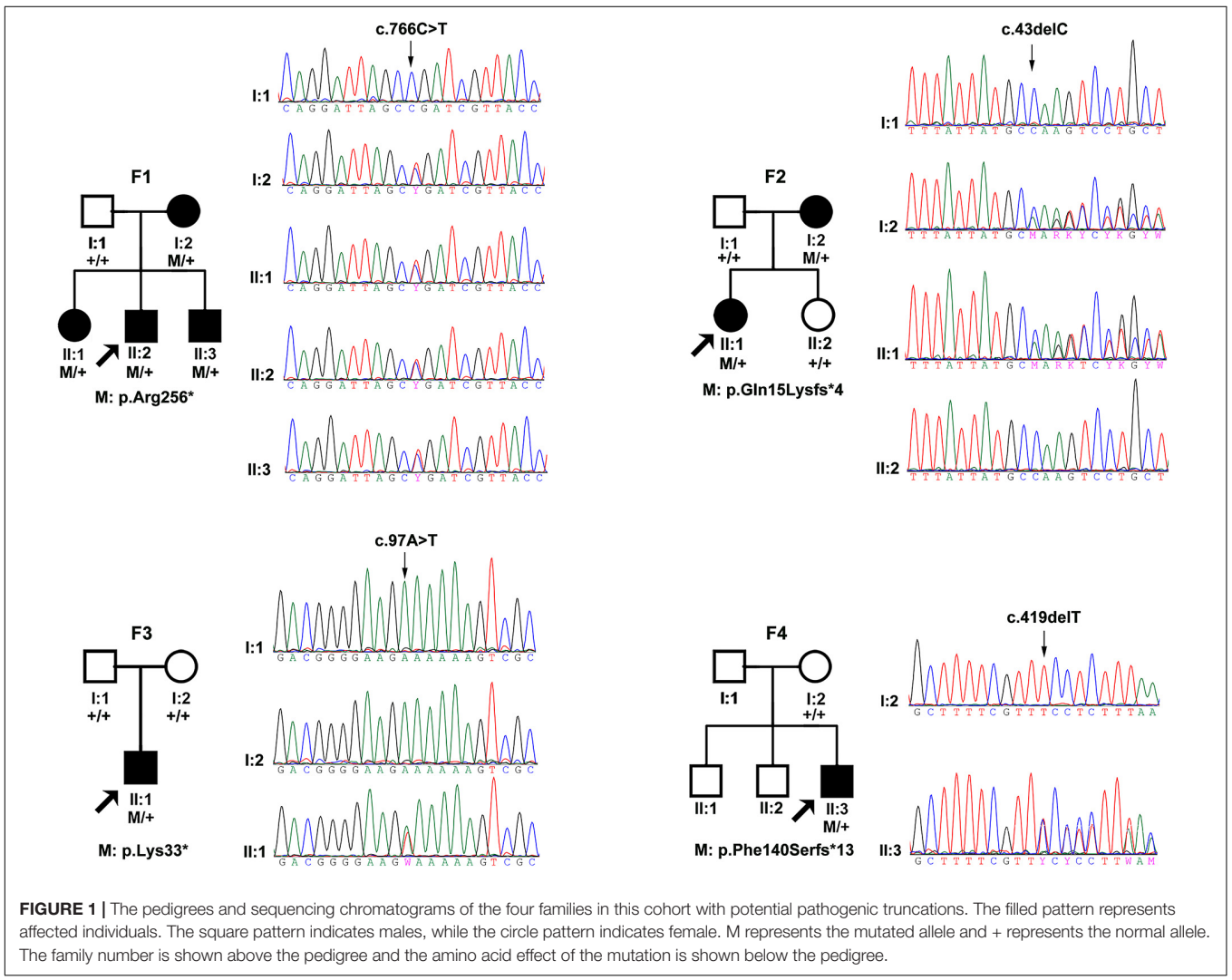

FIGURE 1 | The pedigrees and sequencing chromatograms of the four families in this cohort with potential pathogenic truncations. The filled pattern represents affected individuals. The square pattern indicates males, while the circle pattern indicates female. M represents the mutated allele and + represents the normal allele. The family number is shown above the pedigree and the amino acid effect of the mutation is shown below the pedigree.

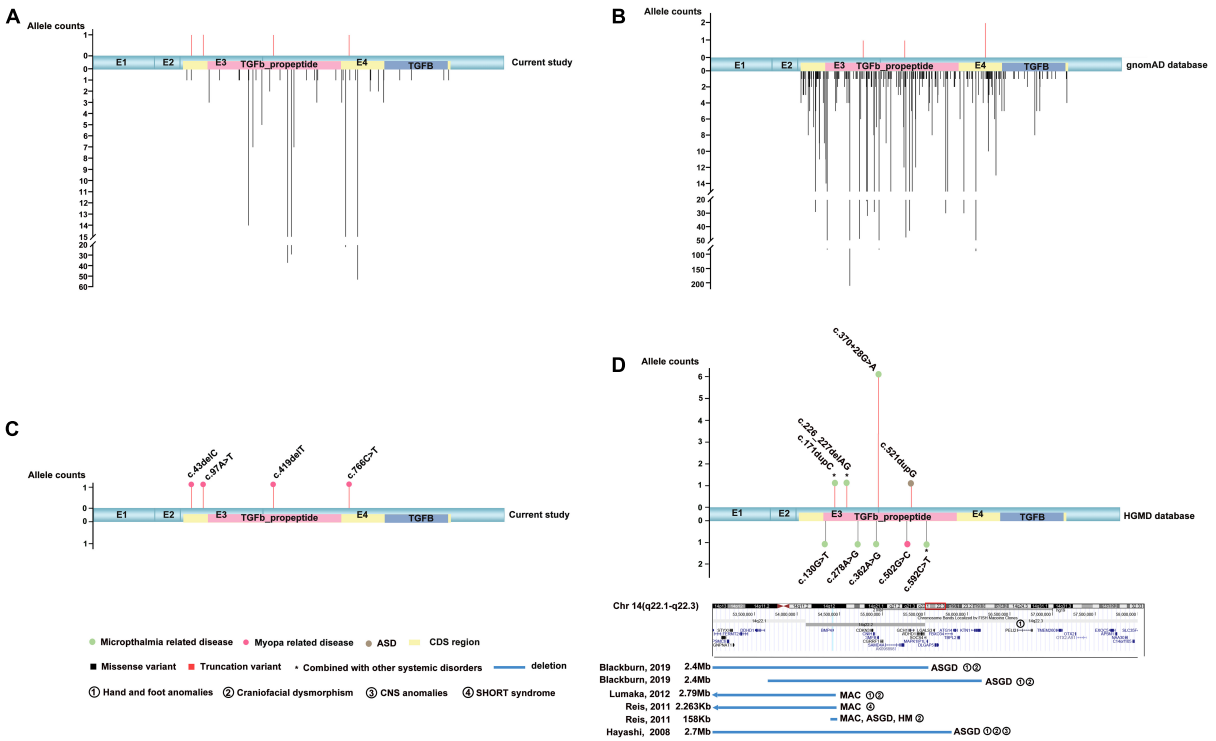

FIGURE 2 | The distribution and frequency of *BMP4* variants in this cohort, the gnomAD database and the HGMD database. MAC, microphthalmia, anophthalmia, coloboma; ASGD, anterior segment dysplasia. **(A)** Diagram of the frequency and location of the detected *BMP4* variants in mRNA sequences from our cohort (accession number NM_001202.6). The truncation variants are shown above and the missense variants are shown below. Compared with allele counts of missense variants in this cohort, the truncation variants are extremely rare. **(B)** Schematic showing the distribution and frequency of *BMP4* variants in the gnomAD database. Truncation variants are rare in the general population (pLI = 0.96). **(C)** The distribution and frequency of potential pathogenic *BMP4* truncation variants in our in-house data. The filled square pattern represents the phenotype related to *BMP4* variants. The corresponding phenotype is shown above locations of the related variants. The potential pathogenic truncation variants in *BMP4* are enriched in patients with pathologic myopia. **(D)** The distribution and frequency of *BMP4* variants in previous studies. The truncation variants are shown above and the missense variants and large deletions are shown below. The blue rectangle patterns represent large deletions in *BMP4*. The position of references are indicated on the left of the pattern and the position of corresponding phenotypes is indicated on the right of the pattern. Based on the HGMD database, most reported disease-causing variants are associated with MAC and/or ASGD.

confirmed by Sanger sequencing and completely cosegregated with pathologic myopia in all eight patients from the four families (**Table 1** and **Figure 1**): the c.97A > T:p.(Lys33*) was a *de novo* variant presented in Family F3; another nonsense variant [c.766C > T:p.(Arg256*)] and two frameshift variants [c.43delC:p.(Gln15Lysfs*4); c.419delT:p.(Phe140Serfs*13)] were segregated with pathologic myopia in the remaining three families. Here, four novel BMP4 truncation variants exclusively segregated with pathologic myopia in eight patients from four unrelated families suggests a novel bidirectional role of BMP4 in the normal and abnormal development of the eye, since most *BMP4* variants were associated with microphthalmia-related disorders based on Human Gene Mutation Database (HGMD) database from previously studies (Bakrania et al., 2008; Hayashi et al., 2008; Reis et al., 2011; Lumaka et al., 2012; Huang X. et al., 2015; Blackburn et al., 2019; Nixon et al., 2019; Thanikachalam et al., 2020; **Figure 2D**).

Clinical Characteristics

The clinical features of eight patients with novel *BMP4* truncation variants were summarized in **Table 1**. Extra-ocular features were only observed in one of the eight patients, i.e., proband F4-II:3, who had tooth malformation, broad nasal bridge, and hyperextensible joints. Of the eight patients, the four probands were identified to have high myopia due to poor vision before school age. Subsequent systemic ocular examination on the probands and family members revealed pathologic myopia in eight patients from the four families. The best-corrected visual acuity (BCVA) among eight patients ranged from counting fingers (CF) to 1.00 (Snellen equivalent) and the mean BCVA was 0.45. The average axial length of eight patients was 30.62 mm (range, 25.32–37.88 mm). Additionally, the axial length of all patients but one family member (F2-I:2) was more than 26.00 mm. The axial length of F2-I:2 was 25.56 mm in the right eye and 25.32 mm in the left eye, her fundus changes showed a trend toward pathologic myopia. The fundus images of these patients demonstrated typical fundus changes for pathologic myopia, including tessellated fundus, posterior staphyloma, macula atrophy, patchy or diffuse chorioretinal atrophy, and peripheral chorioretinal degeneration (**Figure 3**). Interestingly, unique fundus changes were clearly observed in peripheral

TABLE 1 | Clinical information of the patients with BMP4 truncation variants in this study.

Family	Nuleotide acid	Amino acid	Gender	Age (years)	Age (years)	BCVA		Axial length (mm)		Fundus	
ID	Change	Effect		Onset	At exam	OD	OS	OD	OS	OD	OS
F1-I:2	c.766C > T	p.Arg256*	F	EC	46	CF	CF	37.88	36.31	MA; PCA; TF	MA; PCA; TF
F1-II:1	c.766C > T	p.Arg256*	F	EC	23	0.40	0.40	29.38	31.44	PWSD; TF	DCA; PWSD; TF
F1-II:2	c.766C > T	p.Arg256*	M	EC	18	0.06	0.50	35.30	32.5	MA; PCA; PWSD; TF	DCA; PWSD; TF
F1-II:3	c.766C > T	p.Arg256*	M	EC	17	1.00	1.00	26.05	26.25	TF	TF
F2-I:2	c.43delC	p.Gln15Lysfs*4	F	NA	32	1.00	1.00	25.56	25.32	TF	TF
F2-II:1	c.43delC	p.Gln15Lysfs*4	F	3	7	0.80	0.80	29.30	27.72	DCA; PWSD; LD; TF	PWSD; LD; TF
F3-II:1	c.97A > T	p.Lys33*	M	EC	31	CF	HM	33.16	NA[$]	PS; DCA; TF	NA[$]
F4-II:3[#]	c.419delT	p.Phe140Serfs*13	M	3	6	0.20	0.40	32.08	31.19	PS; DCA; TF	PS; DCA; TF

The variant nomenclature is based on the NCBI reference sequence for BMP4 transcript NM_001202.6. All variants are absent in HGMD database and gnomAD database. EC, early childhood; SE, Snellen equivalent; M, male; F, female; NA, not available; SA, affecting splicing acceptor; CF, counting fingers; HM, hand motion; TF, tessellated fundus; DCA, diffuse chorioretinal atrophy; MA, macula atrophy; PCA, patchy chorioretinal atrophy; PWSD, peripheral white spots degeneration; LD, lattice degeneration; BCVA, best corrected visual acuity.

**Translation termination (stop) codon.*

[$]The left eye of proband F3-II:1 has cornea opacity, cataract, and has been performed retinal photocoagulation due to retinal detachment. The fundus photo and axial length of the left eye from this patient is unavailable.

[#]Extra-ocular features were only observed in one of the eight patients (F4-II:3), who had tooth malformation, broad nasal bridge, and hyperextensible joints.

retinas of three patients from two families (F1-II;1, F1-II:2, and F2-II:1), i.e., numerous small white spots in the peripheral retina displayed a "snow grain" appearance (**Figure 4**). This characteristic phenotype has not been described previously in pathologic myopia so that it may be considered as a unique sign of pathologic myopia related to *BMP4* truncation variants. The fundus autofluorescence and ERG test result were available from both eyes from the proband F1-II:2, demonstrating moderate reduction of rod and cone responses on ERG examination and relatively preserved autofluorescence with non-specific minor changes in the posterior and mid-peripheral retina (**Supplementary Figure 1**). Additionally, difference in severity of pathologic myopia between the two eyes was observed in all patients (**Figures 3**, **4**), but such difference was relatively mild as compared with pathologic myopia due to mutations in genes responsible for Stickler syndrome or FEVR (unpublished data). The OCT scans of the four probands illustrated optic nerve fiber layer thinning and choroid atrophy (**Supplementary Figures 2A–D**). The white vitreous strands resembling gossamer anomalies were observed in anterior vitreous cavity in patients from two families (F1, F2) (**Supplementary Figure 2E**).

DISCUSSION

Previously, mutations in *BMP4* were known to cause microphthalmia-related disorders (Bakrania et al., 2008; Reis et al., 2011). On the contrary, in the current study, four novel truncation variants in *BMP4* were identified as PPVs in eight patients with pathologic myopia from four families. Our novel findings were supported by the following lines of evidences: (1) As described above, the truncation variants in *BMP4* were extremely rare and intolerant in general population (gnomAD database, pLI = 0.96). Although the few *BMP4* truncation variants have been reported are related to ocular phenotypes based on HGMD database, the loss of function variant has been identified as a disease-causative mutation related to ocular or systemic disorders. (2) As previously mentioned, the four *BMP4* truncation variants considered PPVs, were highly enriched in 928 patients with early onset high myopia in this cohort. In contrast, none of potential pathogenic *BMP4* truncation variants were identified in 6,386 patients with other eye conditions. Essentially, the clinical evidence supports that these four truncation variants contribute to phenotype—pathologic myopia. This point reflects that truncation variants in *BMP4* are highly related to pathologic myopia. (3) None of these four *BMP4* truncation variants were present in databases. These variants segregated with pathologic myopia in all families in this cohort. (4) In the same pedigree, all individuals with same *BMP4* truncation variant exhibited a similar ocular phenotype. For example, in the family F1, the fundus images of mother and three children with same variant showed typical pathologic myopia fundus changes based on the Meta-Analysis for Pathologic Myopia (META-PM) classification (Ohno-Matsui et al., 2015). The same snow-grain degeneration in the peripheral retina was observed in the proband's sister (F1-II:1) and the proband (F1-II:2). (5) In our study, the BMP4 protein expression mainly located in the inner nuclear layer and inner plexiform layer of adult human retina (**Supplementary Figure 3**), indicating that BMP4 might play pivotal role in visual and retinal development. (6) Previous genome-wide association studies on myopia identified that one of new genetic associations in European population was near the location of *BMP4* (Kiefer et al., 2013). Based on the above evidences, the *BMP4* truncation variants are suggested to cause pathologic myopia.

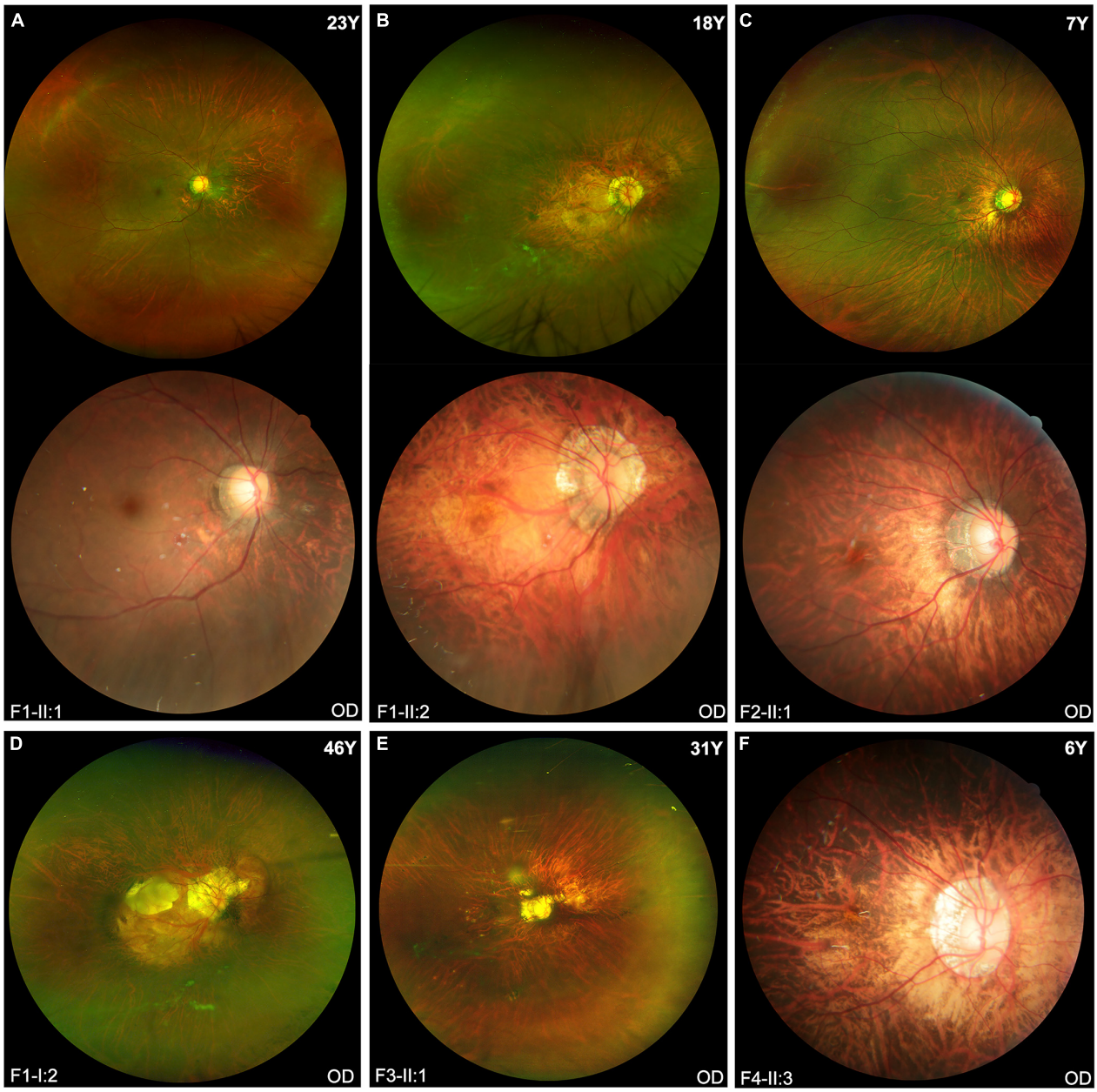

FIGURE 3 | The fundus images of the probands in four families. **(A,B,D)** Typical pathologic myopia fundus changes in the right eyes of three patients from Family F1. All patients carried the same heterozygous truncation variant c.766C > T (p. Arg256*). Fundus photography of Patients F1-II:1 and F1-II:2 shows the ultra-widefield fundus imaging above and traditional fundus imaging of the posterior pole below. **(C)** The fundus images from the right eye of Patient F2-II:1 show diffuse chorioretinal atrophy and white spots in the peripheral retina. **(E)** Scanning laser ophthalmoscopy imaging of Patient F3-II:1 appears diffuse chorioretinal atrophy surrounding the optic disc region, patchy atrophy and posterior staphyloma. **(F)** Posterior staphyloma and diffuse chorioretinal atrophy around the optic disk are observed in the fundus photo of Patient F4-II:3.

Interestingly, the novel phenotype related to *BMP4* truncations observed in our cohort is opposite to previously reported phenotypes. In previous studies, variants in *BMP4* have been mainly reported to be associated with microphthalmia, anophthalmia, coloboma (MAC) (Bakrania et al., 2008; Reis et al., 2011) and anterior segment dysgenesis (ASGD) (Takenouchi et al., 2013) in human. As a member of the BMP family and transforming growth factor-β (TGF-β) superfamily, *BMP4* is known to play the critical role in the embryonic development (Hogan, 1996). In the eye, the *BMP4* gene has been reported to be engaged in normal ocular morphogenesis involving lens induction (Huang J. et al., 2015), ciliary body formation (Rausch et al., 2018), and retinal development (Murali et al., 2005; Maruyama et al., 2006; Thompson et al., 2019). Previous

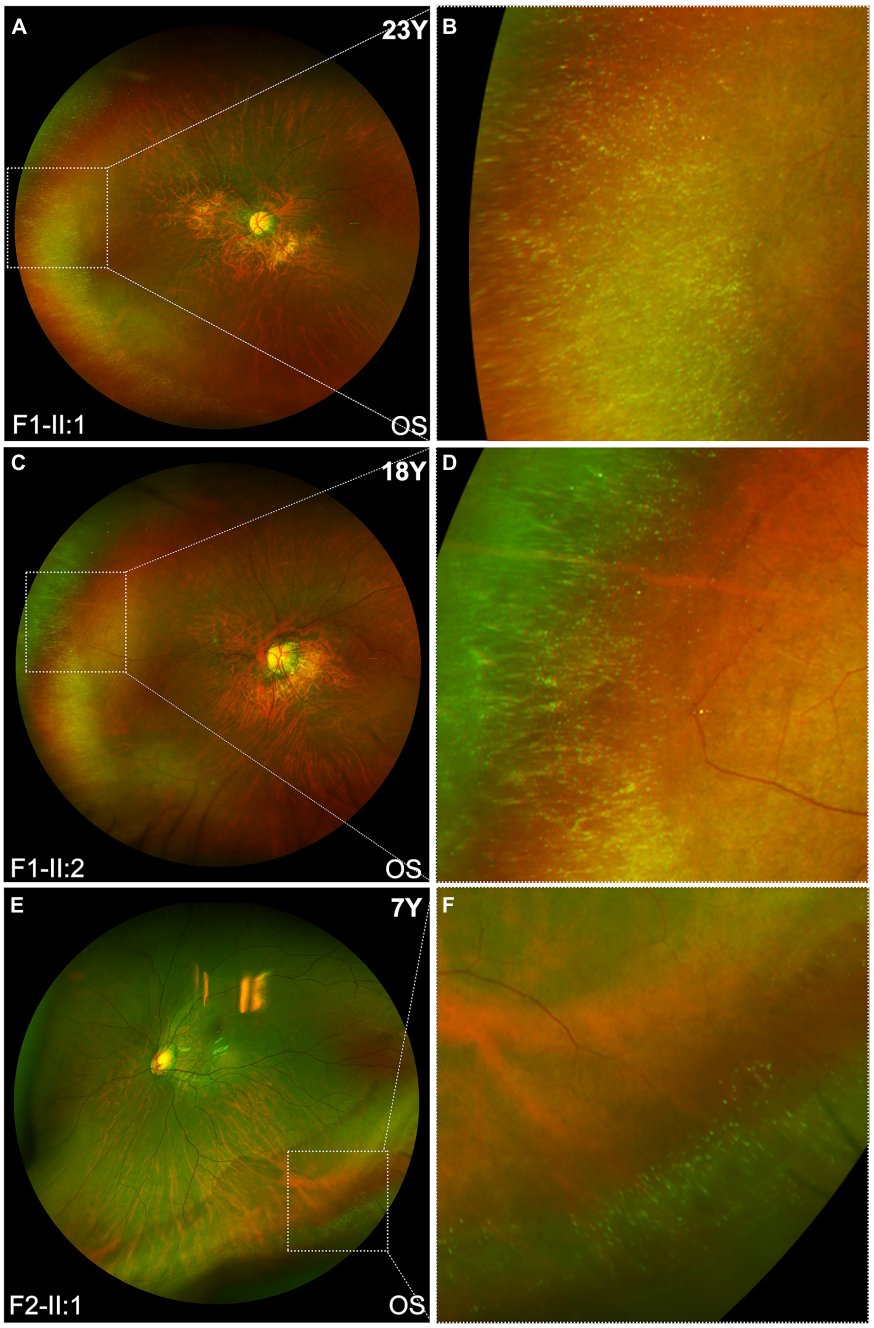

FIGURE 4 | The characteristic snow-grain like retinopathy in peripheral fundus of patients with *BMP4* truncation variants. **(A,C,E)** Representative ultra-widefield fundus imaging of the left eyes from three patients: F1-II:1, F1-II:2, and F2-II:1. **(B,D,F)** The corresponding magnified image demonstrates that white dots in peripheral retina of the three patients closely resemble snow grains.

studies and our current data indicate that *BMP4* may play a bidirectional role in developmental regulation of ocular shape and size. Recently, genome-wide association studies based on a large population of individuals of European and Asian ancestry showed that the same set of variants shared contributions to the genetic risk of high myopia, low myopia and hyperopia (Tideman et al., 2021) in multifactorial manner. In fact, contrary phenotype due to a *BMP4* truncation mutation was reported in one family, where the proband had unilateral anophthalmia, small cornea, and iris and chorioretinal coloboma, while his three family members with the same mutation had high myopia (Bakrania et al., 2008). Except for *BMP4*, opposite ocular phenotypes have been associated with mutations in other genes, such as *FZD5*, in which individuals with the same truncation

variant or different eyes of the same individual exhibited either microphthalmia/uveal coloboma or high myopia (Jiang et al., 2021). Similar situation has been observed for *PAX6*, a gene known to cause aniridia when mutated, in which several single nucleotide polymorphisms are significantly associated with myopia (Hammond et al., 2004). Besides, similar situation also occurs in extraocular system, for example, variants in *M4CR* related to a gain of function tended to result in a lower risk of obesity while *M4CR* variants related to a loss of function contributed to a higher risk of obesity (Lotta et al., 2019). These evidences raise the hypothesis that some genes, such as *BMP4,* may be involved in bidirectional rather than unidirectional control of early ocular development. The mechanism of bidirectional regulation remains unknown and requires further studies.

In our current study, comparative exome sequencing, mutation-specific phenotypic clustering, cosegregation in multiple families, rarity and intolerant of truncations in general population, all provides strong evidence to support that truncation variants in *BMP4* contribute to a novel phenotype of pathologic myopia. The snow-grain degeneration in the peripheral retina may be a characteristic sign specific for *BMP4*-related pathologic myopia. Further studies are expected to confirm our findings and to elucidate the underlying molecular mechanism of bidirectional regulation of eye development.

DATA AVAILABILITY STATEMENT

The datasets presented in this study can be found from the following link: https://bigd.big.ac.cn/gsa-human/browse/HRA001597. The accession number is HRA001597.

ETHICS STATEMENT

The studies involving human participants were reviewed and approved by Institute Review Board of the Zhongshan Ophthalmic Center. Written informed consent to participate in this study was provided by the participants' legal guardian/next of kin.

AUTHOR CONTRIBUTIONS

XX, SL, QZ, XJ, and LZ contributed to the patient recruitment and diagnosis. XX, QZ, XJ, YJ, JO, XL, YW, and LZ collected the clinical records. XX, SL, PW, and QZ performed the whole-exome analysis and targeted-exome sequencing. QZ contributed to the conception and design of this study and revised thoroughly the manuscript. WS, XX, PW, SL, QZ, and YJ performed the statistical analysis. YJ confirmed the variants by Sanger sequencing and family segregation analysis and wrote the first draft of the manuscript. All authors reviewed the manuscript and approved for submission.

FUNDING

This work was supported by the grants from National Natural Science Foundation of China (81770965) and the Fundamental Research Funds of the State Key Laboratory of Ophthalmology.

ACKNOWLEDGMENTS

We are grateful to all the probands and their family members who participated in this study.

SUPPLEMENTARY MATERIAL

The Supplementary Material for this article can be found online at: https://www.frontiersin.org/articles/10.3389/fcell.2021.769636/full#supplementary-material

REFERENCES

Bakrania, P., Efthymiou, M., Klein, J. C., Salt, A., Bunyan, D. J., Wyatt, A., et al. (2008). Mutations in BMP4 cause eye, brain, and digit developmental anomalies: overlap between the BMP4 and hedgehog signaling pathways. *Am. J. Hum. Genet.* 82, 304–319. doi: 10.1016/j.ajhg.2007.09.023

Blackburn, P. R., Zepeda-Mendoza, C. J., Kruisselbrink, T. M., Schimmenti, L. A., García-Miñaur, S., Palomares, M., et al. (2019). Variable expressivity of syndromic BMP4-related eye, brain, and digital anomalies: a review of the literature and description of three new cases. *Eur. J. Hum. Genet.* 27, 1379–1388. doi: 10.1038/s41431-019-0423-424

Chen, Y., Zhang, Q., Shen, T., Xiao, X., Li, S., Guan, L., et al. (2013). Comprehensive mutation analysis by whole-exome sequencing in 41 Chinese families with Leber congenital amaurosis. *Invest. Ophthalmol. Vis. Sci.* 54, 4351–4357. doi: 10.1167/iovs.13-11606

Hammond, C. J., Andrew, T., Mak, Y. T., and Spector, T. D. (2004). A susceptibility locus for myopia in the normal population is linked to the PAX6 gene region on chromosome 11: a genomewide scan of dizygotic twins. *Am. J. Hum. Genet.* 75, 294–304. doi: 10.1086/423148

Hayashi, S., Okamoto, N., Makita, Y., Hata, A., Imoto, I., and Inazawa, J. (2008). Heterozygous deletion at 14q22.1-q22.3 including the BMP4 gene in a patient with psychomotor retardation, congenital corneal opacity and feet polysyndactyly. *Am. J. Med. Genet. A* 146a, 2905–2910. doi: 10.1002/ajmg.a.32519

Hogan, B. L. (1996). Bone morphogenetic proteins in development. *Curr. Opin. Genet. Dev.* 6, 432–438. doi: 10.1016/s0959-437x(96)80064-80065

Huang, J., Liu, Y., Oltean, A., and Beebe, D. C. (2015). Bmp4 from the optic vesicle specifies murine retina formation. *Dev. Biol.* 402, 119–126. doi: 10.1016/j.ydbio.2015.03.006

Huang, X., Xiao, X., Jia, X., Li, S., Li, M., Guo, X., et al. (2015). Mutation analysis of the genes associated with anterior segment dysgenesis, microcornea and microphthalmia in 257 patients with glaucoma. *Int. J. Mol. Med.* 36, 1111–1117. doi: 10.3892/ijmm.2015.2325

Jiang, Y., Ouyang, J., Li, S., Xiao, X., Sun, W., and Zhang, Q. (2021). Confirming and expanding the phenotypes of FZD5 variants: coloboma, inferior chorioretinal hypoplasia, and high myopia. *Mol. Vis.* 27, 50–60.

Kiefer, A. K., Tung, J. Y., Do, C. B., Hinds, D. A., Mountain, J. L., Francke, U., et al. (2013). Genome-wide analysis points to roles for extracellular matrix remodeling, the visual cycle, and neuronal development in myopia. *PLoS Genet.* 9:e1003299. doi: 10.1371/journal.pgen.1003299

Li, J., Jiang, D., Xiao, X., Li, S., Jia, X., Sun, W., et al. (2015). Evaluation of 12 myopia-associated genes in Chinese patients with high myopia.

Invest. Ophthalmol. Vis. Sci. 56, 722–729. doi: 10.1167/iovs.14-14880

Lotta, L. A., Mokrosiński, J., Mendes, de Oliveira, E., Li, C., Sharp, S. J., et al. (2019). Human gain-of-function MC4R variants show signaling bias and protect against obesity. *Cell* 177, 597–607.e9. doi: 10.1016/j.cell.2019.03.044

Lumaka, A., Van Hole, C., Casteels, I., Ortibus, E., De Wolf, V., Vermeesch, J. R., et al. (2012). Variability in expression of a familial 2.79 Mb microdeletion in chromosome 14q22.1-22.2. *Am. J. Med. Genet. A* 158a, 1381–1387. doi: 10.1002/ajmg.a.35353

Maruyama, Y., Mikawa, S., Hotta, Y., and Sato, K. (2006). BMP4 expression in the developing rat retina. *Brain Res.* 1122, 116–121. doi: 10.1016/j.brainres.2006.08.130

Murali, D., Yoshikawa, S., Corrigan, R. R., Plas, D. J., Crair, M. C., Oliver, G., et al. (2005). Distinct developmental programs require different levels of Bmp signaling during mouse retinal development. *Development* 132, 913–923. doi: 10.1242/dev.01673

Nixon, T. R. W., Richards, A., Towns, L. K., Fuller, G., Abbs, S., Alexander, P., et al. (2019). Bone morphogenetic protein 4 (BMP4) loss-of-function variant associated with autosomal dominant Stickler syndrome and renal dysplasia. *Eur. J. Hum. Genet.* 27, 369–377. doi: 10.1038/s41431-018-0316-y

Ohno-Matsui, K., Kawasaki, R., Jonas, J. B., Cheung, C. M., Saw, S. M., Verhoeven, V. J., et al. (2015). International photographic classification and grading system for myopic maculopathy. *Am. J. Ophthalmol.* 159, 877–883.e7. doi: 10.1016/j.ajo.2015.01.022

Ohno-Matsui, K., Lai, T. Y., Lai, C. C., and Cheung, C. M. (2016). Updates of pathologic myopia. *Prog. Retin. Eye Res.* 52, 156–187. doi: 10.1016/j.preteyeres.2015.12.001

Rausch, R. L., Libby, R. T., and Kiernan, A. E. (2018). Ciliary margin-derived BMP4 does not have a major role in ocular development. *PLoS One* 13:e0197048. doi: 10.1371/journal.pone.0197048

Reis, L. M., Tyler, R. C., Schilter, K. F., Abdul-Rahman, O., Innis, J. W., Kozel, B. A., et al. (2011). BMP4 loss-of-function mutations in developmental eye disorders including SHORT syndrome. *Hum. Genet.* 130, 495–504. doi: 10.1007/s00439-011-0968-y

Sankaridurg, P., Tahhan, N., Kandel, H., Naduvilath, T., Zou, H., Frick, K. D., et al. (2021). IMI impact of Myopia. *Invest. Ophthalmol. Vis. Sci.* 62:2. doi: 10.1167/iovs.62.5.2

Spaide, R., Ohno-Matsui, K., and Yannuzzi, L. (2021). Pathologic Myopia. *Invest. Ophthalmol. Visual Sci.* 62:5.

Sun, W., Xiao, X., Li, S., Ouyang, J., Li, X., Jia, X., et al. (2019). Rare variants in novel and known genes associated with primary angle closure glaucoma based on whole exome sequencing of 549 probands. *J. Genet. Genom.* 46, 353–357. doi: 10.1016/j.jgg.2019.06.004

Takenouchi, T., Nishina, S., Kosaki, R., Torii, C., Furukawa, R., Takahashi, T., et al. (2013). Concurrent deletion of BMP4 and OTX2 genes, two master genes in ophthalmogenesis. *Eur. J. Med. Genet.* 56, 50–53. doi: 10.1016/j.ejmg.2012.10.007

Thanikachalam, S., Hodapp, E., Chang, T. C., Swols, D. M., Cengiz, F. B., Guo, S., et al. (2020). Spectrum of genetic variants associated with anterior segment dysgenesis in South Florida. *Genes (Basel)* 11:350. doi: 10.3390/genes11040350

Thompson, A., Berry, M., Logan, A., and Ahmed, Z. (2019). Activation of the BMP4/Smad1 pathway promotes retinal ganglion cell survival and axon regeneration. *Invest. Ophthalmol. Vis. Sci.* 60, 1748–1759. doi: 10.1167/iovs.18-26449

Tideman, J. W. L., Pärssinen, O., Haarman, A. E. G., Khawaja, A. P., Wedenoja, J., Williams, K. M., et al. (2021). Evaluation of shared genetic susceptibility to high and low Myopia and Hyperopia. *JAMA Ophthalmol.* 139, 601–609. doi: 10.1001/jamaophthalmol.2021.0497

Wang, P., Li, S., Sun, W., Xiao, X., Jia, X., Liu, M., et al. (2019). An ophthalmic targeted exome sequencing panel as a powerful tool to identify causative mutations in patients suspected of hereditary eye diseases. *Transl. Vis. Sci. Technol.* 8:21. doi: 10.1167/tvst.8.2.21

Wang, Q., Wang, P., Li, S., Xiao, X., Jia, X., Guo, X., et al. (2010). Mitochondrial DNA haplogroup distribution in Chaoshanese with and without Myopia. *Mol. Vis.* 16, 303–309.

Wong, T. Y., Ferreira, A., Hughes, R., Carter, G., and Mitchell, P. (2014). Epidemiology and disease burden of pathologic myopia and myopic choroidal neovascularization: an evidence-based systematic review. *Am. J. Ophthalmol.* 157, 9–25.e12. doi: 10.1016/j.ajo.2013.08.010

Yi, Z., Ouyang, J., Sun, W., Li, S., Xiao, X., and Zhang, Q. (2020). Comparative exome sequencing reveals novel candidate genes for retinitis pigmentosa. *EBioMedicine* 56:102792. doi: 10.1016/j.ebiom.2020.102792

Zhang, Q. (2021). "Genetics of pathologic Myopia," in *Pathologic Myopia*, eds R. F. Spaide, K. Ohno-Matsui, and L. A. Yannuzzi (Cham: Springer International Publishing), 43–58.

Conflict of Interest: The authors declare that the research was conducted in the absence of any commercial or financial relationships that could be construed as a potential conflict of interest.

Publisher's Note: All claims expressed in this article are solely those of the authors and do not necessarily represent those of their affiliated organizations, or those of the publisher, the editors and the reviewers. Any product that may be evaluated in this article, or claim that may be made by its manufacturer, is not guaranteed or endorsed by the publisher.

Copyright © 2021 Jiang, Ouyang, Li, Wang, Zhou, Li, Jia, Xiao, Sun, Wang and Zhang. This is an open-access article distributed under the terms of the Creative Commons Attribution License (CC BY). The use, distribution or reproduction in other forums is permitted, provided the original author(s) and the copyright owner(s) are credited and that the original publication in this journal is cited, in accordance with accepted academic practice. No use, distribution or reproduction is permitted which does not comply with these terms.

frontiers in Cell and Developmental Biology

ORIGINAL RESEARCH
published: 02 December 2021
doi: 10.3389/fcell.2021.788422

Defect of LSS Disrupts Lens Development in Cataractogenesis

Minglei Zhao[1], Tingfang Mei[1,2], Bizhi Shang[1], Bin Zou[1], Qing Lian[1,3], Wenchang Xu[1], Keling Wu[1], Yuhua Lai[1], Chujun Liu[1], Lai Wei[1], Jie Zhu[4], Kang Zhang[5], Yizhi Liu[1,6,7] and Ling Zhao[1]**

[1]State Key Laboratory of Ophthalmology, Zhongshan Ophthalmic Center, Sun Yat-sen University, Guangdong Provincial Key Laboratory of Ophthalmology and Visual Science, Guangzhou, China, [2]Guangdong Province Key Laboratory of Brain Function and Disease, Zhongshan School of Medicine, Sun Yat-sen University, Guangzhou, China, [3]Dongguan Guangming Ophthalmic Hospital, Dongguan, China, [4]Guangzhou Women and Children's Medical Center, Guangzhou Medical University, Guangzhou, China, [5]Center for Biomedicine and Innovations, Faculty of Medicine, Macau University of Science and Technology and University Hospital, Macau, China, [6]Guangzhou Regenerative Medicine and Health Guangdong Laboratory, Guangzhou, China, [7]Research Unit of Ocular Development and Regeneration, Chinese Academy of Medical Sciences, Guangzhou, China

Congenital cataract is one of the leading causes of blindness in children worldwide. About one-third of congenital cataracts are caused by genetic defects. LSS, which encodes lanosterol synthase, is a causal gene for congenital cataracts. LSS is critical in preventing abnormal protein aggregation of various cataract-causing mutant crystallins; however, its roles in lens development remain largely unknown. In our study, we generated a mouse model harboring Lss G589S mutation, which is homologous to cataract-causing G588S mutation in human LSS. $Lss^{G589S/G589S}$ mice exhibited neonatal lethality at postal day 0 (P0), whereas these mice showed severe opacity in eye lens. Also, we found that cataract was formed at E17.5 after we examined the opacity of embryonic lens from E13.5 to E18.5. Moreover, disrupted lens differentiation occurred at E14.5 prior to formation of the opacity of eye lens, shown as delayed differentiation of lens secondary fiber and disordered lens fiber organization. In addition, RNA-seq analysis indicated that cholesterol synthesis signaling pathways were significantly downregulated. Overall, our findings provide clear evidence that a mouse model harboring a homozygous Lss G589S mutation can recapitulate human congenital cataract. Our study points out that LSS functions as a critical determinant of lens development, which will contribute to better understanding LSS defects in cataractogenesis and developing therapies for cataracts.

Keywords: lanosterol synthase, congenital cataract, mouse model, mutation, lens development

OPEN ACCESS

Edited by:
Zi-Bing Jin,
Capital Medical University, China

Reviewed by:
Ruifang Sui,
Peking Union Medical College Hospital (CAMS), China
Rachida Bouhenni,
Northeast Ohio Medical University, United States

****Correspondence:***
Ling Zhao
zhaoling@gzzoc.com
Yizhi Liu
yzliu62@yahoo.com

Specialty section:
This article was submitted to Molecular and Cellular Pathology, a section of the journal Frontiers in Cell and Developmental Biology

Received: *02 October 2021*
Accepted: *29 October 2021*
Published: *02 December 2021*

Citation:
Zhao M, Mei T, Shang B, Zou B, Lian Q, Xu W, Wu K, Lai Y, Liu C, Wei L, Zhu J, Zhang K, Liu Y and Zhao L (2021) Defect of LSS Disrupts Lens Development in Cataractogenesis. Front. Cell Dev. Biol. 9:788422. doi: 10.3389/fcell.2021.788422

INTRODUCTION

Cataracts occur due to a loss of transparency in the crystalline lens of the eye, which is the most leading cause of blindness and impaired vision worldwide (Liu et al., 2017). Up to one-third of congenital cataracts (CC) are inherited (Hejtmancik, 2008). There are more than 100 genes that have been reported to cause CC (Messina-Baas and Cuevas-Covarrubias, 2017). In known cataract causal genes, half of them belong to the crystallin family. Mutations in genes encoding membrane transport, scaffolding proteins, transcription factors, heat shock transcription factor, and metabolism-related proteins are also identified to cause CC (Shiels and Hejtmancik, 2013; Zhao et al., 2015; Sun et al., 2019).

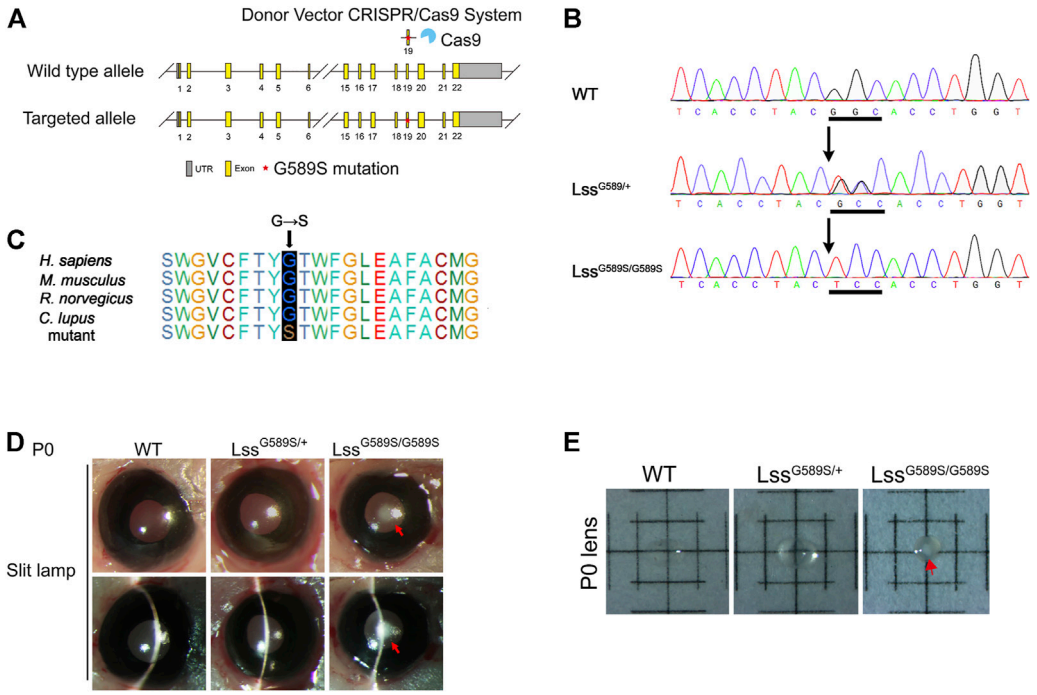

FIGURE 1 | The lens of engineered Lss$^{G589S/G589S}$ mice could recapitulate the phenotype of human congenital cataract. **(A)** Schematic diagram of Lss G589S knock-in mice generated at exon 19 of Lss *via* the CRISPR/Cas9 system. **(B)** Sanger sequencing performed to validate the G589S missense mutation (GGC > TCC) in WT, Lss$^{G589S/+}$, and Lss$^{G589S/G589S}$ mice. Underlined sequences indicate the changed nucleic acids. **(C)** The amino acid residue G588 in human LSS is highly conserved across species, which is homologous to mouse G589. Blue box refers to the homologous site of LSS G588 in *Homo sapiens*, *Mus musculus*, *Rattus norvegicus*, and *Canis lupus*. **(D)** Mouse lens were examined by slit lamp. Red arrows indicated congenital cataract formed in lens of Lss$^{G589S/G589S}$ mice at P0. **(E)** Lenses were isolated and photographed by a dissecting microscope. Red arrows indicated cataract formed in the lens of Lss$^{G589S/G589S}$ mice at P0.

LSS, which encodes lanosterol synthase, is a causal gene for CC (Zhao et al., 2015; Chen and Liu, 2017). LSS is a key early rate-limiting enzyme in the biosynthesis of four-ringed steroid structure intermediate products including cholesterol, steroid hormones, and vitamin D (Huff and Telford, 2005). LSS is critical in preventing abnormal crystallin protein aggregation (Zhao et al., 2015). In our previous study, two distinct homozygous LSS missense mutations (W581R and G588S) impaired key catalytic functions of LSS and were identified in two families with extensive CC (Zhao et al., 2015). Although LSS mutations with an additional mutation in Fdft1 caused cholesterol deficiency-associated cataracts in the Shumiya cataract rat (SCR) and lens-specific Lss knockout mice had cataracts, SCRs developed mature cataracts at around 11 weeks of age and cataracts were shown in lens-specific Lss knockout mice at 14 weeks of age (Mori et al., 2006; Wada et al., 2020). Thus, the roles of LSS in early-stage of lens development remain largely unknown.

In our study, we generated a knock-in mouse model with G589S mutation in Lss, which is homologous to cataract-causing G588S mutation in human LSS. Our finding showed that mice harboring biallelic Lss G589S mutations exhibited CC at E17.5 and disrupted lens fiber differentiation at E14.5. Taken together, our study points out that LSS is a critical determinant in lens development, which will contribute to better understanding of the roles of LSS in cataractogenesis.

MATERIALS AND METHODS

Animals

All the animal procedures were approved by the Animal Ethical Committee at Zhongshan Ophthalmic Center, Sun Yat-sen University (Guangzhou, China), and all the uses of animals were performed in accordance with the Association for Research in Vision and Ophthalmology (ARVO) statement. C57BL/6J wild-type (WT) mice and Lss G589S knock-in (KI) mice produced on the C57BL/6J background were obtained from GemPharmatech Co., Ltd. (Jiangsu, China). The G589S mutation of mouse Lss, homologous to cataract-causing G588S mutation in human LSS, was generated by CRISPR/Cas9-mediated genome editing in GemPharmatech Co., Ltd. (Nanjing, China) (**Figure 1A**). Mice with Lss G589S mutation were genotyped by Sanger sequencing using PCR of tail genomic DNA. PCR primers are 5′-GCCTTAGCCCAGTGCTAGGAAT-3′ and 5′-CATGGTTTC TGCTTCAGTTCCT-3′. To collect mouse embryos at various stages, the day a vaginal plug was observed after mating was designated as embryonic day 0.5 (E0.5). Mouse lens at postnatal day 0 (P0) and E13.5-E18.5 were collected for further studies.

Slit-lamp photography and lens photography

The eyelids of neonatal mice at P0 were removed immediately. A photo was taken on the eyes under a slit lamp with appropriate angle and light intensity under the slit lamp. Lens were enucleated, immersed in lens medium (Medium 199, Earle's Salts, Thermo), and photos were taken immediately under dissection microscopy (M205 FA, Leica, Wetzlar, Germany).

Histology

Histology was performed as previously described (Lian et al., 2019). Enucleated eyeballs from P0 mice and embryos from $Lss^{G589S/G589S}$, $Lss^{G589S/+}$, and WT mice were fixed with 4% paraformaldehyde overnight at 4°C, dehydrated in a series of ethanol with ascending concentrations, cleared in xylene, and embedded in paraffin. The tissues were sectioned in a vertical pupillary optic nerve plane and stained with hematoxylin and eosin. The images were captured using a TissueFAXS microscope (TissueGnostics, Vienna, Austria).

Immunofluorescence

For frozen sections, enucleated eyeballs from P0 mice and embryos were fixed in 4% paraformaldehyde for 30 min at room temperature and 30% sucrose dehydrated over night at 4°C, then embedded in OCT, frozen, and sectioned at 10 μm. Cryosections were permeabilized in 0.5% Triton X-100/PBS for 2 min, blocked in 5% donkey serum and 5% BSA in PBS for 1 h at room temperature, then incubated with primary antibodies overnight at 4°C. After rinsing, the sections were incubated with fluorescence-labeled secondary antibodies (Alexa Fluor 488, or Alexa Fluor 546, Invitrogen, Carlsbad, CA, USA) for 2 h at room temperature and counterstained with DAPI (1:1,000, H-1200, Vector Labs, Burlingame, CA, USA). Primary antibodies used for immunofluorescence were LSS (1:300, 18693-1-AP, Proteintech, Wuhan, China), $p57^{KIP2}$ (1:200, ab75974, Abcam, Cambridge, MA, USA), Pax6 (1:200, PRB-278P, BioLegend, San Diego, CA, USA), and Prox1 (1:200, 11067-2-AP, Proteintech). The images were captured with an LSM980 confocal scanning microscope (Carl Zeiss, Thornwood, NY, USA) or a TissueFAXS microscope (TissueGnostics, Austria).

Transmission electron microscopy

Mouse lens at P0 were fixed and processed as previously described (Morishita et al., 2013). Lenses were immediately placed into fixative consisting of 2.5% glutaraldehyde and 2% formaldehyde in 0.1 mol/l cacodylate buffer with 0.08 mol/l $CaCl_2$ at 4°C. Then, the lens was postfixed for 1.5 h in 1% aqueous OsO_4, dehydrated through graded acetone, transitioned in propylene oxide, infiltrated with propylene oxide and EPON mixtures (TAAB 812 resin; Marivac, Quebec, QC, Canada), embedded in EPON, and cured for 48 h at 60°C. One-micron lens sections across the equatorial plane were collected on glass slides and stained with toluidine-blue in 1% borate buffer. Thin sections were cut at 80-100 nm and stained with saturated, aqueous uranyl acetate, and Sato's lead stain and imaged with a transmission electron microscope (Tecnai G2 Spirit, FEI, Hillsboro, OR, Czech).

RNA-seq analysis

RNA sequencing and analysis were performed by Berry Genomics Corporation, Beijing, China. Lenses were isolated from $Lss^{G589S/G589S}$, $Lss^{G589S/+}$, and WT mice embryos at E14.5 and three biological replicates from $Lss^{G589S/G589S}$, $Lss^{G589S/+}$, and WT, each replicate consisting of nine pups (18 lenses) at E14.5 (Anand et al., 2018). Lenses were dissolved immediately in TRIzol reagent (Invitrogen, USA), and total RNA was extracted according to the manufacturer's instructions (Khan et al., 2015). A total amount of 1 μg RNA per sample was used as input material. Sequencing libraries were generated using NEBNext® Ultra™ RNA Library Prep Kit for Illumina® (NEB, USA) following the manufacturer's recommendations, and index codes were added to attribute sequences to each sample. The clustering of the index-coded samples was performed on a cBot Cluster Generation System using TruSeq PE Cluster Kit v3-cBot-HS (Illumina, San Diego, CA, USA) according to the manufacturer's instructions. After cluster generation, the library preparations were sequenced on an Illumina NovaSeq platform and 150-bp paired-end reads were generated. Clean data with high quality after processed raw data were aligned to the mouse reference genome (GRCm38/mm10) using TopHat v2.0.12. After applying the HTSeq v0.6.1 to extract the raw count tables based on the aligned bam files, DESeq2111 was used to perform normalization and differential gene expression analysis. Ingenuity pathway analysis (IPA) (Qiagen Inc., Hilden, Germany) software was applied to analyze signaling pathways and differentially expressed genes (adjusted p-value < 0.05).

Western blot

Western blot was performed as previously described (Wu et al., 2020). Two isolated lenses from one embryo at E14.5 were homogenized and lysed in lysis buffer (RIPA, protease inhibitors, and PMSF mixture, pH 7.6) on ice for 10 min, and the lysates were centrifuged at 13,000 rpm for 20 min. Each group had three biological replicates. Lens lysates were separated by 10% SDS-PAGE and transferred to PVDF (0.2 mm). Membranes were blotted with 5% milk (fat free) prepared in Tris-buffered saline Plus 0.1% Tween-20 (TBST) at room temperature for 1 h and incubated with primary antibodies diluted in 5% milk overnight at 4°C. Blots were visualized using secondary antibodies by enhanced chemiluminescence (Thermo, Waltham, MA, USA). Primary antibodies used for Western blotting were LSS (18693-1-AP, Proteintech) and tubulin (2146, CST). ImageJ (NIH, Bethesda, MD, USA) was applied in Western blotting analysis.

Statistics

The data are presented as mean ± SEM. Student's t test was applied to determine statistical significance. Statistical significance was defined as $p < 0.05$.

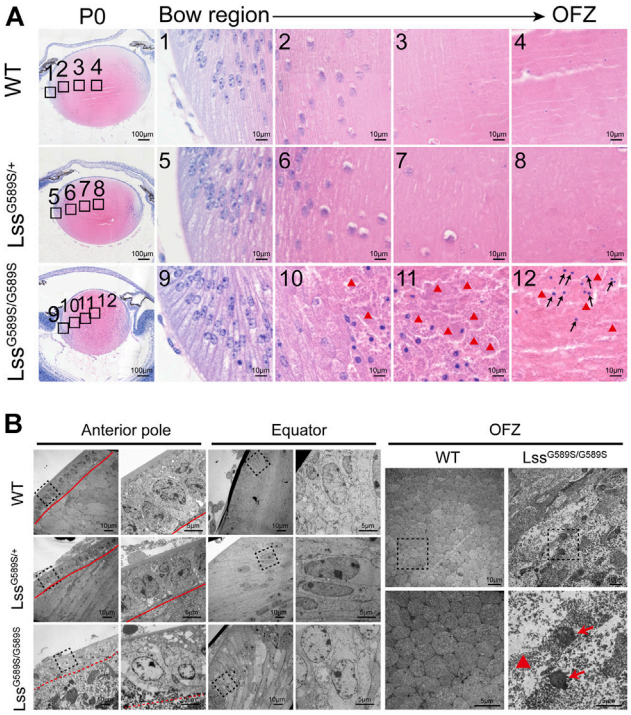

FIGURE 2 | Disrupted lens structure caused by a homozygous Lss G589S mutation at P0. **(A)** Representative hematoxylin and eosin staining images of lens structure in WT, $Lss^{G589S/+}$, and $Lss^{G589S/G589S}$ mice at P0. Boxes of numbers 1–4, 5-8, and 9–12 indicate four continuous and comparable zones from the lens equator to OFZ within the lens fiber cell regions of WT, $Lss^{G589S/+}$, and $Lss^{G589S/G589S}$, respectively (the leftmost panel, black boxes). Scale bar: 100 μm. The enlargements are the magnifications of the boxed inset shown in the left panel (numbers 1–4, 5–8, and 9–12). Scale bar: 10 μm. Red triangles indicate debris and bulks of fibers in $Lss^{G589S/G589S}$ mouse lens. Black arrows indicate that a large number of fiber cell nuclei were still retained at the OFZ region of $Lss^{G589S/G589S}$ mouse lens. **(B)** Electron micrographs of lens morphology at the anterior pole, equator, and OFZ regions in WT, $Lss^{G589S/+}$, and $Lss^{G589S/G589S}$ mice. $n = 4$ lenses per group. At the anterior pole region, representative images of the lens epithelial–fiber interface (EFI) were shown. Red solid lines indicate lens epithelial–fiber interface (EFI) in WT and $Lss^{G589S/+}$ mice. Red dashed line indicates lens EFI in $Lss^{G589S/G589S}$ mice. Boxes indicate morphology of lens epithelial cells and EFI in WT, $Lss^{G589S/+}$, and $Lss^{G589S/G589S}$ mice **(left panel)**. Scale bar: 10 μm. The enlargement is the magnification of the boxed inset shown in the left panel. Scale bar: 5 μm. At the equator region, representative images of alignment and morphology of secondary fiber cells were shown. Boxes indicate the morphology of secondary fiber cells **(left panel)**. Scale bar: 10 μm. The enlargement is the magnification of the boxed inset shown in the left panel. Scale bar: 5 μm. At the OFZ region, representative images of alignment and morphology of fiber cells were shown. Scale bar: 10 μm. The enlargement is the magnification of the boxed inset shown in the upper panel. Red triangle indicates high-density deposits of fiber debris, and red arrows indicate condensed nuclei in the central OFZ of $Lss^{G589S/G589S}$ lens. Scale bar: 5 μm.

RESULTS

The mice harboring a homozygous mutation ($Lss^{G589S/G589S}$) can recapitulate human CC

Based on the evidence of LSS gene mutational analysis in human CC (Zhao et al., 2015; Chen and Liu, 2017), we generated a mouse model harboring Lss G589S mutation, which is homologous to cataract-causing G588S mutation in human LSS. Targeted alleles were introduced in exon 19 of Lss on mouse chromosome 10 *via* CRISPR/Cas9 system (**Figure 1A**). Sanger sequencing was performed to validate the G589S missense mutation (GGC > TCC) in Lss (**Figure 1B**). The amino acid residue G588 in human LSS is highly conserved across species and homologous to mouse G589 (**Figure 1C**). Mouse lenses were examined by slit-lamp and photographed by a dissecting microscope. WT and $Lss^{G589S/+}$ mice showed transparent lenses under a slit lamp (**Figure 1D**) and dissecting microscope (**Figure 1E**). Compared to WT and $Lss^{G589S/+}$ mice, $Lss^{G589S/G589S}$ showed severe opacity of eye lens at postal day 0 (P0), whereas these mice exhibited neonatal lethality at P0 (**Figure 1D**). The cataract plaque was mainly located in the nucleus of lens (**Figure 1E**). Another line of $Lss^{G589S/G589S}$ mice also showed the same phenotypes with CC (**Supplemental Figure 1A,B**) and died at P0. Thus, our finding showed that a mouse model harboring an Lss G589S mutation was generated and the mice harboring a biallelic mutation of Lss G589S exhibited CC.

Disrupted lens structure caused by a homozygous $Lss^{G589S/G589S}$ mutation at P0

The pups with a homozygous $Lss^{G589S/G589S}$ mutation were born with abnormally small lenses with severely structural defects at P0, while the lens structure is normal in WT and $Lss^{G589S/+}$ mice at P0 (**Figure 2A**). The process of denucleation and organization of lens fibers was investigated from the lens bow region to the organelle-free zone (OFZ) in WT, $Lss^{G589S/+}$, and $Lss^{G589S/G589S}$ mice (**Figure 2A**). Our results showed that the process of denucleation had been completed at OFZ and the lens fiber was normally arranged in WT and $Lss^{G589S/+}$ mouse lens (**Figure 2A** 1-4, **Figure 2A** 5-8). However, in the lens of $Lss^{G589S/G589S}$ mice, the process of denucleation failed to complete at OFZ (**Figure 2A** 9-12) and a large number of fiber cell nuclei were still retained at the OFZ region (**Figure 2A** 12, black arrows). Also, compared with WT and $Lss^{G589S/+}$ mouse lens, the fiber nuclei at the OFZ region were more highly condensed in the lens of $Lss^{G589S/G589S}$ mice. Moreover, debris and bulks of fibers were clearly observed in the lens of $Lss^{G589S/G589S}$ mice (**Figure 2A** 10-12, red triangles).

High-resolution structural features of lens were provided by transmission electron microscopy (TEM) examination. A monolayer of anterior lens epithelial cells and well-aligned lens fiber cells at the anterior pole were shown in the lens of WT and $Lss^{G589S/+}$ mice (**Figure 2B**, **Supplementary Figure 2A**). Also, the epithelial–fiber interface (EFI) was intact in WT and $Lss^{G589S/+}$ lens (**Figure 2B**, **Supplementary Figure 2A**, red solid lines), while the EFI was severely disrupted in $Lss^{G589S/G589S}$ homozygous lens (**Figure 2B**, **Supplementary Figure 2A**, red dashed line). At the lens equator, secondary fiber cells were well organized with elongated shape in WT and $Lss^{G589S/+}$ heterozygous lens, while secondary fiber cells were disorganized in alignment with the swollen shape in $Lss^{G589S/G589S}$ lens (**Figure 2B**). In addition, compared with WT mice, high-density deposits of fiber debris (**Figure 2B**,

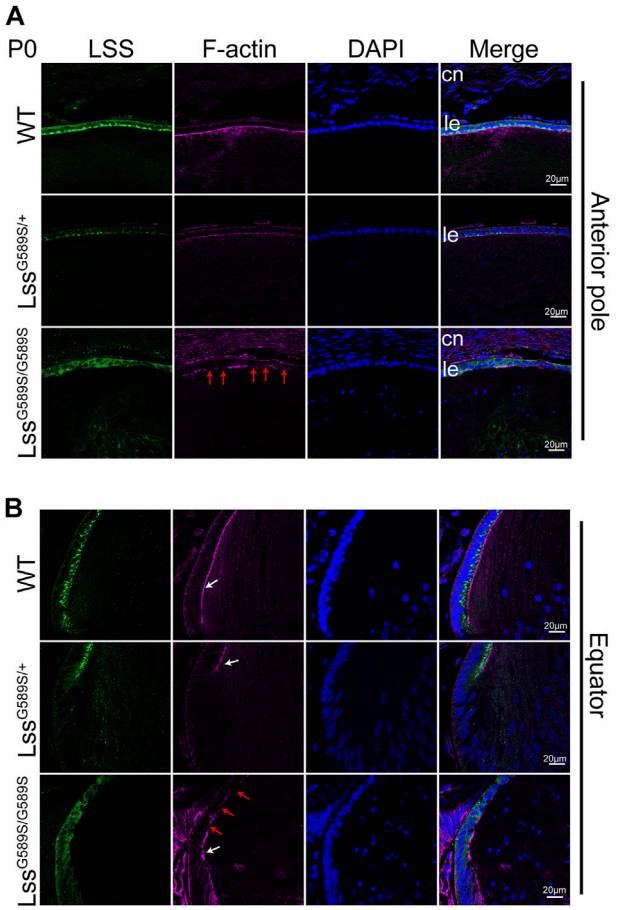

FIGURE 3 | Different distributions of LSS protein in lens epithelial cells at P0. **(A)** The expression of LSS and its distribution in lens epithelial cells at the anterior pole region of WT, $Lss^{G589S/+}$, and $Lss^{G589S/G589S}$ mice at P0. **(B)** The expression of LSS and its distribution in lens epithelial cells at the equator region. White arrows indicate EFI, and red arrows indicate discontinuous EFI stained by F-actin. cn, cornea. Le, lens epithelial layer. Scale bar: 20 μm.

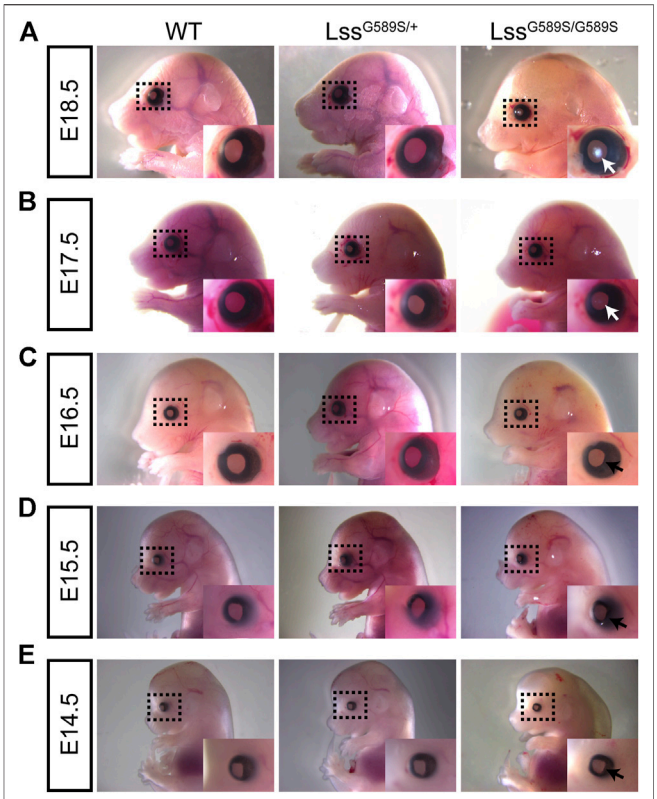

FIGURE 4 | Lens opacity caused by LssG589S/G589S mutation was formed at the embryonic stage. Examination of lens transparency in WT, $Lss^{G589S/+}$, and $Lss^{G589S/G589S}$ mice at **(A)** E18.5, **(B)** E17.5, **(C)** E16.5, **(D)** E15.5, and **(E)** E14.5 by stereomicroscopy. White arrows indicate that mild cataract was formed at E17.5 and serious cataract was formed at E18.5 in the lens of $Lss^{G589S/G589S}$ mice. Black arrows indicate that no visible cataract was observed at E14.5, E15.5, and E16.5 in the lens of $Lss^{G589S/G589S}$ mice.

Supplementary Figure 2B, red triangle) and condensed nuclei (**Figure 2B**, red arrows, **Supplementary Figure 2B**) were observed in the central organelle-free zone (OFZ) of $Lss^{G589S/G589S}$ lens.

Different distribution of LSS protein in lens epithelial cells at P0

We detected the expression of LSS and its distribution in lens epithelial cells of the anterior pole and equator among WT, $Lss^{G589S/+}$, and $Lss^{G589S/G589S}$ mice at P0. In lens of WT mice, abundant LSS was mainly located in the lens epithelial layer adjacent to the EFI. In lens of $Lss^{G589S/+}$ heterozygous mice, decreased LSS expression was observed in the lens epithelial layer, while its distribution was also mainly located in the lens epithelial layer adjacent to the EFI (**Figure 3B**, white arrows). In $Lss^{G589S/G589S}$ homozygous mice, LSS was not located in the lens epithelial layer adjacent to the EFI and mainly diffused in the whole lens epithelial layer, as well as discontinuous EFI shown by F-actin staining (**Figures 3A,B**, red arrows). Thus, our finding showed that the distribution of lens LSS in $Lss^{G589S/G589S}$ mice was distinctly different in WT and $Lss^{G589S/+}$ heterozygous mice.

Lens opacity in $Lss^{G589S/G589S}$ mice was formed at the embryonic stage

Our results above showed that the mouse model harboring a biallelic mutation of Lss G589S exhibited CC at P0; however, the time when the lens formed cataract is not clear. Thus, we investigated cataract formation time in $Lss^{G589S/G589S}$ homozygous mouse lens at different embryonic stages (E14.5, E15.5, E16.5, E17.5, and E18.5). Ocular phenotypes of embryonic mice were observed by stereomicroscope. Our results demonstrated that mild cataract was formed at E17.5 (**Figure 4B**, E17.5, white arrow) and serious cataract was formed at E18.5 in the lens of $Lss^{G589S/G589S}$ mice (**Figure 4A**, E18.5, white arrow). No visible cataract was observed at E14.5, E15.5, and E16.5 in the lens of $Lss^{G589S/G589S}$ homozygous mice

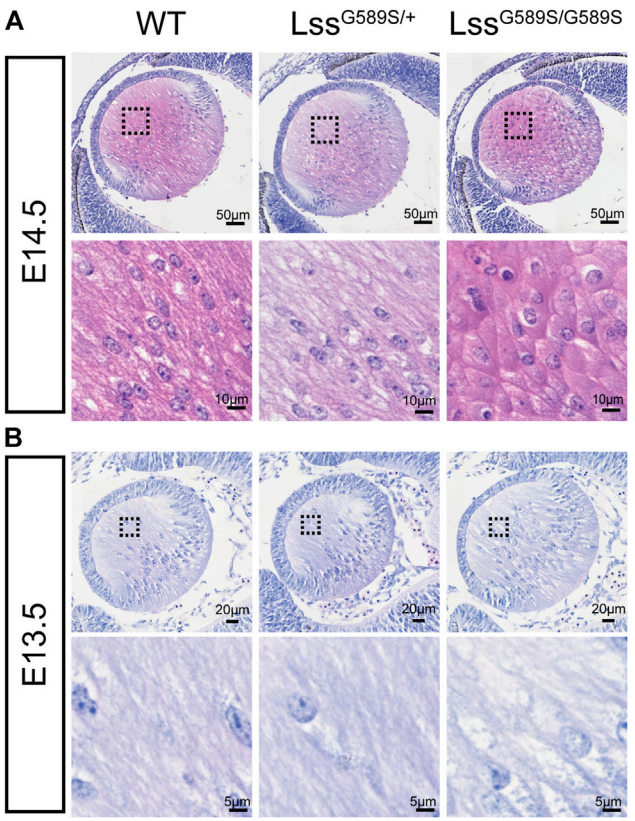

FIGURE 5 | Morphology of fiber cells in embryonic lens of Lss$^{G589S/G589S}$ mice. **(A)** Morphology of fiber cells stained with hematoxylin and eosin in embryonic lens of WT, Lss$^{G589S/+}$, and Lss$^{G589S/G589S}$ mice at E14.5. Scale bar: 50 μm. The enlargement is the magnification of the boxed inset shown in the upper panel. Scale bar: 10 μm. **(B)** Morphology of fiber cells in embryonic lens of WT, Lss$^{G589S/+}$, and Lss$^{G589S/G589S}$ mice at E13.5. Scale bar: 20 μm. The enlargement is the magnification of the boxed inset shown in the upper panel. Scale bar: 5 μm.

(**Figures 4C–E**, black arrow). Our findings indicated that visible opacity was formed in embryonic lens of Lss$^{G589S/G589S}$ homozygous mice at E17.5.

Abnormal morphology of fiber cells in embryonic lens of Lss$^{G589S/G589S}$ mice

We then further investigated when structural defects were formed in embryonic lens of Lss$^{G589S/G589S}$ mice. We found that refractive error could be observed in the lenses of Lss$^{G589S/G589S}$ mice at E14.5, E15.5, and E16.5 after checking dissected eyeballs. Compared with fiber cells showing a long spindle shape in lens of WT and Lss$^{G589S/+}$ heterozygous mice, fiber cells displayed an irregular rounded shape at the posterior pole in the lens of Lss$^{G589S/G589S}$ homozygous mice at E14.5 (**Figure 5A**). At E13.5, a large part of fiber cells showed a normally elongated shape in the lens of Lss$^{G589S/G589S}$ homozygous mice (**Figure 5B**). Our results showed that morphology of fiber cells was obviously abnormal in embryonic lens of Lss$^{G589S/G589S}$ mice at E14.5.

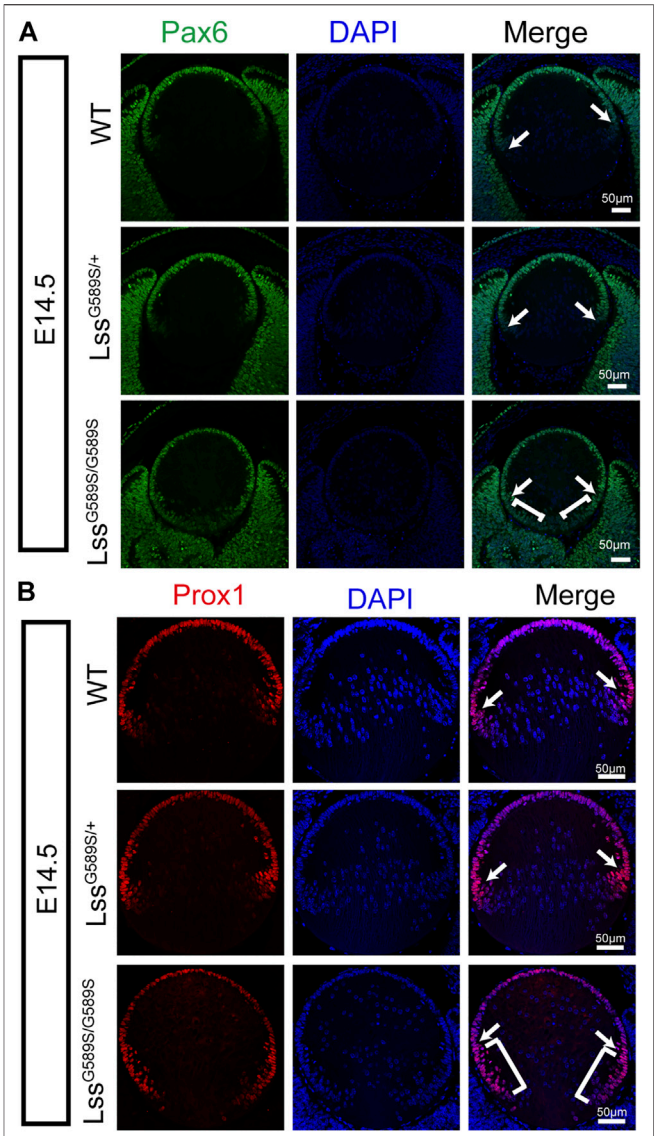

FIGURE 6 | Altered expression and localization of Pax6 and Prox1 in lens epithelial cells of Lss$^{G589S/G589S}$ mice at E14.5. **(A)** Expression and localization of Pax6 in lens epithelial cells of WT, Lss$^{G589S/+}$, and Lss$^{G589S/G589S}$ mice at E14.5. White arrows indicate that Pax6 was highly expressed in epithelial cells at the equator region of WT, Lss$^{G589S/+}$, and Lss$^{G589S/G589S}$ mice. White square brackets indicate that Pax6 was highly expressed at the transition zone and posterior terminals of lens in Lss$^{G589S/G589S}$ mice. Scale bar: 50 μm. **(B)** Expression and localization of Prox1 in lens epithelial cells of WT, Lss$^{G589S/+}$, and Lss$^{G589S/G589S}$ mice at E14.5. White arrows indicate that Prox1 was highly expressed in epithelial cells at the equator region of WT, Lss$^{G589S/+}$, and Lss$^{G589S/G589S}$ mice. White square brackets indicate that Prox1 was highly expressed at the transition zone and posterior terminals of lens in Lss$^{G589S/G589S}$ mice. Scale bar: 50 μm.

Altered expression and localization of Pax6 and Prox1 in lens fiber differentiation of Lss$^{G589S/G589S}$ mice

As abnormal lens development exhibited in Lss$^{G589S/G589S}$ mouse embryos, we then investigated the expression of two transcription

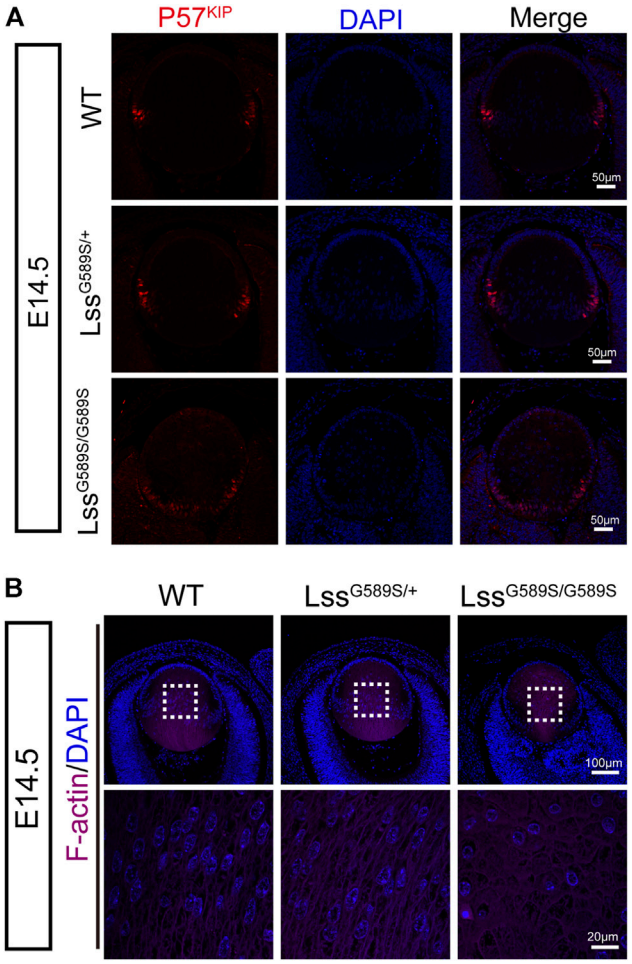

FIGURE 7 | Incomplete differentiation of lens fiber cells in $Lss^{G589S/G589S}$ mice. **(A)** The expression of $p57^{KIP2}$ in WT, $Lss^{G589S/+}$, and $Lss^{G589S/G589S}$ mice lens at E14.5. Scale bar: 50 μm. **(B)** The distribution of lens fiber nuclei and alignment of lens fiber cells in WT, $Lss^{G589S/+}$, and $Lss^{G589S/G589S}$ mice at E14.5 using F-actin staining. Scale bar: 100 μm. The enlargement is the magnification of the boxed inset shown in the upper panel. Scale bar: 20 μm.

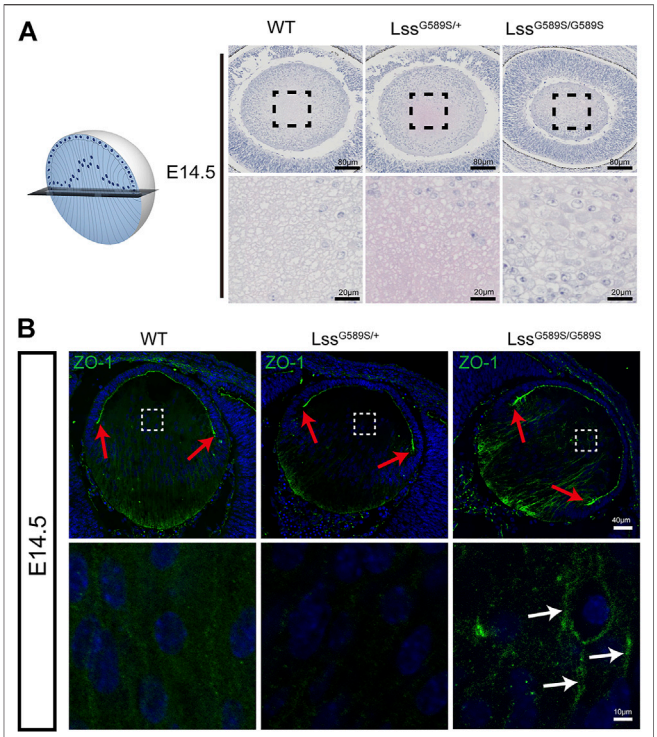

FIGURE 8 | Disrupted polarity of lens fiber cells in $Lss^{G589S/G589S}$ mice. **(A)** Alignment of lens fiber cells stained with hematoxylin and eosin and distribution of cell nuclei in sagittally sectioned lenses in the equator plane of WT, $Lss^{G589S/+}$, and $Lss^{G589S/G589S}$ mice at E14.5. Scale bar: 80 μm. The enlargement is the magnification of the boxed inset shown in the upper panel. Scale bar: 20 μm. **(B)** The expression of ZO-1 in lens of WT, $Lss^{G589S/+}$, and $Lss^{G589S/G589S}$ mice at E14.5. Scale bar: 40 μm. The enlargement is the magnification of the boxed inset shown in the upper panel. Red arrows indicate lens fulcrums. White arrow indicates that ZO-1 was strongly retained in the zones between lens fiber cells of $Lss^{G589S/G589S}$ mice. Scale bar: 10 μm.

factors (Pax6 and Prox1) which are critical for normal differentiation of transparent lens in $Lss^{G589S/G589S}$ embryos at E14.5. Pax6 plays a vital role in lens induction and fate determination, and Prox1 governs lens fiber cell differentiation and crystallin expression (Ashery-Padan et al., 2000; Cui et al., 2004; Audette et al., 2016; Collins et al., 2018). In our study, compared with WT and $Lss^{G589S/+}$ heterozygous mice at E14.5, the expression and localization of Pax6 and Prox1 were significantly altered in the lens of $Lss^{G589S/G589S}$ homozygous mice at E14.5 (**Figures 6A,B**). Most epithelial cells were still stained with Pax6 at the equator region (**Figure 6A**, white arrows) and posterior terminals of lens in $Lss^{G589S/G589S}$ homozygous mice (**Figure 6A**, white square brackets). Also, Prox1 protein was highly expressed in epithelial cells not only at the equator region (**Figure 6B**, white arrow) but also at the transition zone and posterior terminals of lens in $Lss^{G589S/G589S}$ homozygous mice (**Figure 6B**, white square brackets). These results revealed that an Lss G589S biallelic mutation led to significant change in the expression and localization of lens Pax6 and Prox1, which indicated that the process of lens fiber differentiation had been delayed in $Lss^{G589S/G589S}$ homozygous mice at E14.5.

Incomplete differentiation of lens fiber cells in $Lss^{G589S/G589S}$ mice

Cyclin-dependent kinase inhibitor $p57^{KIP2}$, one of the downstream targets of Prox1, is required for the cells at lens equator withdrawal from the cell cycle and elongated to form fiber cells (Wigle et al., 1999; Shaham et al., 2009; Wiley et al., 2010). In $Lss^{G589S/G589S}$ mice at E14.5, since Prox1 as a marker of fiber cell differentiation was strongly expressed in lens epithelial cells especially at the transition zone, we then assessed the expression and location of lens $p57^{KIP2}$. In WT and $Lss^{G589S/+}$ mice at E14.5, $p57^{KIP2}$ was mainly located in lens epithelial cells at the lens equator (**Figure 7A**). In $Lss^{G589S/G589S}$ mice at E14.5, more $p57^{KIP2}$ was detected in lens epithelial cells at the region close to the posterior pole (**Figure 7A**). Moreover, the cells with nuclei are almost located at the regions from the lens equator to

the anterior pole in WT and $Lss^{G589S/+}$ mice at E14.5, while the cells with nuclei were seen almost throughout all the regions of lens in $Lss^{G589S/G589S}$ mice at E14.5 (**Figure 7B**). In addition, F-actin staining revealed oval-shaped fiber cells with disordered arrangement located in the lens of $Lss^{G589S/G589S}$ mice at E14.5, rather than elongated and well-organized fiber cells located in the lens of WT and $Lss^{G589S/+}$ mice at E14.5 (**Figure 7B**). Thus, the Lss G589S homozygous mutation resulted in failure of epithelial cells at the lens posterior near the equator to exit the cell cycle and incomplete differentiation of lens fiber cells.

Disrupted polarity of lens fiber cells in $Lss^{G589S/G589S}$ mice

Our results above showed that F-actin was disorganized during fiber cell differentiation in $Lss^{G589S/G589S}$ homozygous mice at E14.5. To further study the polarity of lens fibers at E14.5, lenses were sagittally sectioned in the equator plane (**Figure 8A**). At the equator plane, irregular size and swollen shape of fiber cells with plenty of nuclei were in the lens of $Lss^{G589S/G589S}$ homozygous mice, while uniform size and round shape of fiber cells with a few nuclei were in the lens of WT and $Lss^{G589S/+}$ heterozygous mice (**Figure 8A**). ZO-1, a tight-junction protein, has been reported to localize in the apical membrane of lens epithelial cells (indicated as the EFI) during the lens development stage (Nielsen et al., 2003; Wiley et al., 2010; Arora et al., 2012). In WT and heterozygous lenses at E14.5, ZO-1 was mainly expressed at the apical ends of the lens epithelial layer and prominently expressed at the lens fulcrum close to the equator (**Figure 8B**, red arrows). In $Lss^{G589S/G589S}$ homozygous mice, ZO-1 was mainly expressed at the posterior fiber cell region and intensely expressed along the lens fulcrum (**Figure 8B**, red arrows); meanwhile, ZO-1 was strongly retained in the fiber zone between lens fiber cells (**Figure 8B**, white arrows). Taken together, our findings indicated that the lens fiber cells from homozygous mice lost their polarity in the apical–basal direction and failed to differentiate normally.

$Lss^{G589S/G589S}$ homozygous mutant resulted in a prominent disturbance of cholesterol biosynthesis pathways

To explore potential mechanisms in lens development defects by the Lss G589S homozygous mutation, we performed transcriptomic profiling of lens collected from WT, $Lss^{G589S/+}$, and $Lss^{G589S/G589S}$ mice at E14.5. Due to normal lens development in wild-type and heterozygote mice, a Venn diagram was performed to analyze differentially expressed genes (DEGs) only overlapped in two groups (homozygous vs. WT, homozygous vs. heterozygous) by comparing DEGs in three groups (homozygous vs. WT, homozygous vs. heterozygous, and heterozygous vs. WT). It was found that 1063 DEGs were involved in the lens fiber differentiation process by comparing $Lss^{G589S/G589S}$ homozygous mice with WT and $Lss^{G589S/+}$ heterozygous mice (**Figure 9A**). The top 10 pathways were enriched by IPA (IPA) including cholesterol biosynthesis pathways and related metabolic pathways (**Figure 9B**). Several cholesterol biosynthesis genes such as Hmgcs1, methylsterol monooxygenase 1 (Msmo1), squalene epoxidase (Sqle), Lss, Fdft1, cytochrome P450 family 51 (Cyp51), Scap, and Tm7sf2 were significantly downregulated in the cholesterol biosynthesis pathway. Also, LXR/RXR pathway-related genes such as Abca1, Abcg1, Scd1, and Srebf1 were remarkably upregulated in lens from $Lss^{G589S/G589S}$ mice (**Figure 9C**). Decreased expression of LSS in the lens of $Lss^{G589S/G589S}$ mice at E14.5 was validated by Western blot analysis (**Figure 9D**). Herein, the downregulated cholesterol biosynthesis pathway caused by an Lss G589S homozygous mutation might partially account for lens development defects in cataractogenesis.

DISCUSSION

LSS is a cataract causal gene, and its mutations (G588S, W581R, I342S/W629C) result in CC (Mori et al., 2006; Zhao et al., 2015; Chen and Liu, 2017). Lanosterol synthase is the rate-limiting enzyme in the cholesterol biosynthesis pathway (Mori et al., 2006; Zhao et al., 2015) and crucial for maintenance of lens transparency *via* preventing abnormal protein aggregation (Zhao et al., 2015; Shen et al., 2018; Hua et al., 2019). Thus, it is important to investigate more functions of LSS. SCRs harboring hypomorphic Lss mutations and lens-specific Lss knockout mice were found to have cataracts at adult age (Mori et al., 2006; Wada et al., 2020); however, the roles of LSS during lens development remain largely unknown.

In our study, a mouse model harboring a $Lss^{G589S/G589S}$ mutation (homologous to human $LSS^{G588S/G588S}$ mutation) was generated to recapitulate CC. Similar to the phenotypes of human lens, there is no cataract found in the lens of WT and $Lss^{G589S/+}$ heterozygous mice, while severe opacity was detected in the lens of $Lss^{G589S/G589S}$ homozygous mice at P0, shown as disrupted EFI and disordered organization of lens fibers, and plenty of lens fiber nuclei were still retained in OFZ. Further studies on cataract formation at embryonic stages showed that visible cataracts formed in the embryonic stage at E17.5, and lens fibers failed to differentiate maturely at E14.5. Our study demonstrated that an $Lss^{G589S/G589S}$ homozygous mutation resulted in disrupted lens structure and cataract at embryonic stages.

The main process of lens development includes induction, morphogenesis, differentiation, and growth (McAvoy et al., 1999; Collins et al., 2018). Many factors play an important role in lens epithelial proliferation and fiber differentiation (Cvekl and Zhang, 2017). Chromatin remodeling enzymes Brg1 and Snf2h regulate embryonic lens differentiation through the denucleation process (He et al., 2010; He et al., 2016). HSF4 regulated DLAD and promoted lens differentiation (Bu et al., 2002; Cui et al., 2013). CDK1 took part in nuclear removal during terminal lens fiber cell differentiation (Chaffee et al., 2014). Posttranslational modifications such as SUMOylation play fundamental roles in regulating lens differentiation (Nie et al., 2021). In our study, incomplete karyolysis (denucleation) was observed in the OFZ of lens in $Lss^{G589S/G589S}$ homozygous mice at P0. $Lss^{G589S/G589S}$ biallelic mutation might block lens primary fiber differentiation and subsequently lead to delayed differentiation

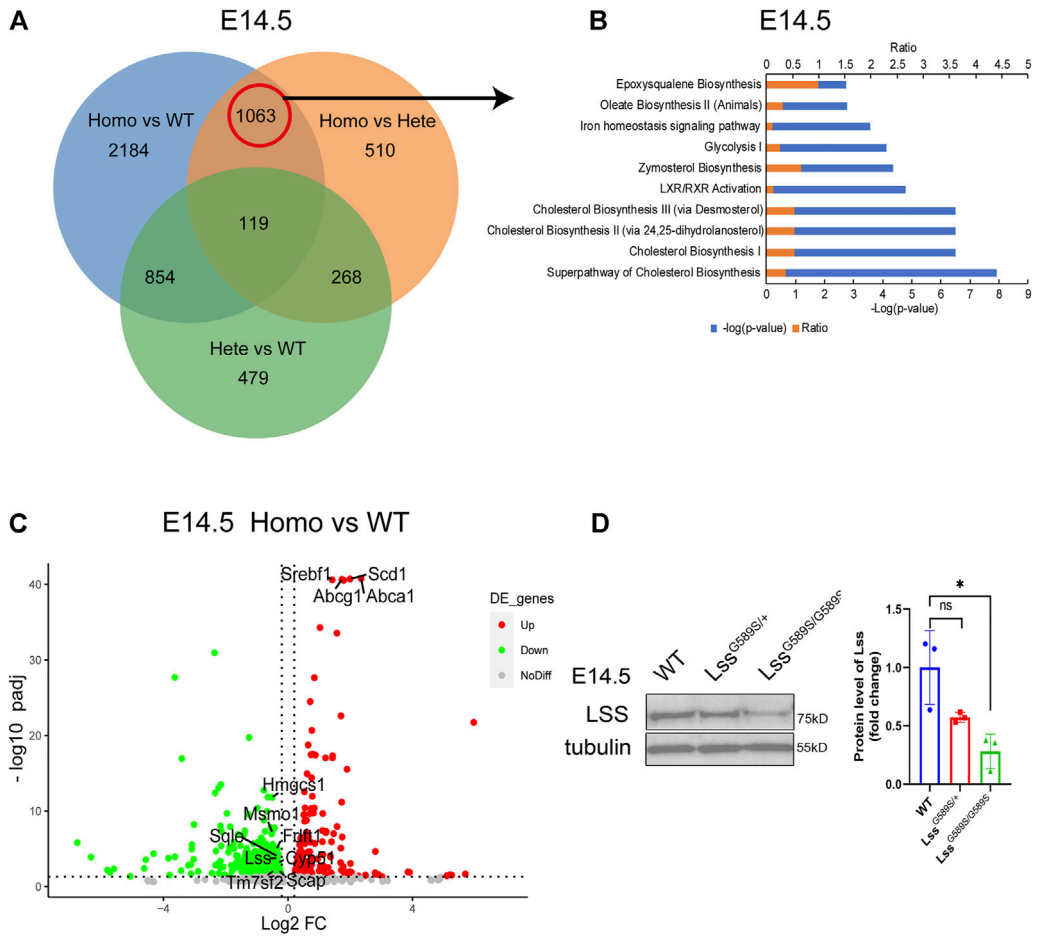

FIGURE 9 | RNA-seq profiling in the lens of WT, $Lss^{G589S/+}$, and $Lss^{G589S/G589S}$ mice at E14.5. **(A)** Venn diagram analysis of differentially expressed genes (DEG) only overlapped in two groups (homozygous vs. WT, homozygous vs. heterozygous). **(B)** IPA pathway analysis of 1063 DEGs from the above results in **(A)**. Top 10 enriched canonical pathways were identified by applying the –log(*p*-value) > 2 threshold. Cholesterol biosynthesis pathways were significantly altered. **(C)** Volcano plot analysis showing downregulated and upregulated DEGs in the terms "cholesterol biosynthesis pathway" and "LXR/RXR pathway" (*p* adjust <0.05). **(D)** Western blot analysis of Lss from the lens of WT, $Lss^{G589S/+}$, and $Lss^{G589S/G589S}$ mice at E14.5. Anti-tubulin immunoblot was used as the reference. Statistics of Western blot **(right)**, *n* = 3 embryos per group. The data represent mean ± SEM. Significance was determined by two-tailed, unpaired Student's t test. ns: no significance. **p* < 0.05 versus WT group.

of the secondary fiber. Thus, our results showed that LSS is required for lens fiber cell terminal differentiation and its denucleation.

Lens fiber cells maintain the same apical–basal polarity during the whole differentiation process of lens epithelial to fibers (Lo et al., 2000). The retained apical–basal polarity or apical cell junctions contribute to forming highly ordered and precisely aligned fiber cells, which is required for light transmission and lens transparency (Sugiyama et al., 2009). Lens-specific conditional knockout atypical protein kinase C (aPKC) was observed with disorganized fiber cell alignment (Sugiyama et al., 2009). Knockout of the neurofibromatosis type 2 (NF2) factor in lens caused lens cells to lose apical–basal polarity (Wiley et al., 2010). In our study, we found that $Lss^{G589S/G589S}$ biallelic mutation caused a loss of apical–basal polarity in lens fiber cells and led to disturbed lens fiber differentiation at E14.5. Our results revealed that LSS is also required for the polarity of lens fiber during elongation.

LSS converts (S)-2,3-epoxysqualene to lanosterol in the cholesterol biosynthesis pathway, and lanosterol reverses protein aggregation in cataracts (Zhao et al., 2015; Wada et al., 2020). Lens-specific Lss knockout mice generated using Pax6-cre showed microphthalmia and small cloudy lenses (Wada et al., 2020). Also, the lens of tamoxifen-induced QKI knockout mouse formed cataract at P19 and developed a more severe cataract at P30 and exhibited a significantly downregulated cholesterol biosynthesis pathway including the Lss gene (Shin et al., 2021). Moreover, it is reported that lanosterol selectively stimulates HMGCR degradation and intermediates from the mevalonate pathway of cholesterol biosynthesis (Chen et al., 2019). In our study, $Lss^{G589S/G589S}$ biallelic mutation led to a

significantly decreased level of LSS protein and disturbed cholesterol synthesis pathways. Our RNA-seq profile of $Lss^{G589S/G589S}$ lens showed that the expressions of Lss, Cyp51, Tm7sf2, Msmo1, Fdft1, and Sqle were significantly downregulated, which suggested that loss of function of LSS might disrupt the mevalonate pathway in regulating HMGCR degradation.

Lanosterol synthase is composed of two major domains at the N terminus (amino acid residues 84–325) and C terminus (amino acid residues 384–720) (Thoma et al., 2004; Romano et al., 2018). It is interesting that four LSS mutations causing CC are located toward the C terminus (Zhao et al., 2015; Chen and Liu, 2017), while five LSS mutation-causing autosomal-recessive hair loss disorders (hypotrichosis) are located toward the N terminus (Romano et al., 2018). Consequently, the mutations located at the C-terminus of LSS are more likely to cause cataract, whereas the mutations located at the N-terminus of LSS tends to cause hair loss. In addition, mutations of LSS can cause alopecia-mental retardation syndrome (APMR), which is a rare autosomal recessive neuro-dermal disorder (Muzammal et al., 2021). Thus, the studies on LSS mutations suggested that dysfunctions of LSS are far more complex and lead to autosomal-recessive diseases. It is also notable that two independent lines of $Lss^{G589S/G589S}$ homozygous mice exhibited neonatal lethality at P0, which is distinctly different from humans as the patients are still alive at their teenage years. This means that Lss is required for mouse survival and the mice might be more sensitive to loss of function of Lss.

In summary, our study demonstrated that a mouse model harboring an $Lss^{G589S/G589S}$ homozygous mutation can recapitulate human CC. Our findings confirmed loss of function of LSS disrupted differentiation and polarity of lens fibers in $Lss^{G589S/G589S}$ mice. Thus, our study provides direct evidence that LSS plays an essential role in lens development, which will contribute to a better understanding of LSS functions in cataractogenesis and develop therapeutic approaches to cataracts.

DATA AVAILABILITY STATEMENT

The datasets presented in this study can be found in online repositories. The names of the repository/repositories and accession number(s) can be found below: https://www.ncbi.nlm.nih.gov/geo/, GSE185143.

ETHICS STATEMENT

The animal study was reviewed and approved by IACUC (Institutional Animal Care and Use Committee), Zhongshan Ophthalmic Center, Sun Yat-sen University.

AUTHOR CONTRIBUTIONS

LZ and YL conceived the study. LZ, YL, and MZ designed the study. MZ, TM, BS, BZ, WX, KW, QL, CL, LW, JZ, and KZ performed the experiments, provided reagents and intellectual contributions, and analyzed the data. LZ and MZ wrote the paper.

FUNDING

This study is supported by the State Key Laboratory of Ophthalmology (Zhongshan Ophthalmic Center, Sun Yat-Sen University), National Natural Science Foundation of China (NSFC: 81670894; 81721003; 82000915), National Key Research and Development Program of China (2020YFA0112701), Pearl River Talents Program-Local Innovative and Research Teams (2017BT01S138), "100 talents plan" from Sun Yat-sen University (Guangzhou, Guangdong Province, China), Open Research Funds of the State Key Laboratory of Ophthalmology (2017KF05, Guangzhou, Guangdong Province, China), and Guangdong Provincial Key Laboratory of Ophthalmology and Visual Science (2017B030314025, Guangzhou, Guangdong Province, China).

ACKNOWLEDGMENTS

We thank the staff of the Laboratory Animal Center and Core Facilities at the State Key Laboratory of Ophthalmology, Zhongshan Ophthalmic Center, for technical support. We also thank Dr. David Wan-Cheng Li and Dr. J. Fielding Hejtmancik for valuable suggestions.

SUPPLEMENTARY MATERIAL

The Supplementary Material for this article can be found online at: https://www.frontiersin.org/articles/10.3389/fcell.2021.788422/full#supplementary-material

REFERENCES

Anand, D., Kakrana, A., Siddam, A. D., Huang, H., Saadi, I., and Lachke, S. A. (2018). RNA Sequencing-Based Transcriptomic Profiles of Embryonic Lens Development for Cataract Gene Discovery. *Hum. Genet.* 137 (11), 941–954. doi:10.1007/s00439-018-1958-0

Arora, A. I., Johar, K., Gajjar, D. U., Ganatra, D. A., Kayastha, F. B., Pal, A. K., et al. (2012). Cx43, ZO-1, Alpha-Catenin and Beta-Catenin in Cataractous Lens Epithelial Cells. *J. Biosci.* 37 (6), 979–987. doi:10.1007/s12038-012-9264-9

Ashery-Padan, R., Marquardt, T., Zhou, X. L., and Gruss, P. (2000). Pax6 Activity in the Lens Primordium Is Required for Lens Formation and for Correct Placement of a Single Retina in the Eye. *Genes Develop.* 14 (21), 2701–2711. doi:10.1101/gad.184000

Audette, D. S., Anand, D., So, T., Rubenstein, T. B., Lachke, S. A., Lovicu, F. J., et al. (2015). Prox1 and Fibroblast Growth Factor Receptors Form a Novel Regulatory Loop Controlling Lens Fiber Differentiation and Gene Expression. *Development* 143 (2), 318–328. doi:10.1242/dev.127860

Bu, L., Jin, Y., Shi, Y., Chu, R., Ban, A., Eiberg, H., et al. (2002). Mutant DNA-Binding Domain of HSF4 Is Associated with Autosomal Dominant Lamellar and Marner Cataract. *Nat. Genet.* 31 (3), 276–278. doi:10.1038/ng921

Chaffee, B. R., Shang, F., Chang, M.-L., Clement, T. M., Eddy, E. M., Wagner, B. D., et al. (2014). Nuclear Removal during Terminal Lens Fiber Cell Differentiation Requires CDK1 Activity: Appropriating Mitosis-Related Nuclear Disassembly. *Development* 141 (17), 3388–3398. doi:10.1242/dev.106005

Chen, X., and Liu, L. (2017). Congenital Cataract with LSS Gene Mutations: a New Case Report. *J. Pediatr. Endocrinol. Metab.* 30 (11), 1231–1235. doi:10.1515/jpem-2017-0101

Chen, L., Ma, M.-Y., Sun, M., Jiang, L.-Y., Zhao, X.-T., Fang, X.-X., et al. (2019). Endogenous Sterol Intermediates of the Mevalonate Pathway Regulate HMGCR Degradation and SREBP-2 Processing. *J. Lipid Res.* 60 (10), 1765–1775. doi:10.1194/jlr.RA119000201

Collins, T. N., Mao, Y., Li, H., Bouaziz, M., Hong, A., Feng, G.-S., et al. (2018). Crk Proteins Transduce FGF Signaling to Promote Lens Fiber Cell Elongation. *Elife* 7, e32586. doi:10.7554/eLife.32586

Cui, W., Tomarev, S. I., Chepelinsky, A. B., and Duncan, M. K. (2004). Mafs, Prox1, and Pax6 can regulate chicken beta B1-crystallin gene expression. *J. Biol. Chem.* 279, 11088–11095. doi:10.1074/jbc.M312414200

Cui, X., Wang, L., Zhang, J., Du, R., Liao, S., Li, D., et al. (2013). HSF4 Regulates DLAD Expression and Promotes Lens De-nucleation. *Biochim. Biophys. Acta (Bba) - Mol. Basis Dis.* 1832 (8), 1167–1172. doi:10.1016/j.bbadis.2013.03.007

Cvekl, A., and Zhang, X. (2017). Signaling and Gene Regulatory Networks in Mammalian Lens Development. *Trends Genet.* 33 (10), 677–702. doi:10.1016/j.tig.2017.08.001

He, S., Pirity, M. K., Wang, W.-L., Wolf, L., Chauhan, B. K., Cveklova, K., et al. (2010). Chromatin Remodeling Enzyme Brg1 Is Required for Mouse Lens Fiber Cell Terminal Differentiation and its Denucleation. *Epigenetics Chromatin* 3 (1), 21. doi:10.1186/1756-8935-3-21

He, S., Limi, S., McGreal, R. S., Xie, Q., Brennan, L. A., Kantorow, W. L., et al. (2016). Chromatin Remodeling Enzyme Snf2h Regulates Embryonic Lens Differentiation and Denucleation. *Development* 143 (11), 1937–1947. doi:10.1242/dev.135285

Hejtmancik, J. F. (2008). Congenital Cataracts and Their Molecular Genetics. *Semin. Cel Develop. Biol.* 19 (2), 134–149. doi:10.1016/j.semcdb.2007.10.003

Hua, H., Yang, T., Huang, L., Chen, R., Li, M., Zou, Z., et al. (2019). Protective Effects of Lanosterol Synthase Up-Regulation in UV-B-Induced Oxidative Stress. *Front. Pharmacol.* 10, 947. doi:10.3389/fphar.2019.00947

Huff, M., and Telford, D. (2005). Lord of the Rings - the Mechanism for Oxidosqualene:lanosterol Cyclase Becomes crystal clear. *Trends Pharmacol. Sci.* 26 (7), 335–340. doi:10.1016/j.tips.2005.05.004

Khan, S. Y., Hackett, S. F., Lee, M.-C. W., Pourmand, N., Talbot, C. C., and Riazuddin, S. A. (2015). Transcriptome Profiling of Developing Murine Lens through RNA Sequencing. *Invest. Ophthalmol. Vis. Sci.* 56 (8), 4919–4926. doi:10.1167/iovs.14-16253

Lian, Q., Zhao, M., Li, T., Wu, K., Zhu, D., Shang, B., et al. (2019). *In Vivo* detecting Mouse Persistent Hyperplastic Primary Vitreous by Spectralis Optical Coherence Tomography. *Exp. Eye Res.* 181, 271–276. doi:10.1016/j.exer.2019.02.017

Liu, Y.-C., Wilkins, M., Kim, T., Malyugin, B., and Mehta, J. S. (2017). Cataracts. *Lancet* 390 (10094), 600–612. doi:10.1016/S0140-6736(17)30544-5

Lo, W.-K., Shaw, A. P., Paulsen, D. F., and Mills, A. (2000). Spatiotemporal Distribution of Zonulae Adherens and Associated Actin Bundles in Both Epithelium and Fiber Cells during Chicken Lens Development. *Exp. Eye Res.* 71 (1), 45–55. doi:10.1006/exer.2000.0848

McAvoy, J. W., Chamberlain, C. G., de Longh, R. U., Hales, A. M., and Lovicu, F. J. (1999). Lens Development. *Eye* 13 (Pt 3b), 425–437. doi:10.1038/eye.1999.117

Messina-Baas, O., and Cuevas-Covarrubias, S. A. (2017). Inherited Congenital Cataract: A Guide to Suspect the Genetic Etiology in the Cataract Genesis. *Mol. Syndromol.* 8 (2), 58–78. doi:10.1159/000455752

Mori, M., Li, G. X., Abe, I., Nakayama, J., Guo, Z. J., Sawashita, J., et al. (2006). Lanosterol Synthase Mutations Cause Cholesterol Deficiency-Associated Cataracts in the Shumiya Cataract Rat. *J. Clin. Invest.* 116 (2), 395–404. doi:10.1172/JCI20797

Morishita, H., Eguchi, S., Kimura, H., Sasaki, J., Sakamaki, Y., Robinson, M. L., et al. (2013). Deletion of Autophagy-Related 5 (Atg5) and Pik3c3 Genes in the Lens Causes Cataract Independent of Programmed Organelle Degradation. *J. Biol. Chem.* 288 (16), 11436–11447. doi:10.1074/jbc.M112.437103

Muzammal, M., Ahmad, S., Ali, M. Z., and Khan, M. A. (2021). Alopecia-mental Retardation Syndrome: Molecular Genetics of a Rare Neuro-dermal Disorder. *Ann. Hum. Genet.* 85 (5), 147–154. doi:10.1111/ahg.12425

Nie, Q., Chen, H. M., Zou, M., Wang, L., Hou, M., Xiang, J. W., et al. (2021). The E3 Ligase PIAS1 Regulates P53 Sumoylation to Control Stress-Induced Apoptosis of Lens Epithelial Cells through the Proapoptotic Regulator Bax. *Front. Cel Develop. Biol.* 9, 660494. doi:10.3389/fcell.2021.660494

Nielsen, P. A., Baruch, A., Shestopalov, V. I., Giepmans, B. N. G., Dunia, I., Benedetti, E. L., et al. (2003). Lens Connexins α3Cx46 and α8Cx50 Interact with Zonula Occludens Protein-1 (ZO-1). *MBoC* 14 (6), 2470–2481. doi:10.1091/mbc.E02-10-0637

Romano, M.-T., Tafazzoli, A., Mattern, M., Sivalingam, S., Wolf, S., Rupp, A., et al. (2018). Bi-allelic Mutations in LSS, Encoding Lanosterol Synthase, Cause Autosomal-Recessive Hypotrichosis Simplex. *Am. J. Hum. Genet.* 103 (5), 777–785. doi:10.1016/j.ajhg.2018.09.011

Shaham, O., Smith, A. N., Robinson, M. L., Taketo, M. M., Lang, R. A., and Ashery-Padan, R. (2009). Pax6 Is Essential for Lens Fiber Cell Differentiation. *Development* 136 (15), 2567–2578. doi:10.1242/dev.032888

Shen, X., Zhu, M., Kang, L., Tu, Y., Li, L., Zhang, R., et al. (2018). Lanosterol Synthase Pathway Alleviates Lens Opacity in Age-Related Cortical Cataract. *J. Ophthalmol.* 2018, 1–9. doi:10.1155/2018/4125893

Shiels, A., and Hejtmancik, J. F. (2013). Genetics of Human Cataract. *Clin. Genet.* 84 (2), 120–127. doi:10.1111/cge.12182

Shin, S., Zhou, H., He, C., Wei, Y., Wang, Y., Shingu, T., et al. (2021). Qki Activates Srebp2-Mediated Cholesterol Biosynthesis for Maintenance of Eye Lens Transparency. *Nat. Commun.* 12 (1), 3005. doi:10.1038/s41467-021-22782-0

Sugiyama, Y., Akimoto, K., Robinson, M. L., Ohno, S., and Quinlan, R. A. (2009). A Cell Polarity Protein aPKCλ Is Required for Eye Lens Formation and Growth. *Develop. Biol.* 336 (2), 246–256. doi:10.1016/j.ydbio.2009.10.010

Sun, M., Chen, C., Hou, S., Li, X., Wang, H., Zhou, J., et al. (2019). A Novel Mutation of PANK4 Causes Autosomal Dominant Congenital Posterior Cataract. *Hum. Mutat.* 40 (4), 380–391. doi:10.1002/humu.23696

Thoma, R., Schulz-Gasch, T., D'Arcy, B., Benz, J., Aebi, J., Dehmlow, H., et al. (2004). Insight into Steroid Scaffold Formation from the Structure of Human Oxidosqualene Cyclase. *Nature* 432 (7013), 118–122. doi:10.1038/nature02993

Wada, Y., Kikuchi, A., Kaga, A., Shimizu, N., Ito, J., Onuma, R., et al. (2020). Metabolic and Pathologic Profiles of Human LSS Deficiency Recapitulated in Mice. *Plos Genet.* 16 (2), e1008628. doi:10.1371/journal.pgen.1008628

Wigle, J. T., Chowdhury, K., Gruss, P., and Oliver, G. (1999). Prox1 Function Is Crucial for Mouse Lens-Fibre Elongation. *Nat. Genet.* 21 (3), 318–322. doi:10.1038/6844

Wiley, L. A., Dattilo, L. K., Kang, K. B., Giovannini, M., and Beebe, D. C. (2010). The Tumor Suppressor Merlin Is Required for Cell Cycle Exit, Terminal Differentiation, and Cell Polarity in the Developing Murine Lens. *Invest. Ophthalmol. Vis. Sci.* 51 (7), 3611–3618. doi:10.1167/iovs.09-4371

Wu, D., Jian, C., Peng, Q., Hou, T., Wu, K., Shang, B., et al. (2020). Prohibitin 2 Deficiency Impairs Cardiac Fatty Acid Oxidation and Causes Heart Failure. *Cell Death Dis.* 11 (3), 181. doi:10.1038/s41419-020-2374-7

Zhao, L., Chen, X.-J., Zhu, J., Xi, Y.-B., Yang, X., Hu, L.-D., et al. (2015). Lanosterol Reverses Protein Aggregation in Cataracts. *Nature* 523 (7562), 607–611. doi:10.1038/nature14650

Conflict of Interest: The authors declare that the research was conducted in the absence of any commercial or financial relationships that could be construed as a potential conflict of interest.

Publisher's Note: All claims expressed in this article are solely those of the authors and do not necessarily represent those of their affiliated organizations, or those of the publisher, the editors, and the reviewers. Any product that may be evaluated in this article, or claim that may be made by its manufacturer, is not guaranteed or endorsed by the publisher.

Copyright © 2021 Zhao, Mei, Shang, Zou, Lian, Xu, Wu, Lai, Liu, Wei, Zhu, Zhang, Liu and Zhao. This is an open-access article distributed under the terms of the Creative Commons Attribution License (CC BY). The use, distribution or reproduction in other forums is permitted, provided the original author(s) and the copyright owner(s) are credited and that the original publication in this journal is cited, in accordance with accepted academic practice. No use, distribution or reproduction is permitted which does not comply with these terms.

frontiers in Cell and Developmental Biology

ORIGINAL RESEARCH
published: 17 December 2021
doi: 10.3389/fcell.2021.802457

A Single-Cell Transcriptome Atlas of the Human Retinal Pigment Epithelium

Zongren Xu[1,2,3,4†], Xingyun Liao[1,2,3,4†], Na Li[5], Hongxiu Zhou[1,2,3], Hong Li[1,2,3], Qi Zhang[1,2,3], Ke Hu[1,2,3], Peizeng Yang[1,2,3,4] and Shengping Hou[1,2,3,4*]*

[1]The First Affiliated Hospital of Chongqing Medical University, Chongqing, China, [2]Chongqing Key Laboratory of Ophthalmology, Chongqing, China, [3]Chongqing Eye Institute, Chongqing, China, [4]Chongqing Branch of National Clinical Research Center for Ocular Diseases, Chongqing, China, [5]College of Basic Medicine, Chongqing Medical University, Chongqing, China

Human retinal pigment epithelium cells are arranged in a monolayer that plays an important supporting role in the retina. Although the heterogeneity of specific retinal cells has been well studied, the diversity of hRPE cells has not been reported. Here, we performed a single-cell RNA sequencing on 9,302 hRPE cells from three donors and profiled a transcriptome atlas. Our results identified two subpopulations that exhibit substantial differences in gene expression patterns and functions. One of the clusters specifically expressed *ID3*, a macular retinal pigment epithelium marker. The other cluster highly expressed *CRYAB*, a peripheral RPE marker. Our results also showed that the genes associated with oxidative stress and endoplasmic reticulum stress were more enriched in the macular RPE. The genes related to light perception, oxidative stress and lipid metabolism were more enriched in the peripheral RPE. Additionally, we provided a map of disease-related genes in the hRPE and highlighted the importance of the macular RPE and peripheral RPE clusters P4 and P6 as potential therapeutic targets for retinal diseases. Our study provides a transcriptional landscape for the human retinal pigment epithelium that is critical to understanding retinal biology and disease.

Keywords: retina, HRPE, macula, periphery, single-cell RNA sequencing

OPEN ACCESS

Edited by:
Qingjiong Zhang,
Sun Yat-sen University, China

Reviewed by:
Jiang Qian,
Johns Hopkins Medicine, United States
Xianjun Zhu,
Sichuan provincial people's hospital, China

****Correspondence:***
Peizeng Yang
peizengycmu@126.com
Shengping Hou
sphou828@163.com

[†]These authors have contributed equally to this work

Specialty section:
This article was submitted to Molecular and Cellular Pathology, a section of the journal Frontiers in Cell and Developmental Biology

Received: *26 October 2021*
Accepted: *23 November 2021*
Published: *17 December 2021*

Citation:
Xu Z, Liao X, Li N, Zhou H, Li H, Zhang Q, Hu K, Yang P and Hou S (2021) A Single-Cell Transcriptome Atlas of the Human Retinal Pigment Epithelium. Front. Cell Dev. Biol. 9:802457. doi: 10.3389/fcell.2021.802457

INTRODUCTION

Generally, the retina is a complex structure and contains 10 layers of tissue that are responsible for detecting and converting light into neurochemical information that is ultimately transmitted to the brain, resulting in vision. Near the posterior pole of the human and primate retina is a small shallow funnel-shaped depression 2.5–3 mm in diameter known as the yellow spot or macula. The central depression of the macula is called the fovea, where the retina is the thinnest and has only two layers of cells: the retinal pigment epithelium (RPE) and cone cells. Cone cells and bipolar cells are arranged one-to-one in the fovea, so the fovea, which is the most sensitive and accurate region in the retina, provides a sharp and clear image of central vision. Many ocular diseases that cause blindness, such as age-related macular degeneration (AMD), mainly affect this area, indicating that it is of great significance to study the cellular function of the retina and, particularly, the macula.

The visual formation process requires many types of neurons and supporting cell types. Among these neurons and cells, photoreceptor (PR) cells (rods and cones) convert light into an electrical signal that is then transferred to interneurons, including horizontal cells (HCs), bipolar cells (BCs), and amacrine cells (ACs). Interneurons deliver information to retinal ganglion cells (RGCs) and then input it into the brain. In addition, RPE cells, astrocytes, Müller glia and microglial cells mainly support the metabolism of the retina and play an important role in homeostasis of the retina.

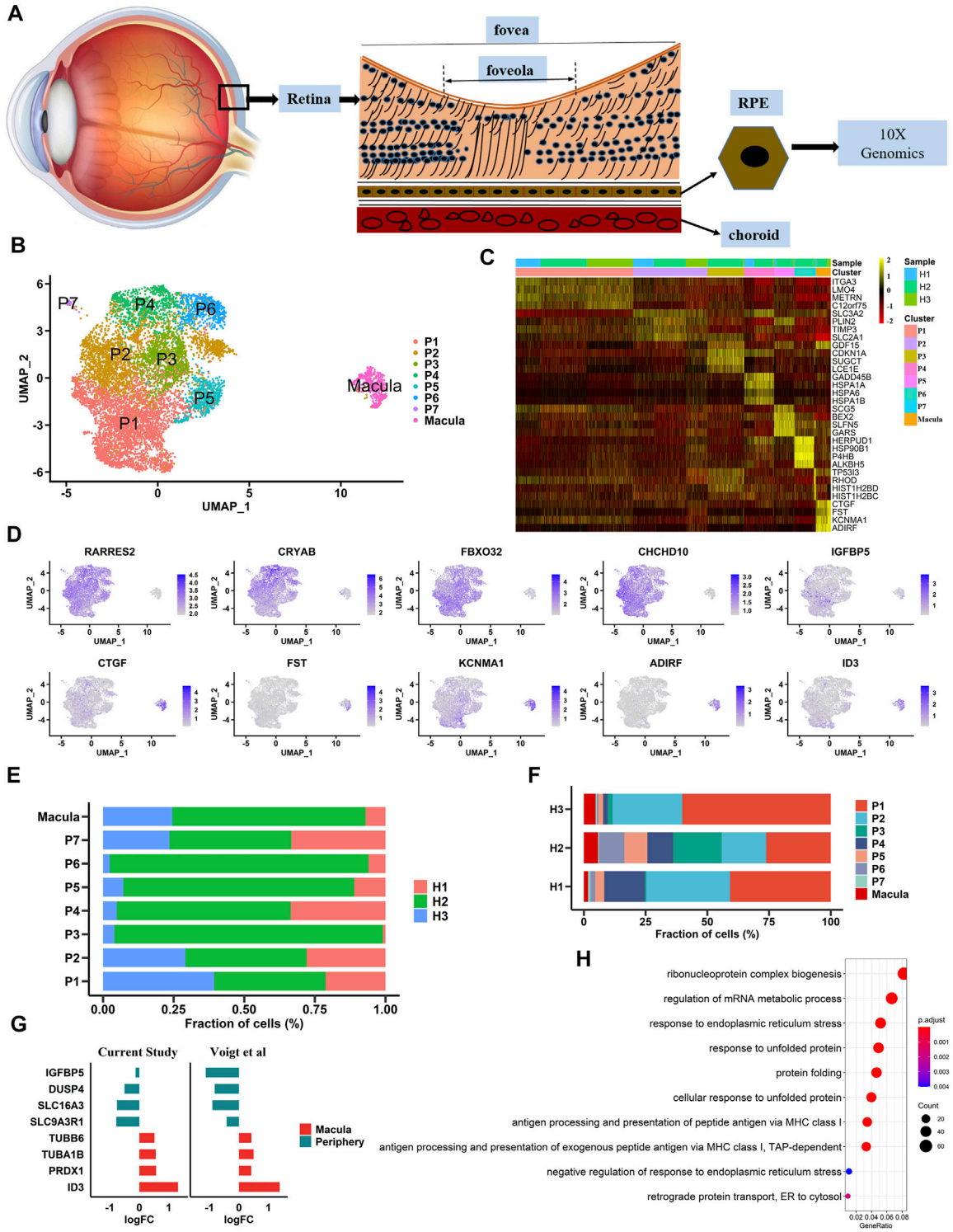

FIGURE 1 | Single-cell RNA-seq transcriptome profiling of hRPE **(A).** A schematic diagram of the extracted sample cells is shown. Single cells were extracted from human RPE tissue to complete next-generation sequencing **(B)**. Identification of cell populations. UMAP projection of 9,302 single cells from three samples showed a total of eight cell type populations. Each point is a cell, and different cell types are differentiated by different colors **(C)**. Heatmaps of cell types. Columns represent groups of cells, and rows represent specific, highly expressed differentially expressed genes for each cell type. The heatmap scale represents the normalized expression value **(D)**. Differential gene expression in large and small clusters is shown in the UMAP plot **(E)**. The proportion of each sample in each cluster **(F)**. The proportion of each cluster in each sample **(G)**. The expression patterns of differential genes in our data were consistent with those in previous studies **(H)**. Gene Ontology (GO) terms associated with genes with upregulated expression in the macula cluster.

Some retinal cell types have been studied for their gene expression patterns and gene functions by bulk sequencing, even at the single-cell level. Recent research found that RGCs are divided into 40 cell types by single-cell RNA sequencing (scRNA-seq) (Rheaume et al., 2018). Additionally, rods and cones have exhibited heterogeneous subpopulations (Yan et al., 2020). Many studies have reported retinal cell subtypes, including RGCs, rods, cones and other nonneuronal cells, in humans and other primates as determined by scRNA-seq (Shekhar et al., 2016; Rheaume et al., 2018; Lukowski et al., 2019; Menon et al., 2019); however, the heterogeneity and detailed molecular map of human RPE cells has not been well studied.

The RPE is a monolayer tissue layer that is fundamentally important for retinal development and function. The RPE also plays critical roles in supporting the retina, including transepithelial transport, phagocytosis, blood-retina barrier function, metabolism, oxidative stress (OS), growth factor secretion, visual cycle processes (Strauss, 2005) and retinal integrity and viability maintenance (Boulton and Dayhaw-Barker, 2001; Bharti et al., 2011). An increasing number of studies have shown that RPE dysfunction may lead to multiple retinal degenerative diseases, such as AMD, Stargardt's macular dystrophy (SMD), best vitelliform macular dystrophy (BVMD) and proliferative vitreoretinopathy (PVR). Although a number of studies have focused on deriving RPE cells from various stem cell sources or cell lines and have even focused on the functions of RPE cells, precise cell-type division has not been examined in human RPE (hRPE) cells. Therefore, it is necessary to explore the heterogeneity and molecular map of hRPE cells to elucidate the mechanism of hRPE-related retinal diseases and discover more treatments for these diseases. In view of the important roles of hRPE cells, we therefore performed scRNA-seq from three human donor eyes to study the heterogeneity and gene expression in RPE tissues.

RESULTS

The Preparation of hRPE Samples and Generation of a Single-Cell Transcriptome Atlas

In this study, three postmortem human adult eyes were obtained after corneal transplantation. As the transcriptome profile of human retinal cells, including HCs, BCs, and microglia, has been reported, we focused solely on building a single-cell transcriptome atlas of hRPE cells with a 10× Genomics Chromium platform (**Figure 1A**). A total of 10,074 cells were obtained by single-cell sequencing with an average of 200,801 reads and 5,522 median genes per cell. After rigorous quality control and filtering using the Seurat package (version 3.1.5) (Stuart et al., 2019), 9,302 cells were included in the follow-up unsupervised graph clustering approach. The hRPE cell atlases yielding high-quality cell profiles were divided into two populations: one population had 8,863 cells, and the other population had 439 cells (**Figures 1B, C** and **Supplementary Figure S1A-B**). Both populations expressed RPE marker genes such as *PAX6* and *BEST1* (**Supplementary Figure S1C**). Previous transcriptome studies showed that *ID3* and *IGFBP5* were highly expressed in the macular and peripheral regions of hRPE cells, respectively (Voigt et al., 2019). Interestingly, our study also found that specific expression of *ID3* was limited to a small population (439 cells) and that *IGFBP5* was highly enriched in the other population (8,863 cells). Thus, we hypothesized that one cluster was the macular RPE and the other was the peripheral cluster. In addition to the two specifically expressed genes, we found that *CTGF*, *FST*, *KCNMA1,* and *ADIRF* were highly expressed in the macular RPE, and *RARRES2*, *CRYAB*, *FBX O 32*, and *CHCHD10* were specifically expressed in the peripheral RPE (**Figure 1D** and **Supplementary Table S1**). In addition, we found two populations with similar ratios in the three human samples (**Supplementary Figure S1E–F**). We also found that the proportions of these subpopulations were similar among samples (**Figures 1E, F**). At the same time, we compared the work reported by Voigt and others to reproduce the expression of these differentially expressed genes (**Figure 1G**). Next, we performed Gene Ontology (GO) pathway enrichment analysis on highly expressed genes in peripheral and macular RPE cells (**Figure 1H**, **Supplementary Figure S1D** and **Supplementary Table S2**). The results showed that there may be significant differences between peripheral RPE cells and macular RPE cells in proton transmembrane transport, endoplasmic reticulum (ER) stress and ATP metabolic processes.

Profiling of Human Macular RPE Cell Subpopulations

To gain insight into the heterogeneity of macular RPE cells, we analyzed the macular RPE cluster and found that it could be divided into two subpopulations (M1 and M2 clusters) according to the gene expression profile (**Figures 2A, B**). After differential expression analysis, we obtained a total of 585 differentially expressed genes (**Supplementary Table S3**). These genes were clearly identified in two subpopulations and showed similar expression patterns in all three samples (**Figures 2B–D**). In addition, the statistical proportions of the two subgroups were very similar (**Figures 2E, F**). We further performed GO analysis to explore the physiological functions of the two clusters. The results indicated that the M1 cluster was enriched in cell adhesion and cell junctions, and the M2 cluster was predominantly enriched in OS and ER stress in response to illness or trauma (**Figure 2G**, **Supplementary Figure S2** and **Supplementary Table S4**). The results demonstrated that the macular RPE could also be divided into smaller subpopulations that perform different functions.

The Subpopulations and Expression Profile of Human Peripheral RPE Cells

To study the heterogeneity of peripheral RPE cells, we mapped their atlas and showed that peripheral RPE cells could be classified into eight populations with distinct gene expression (**Figures 3A, B**). We calculated and attained specific differential genes for each subpopulation and then found similar expression patterns in all three samples (**Figures 3B–D** and **Supplementary Table S5**). In addition, the statistical graph also showed the

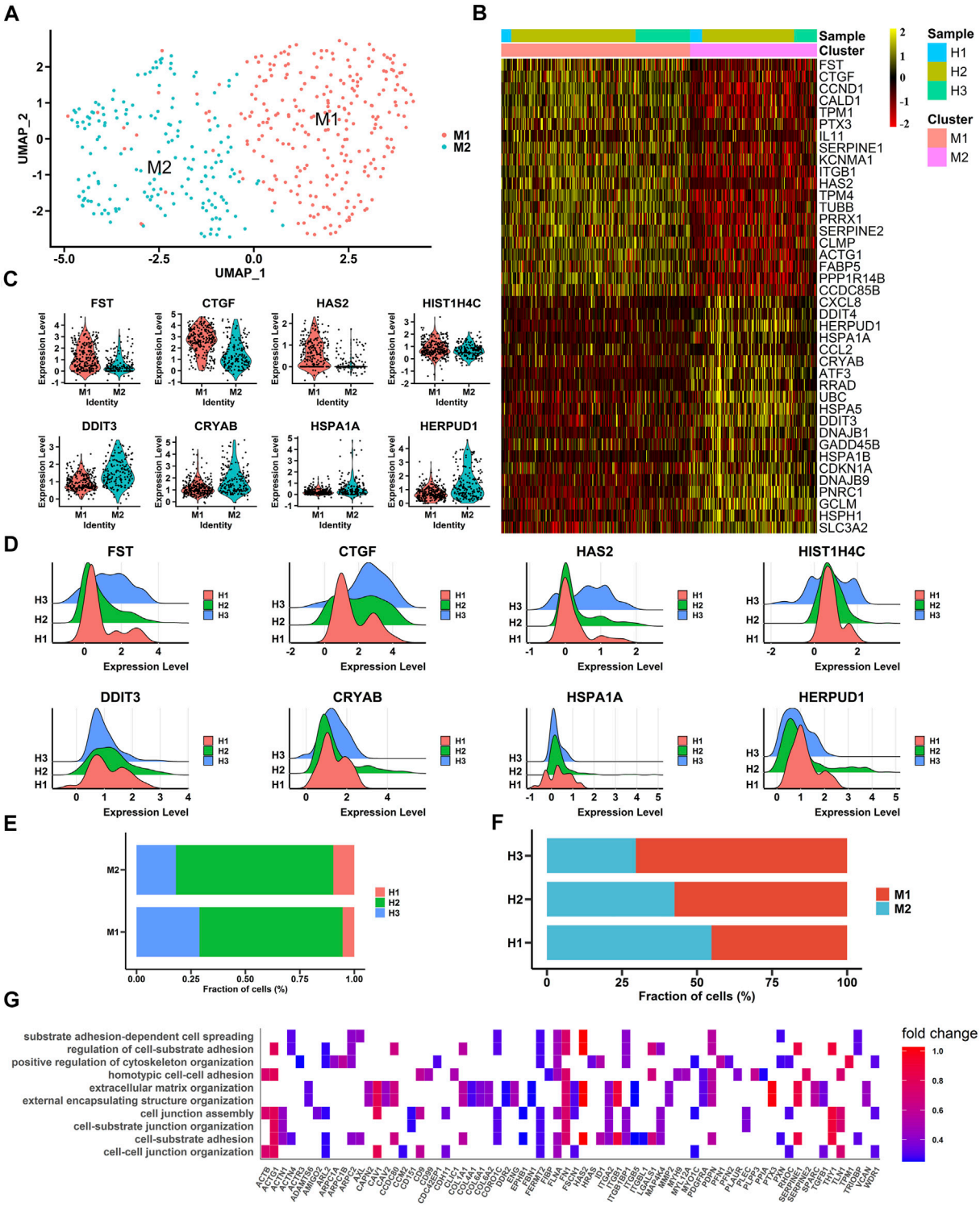

FIGURE 2 | Single-cell RNA-seq transcriptome profiling of macular RPE **(A)**. UMAP plot shows the cell classification of macular RPE cell clusters in three samples **(B).** Heatmap of two macular RPE subpopulations. Columns are divided into two types of cells, rows represent gene names and can be used to identify two subpopulations. The heatmap scale represents the normalized expression value **(C).** Violin plots show the expression of differentially expressed genes, M1 **(top)** and M2 **(bottom) (D).** Ridge plots show the expression patterns of differentially expressed genes in three samples. The *X*-axis shows the level of gene expression. M1 **(top)** and M2 **(bottom) (E).** The proportion of each sample in each cluster (M1, M2) **(F).** The proportion of each cluster (M1, M2) in each sample **(G).** Gene Ontology (GO) terms associated with genes with upregulated expression in the M1 subpopulation.

number of three samples in the subpopulations (**Figures 3E, F**). To further determine the functional differences among the peripheral subpopulations, we profiled the GO analysis results; the findings showed that these subpopulations had functional differences (**Figure 3G** and **Supplementary Table S6**). The P1 cluster, the largest peripheral subpopulation, was found to be mainly responsible for extracellular matrix organization, indicating that this cluster played an important role in maintaining the structure and stability of RPE tissue. Intriguingly, the P2 cluster could be divided into P2-1 and P2-2, and these subclusters had obviously different functions. The P2-1 cluster was mainly related to retinol metabolic processes and visual perception. However, the P2-2 cluster was involved in lipid transport. The P3 cluster was associated with OS. In addition, the P5 cluster was associated with nutrient transport. Although the two clusters P4 and P6 had similar functions, which were both related to ER stress, there were differences between them. We observed that the P4 cluster was more strongly associated with growth factors and ions; however, the P6 cluster was related to nutrient transport. The P7 cluster may be associated with cell cycle. In summary, we first profiled the transcriptomes of peripheral RPE cells in the human retina, and the presented data showed the heterogeneity of these peripheral RPE cells.

Our scRNA-seq results showed a low specificity of *IGFBP5* in the data (**Figure 1D**). Therefore, real-time quantitative polymerase chain reaction (RT-PCR) analysis of some differentially expressed genes was conducted, and the results showed that *CRYAB* expression was significantly higher in peripheral RPE than that of other differentially expressed genes (**Figure 3H**). Therefore, we determined that *CRYAB* was more specific than *IGFBP5* and could serve as a new marker gene of peripheral RPE. Then, we also verified the peripheral RPE marker gene (*CRYAB*) and macular RPE marker gene (*ID3*) by RT-PCR analysis (**Figure 3I**).

Different Gene Expression Patterns Between Macular and Peripheral RPE

Transcription factors are necessary for RPE development. We therefore used single-cell regulatory network inference and clustering (SCENIC) (Aibar et al., 2017) to analyze the activity of the gene regulatory networks (GRNs) in each cell. Based on a previous study, transcription factors that were active in more than 50% of cells in a particular cell class were retained (Hu et al., 2019). High activities of transcription factors were detected from the data using the AUCell algorithm (**Figure 4A, B**). Our results showed that *NFIB* was active and highly expressed in peripheral hRPE cells and that its target genes were involved in basement membrane organization and sodium ion transmembrane transport (**Figure 4C**). *IRX3, FOXP1, KLF2, TWIST1* and *PBX1* were highly expressed in macular hRPE cells and were considered active transcription factors. Target genes of *IRX3* were related to cell growth and cell-substrate adhesion. Target genes of *KLF2* were involved in extracellular structure organization and matrix organization. Target genes of *FOXP1* were enriched in regions involved in visual system development, proteoglycan metabolic processes and camera-type eye development. Therefore, these results indicate that most of the transcription factors were active in the macular cluster, suggesting that the macular cluster may play an important role in the differentiation of RPE cells during retinal development.

To further investigate the importance of macular clusters, we analyzed the interaction between peripheral and macular populations and then examined receptor-ligand pairs between the subpopulations. We found that 17 of the top 20 receptor-ligand pairs were enriched in the macular RPE, suggesting that the macular RPE cluster was closely involved in visual system development (**Figures 4D, E**). For example, *EGFR* receptors account for a large proportion of the macular RPE and mainly bind to *VEGFA* and *EFEMP1* (Fernandez-Godino et al., 2015; Mackay et al., 2015). Moreover, *NRP1* is another key receptor of the macular PRE whose signaling pathways are primarily related to angiogenesis and neural development (Raimondi et al., 2016). In summary, our data revealed the expression patterns of transcription factors in the human RPE, as well as the interactions between RPE subpopulations, both of which suggest the importance of the macular RPE in visual development.

The Development of the hRPE and Its Dynamic Transcriptome Features

We performed pseudotemporal analysis to elucidate the transcriptome dynamics of peripheral and macular RPE clusters using the R package Monocle2 (Trapnell et al., 2014). The discriminative dimensionality reduction tree (DDRTree) algorithm was used to determine the pseudodevelopmental time and then to map the developmental trajectory (**Figures 5A–C** and **Figure 5E**). It is well known that the anatomical development of the macula is complete at a late stage after being born (Alabduljalil et al., 2019). Therefore, we wanted to investigate the dynamics between the subpopulations of macular RPE and peripheral RPE. In macular RPE, M1 cluster cells were in the early stage of development, and M2 cluster cells were in the late stage of development (**Figure 5A** and **Figure 5C**). In peripheral RPE, we also found that these subpopulations had a specific developmental sequence (**Figure 5B** and **Figure 5E**).

Further studies also observed that the specific transcription factors of the macular and peripheral RPE, including *IRX3*, *TWIST1*, *FOXP1*, *KLF2*, *PBX1* and *NFIB,* were changed along the pseudotime axis (**Figures 5D–F**). For example, the expression of *IRX3*, *TWIST1*, *FOXP1*, *KLF2* and *PBX1* was decreased gradually in macular RPE (**Figure 5D**). The expression of *NFIB* was also decreased gradually in peripheral RPE (**Figure 5F**). Additionally, we analyzed the changes in receptors that are key for the function of the RPE (**Figures 5D–F**). The results showed that the expression of EGFR and NRP1 receptors decreased during development in macular RPE (**Figure 5D**). However, the expression of the *VEGFA* ligand increased gradually in peripheral RPE (**Figure 5F**).

Profiling of Specific Expression Patterns of Human Retinal Disease-Associated Genes

We used the RetNet (https://sph.uth.edu/retnet/) database to identify genes associated with retinal diseases and to

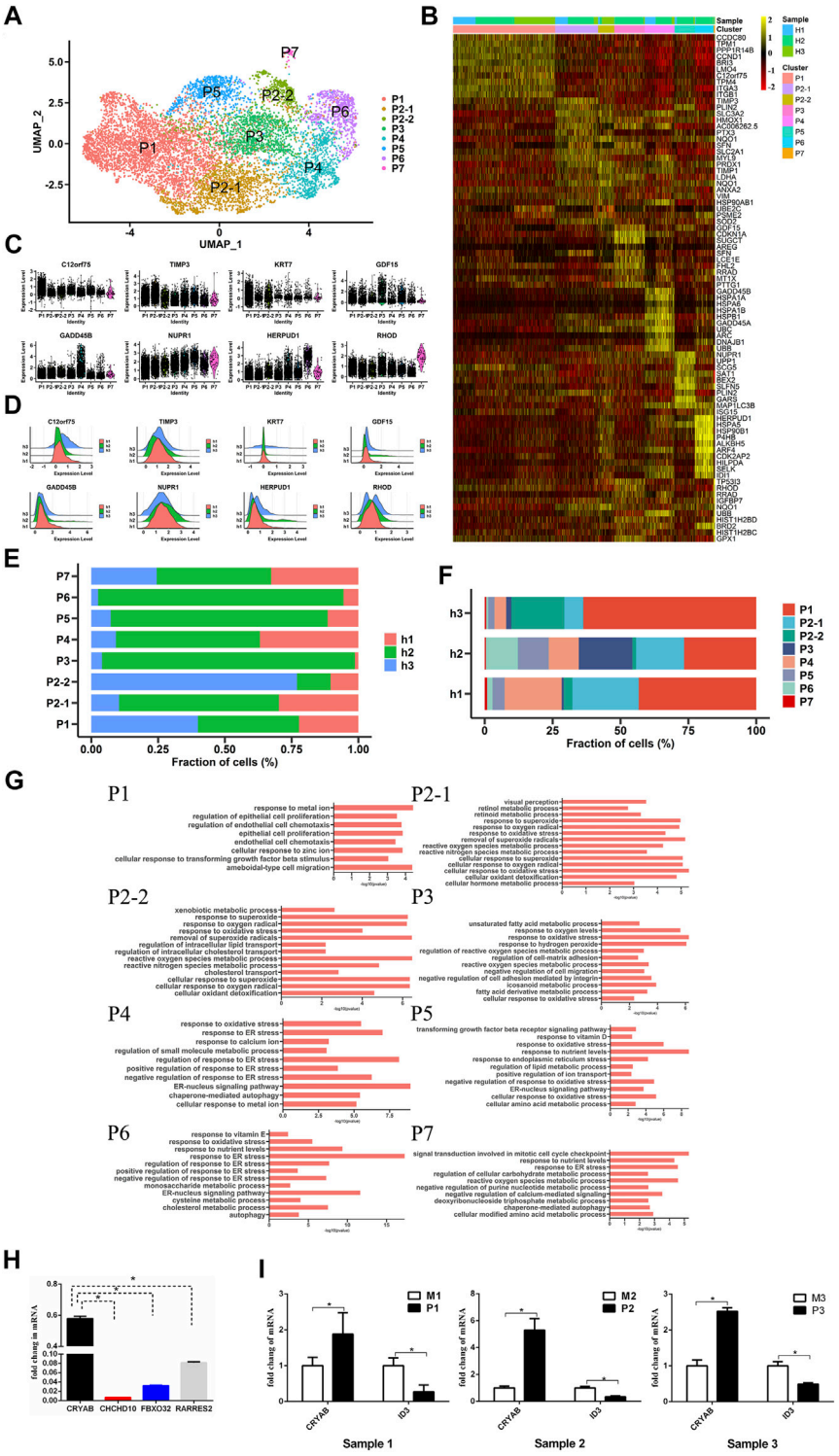

FIGURE 3 | Single-cell RNA-seq transcriptome profiling of peripheral RPE **(A).** UMAP plot shows the cell classification of peripheral RPE cells in three samples **(B).** Heatmap of eight peripheral RPE subpopulations. Columns are divided into eight types of cells, and rows represent gene names and can be used to identify eight subpopulations. The heatmap scale represents the normalized expression value **(C).** Violin plots showing 8 clusters of peripheral RPE-specific genes **(D).** The expression patterns of the differentially expressed genes in the three samples. The *X*-axis shows the level of gene expression **(E).** The proportion of each sample in each cluster (P1, P2-1, P2-2, P3, P4, P5, P6, P7) **(F).** The proportion of each cluster (P1, P2-1, P2-2, P3, P4, P5, P6, P7) in each sample **(G).** Gene Ontology (GO) terms associated with genes with upregulated expression in each peripheral RPE population **(H).** RT-PCR analysis of differentially expressed genes with high specific expression in peripheral RPE. *: $p < 0.05$ **(I).** Verification of peripheral RPE markers and macular RPE markers by RT-PCR.

determine the cluster distribution of these genes in our data. Studies have reported that *USH2A*, *EYS* and *CRB1* are the top three genes responsible for inherited retinal dystrophy (Huang et al., 2015). In our data, *CRB1* and *EYS* were related to the development of the autosomal recessive disorder retinitis pigmentosa (RP). These genes were mainly expressed in the P3, P4, P5 and P7 clusters. The genes *LRAT*, *RPE65* and *RLBP1* are associated with the visual cycle (Strauss, 2005; Lima de Carvalho et al., 2020). *LRAT* was a susceptible gene of autosomal recessive RP that was highly expressed in the P5 cluster in our data. Our results demonstrated that the *PRPH2*, *PRPF6*, and *IMPG1* genes associated with autosomal dominance of RP were highly expressed in the macular RPE and clusters P6 and P7 (**Supplementary Figure S3A, B**). *RPE65* and *RLBP1*, which were highly and specifically expressed in the P4 cluster, are susceptible genes contributing to RP and congenital stationary night blindness (CSNB) (**Figure 6A**). In previous studies, *VTN* and *HTRA1* associated with AMD were highly expressed in PR cells and HCs in the retina, respectively (Fritsche et al., 2016; Peng et al., 2019; Orozco et al., 2020). Interestingly, in our hRPE data, we found that the *VTN* and *HTRA1* genes were highly expressed in clusters P2 and P7 (**Supplementary Figure S3C**). In addition, other retinal disease-causing genes related to AMD were mainly expressed in clusters P4, P6 and P7, but some susceptibility genes, such as *C2*, *FBLN5*, and *TLR4,* were highly expressed in the macular cluster (**Supplementary Figure S3C**).

From the genome-wide association study (GWAS) results (Hou et al., 2014; Wang et al., 2019a), we found region-specific expression of genes implicated in human retinal diseases such as Behcet's disease (BD) and Vogt-Koyanagi-Harada syndrome (VKH). VKH-related genes were mainly highly expressed in clusters P3 and P4, and *PTPN22* was specifically expressed in macular RPE cells (**Figure 6B**). BD-related genes were mainly highly expressed in P3, P4, P6 and macular RPE clusters (**Figure 6C**). Next, we analyzed ocular disease-associated gene expression in subpopulations and found that many human retinal diseases primarily affected the macular RPE cluster and some peripheral RPEs, such as clusters P4 and P6 (**Figures 6D, E**). In summary, these results identify the subpopulation distribution of multiple ocular disease-related genes in the RPE and may provide information for future genetic correlation analysis and disease treatments.

DISCUSSION

Single-cell sequencing technology is helpful to analyze cell types and gene expression patterns for many complex tissues in detail. Single-cell sequencing of hRPE cells from three adult donor eyes was performed to investigate the heterogeneity of the RPE, including cell classification and functional differences. Our results showed that RPE tissues could be categorized into two clusters, one of which is macular RPE highly expressing *ID3* and the other is peripheral RPE cluster expressing *CRYAB*. A recent study of single-cell sequencing of the RPE found that the expression of *ID3* and *IGFBP5* was enriched in the macular and peripheral RPE, respectively (Voigt et al., 2019). Similarly, our results showed that the hRPE was divided into two clusters and that one cluster had a small number of cells, a total of 439 cells, highly expressing *ID3*. However, we found that *CRYAB* was more specific than *IGFBP5* in peripheral hRPE cells, indicating that *CRYAB* may be firstly identified as a new marker gene of peripheral RPE cells. In addition, we found that the expression of *BEST1* in the macular cluster was lower than that in the peripheral cluster, which was consistent with a previous study (Mullins et al., 2007; Voigt et al., 2019). Furthermore, according to their transcriptome expression profiles, the two clusters could be divided into more elaborate subpopulations, including P1, P2-1, p2-2, P3, P4, P5, P6, and P7 and M1 and M2 clusters. Further studies are needed to elucidate the biological functions of each hRPE subpopulation.

Previous studies have described the transcriptome landscape of the human retinal tissues by scRNA-seq (Hu et al., 2019) and snRNA-seq analysis (Liang et al., 2019). As we did not examine the photoreceptor cells using scRNA-seq analysis, further study was needed to clarify the interaction of the RPE and the retinal cells.

As we all know, the RPE has various functions. Our results showed that OS-related genes were more highly expressed in the macular cluster than in the peripheral cluster, which may imply the stronger ability of the macula to respond to external stimuli and injuries. Although the RPE has metabolic and transport functions, the peripheral cluster of the hRPE was found to be involved in lipid metabolism, while the macular cluster favored metal ion transport. Further studies revealed that the two subpopulations of macular RPE cells performed different functions. One of the populations was related to cell adhesion (M1); however, the other population (M2) highly expressed several genes, such as *HERPUD1*, *HMOX1*, *MDM2*, and *XBP1*, which are related to OS and ER stress. Interestingly, the aforementioned genes were also found to play a crucial role in human macula development and cone functions (Kohl et al., 2015). These aforementioned results strongly indicated the heterogeneity of molecular expression and functions between the macula and the peripheral hRPE.

Transcription factor and intercellular communication analyses on hRPE cells were also performed; the results of these analyses indicated that macular and peripheral hRPE clusters had different expression patterns of transcription factors. Interestingly, EGFR plays an important role in cell growth, proliferation and differentiation (Martín-Bermudo et al., 2015; Malartre, 2016) and was found to be enriched in the macular hRPE cluster but not in the peripheral hRPE cluster. In contrast, several ligands of EGFR were highly expressed in the peripheral hRPE. EGFR has been shown to regulate autophagy and phagocytosis of RPE cells (Muniz-Feliciano et al., 2017) and the proliferation of retinal progenitor cells (Close et al., 2006). Accumulating evidence suggests that macular clusters with high expression of EGFR may have more important functions, such as autophagy, phagocytosis and cell proliferation, in the RPE. Interestingly, *TYRP1* has been reported to be involved in melanin synthesis (Rai et al., 2020), and *RLBP1* is related to the visual cycle (Wen et al., 2016). Our study showed that both of these genes were highly expressed in the peripheral P2-1 cluster (**Figure 3G**).

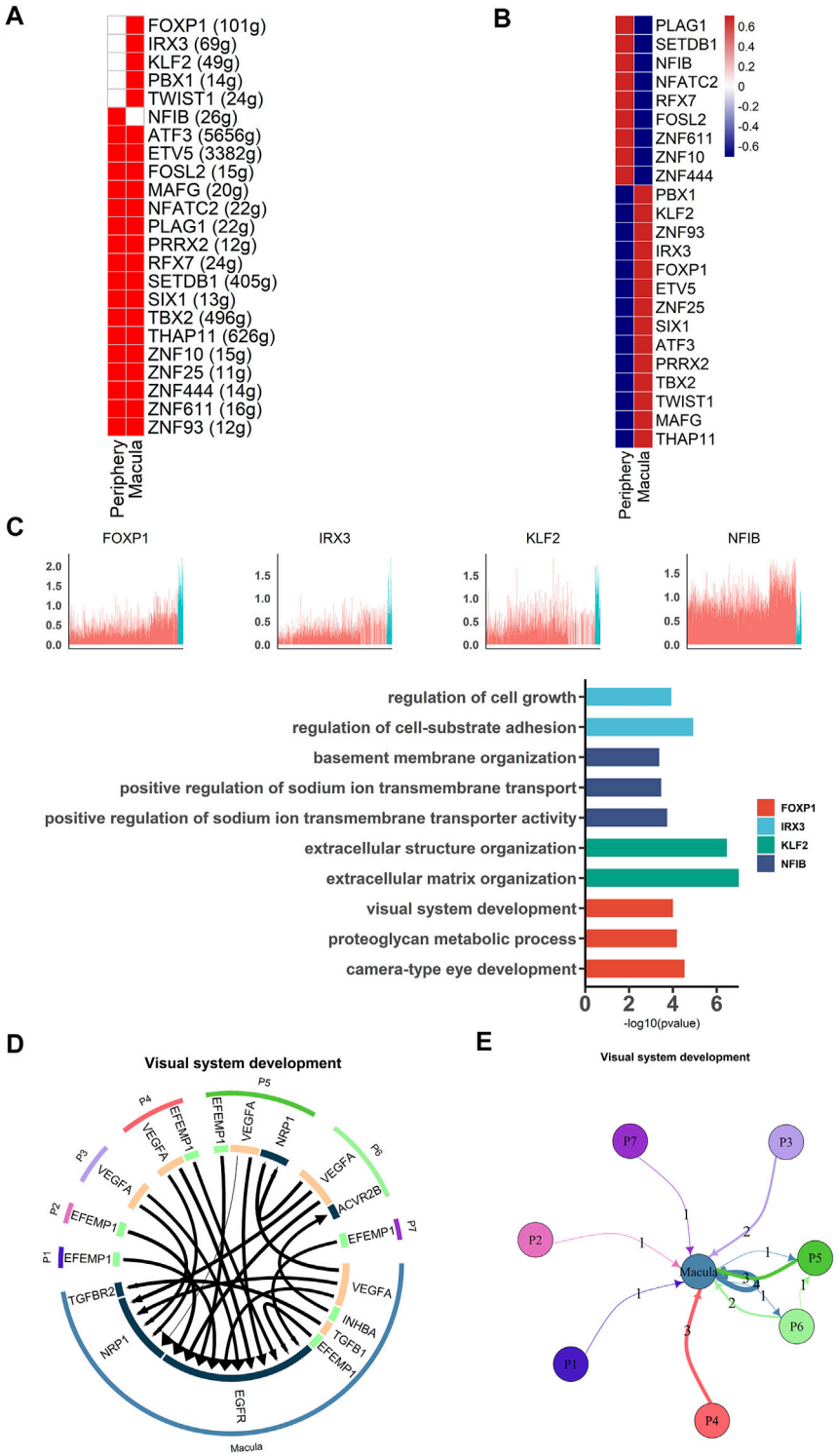

FIGURE 4 | Different gene expression patterns between macular and peripheral RPE **(A).** SCENIC results for the macular RPE and peripheral RPE. Heatmap showing the active and expressed transcription factors in each cell cluster. The states of the transcription factors in each cell class are indicated in red (active) and white (inactive) **(B).** Heatmap shows the average expression of active transcription factors in each cell cluster. The expression level is indicated by the color level; red indicates high expression, and blue indicates low expression **(C).** Expression of specific highly expressed transcription factors and GO functional analysis of their corresponding target genes. The upper part of the figure represents the expression of transcription factors, and the lower part of the figure represents the functional annotation of target genes regulated by transcription factors **(D).** Analysis of cell communication between macular RPE and peripheral RPE. The visual system development of the hRPE among the top 20 ligand-receptor pairs **(E).** Connections between the peripheral RPE subpopulations and the macular RPE cluster of ligand-receptor pairs of the visual development system.

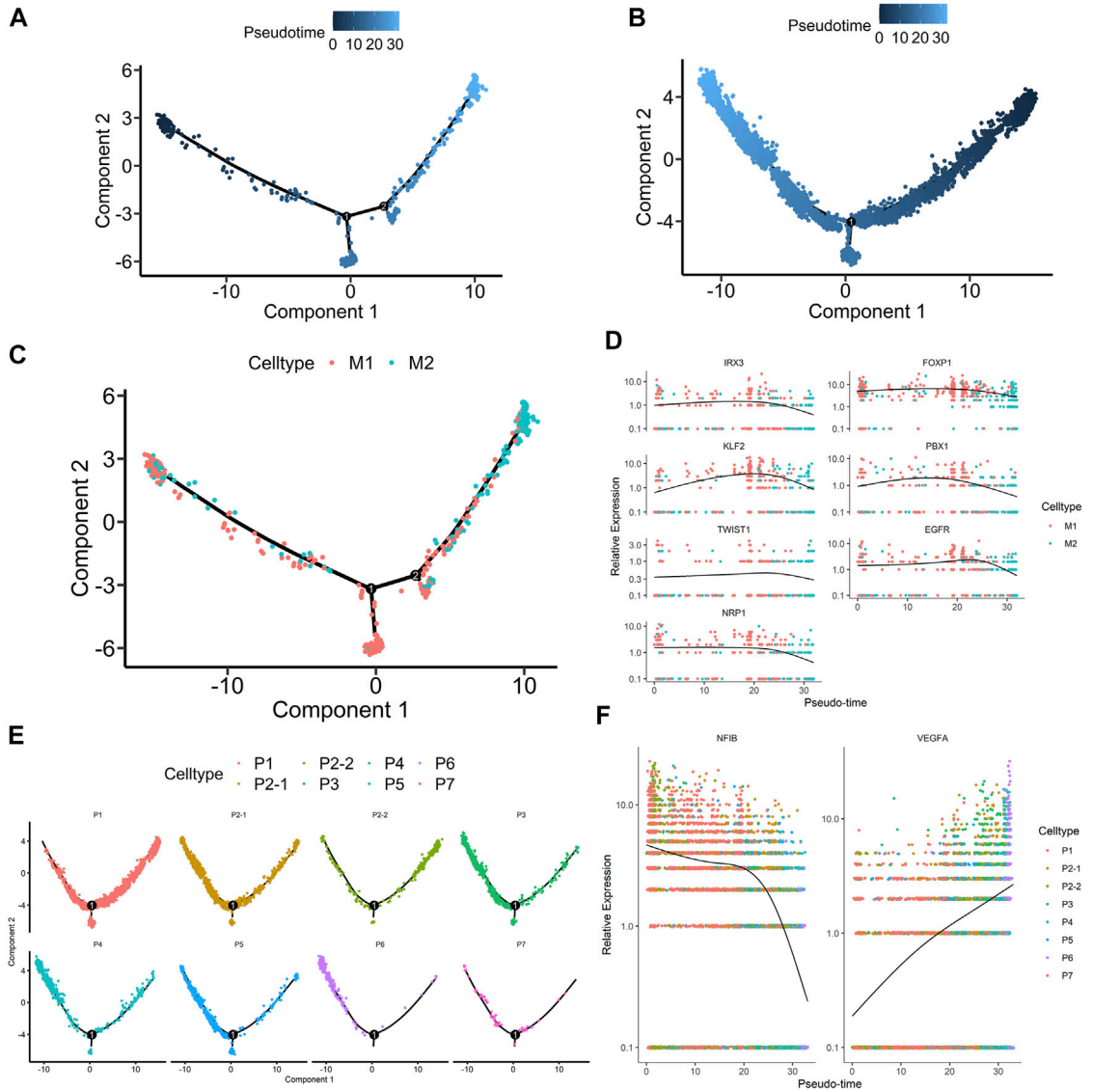

FIGURE 5 | The development of human peripheral RPE and macular RPE **(A-B).** Trajectory analysis of the transition of the hRPE along pseudotime. The shades of color represent the order of the time **(A).** macular RPE **(B).** peripheral RPE **(C).** Trajectory analysis of macular RPE subpopulations over pseudotime. Cell types are distinguished by different colors **(D).** Pseudotime changes in important transcription factors and receptors associated with macular RPE **(E).** Trajectory analysis for peripheral RPE subpopulations along pseudotime. Cell types are distinguished by different colors **(F).** Pseudotime changes in important transcription factors and receptors associated with peripheral RPE.

In the pseudotemporal analysis, it is evident that these subpopulations had a chronological developmental sequence. In macular RPE, the results combined with the GO analysis results showed that M1 cluster cells grew to M2 cluster cells. In the peripheral RPE, these results suggested that the more complex the function of subpopulations was, the later the developmental time. In addition, these important transcription factors, receptors and ligands may play important roles in early development except *VEGFA*, *and* it is possible that *VEGFA* acts later in the development of RPE cells.

About 200 susceptibility genes related with VKH, BD, AMD, and other human ocular diseases were also analyzed. Although these many genes implicated in ocular diseases were found to be mainly expressed in PRs and nonneuronal cells (Peng et al., 2019), our results showed that some susceptible genes were also expressed in the hRPE subgroups. Additionally, primary open-angle glaucoma (POAG), primary angle-closure glaucoma (PACG), diabetic macular edema and retinopathy (DME/DR), AMD and BD were closely related to the population of the macula or P4 clusters. This evidence suggests that a specific hRPE subpopulation is associated with certain ocular diseases, and more attention to specific cell subsets of the hRPE should be paid when studying disease mechanisms.

It is also worthwhile to point out that some questions need to be further investigated. Many ocular diseases such as AMD and

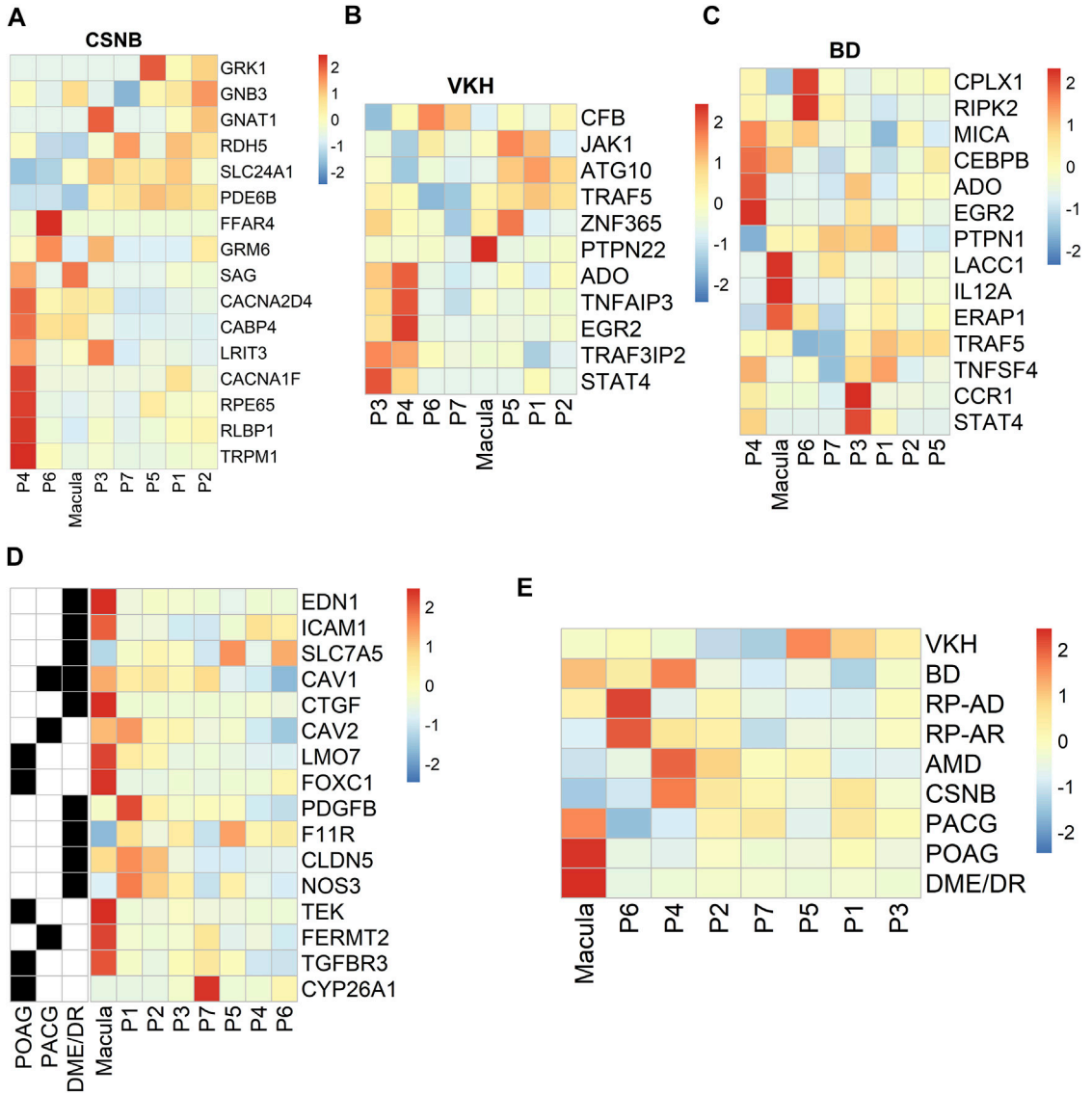

FIGURE 6 | Profiling of specific expression patterns of human retinal disease-associated genes. Aggregated expression of disease-associated genes in macular and peripheral cell types. CSNB, congenital stationary night blindness; BD, Behcet disease; VKH, Vogt-Koyanagi-Harada syndrome. Colorbar: red represents highly expressed and blue represents lowly expressed, scale method is Z-score normalization **(A).** CSNB **(B).** VKH **(C).** BD **(D).** Expression patterns of specific retinal disease-associated genes (rows) by HRPE in the macula and periphery (columns) **(E).** Known or candidate genes for multiple ocular diseases. Ocular diseases are shown in rows, columns are cell clusters identified.

RP are closely related to the macular retina, especially RGCs, cones, and rod cells; however, our results showed that many susceptibility genes associated with these diseases were selectively expressed in a particular macular RPE subpopulation. The pathogenesis of hRPE cell subsets in these diseases needs to be further explored. Additionally, due to the heterogeneity of hRPE cells and the influence of age on their heterogeneity, further studies are needed to clarify the physiological and pathological function of hRPE clusters.

In conclusion, although the RPE is a single-layer epithelium, we constructed the transcriptome landscape of the human RPE, as well as a retinal disease map of the hRPE atlas, and obtained key information about the heterogeneity and specific functions of cell subpopulations in the human RPE; this information is likely to be an important clue for understanding the cellular mechanisms and curing pathological conditions of the hRPE related to ocular diseases.

MATERIALS AND METHODS

Ethics Statement

The present study was approved by the Ethics Committee of the First Affiliated Hospital of Chongqing Medical University, China

(Permit Number: 2019-099) and adhered to the tenets of the Declaration of Helsinki. All eye tissue samples used in this study were collected from Chongqing Eye Bank, the First Affiliated Hospital of Chongqing Medical University. Written informed consent was obtained from the patients prior to the study.

Reagents

All the primers used in this study were synthesized by Shanghai Sangon Biological Engineering Technology and Services. The primers were ID3-F:

5′ GAGAGGCACTCAGCTTAGCC3', ID3-R:

5′TCCTTTTGTCGTTGGAGATGAC3'; RARRES2-F: 5′GCA TCAAACTGGGCTCTGAG3′, RARRES2-R: 5′AGGGAAGTA GAAGCTGTGGG3'; CRYAB-F: 5′GGGAGATGTGATTGA GGTGC3′, CRYAB-R: 5′TTCACAGTGAGGACCCCATC3'; FBXO32-F: 5′TGTGGGTGTATCGGATGGAG3′, FBXO32-R: 5′GAGTTTCTTCCACAGCAGCC3'; CHCHD10-F: 5′CAG AGTGACCTGTCCCTGTG3′, and CHCHD10-R: 5′CCTCCT CACTTCCAATCCCA3'. Cy3-labeled goat anti-rabbit IgG (H + L) (Beyotime, A0516, 1:500), Cy3-labeled goat anti-mouse IgG (H + L) (Beyotime, A0521, 1:500), Alexa Fluor 488-labeled goat anti-mouse IgG (H + L) (Beyotime, A0428, 1:500) and DAPI were purchased from Beyotime. RPE-65 (Abcam ab231782, 1:1,000), ID3 (Cell Signaling Technology #9837, 1:500), and crystallin antibodies (Abcam, ab230722, 1:500) were used for immunofluorescence visualization (SP8; Leica).

Tissue and Cell Processing

Adult hRPE samples were obtained from three donors (age 29–64 years old) within 24 h of death (postmortem time, 12 h). After dissecting the cornea, whole RPE tissues were collected from the remaining ocular tissue. The RPE tissues were rinsed three times with phosphate-buffered saline (PBS). First, the tissues were digested using 0.25% trypsin for approximately 30 min at 37°C until a single-cell suspension was made, and then complete Dulbecco's Modified Eagle Mediummodified Eagle's medium (DMEM) was used to neutralize the cell suspension. The single-cell samples were passed through a 40 μm cell strainer. Second, the cell suspension was rinsed three times with PBS and centrifuged for 5 min (1,450 rpm, 4°C). Next, a hemocytometer with trypan blue was used to count the number of cells and ensure that the level of cell viability was approximately 90%. Finally, single-cell samples were subjected to scRNA-seq analysis with a high-throughput droplet-mediated scRNA-seq platform (10× Genomics Chromium).

Single RNA-Seq Library Construction

The appropriate volume of each sample was diluted to contain approximately 5,000 hRPE cells. Subsequently, the single-cell suspension, gel beads and oils were all added to the 10× Genomics single-cell A chip. After droplet generation, samples were transferred into 200 μL PCR tubes, and reverse transcription was performed using a T100 Thermal Cycler (Bio-Rad, California, United States). After reverse transcription, cDNA was recovered using a recovery agent provided by 10× Genomics. SPRIselect beads were used for cDNA clean-up, and then the cDNA was amplified for 10 cycles. The concentration of cDNA was detected by a Qubit2.0 fluorometer (Invitrogen, Canada). Single-cell cDNA libraries were prepared according to the Chromium Single Cell 3' Reagent Kit v2 user guidance (https://support.10xgenomics.com/single-cell-gene-expression/index/doc/user-guide-chromium-single-cell-3-reagent-kits-user-guide-v2-chemistry).

Real-Time PCR Analysis

We isolated total RNA using TRIzol Reagent (Ambion, Carlsbad, CA, United States). For RT-PCR, total RNA was reverse-transcribed using RT Primer Mix and oligo dT primers (MCE, China). cDNA was quantified using primers specific for mice by the ABI 7500 real-time PCR system (Applied Biosystems, Foster City, CA, United States). The sequences of the primers are provided above. PCR amplification was performed in a volume of 20 μL using RT-PCR Mix (MCE, China). The results were analyzed based on group assignment.

Data Processing

Single cells were assessed using a 10× Chromium system (10× Genomics) and V2 single-cell reagent kits. After the library was built, the reads were aligned to the GRch38 human genome using the 10× analysis tool Cellranger Toolkit (Version 2.1.1) (Zheng et al., 2017), and a unique molecular identifier (UMI) was used to quantify gene expression. Cellranger Count was used to preprocess and preliminarily filter the data.

Then, the obtained matrix, barcode and gene files were imported into R software (version 3.6.1) for further analysis by Seurat (version 3.1.5) (Stuart et al., 2019). The cells with fewer than 200 expressed genes among the three samples were discarded. Similarly, the outliers of each sample were filtered to eliminate the signal interference of the double cells. The data were normalized using the LogNormalize method. We regressed out mitochondrial gene expression causing inherent variations, the number of UMIs per cell and even the cell cycle genes.

The FindVariableFeatures function was used to find the top 2000 highly variable genes for variable genetic parameters. Then, we used canonical correlation analysis (CCA) to correct the batch effect of the samples.

We constructed a shared nearest neighbors (SNN) diagram for the data using principal component analysis (PCA)-reduced expression data for the top 49 principal components and then used modularity optimization through the SNN clustering algorithm to identify cell clusters. We first calculated the k-nearest neighbor and performed SNN analysis; then, we optimized the modular function. Finally, the number of clusters based on the parameter resolution was determined. Next, our clusters were displayed on a 2-dimensional diagram by nonlinear dimensional reduction. We used the Seurat function RunUMAP to achieve dimension reduction. Seurat function Findmarkers were used to identify marker genes for each cluster (p.adj <0.05, avg_log2FC > 0.25).

Cell-type-specific Transcription Factors

We used SCENIC software to select the specific transcription factors and their corresponding target genes of the hRPE clusters. Transcription factors that were active among more than 50% of cells in the macular and peripheral RPE clusters were retained by SCENIC (Aibar et al., 2017).

Cell-Cell Interaction Analysis

iTALK (version 0.1.0) was used to analyze cell-cell interactions among hRPE clusters (Wang et al., 2019b). We used the top 50% highly expressed genes to explore the corresponding receptor-ligand pairs. The relationship between macular and peripheral RPE clusters was systematically predicted, and the top 20 pairs were displayed in the present study.

Identification of the Cell Trajectory in hRPE Clusters

The trajectory landscape of hRPE cluster development was constructed by Monocle2 (version 2.16.0) (Trapnell et al., 2014). The highly variable genes revealed in the previous clustering examination were used to carry out pseudotime analysis. The track was then established using the DDRTree algorithm in Monocle2, and the pseudodevelopmental time was then obtained from the trajectory data.

GO Analysis

The R package ClusterProfiler (version 3.16.0) (Yu et al., 2012) was used to perform gene enrichment analysis. The p value was corrected by the Benjamini & Hochberg method.

DATA AVAILABILITY STATEMENT

The datasets presented in this study can be found in online repositories. The names of the repository/repositories and accession number(s) can be found below: GSE189770.

ETHICS STATEMENT

The studies involving human participants were reviewed and approved by The Ethics Committee of The First Affiliated Hospital of ChongQing Medical University. The patients/participants provided their written informed consent to participate in this study.

AUTHOR CONTRIBUTIONS

Conceived and designed the experiments: XL, ZX and SH. Performed the experiments: XL, ZX, NL, HZ. Analyzed the data: ZX. Contributed reagents/materials/analysis/tools: HL, KH, QZ. Wrote the paper: XL, ZX, NL, PY and SH.

FUNDING

This work was supported by the National Natural Science Foundation Project of China (81873678, 82070951), the Innovative Research Group Project of Chongqing Education Commission (CXQT19015), the Chongqing Natural Science Foundation (cstc2019jcyj-msxmX0120), the Grant of Chongqing Education Commission (KJQN202000406), the National Key Clinical Specialties Construction Program of China, grants from the Bureau of Human Resources and Social Security of Chongqing (cx2018010) and the Chongqing Key Laboratory of Ophthalmology (CSTC, 2008CA5003).

SUPPLEMENTARY MATERIAL

The Supplementary Material for this article can be found online at: https://www.frontiersin.org/articles/10.3389/fcell.2021.802457/full#supplementary-material

REFERENCES

Aibar, S., González-Blas, C. B., Moerman, T., Huynh-Thu, V. A., Imrichova, H., Hulselmans, G., et al. (2017). SCENIC: Single-Cell Regulatory Network Inference and Clustering. *Nat. Methods* 14 (11), 1083–1086. doi:10.1038/nmeth.4463

Alabduljalil, T., Westall, C. A., Reginald, A., Farsiu, S., Chiu, S. J., Arshavsky, A., et al. (2019). Demonstration of Anatomical Development of the Human Macula within the First 5 Years of Life Using Handheld OCT. *Int. Ophthalmol.* 39 (7), 1533–1542. doi:10.1007/s10792-018-0966-3

Bharti, K., Miller, S. S., and Arnheiter, H. (2011). The New Paradigm: Retinal Pigment Epithelium Cells Generated from Embryonic or Induced Pluripotent Stem Cells. *Pigment Cell Melanoma Res* 24 (1), 21–34. doi:10.1111/j.1755-148X.2010.00772.x

Boulton, M., and Dayhaw-Barker, P. (2001). The Role of the Retinal Pigment Epithelium: Topographical Variation and Ageing Changes. *Eye* 15, 384–389. doi:10.1038/eye.2001.141

Close, J. L., Liu, J., Gumuscu, B., and Reh, T. A. (2006). Epidermal Growth Factor Receptor Expression Regulates Proliferation in the Postnatal Rat Retina. *Glia* 54 (2), 94–104. doi:10.1002/glia.20361

Fernandez-Godino, R., Garland, D. L., and Pierce, E. A. (2015). A Local Complement Response by RPE Causes Early-Stage Macular Degeneration. *Hum. Mol. Genet.* 24 (19), 5555–5569. doi:10.1093/hmg/ddv287

Fritsche, L. G., Igl, W., Bailey, J. N., Grassmann, F., Sengupta, S., Bragg-Gresham, J. L., et al. (2016). A Large Genome-wide Association Study of Age-Related Macular Degeneration Highlights Contributions of Rare and Common Variants. *Nat. Genet.* 48 (2), 134–143. doi:10.1038/ng.3448

Hou, S., Du, L., Lei, B., Pang, C. P., Zhang, M., zhuang, W., et al. (2014). Genome-wide Association Analysis of Vogt-Koyanagi-Harada Syndrome Identifies Two New Susceptibility Loci at 1p31.2 and 10q21.3. *Nat. Genet.* 46 (9), 1007–1011. doi:10.1038/ng.3061

Hu, Y., Wang, X., Hu, B., Mao, Y., Chen, Y., Yan, L., et al. (2019). Dissecting the Transcriptome Landscape of the Human Fetal Neural Retina and Retinal Pigment Epithelium by Single-Cell RNA-Seq Analysis. *Plos Biol.* 17 (7), e3000365. doi:10.1371/journal.pbio.3000365

Huang, X.-F., Huang, F., Wu, K.-C., Wu, J., Chen, J., Pang, C.-P., et al. (2015). Genotype-phenotype Correlation and Mutation Spectrum in a Large Cohort of Patients with Inherited Retinal Dystrophy Revealed by Next-Generation Sequencing. *Genet. Med.* 17 (4), 271–278. doi:10.1038/gim.2014.138

Kohl, S., Zobor, D., Chiang, W.-C., Weisschuh, N., Staller, J., Menendez, I. G., et al. (2015). Mutations in the Unfolded Protein Response Regulator ATF6 Cause the Cone Dysfunction Disorder Achromatopsia. *Nat. Genet.* 47 (7), 757–765. doi:10.1038/ng.3319

Liang, Q., Dharmat, R., Owen, L., Shakoor, A., Li, Y., Kim, S., et al. (2019). Single-nuclei RNA-Seq on Human Retinal Tissue Provides Improved Transcriptome Profiling. *Nat. Commun.* 10 (1), 5743. doi:10.1038/s41467-019-12917-9

Lima de Carvalho, J. R., Jr., Kim, H. J., Ueda, K., Zhao, J., Owji, A. P., Yang, T., et al. (2020). Effects of Deficiency in the RLBP1-Encoded Visual Cycle Protein CRALBP on Visual Dysfunction in Humans and Mice. *J. Biol. Chem.* 295 (19), 6767–6780. doi:10.1074/jbc.RA120.012695

Lukowski, S. W., Lo, C. Y., Sharov, A. A., Nguyen, Q., Fang, L., Hung, S. S., et al. (2019). A Single-cell Transcriptome Atlas of the Adult Human Retina. *EMBO J.* 38 (18), e100811. doi:10.15252/embj.2018100811

Mackay, D. S., Bennett, T. M., and Shiels, A. (2015). Exome Sequencing Identifies a Missense Variant in EFEMP1 Co-segregating in a Family with Autosomal Dominant Primary Open-Angle Glaucoma. *PLoS One* 10 (7), e0132529. doi:10.1371/journal.pone.0132529

Malartre, M. (2016). Regulatory Mechanisms of EGFR Signalling during Drosophila Eye Development. *Cell. Mol. Life Sci.* 73 (9), 1825–1843. doi:10.1007/s00018-016-2153-x

Martín-Bermudo, M. D., Bardet, P. L., Bellaïche, Y., and Malartre, M. (2015). The Vav Oncogene Antagonises EGFR Signalling and Regulates Adherens junction Dynamics during Drosophila Eye Development. *Development* 142 (8), 1492–1501. doi:10.1242/dev.110585

Menon, M., Mohammadi, S., Davila-Velderrain, J., Goods, B. A., Cadwell, T. D., Xing, Y., et al. (2019). Single-cell Transcriptomic Atlas of the Human Retina Identifies Cell Types Associated with Age-Related Macular Degeneration. *Nat. Commun.* 10 (1), 4902. doi:10.1038/s41467-019-12780-8

Mullins, R. F., Kuehn, M. H., Faidley, E. A., Syed, N. A., and Stone, E. M. (2007). Differential Macular and Peripheral Expression of Bestrophin in Human Eyes and its Implication for Best Disease. *Invest. Ophthalmol. Vis. Sci.* 48 (7), 3372–3380. doi:10.1038/ng.331910.1167/iovs.06-0868

Muniz-Feliciano, L., Doggett, T. A., Zhou, Z., and Ferguson, T. A. (2017). RUBCN/rubicon and EGFR Regulate Lysosomal Degradative Processes in the Retinal Pigment Epithelium (RPE) of the Eye. *Autophagy* 13 (12), 2072–2085. doi:10.1080/15548627.2017.1380124

Orozco, L. D., Chen, H.-H., Cox, C., Katschke, K. J., Jr., Arceo, R., Espiritu, C., et al. (2020). Integration of eQTL and a Single-Cell Atlas in the Human Eye Identifies Causal Genes for Age-Related Macular Degeneration. *Cell Rep.* 30 (4), 1246–1259. doi:10.1016/j.celrep.2019.12.082

Peng, Y.-R., Shekhar, K., Yan, W., Herrmann, D., Sappington, A., Bryman, G. S., et al. (2019). Molecular Classification and Comparative Taxonomics of Foveal and Peripheral Cells in Primate Retina. *Cell* 176 (5), 1222–1237. doi:10.1016/j.cell.2019.01.004

Rai, A., Chatterjee, B., Bhowmick, S., Sagar, S., and Roy, S. S. (2020). Beclin 1 Controls Pigmentation by Changing the Nuclear Localization of Melanogenic Factor MITF. *Biochem. Biophysical Res. Commun.* 528 (4), 719–725. doi:10.1016/j.bbrc.2020.05.118

Raimondi, C., Brash, J. T., Fantin, A., and Ruhrberg, C. (2016). NRP1 Function and Targeting in Neurovascular Development and Eye Disease. *Prog. Retin. Eye Res.* 52, 64–83. doi:10.1016/j.preteyeres.2016.02.003

Rheaume, B. A., Jereen, A., Bolisetty, M., Sajid, M. S., Yang, Y., Renna, K., et al. (2018). Single Cell Transcriptome Profiling of Retinal Ganglion Cells Identifies Cellular Subtypes. *Nat. Commun.* 9 (1), 2759. doi:10.1038/s41467-018-05134-3

Shekhar, K., Lapan, S. W., Whitney, I. E., Tran, N. M., Macosko, E. Z., Kowalczyk, M., et al. (2016). Comprehensive Classification of Retinal Bipolar Neurons by Single-Cell Transcriptomics. *Cell* 166 (5), 1308–1323. doi:10.1016/j.cell.2016.07.054

Strauss, O. (2005). The Retinal Pigment Epithelium in Visual Function. *Physiol. Rev.* 85 (3), 845–881. doi:10.1152/physrev.00021.2004

Stuart, T., Butler, A., Hoffman, P., Hafemeister, C., Papalexi, E., Mauck, W. M., et al. (2019). Comprehensive Integration of Single-Cell Data. *Cell* 177 (7), 1888–1902. doi:10.1016/j.cell.2019.05.031

Trapnell, C., Cacchiarelli, D., Grimsby, J., Pokharel, P., Li, S., Morse, M., et al. (2014). The Dynamics and Regulators of Cell Fate Decisions Are Revealed by Pseudotemporal Ordering of Single Cells. *Nat. Biotechnol.* 32 (4), 381–386. doi:10.1038/nbt.2859

Voigt, A. P., Mulfaul, K., Mullin, N. K., Flamme-Wiese, M. J., Giacalone, J. C., Stone, E. M., et al. (2019). Single-cell Transcriptomics of the Human Retinal Pigment Epithelium and Choroid in Health and Macular Degeneration. *Proc. Natl. Acad. Sci. USA* 116 (48), 24100–24107. doi:10.1073/pnas.1914143116

Wang, Q., Su, G., Tan, X., Deng, J., Du, L., Huang, X., et al. (2019). UVEOGENE: An SNP Database for Investigations on Genetic Factors Associated with Uveitis and Their Relationship with Other Systemic Autoimmune Diseases. *Hum. Mutat.* 40 (3), 258–266. doi:10.1002/humu.23702

Wang, Y., Wang, R., Zhang, S., Song, S., Jiang, C., Han, G., et al. (2019). iTALK: an R Package to Characterize and Illustrate Intercellular Communication. *bioRxiv*, 507871. doi:10.1101/507871

Wen, B., Li, S., Li, H., Chen, Y., Ma, X., Wang, J., et al. (2016). Microphthalmia-associated Transcription Factor Regulates the Visual Cycle Genes Rlbp1 and Rdh5 in the Retinal Pigment Epithelium. *Sci. Rep.* 6, 21208. doi:10.1038/ncomms1404910.1038/srep21208

Yan, W., Peng, Y.-R., van Zyl, T., Regev, A., Shekhar, K., Juric, D., et al. (2020). Cell Atlas of the Human Fovea and Peripheral Retina. *Sci. Rep.* 10 (1), 9802. doi:10.1038/s41598-020-66092-9

Yu, G., Wang, L.-G., Han, Y., and He, Q.-Y. (2012). clusterProfiler: an R Package for Comparing Biological Themes Among Gene Clusters. *OMICS: A J. Integr. Biol.* 16 (5), 284–287. doi:10.1089/omi.2011.0118

Zheng, G. X. Y., Terry, J. M., Belgrader, P., Ryvkin, P., Bent, Z. W., Wilson, R., et al. (2017). Massively Parallel Digital Transcriptional Profiling of Single Cells. *Nat. Commun.* 8, 14049. doi:10.1038/ncomms14049

Conflict of Interest: The authors declare that the research was conducted in the absence of any commercial or financial relationships that could be construed as a potential conflict of interest.

Publisher's Note: All claims expressed in this article are solely those of the authors and do not necessarily represent those of their affiliated organizations, or those of the publisher, the editors and the reviewers. Any product that may be evaluated in this article, or claim that may be made by its manufacturer, is not guaranteed or endorsed by the publisher.

Copyright © 2021 Xu, Liao, Li, Zhou, Li, Zhang, Hu, Yang and Hou. This is an open-access article distributed under the terms of the Creative Commons Attribution License (CC BY). The use, distribution or reproduction in other forums is permitted, provided the original author(s) and the copyright owner(s) are credited and that the original publication in this journal is cited, in accordance with accepted academic practice. No use, distribution or reproduction is permitted which does not comply with these terms.

frontiers in Cell and Developmental Biology

ORIGINAL RESEARCH
published: 12 January 2022
doi: 10.3389/fcell.2021.810020

Retinal Development and Pathophysiology in Kcnj13 Knockout Mice

*Xiaodong Jiao[1†], Zhiwei Ma[1†], Jingqi Lei[2], Pinghu Liu[2], Xiaoyu Cai[2], Pawan K. Shahi[3], Chi-Chao Chan[1], Robert Fariss[4], Bikash R. Pattnaik[3], Lijin Dong[2] and J. Fielding Hejtmancik[1]**

[1]Ophthalmic Genetics and Visual Function Branch, National Eye Institute, National Institutes of Health, Bethesda, MD, United States, [2]Genetic Engineering Core, National Eye Institute, National Institute of Health, Bethesda, MD, United States, [3]Departments of Pediatrics and Ophthalmology and Visual Sciences and the McPherson Eye Research Institute, University of Wisconsin, Madison, AL, United States, [4]Imaging Core, National Eye Institute, National Institutes of Health, Bethesda, MD, United States

OPEN ACCESS

Edited by:
Ling Zhao,
Sun Yat-sen University, China

Reviewed by:
Haiwei Xu,
Army Medical University, China
Steven J. Fliesler,
University at Buffalo, United States

***Correspondence:**
J. Fielding Hejtmancik
hejtmancikj@nei.nih.gov

[†]These authors have contributed equally to this work

Specialty section:
This article was submitted to Molecular and Cellular Pathology, a section of the journal Frontiers in Cell and Developmental Biology

Received: 05 November 2021
Accepted: 10 December 2021
Published: 12 January 2022

Citation:
Jiao X, Ma Z, Lei J, Liu P, Cai X, Shahi PK, Chan C-C, Fariss R, Pattnaik BR, Dong L and Hejtmancik J (2022) Retinal Development and Pathophysiology in Kcnj13 Knockout Mice. Front. Cell Dev. Biol. 9:810020. doi: 10.3389/fcell.2021.810020

Purpose: We constructed and characterized knockout and conditional knockout mice for KCNJ13, encoding the inwardly rectifying K^+ channel of the Kir superfamily Kir7.1, mutations in which cause both Snowflake Vitreoretinal Degeneration (SVD) and Retinitis pigmentosa (RP) to further elucidate the pathology of this disease and to develop a potential model system for gene therapy trials.

Methods: A Kcnj13 knockout mouse line was constructed by inserting a gene trap cassette expressing beta-galactosidase flanked by FRT sites in intron 1 with LoxP sites flanking exon two and converted to a conditional knockout by FLP recombination followed by crossing with C57BL/6J mice having Cre driven by the VMD2 promoter. Lentiviral replacement of Kcnj13 was driven by the EF1a or VMD2 promoters.

Results: Blue-Gal expression is evident in E12.5 brain ventricular choroid plexus, lens, neural retina layer, and anterior RPE. In the adult eye expression is seen in the ciliary body, RPE and choroid. Adult conditional Kcnj13 ko mice show loss of photoreceptors in the outer nuclear layer, inner nuclear layer thinning with loss of bipolar cells, and thinning and disruption of the outer plexiform layer, correlating with Cre expression in the overlying RPE which, although preserved, shows morphological disruption. Fundoscopy and OCT show signs of retinal degeneration consistent with the histology, and photopic and scotopic ERGs are decreased in amplitude or extinguished. Lentiviral based replacement of Kcnj13 resulted in increased ERG c- but not a- or b- wave amplitudes.

Conclusion: Ocular KCNJ13 expression starts in the choroid, lens, ciliary body, and anterior retina, while later expression centers on the RPE with no/lower expression in the neuroretina. Although KCNJ13 expression is not required for survival of the RPE, it is necessary for RPE maintenance of the photoreceptors, and loss of the photoreceptor, outer plexiform, and outer nuclear layers occur in adult KCNJ13 cKO mice, concomitant with decreased amplitude and eventual extinguishing of the ERG and signs of retinitis pigmentosa on fundoscopy and OCT. Kcnj13 replacement resulting in recovery of the ERG

c- but not a- and b-waves is consistent with the degree of photoreceptor degeneration seen on histology.

Keywords: retina, retinal dystrophy, snowflake vitreoretinal dystrophy, kcnj13/kir7.1, retinal degeneration

INTRODUCTION

Mutations in the inwardly rectifying potassium channel gene KCNJ13 have been shown to cause both snowflake vitreoretinal degeneration (SVD) (Hejtmancik et al., 2008) and Leber congenital amaurosis (LCA) (Sergouniotis et al., 2011). SVD, first described in 1974 by Hirose et al. (1974), is a vitreoretinal degeneration characterized by corneal guttae, cataract, fibrillar vitreous degeneration, and peripheral retinal abnormalities including characteristic small yellow-white dots, and sheathing followed by disappearance of retinal vessels, chorioretinal pigmentation and atrophy at later stages (Lee et al., 2003). LCA, the most severe form of retinal degeneration, shows severe visual impairment and retinal dysfunction in the first year of life, with night blindness and constricted visual fields often accompanied by nystagmus. While these retinal diseases have some overlapping features, they are distinguished by the relatively preserved vision and the higher frequency of vitreal changes in SVD. It appears that the autosomal dominant inheritance pattern of SVD due to the Kir7.1 R162W mutation probably results from depolarization of the resting membrane potential of the RPE by the mutant protein, perhaps exacerbated by insertion of R162W mutant Kir7.1 molecules into the tetrameric Kir7.1 channels in a partial dominant negative effect (Hejtmancik et al., 2008; Pattnaik et al., 2013; Zhang et al., 2013); while the autosomal recessive LCA phenotype results from a complete loss of channel function (Sergouniotis et al., 2011; Pattnaik et al., 2015; Perez-Roustit et al., 2017).

The Kcnj13 gene encodes Kir7.1, a K^+ channel belonging to the Kir family, a group of inwardly rectifying K^+-transport channels. Kir7.1, first described in 1998 (Krapivinsky et al., 1998), shows marked differences in both sequence and functional properties from other members of the Kir channel superfamily (Krapivinsky et al., 1998; Shimura et al., 2001). Kir 7.1 channels show low single channel conductance and low sensitivity to external Ba^{2+} blockade and are relatively independent of voltage and K+ concentration, whereas other members of the Kir family, which present strong inward rectification properties, primarily provide currents involving K^+ influx into cells (Hughes and Takahira, 1996; Krapivinsky et al., 1998; Shimura et al., 2001). At hyperpolarized membrane potentials, Kir7.1 exhibits a large inward K^+ current, but at physiological membrane potentials, the channel facilitates the efflux of intracellular K^+ (Krapivinsky et al., 1998; Shimura et al., 2001). Among other tissues including hypothalamic neurons in which it is regulated by the melanocortin-4-receptor (Ghamari-Langroudi et al., 2015), brain choroid plexus, lung, renal and intestinal epithelia and thyroid follicular cells (Döring et al., 1998; Ookata et al., 2000; Cornejo et al., 2018), Kir7.1 is present in the apical membrane of retinal pigmented epithelium (RPE) and the choroid, in which the Na^+/K^+-pump is also expressed apically (Hughes and Takahira, 1996; Shimura et al., 2001). Here, it is regulated by membrane phospholipids including phosphatidylinositol 4,5-biphosphate which is cleaved upon binding of oxytocin by the oxytocin receptor, a G protein-coupled receptor (Pattnaik and Hughes, 2009; York et al., 2017).

Since mutations in KCNJ13 were identified as a cause of SVD and LCA a number of approaches and model systems have been applied to verify causality and dissect the mechanisms and pathogenesis of these diseases. Mice with a loss-of-function Kcnj13 mutation were generated by N-ethyl-N-nitrosourea (ENU) mutagenesis and homozygotes were found to have neonatal lethal tracheal and smooth muscle defects (Yin et al., 2018). Similarly, mice in which the Kcnj13 gene locus was deleted were generated using VelociGene (Valenzuela et al., 2003) and found to die of respiratory and palatal deformities in the first day of life (Villanueva et al., 2015). Zhong et al. took advantage of mosaicism in CRISPR-mediated genomic indels of Kcnj13 in mice and were able to show that while RPE cells lacking Kir7.1 survived the underlying photoreceptors degenerated but could be rescued by nearby wild type or heterozygous RPE cells with an intact Kcnj13 gene (Zhong et al., 2015). They later used a Best1-cre conditional knockout of Kcnj13 in the retina, observing thinning of the outer nuclear layer and reduced light responses in mice with a high percentage of cells lacking the Kcnj13 gene (Roman et al., 2018) However, in this model Cre is expressed in only 10–90% of RPE cells, leading to patchy Kcnj13 expression in the conditional ko mouse retinas so that only 45% of the mice had a retinal phenotype. They were, however, able to overcome this in part by use of a TdTomato fluorescent indicator of Cre to select mice with high levels of Cre expression.

Here, we describe a Kcnj13 knockout mouse model with an initial 'knockout first' construct removing Kcnj13 universally with expression of beta-galactosidase as a marker followed by FLP recombination generating a conditional RPE specific conditional knockout using a VMD2-Cre mouse line. With these models we confirm the previous findings regarding Kcnj13 expression and the retinal phenotype of conditional ko mice, delineate early expression patterns of Kcnj13 in the mouse eye and brain and extend these to show complete loss of the photoreceptors including the outer nuclear layer, and outer plexiform layer accompanied by extinguished ERGs and fundus findings typical for retinal degeneration in mice with widespread absence of Kcnj13 expression. Finally, we show that replacement of Kcnj13 expression using recombinant Lentivirus can partially rescue potassium pump activity in the RPE and hence the ERG c-wave but not a- and b-wave amplitudes.

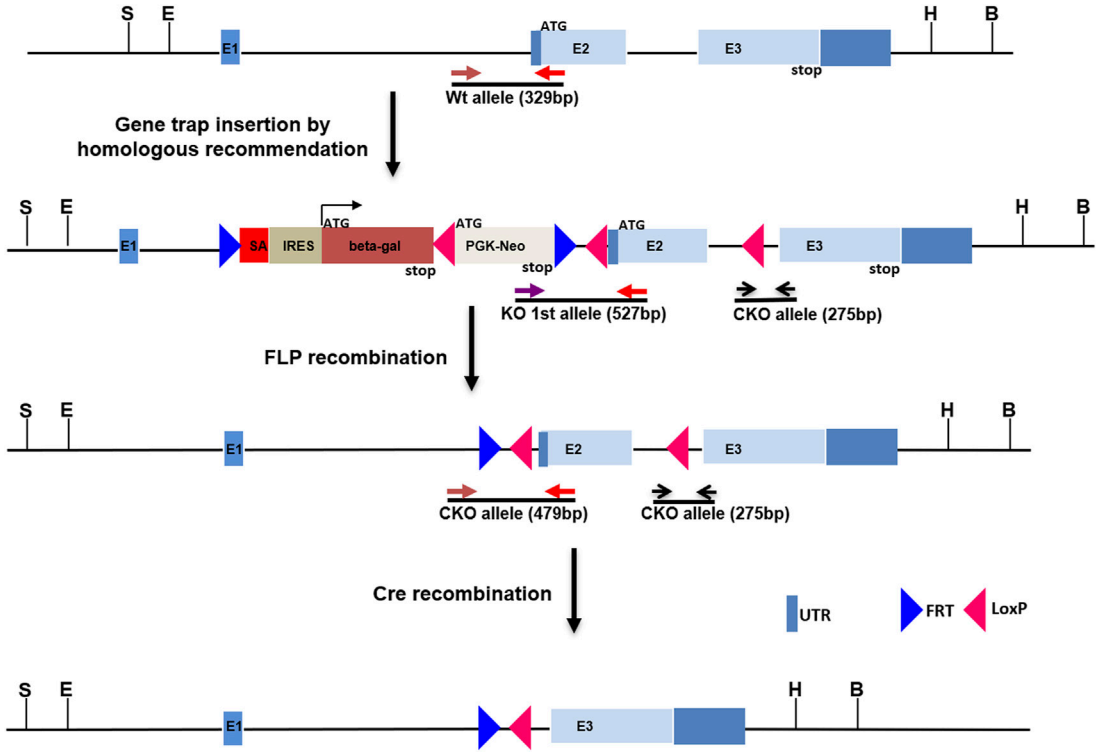

FIGURE 1 | Construction of Kcnj13 knockout alleles. For the knockout first (KO 1st) allele a cassette consisting of a splice acceptor followed by the beta-galactosidase gene, a LoxP site, and PGK-Neo and flanked by FRT sites is inserted into the first intron of the Kcnj13 gene and LoxP sites are inserted flanking Exon 2. The KO 1st allele is converted to a conditional knockout allele by FLP recombination leaving LoxP sites flanking exon 2, critical for Kcnj13 function, for removal in the presence of Cre. Positions of genotyping primers are shown.

MATERIALS AND METHODS

Generation of the Kcnj13 Knockout First Allele and Subsequent Conversion to Conditional Knockout Allele

All animal procedures were approved by the Institutional Animal Care and Use Committee (IACUC) of the National Eye Institute and the University of Wisconsin- Madison. The Kcnj13 knockout (KO) first allele was constructed with classic homologous recombination in mouse R1 (SV129) embryonic stem (ES) cells by inserting an intron trap cassette consisting of a splice acceptor En2 followed by the β-galactosidase gene (PMID: 1592261) downstream of exon one of the Kcnj13 gene. LoxP sites were included as well flanking Exon two of the gene (**Figure 1**). Homologous recombination of the intron trap cassette at the target locus created a KO allele first which disrupted splicing of Kcnj13 mRNA by trapping upstream exon onto En2 splicing acceptor. As a result, the beta-gal coding sequence is rendered under the control of Kcnj13 locus and can be used as a reporter, tracking expression pattern of the target gene. Upon removal of the intron trap cassette by FLP recombination, the KO allele is converted to a conditional allele of Kcnj13 gene as diagrammed in **Figure 1**. Germline transmission was readily achieved and the F1 founders with the KO first allele were crossed back into the C57bl6/j background in several generations until they reached a congenic state. For postnatal studies the KO first allele was converted to a conditional RPE knockout allele by crossing to an RPE-specific VMD2-Cre line.

Genotyping of both KO first and conditional alleles were conducted by genomic PCR with primers listed in **Supplementary Table S1**.

DNA Sequencing

Constructs and modifications to the Kcnj13 gene were amplified using primers shown in **Supplementary Table S1**. PCR reagents included: 10x PCR buffer: 1.0 ul, Mg2+ 0.6 ul, dNTP 0.5 ul, 10 pm primer 0.5 + 0.5 ul. Taq 1 u, DNA 40 ng, H2O up to 10 ul. Cycling including a touchdown PCR reaction for the first 15 cycles: 94 °C for 4 min, followed by decreasing the annealing temperature from an initial 64 °C in a stepwise fashion by 0.5 °C every second cycle. For the later 20 cycles: 94 °C for 40 sec, 57 °C for 30 sec and 72 °C for 1.5 min, and finally a prolonged elongation step at 72 °C for 10 min. PCR product was purified and analyzed by Sanger sequencing using an ABI 3130 sequencer with Big Dye Terminator Ready reaction mix according to the manufacturer's instructions (Applied Biosystems, Foster City, CA). Sequencing results were analyzed using Mutation Surveyor v3.30 (Soft Genetics, State College, PA) or DNASTAR Navigator 17 (DNASTAR, Madison, WI).

Histology

Mice were euthanized by CO_2 inhalation after ERG data acquisition, and each eye was washed immediately with 1×PBS (Life Technologies, United States) and 10% neutral buffered formalin (Sigma-Aldrich, United States). The eyes were fixed for 48 h in formalin and processed for histological analysis. The tissue was embedded in paraffin, and 3 μm sections were prepared using a Microtome. The sections through the pupillary-optic nerve axis were deparaffinized, hydrated, and finally stained with Hematoxylin and Eosin (H&E). Five fields per section were selected for examination using an Olympus BX-51 microscope (Olympus, United States), while three sections (30 μm apart) from each eye (n = 3 mice per group) were used for analysis.

Beta-Galactosidase Staining

β-galactosidase staining was performed by following an established protocol. For staining of mouse embryos, embryos of E11.5 to E15.5 were isolated in cold PBS, and switched to 4% paraformaldehyde (PFA) in 1x PBS on ice for 30 min and then washed in PBS for 5 min at room temperature. Embryos were incubated in β-galactosidase staining solution (1 mg/ml X-gal dissolved in dimethylformamide, 4 mM K4 Fe(CN)6.3H2O, 4 mM K3Fe(CN)6, 2 mM MgCl2) overnight at room temperature in the dark, washed 3 times for 15 min each in PBS, and further fixed in 2% paraformaldehyde with 2% glutaraldehyde.

β-Galactosidase staining of frozen sections was performed as follows. Embryos were pre-fixed in 4% PFA on ice for 30 min and embedded in OCT. Frozen sections were cut at 30–50 μm and placed on slides. After drying, slides were stained with the same β-galactosidase staining solution at 37°C for up to 30 min, washed in PBS for 5 min at room temperature, and mounted with mounting medium and cover slips and viewed under a Nikon microscope.

Fundus Photography of Mouse Retinas

Funduscopic examinations of nine-month- old KCNJ13CKO ko/ko/ VMD2-Cre +/+ and KCNJ13CKO ko/ko/ VMD2-Cre −/− control mice (age and sex matched) were anesthetized with a mixture of xylazine (6 mg/kg) and ketamine (100 mg/kg), and pupils were dilated with a topical drop of tropicamide and phenylephrine. After pupil dilation, lubricant eye gel (Alcon) was applied to the cornea. Fundus images were captured by Micron III fundus camera (Phoenix Research Laboratories, Inc., Pleasanton, CA).

Immunofluorescent Assessment of Mouse Retinas

Mouse eyes were fixed in 4% paraformaldehyde in 1x PBS for 2 h. After embedding in Optimal Cutting Temperature (OCT) (Tissue-Tek, Torrance, CA) with appropriate orientation to allow cutting of sagittal sections, the eye was cut into frozen sections of 10 μm thickness and cryosections were permeabilized with 0.3% Triton X-100 in PBS, the sections were blocked with blocking buffer (PBST, 5% BSA, 1% goat or donkey serum) for 1 h at room temperature. The sections were then incubated in a humidified chamber to prevent evaporation with primary antibodies overnight at room temperature. After three washes in PBST for 15 min each, sections were incubated with the corresponding secondary antibodies at room temperature for 1.5 h followed by three PBST washes and finally staining with DAPI (Sigma-Aldrich, (United States) for 15 min. Five fields per section were selected for examination using a confocal laser scanning

microscope (Zeiss LSM 700, Carl Zeiss Inc, Thornwood, NJ), while three sections (30 μm apart) from each eye (n = 3 mice per group) were used for analysis. Antibodies used were 1:200 mouse anti-Kir7.1 (C-12, Santa Cruz Biotechnology) and 1:200 rabbit anti-Cre (Novagen #69050-3, Millipore Sigma). Secondary antibodies 1:300 Alexa Fluor555 donkey anti-mouse and 680 donkey Anti-rabbit IgG. F-actin was labeled by incubating for 4 h with phalloidin1:500(Invitrogen) to enable visualization of RPE cell morphology. Rod bipolar cells were visualized with anti-PKCα (Invitrogen).

Optical Coherence Tomography

OCT was performed using a Spectralis multi-modality diagnostic imaging system (Heidelberg Engineering). The system has a platform designed for easy orientation and aligning of mice for retinal imaging and provides a resolution of 2 μm. The mice were anesthetized by intraperitoneal injection with a mixed solution of ketamine and xylazine. The pupils were dilated with 1% tropicamide eye drops prior to imaging. Radial volume scan (centered on the optic disc, consisting of 100 B-scans) was acquired using image analysis software provided by Spectralis.

Mouse Electroretinography

Electroretinography (ERG) responses were recorded for seven-month-old Kcnj13 Cre homozygous KO and control mice (age- and sex-matched) using an Espion E2 system (Diagnosys. Lowell, MA). Briefly, the mice were dark adapted for 12 h before the ERG examination. Prior to the scotopic examination, mice were anesthetized under red light by intraperitoneal injection of ketamine and xylazine. Additionally, Proparacaine hydrochloride ophthalmic solution (0.5%) was used to anesthetize the cornea while tropicamide (1%) and phenylephrine hydrochloride (2.5%) solutions were used to dilate the pupil. Flash ERG recordings were obtained simultaneously from both eyes using gold wire loop electrodes, with the reference electrode placed in the animal's mouth and the ground subdermal electrode at the tail. ERG responses were obtained at increasing light intensities over the ranges of 1×10^{-4}–10 cd s/m^2 under dark-adapted conditions, and 0.3–100 cd s/m^2 under a background light that saturates rod function. The stimulus intervals between flashes varied from 5 s at the lowest stimulus strengths to 60 s at the highest ones. Two to ten responses were averaged depending on flash intensity. ERG signals were sampled at 1 kHz and recorded with 0.3 Hz low-frequency and 300 Hz high-frequency cutoffs. For acquisition of c-wave, the eyes were flashed with light intensities of 25 cd s/m^2 for 4 s. Analysis of a-wave and b-wave amplitudes was performed using a customized version of Espion

TABLE 1 | Survival of Kcnj13 knockout first and conditional knockout mice identified at increasing gestational ages and surviving to adulthood. No knockout first homozygous mice were identified after E15.5.

Genotype	Knockout first allele					Conditional allele
	adult	E18.5	E15.5	E14.5	E12.5	adult
	# pups (%)	# pups (%)	#pups (%)	#pups (%)	#pups (%)	#pups (%)
WT	95(43%)	6 (46%)	13 (52%)	1 (14%)	9 (32%)	3 (27%)
Heterozygous	128 (57%)	7 (54%)	12 (48%)	5 (72%)	11 (39%)	6 (55%)
Homozygous	0	0	0	1 (14%)	8 (29%)	1 (9%)[a]
Total	223	13	25	7	28	11

[a]*While additional mouse litters were not genotyped for segregation analysis, a large number of KCNJ13CKO ko/ko, VMD2-Cre +/+ mice were bred for further functional and histological studies.*

ERG Data Analyzer software (v2.2) that digitally filters out high-frequency oscillatory potential wavelets. Statistical significance between two groups, was assessed by Student's t-test. The level of significance was chosen to be $p = 0.05$ using GraphPad Prism 7 (GraphPad Software, San Diego, CA).

Gene Therapy of Kcnj13 Ko Mouse

Gene therapy was performed on conditional knock out mice of either sex that showed no c-wave when ERG was screened at 4 weeks of age. The a- and b-waves of these mice were either completely absent or had a small amplitude. An intraperitoneal injection of a Ketamine (80 mg/kg)/Xylazine (16 mg/kg) cocktail was used to anesthetize these animals. The eyes were dilated with 1% tropicamide solution after being anesthetized with 0.5% proparacaine HCl. Before the injection, the mice were placed on a heating pad that was maintained at 37°C. The injections were carried out using UMP3 ultramicropump with a Nanofil syringe and RPE-KIT (World Precision Instruments, Sarasota, FL) while the mice were under the surgical microscope. These mice were injected with lentiviruses containing the Kir7.1 gene, which was tagged with GFP protein at the N-terminus and was either driven by the Ef1a promoter or the VMD2 promoter (VectorBuilder Inc., Chicago, IL). As a control, buffer was injected without the viral particles. The formation of the bleb was used to determine whether or not the injection was successful. The transduction of the RPE with lentivirus was confirmed by imaging RPE fluorescence using a Nikon C2 confocal microscope (Nikon Instruments Inc.) 4 weeks after the injection. ERGs were performed on the treated mice 1, 2, and 4 weeks after injection.

RESULTS

In order to investigate further the pathophysiological role of KCNJ13 mutations in snowflake vitreoretinal degeneration (SVD, MIM 193230) and Leber congenital amaurosis (LCA16, MIM 614186) a knockout mouse model was constructed by inserting a gene trap cassette in intron 1, which consisted of a splice accepter (SA) followed by IRES and beta galactosidase sequences. The gene trap cassette is flanked by FRT sites and the gene trap targeting vector is constructed so that exon two of the Kcnj13 gene is flanked by LoxP sites (**Figure 1**). This intron gene trap disrupted splicing of the target gene by forced splicing of the exon one transcript to the SA forming an exon1-SA fused transcript. Expression of beta-galactosidase driven by the Kcnj13 promoter was then be detected by Blue-gal assay. As has been reported (Villanueva et al., 2015), while heterozygous mice showed no obvious differences from wild type, no homozygous knockout mice were seen in any litters. However, while previous reports documented liveborn knockout pups that died shortly after birth (Villanueva et al., 2015; Zhong et al., 2015; Yin et al., 2018), in this study no homozygous ko mice were detected at or after E15.5 (**Table 1**), strongly suggesting that death occurred before E15.5 ($p \leq 0.0075$).

Galactosidase staining was apparent in intact E12.5-day embryos in the eye lens, the choroidal plexus of the fourth and fifth ventricles of the brain, and the anterior retina (**Figure 2**). It increases by E15, being present to a lesser extent in other parts of the embryos. In addition, the Kcnj13 KO 1st homozygous embryos were smaller than the heterozygous or homozygous wild type embryos at this stage. The localization of Kcnj13 expression at E 12.5 was confirmed by examination of tissue sections stained for β-galactosidase. Notably, Blue-gal staining was apparent in sections of the anterior retina near the presumptive ciliary body and especially those cells adjacent to the presumptive vitreous and choroid but not the posterior regions of the retina (**Figures 3A–C**). Staining is also prominent in the choroid plexus of the lateral, third, and fourth ventricles (**Figures 3D–I**), and the primary fiber cells and to a lesser extent the anterior epithelia of the lens (**Figures 3A–C**). Because the Kcnj13 KO is lethal before E15.5, β-galactosidase localization and staining of adult mice could only be carried out in heterozygotes (**Figures 4A–D**). These sections show strong β-galactosidase staining in the retinal pigment epithelial cells (RPE) across the retina, and the ciliary body but not in the photoreceptor layers adjacent to the RPE (**Figures 4A,C**).

Because the embryonic lethality in the absence of Kcnj13 prevented detailed examination of the pathological processes in the retina, the KO 1st allele was converted to a conditional knockout allele by FLP recombination (**Figure 1**). Mice homozygous for the conditional knockout allele with LoxP sites flanking exon two were crossed with a RPE specific VMD2-Cre line (Iacovelli et al., 2011) to generate mice heterozygous for the KO 1st allele. Mice of the next generation homozygous for the KO 1st allele and the VMD 2 Cre allele showed Cre expression in up to 90% of RPE cells with greatly decreased or absent expression of Kir7.1 (**Figures 5A,B**). In

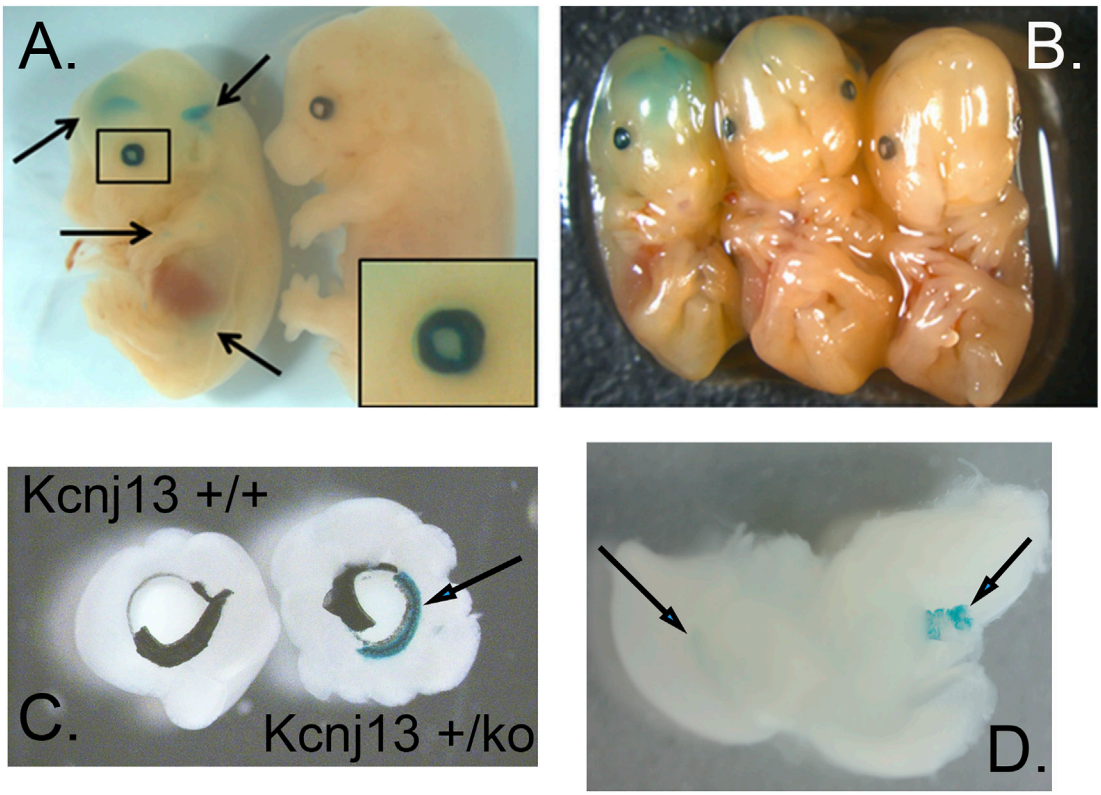

FIGURE 2 | Expression of Kcnj13 as monitored by β-galactosidase expression from the ko1st allele in E13.5 mouse embryos. **(A,B)** Whole mount showing β-gal staining in cerebral ventricles and the eye. Arrows show the lateral and third ventricles as well as lower diffuse expression in other tissues, and the enlarged box shows expression in the eye, including the lens. Note that the homozygous embryo on the left is slightly smaller than the heterozygous [**(B) middle**] or wild type [**(A,B) right**] embryos. **(C)** Beta-gal staining of the anterior retina and ciliary body revealed after peeling of attached iris. **(D)** Beta-gal staining seen in the lateral ventricle (left arrow) and choroid plexus of the 4th ventricle (right arrow).

control mouse retinas where no Cre is present, there is widespread expression of high levels of Kir7.1 (**Figure 5A**, top row). In some CKO mice Cre is expressed at intermediate levels in the RPE as estimated by fluorescence intensity (**Supplementary Figure S1A**) and there is spotty expression of Kir7.1, including in some cells expressing Cre. As has been reported (Keeling et al., 2020), many of the RPE cells are binucleate. In the majority of cKO mouse retinas, which showed high levels of Cre expression by fluorescence intensity, there is a complete absence of Kir7.1 expression (**Figure 5A**, bottom row). In the retinal sections shown in **Figure 5B**, while Kir7.1 staining is seen in the choroid in both the KCNJ13CKO ko/ko, VMD2-Cre −/− and KCNJ13CKO ko/ko, VMD2-Cre +/+ mice (top and bottom rows, respectively), it is only seen in the apical surface of the RPE, above the RPE nuclei indicated by arrows, in the KCNJ13CKO ko/ko, VMD2-Cre −/− mice shown in the top row. In comparison to the images in the Cre$^-$ top row, there appears to be some irregularity in the size and shape of the RPE cell outlines, with occasional open areas that appear to be formed by fusion of adjacent RPE cells. These contain multiple nuclei, some of which are small and irregularly shaped, suggesting pyknosis. This is confirmed by the phalloidin and Cre stained retinal sections shown in **Figure 5D**, in which the RPE in the Cre$^-$ retina appears as a regular array of healthy cuboidal epithelial cells. In contrast, those in the Cre$^+$ retina have irregular and flattened shapes with uneven density of staining and smaller dense nuclei stained with Cre as well as condensation of the actin microfilament network.

Fundus photographs of wild type and Kcnj13 cKO mice are shown in **Figures 6A–D**. The top two panels, A. and B., show typical retinas from wild type mice with some retinal stippling but no specks or inclusions. The bottom two panels, C. and D., show typical fundi from a Kcnj13 cKO mouse, which have distinct inclusions, especially seen in the OS, and some attenuation of the retinal vessels. In some retinas, e.g., OD in panel 5C, the optic disc appeared pale, but this was not a consistent finding.

Retinal OCTs from Cre$^-$ mice show all retinal layers visible across the fundus with only a few hyperreflective foci in the nerve fiber layer (**Figure 6E**, top panel). The retina shown in the middle panel is from a cKO mouse with moderate Cre expression and shows an increased number of hyperreflective deposits in the NFL but with most of the retinal layers intact on the right and center. However, there is successive loss of the photoreceptor cells followed by the OPL in the left part of the retina. A more severely affected cko retina is shown in the bottom panel, having loss of the outer nuclear layer throughout but with preservation of the inner retinal layers including the NFL,

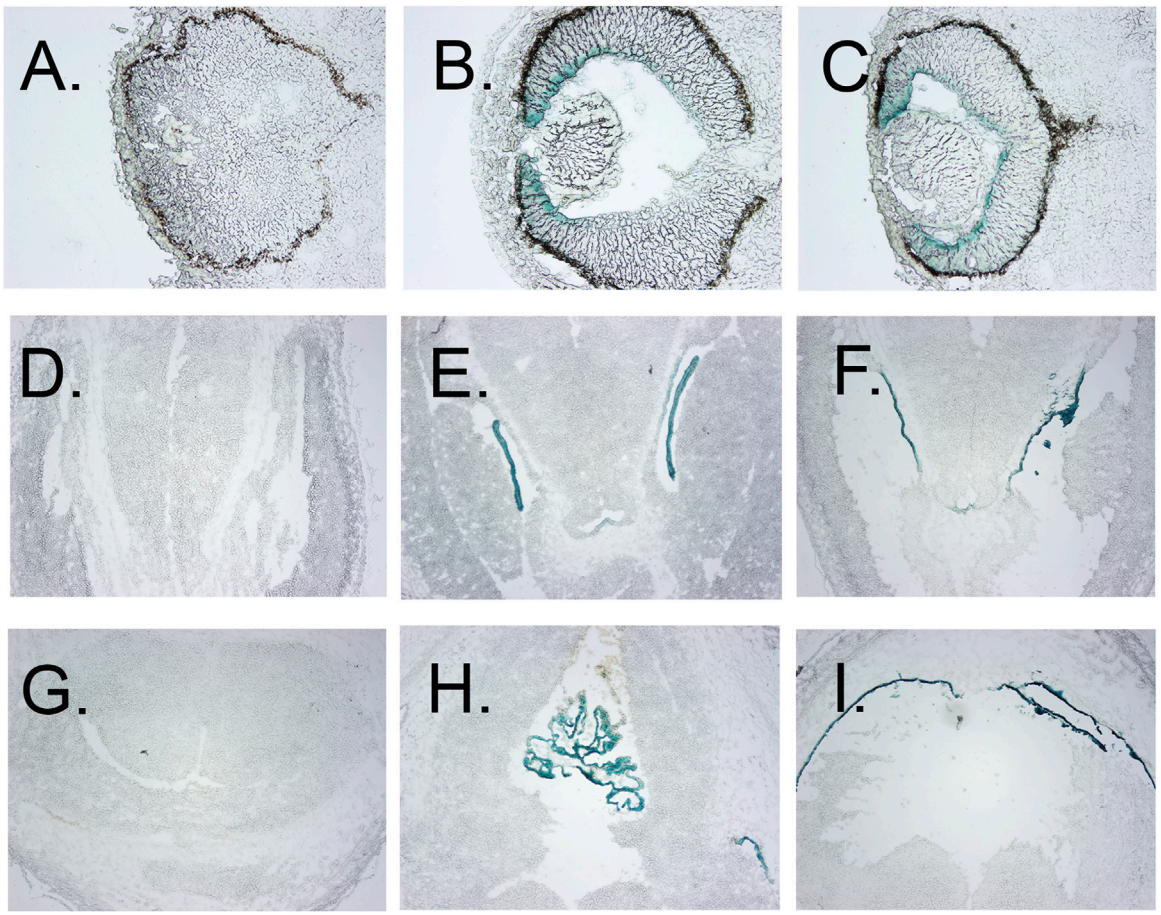

FIGURE 3 | Localization of β-gal staining in tissue sections. **(A–C)** β-Gal staining of eyes of E12.5 wt, heterozygous, and homozygous KO1st mice, respectively, showing staining of the anterior but not posterior retina, less in the lens primary nuclear fibers and even lighter staining in the anterior epithelia. **(D–F)** β-galactosidase staining of the choroid plexus of the lateral ventricles of E12.5 wt, heterozygous, and homozygous KO1st mice, respectively. I-K. β-galactosidase staining of choroid plexus of the third ventricle of E12.5 wt, heterozygous, and homozygous KO1st mice, respectively. showing staining in the areas of the primary nuclear fibers and lighter staining in the anterior epithelia. **(H)** Section through the lens of a wt control. **(I)** β-galactosidase staining of a section through the retina showing activity in the cells of the anterior but not posterior retina. J. Section through the retina of a wt control mouse.

GCL, IPL, and INL as well as the RPE and Bruch's membrane. Increased hyperreflective foci are also seen not only in the NFL but also in the RPE/Bruch's layer.

The effects of knocking out Kcnj13 on the retinal structure are shown in more detail in **Figures 4E–G**. **Figure 4E** shows an H&E-stained retina from a 9-month-old wild type mouse (Kcnj13CKO +/+, VMD2-Cre +/+) with good preservation of all retinal layers. **Figure 4F** shows a conditional ko (Kcnj13CKO ko/ko, VMD2-Cre +/+) retina with the retinal layers initially relatively well preserved on the left side of the optic nerve, but with more severe changes on the right and peripherally on both sides, while **Figure 4G** shows a conditional ko (Kcnj13CKO ko/ko, VMD2-Cre +/+) retina with severe changes throughout. The well-preserved retinal area in **Figure 4F** reflects a lack or lower level of Cre expression in that region (see above and **Figure 5A**; **Supplementary Figure S1**). The transition from the preserved retina immediately to the left of the optic nerve to the affected area farther left is particularly informative. Degeneration of the inner and outer segments of the photoreceptor layers can be seen, followed by loss of the outer nuclear layer. In contrast, the inner nuclear layer and the rest of the inner retina appear well preserved even in areas affected by retinal degeneration. In addition, the RPE itself is also preserved, although somewhat more widely and irregularly spaced, separated by clear lacunae and irregularly shaped hematoxylin positive material.

Confocal fluorescent microscopy of retinal sections from KCNJ13CKO ko/ko, VMD2-Cre −/− mice shows no Cre but Kir7.1 signal in the apical borders of the RPE (**Figure 5B**, top row, arrows), along with significant background shown by both the Cre and Kir7.1 antibodies. With Cre expression in the RPE (**Figure 5B**, bottom row, arrows) Kir7.1 staining in the apical borders of the RPE is decreased or absent, leaving only background staining of Bruch's membrane confirming the effectiveness of the conditional CRE ko on Kcnj13 expression.

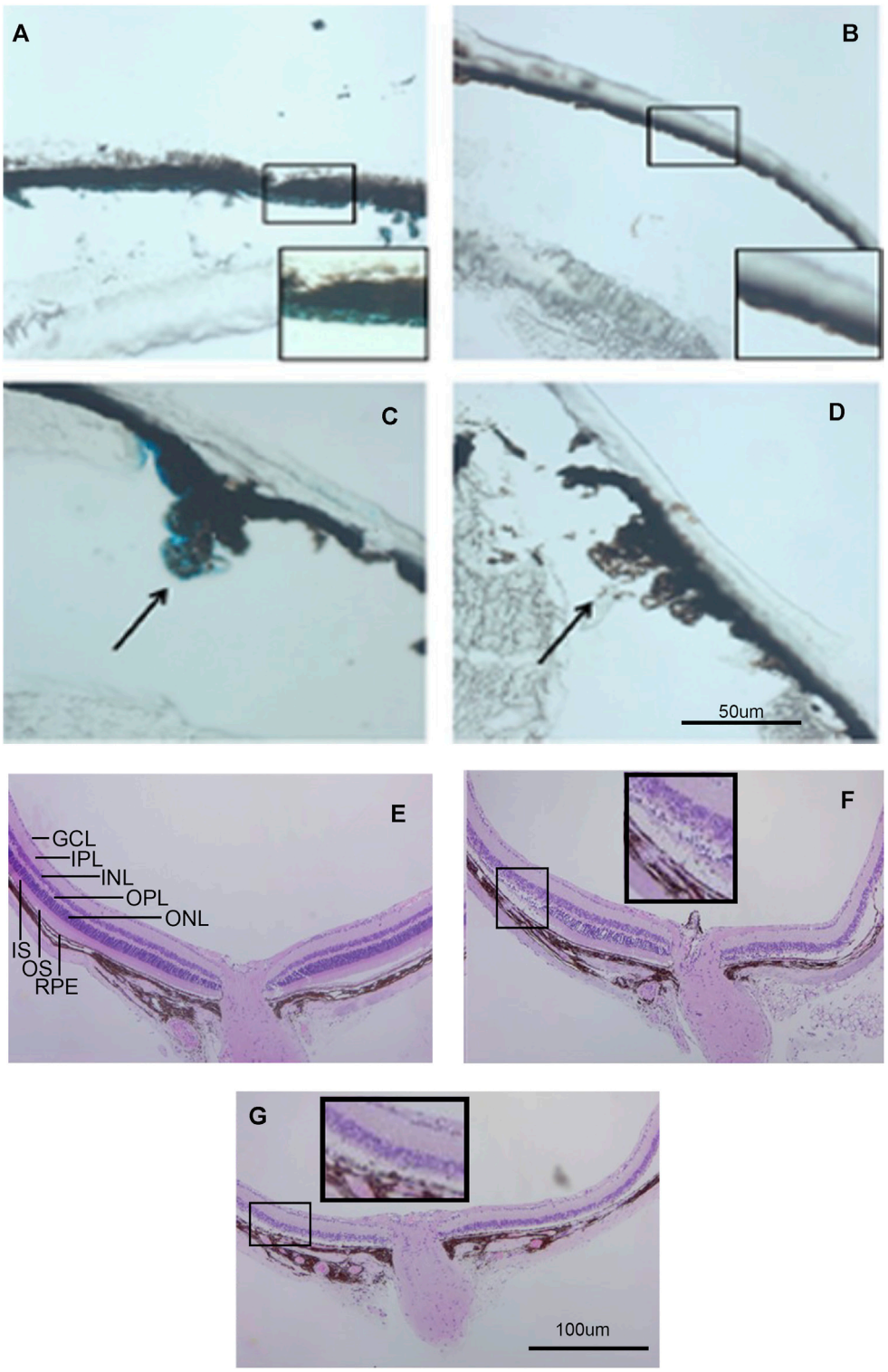

FIGURE 4 | Kcnj13 expression in adult mice. **(A)** β-gal staining of adult heterozygous mouse retina showing positive staining in the RPE. **(B)** β-gal staining of a wt control retina. **(C)** β-gal staining of the ciliary body in an adult heterozygous mouse tissue section. **(D)** β-gal staining of a wt control retina. **(E)** H&E-stained retinal section from a 6-month-old KCNJ13CKO ko/ko, VMD2-Cre –/– mouse. **(F)** H&E-stained retinal section from a 6-month-old homozygous KCNJ13CKO ko/ko, VMD2-Cre +/+ mouse showing loss of photoreceptor cells on the right side and preservation of retinal morphology on the left near the optic nerve. **(G)** H&E-stained retinal section from a 6-month-old homozygous KCNJ13CKO ko/ko, VMD2-Cre +/+ mouse showing severe retinal degeneration throughout the retina.

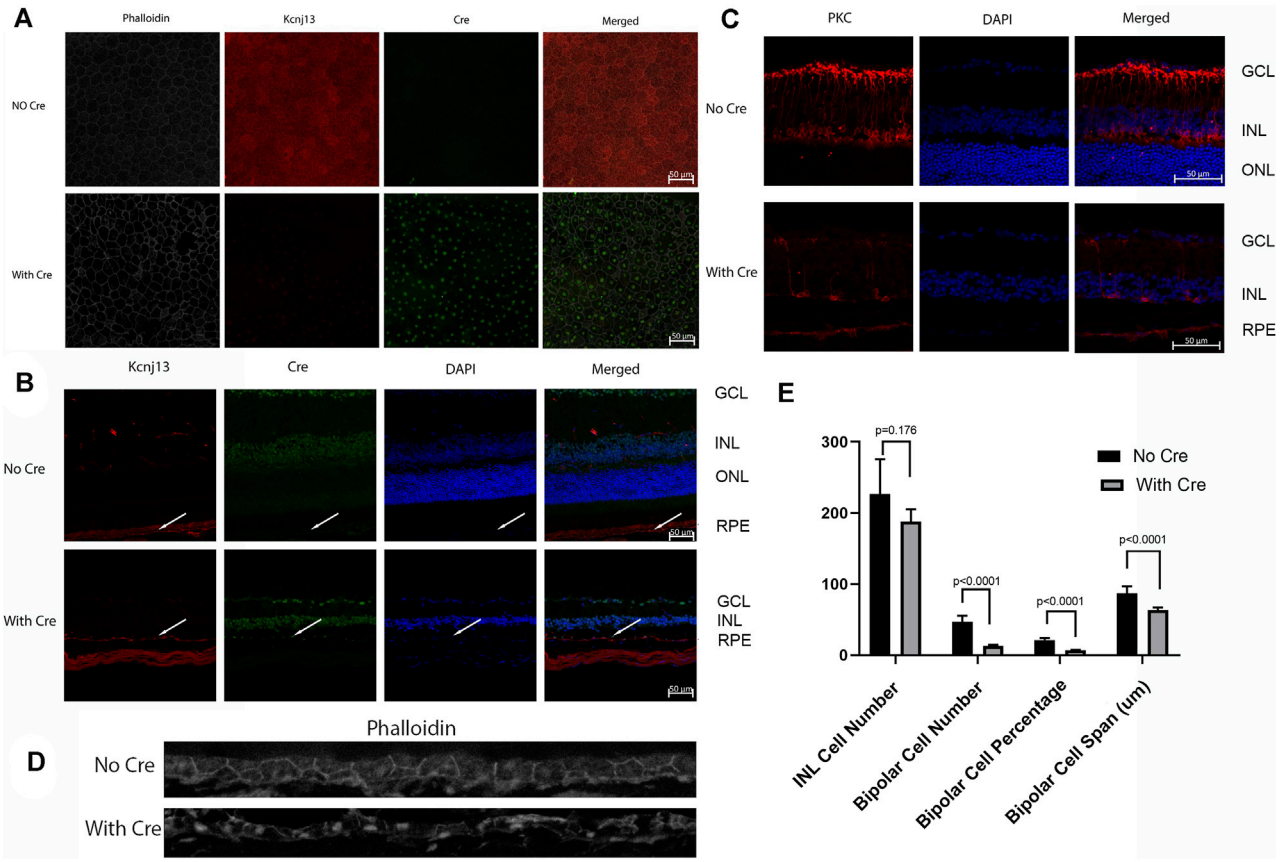

FIGURE 5 | Cre and Kcnj13 expression. **(A)** RPE flatmounts of 9-month-old KCNJ13CKO ko/ko, VMD2-Cre –/– (top row) and KCNJ13CKO ko/ko, VMD2-Cre +/+ mice with high expression of Cre (bottom row). The left column shows phalloidin stained flatmounts delineating the RPE cells, the second column shows Kcnj13 expression by immunofluorescence to Kir7.1, the third column shows Cre expression by immunofluorescence, and the right column shows an overlay of the first three images. **(B)** Confocal microscopy of retinal sections from 9-month-old KCNJ13CKO ko/ko, VMD2-Cre –/– mice (top row), KCNJ13CKO ko/ko, and KCNJ13CKO ko/ko, VMD2-Cre +/+ mice with high levels of Cre expression (bottom row). The first column shows Kcnj13 expression by immunofluorescence to Kir7.1, the second column shows immunofluorescence to Cre, the third column shows nuclei by DAPI staining, and the far-right column shows an overlay of the first three images. **(C)** Confocal microscopy of retinal sections from 9-month-old KCNJ13CKO ko/ko, VMD2-Cre –/– mice (top row), and KCNJ13CKO ko/ko, VMD2-Cre +/+ mice with high levels of Cre expression (bottom row). The first column shows rod bipolar cells as shown by immunofluorescence to PKCα, the second column shows nuclei by DAPI staining, and the far-right column shows an overlay of the first two images. **(D)** Phalloidin and Cre staining of the RPE sections in 9-month-old KCNJ13CKO ko/ko, VMD2-Cre –/– mice (top row), and KCNJ13CKO ko/ko, VMD2-Cre +/+ mice with high levels of Cre expression (bottom row) showing cellular disarray and some small dense nuclei. Fluorescent channels were collected sequentially to minimize potential cross-talk between channels. **(E)** Statistical analysis of nuclei and bipolar cell number, percentage, and span (INL) in **Figure 4C**. Note that the decrease in bipolar cell number and INL span are greater in **Figure 4B**, but the statistical estimates are taken from counts distributed across the entire retina rather than a limited section.

It is also noteworthy that the Kcnj13 cKO mouse retinas have lost the photoreceptor layer and much of the OPL, and that Kcnj13 staining is not seen at the apical surfaces of the RPE as in the control retinas (arrows). Use of an anti-mouse secondary antibody to detect the Kir 7.1 mouse primary results in background labelling of choroid due to presence of mouse IgG in this vascularized layer just below the RPE nuclei. The relationship between Cre expression and the absence of Kcnj13 expression can be seen more clearly in **Supplementary Figure S1B**. Here, Kir7.1 staining in the apical RPE above Bruch's membrane is evident in the control retinal sections without Cre expression shown in the upper row of panels. When Cre is expressed at high levels Kir7.1 is absent from the apical RPE (**Supplementary Figure S1B**, middle panels), and RPE nuclei can be seen to be expressing Cre. In contrast, retinas in which Cre expression is inconstant show patchy expression of Kir7.1 in the apical RPE (**Supplementary Figure S1B**, bottom panels). Here, RPE cells expressing Cre (arrows on the right and left of each panel) show no overlying apical Kcnj13 expression. In contrast, the center cell (middle arrow) does not express Cre and has patchy apical staining for Kir7.1 overlying the nucleus.

To investigate cell loss in the retina of the Kcnj13 cKO mice further, retinal sections were subjected to immunofluorescence confocal microscopy with antibody to PKCα, which serves as a marker for rod bipolar cells (RBCs) (Caminos et al., 2000). The top row of panels in **Figure 5C** shows the distribution of rod bipolar cells in a KCNJ13CKO ko/ko, VMD2-Cre –/– control mouse. The cell bodies occupy most of the outer row or, in

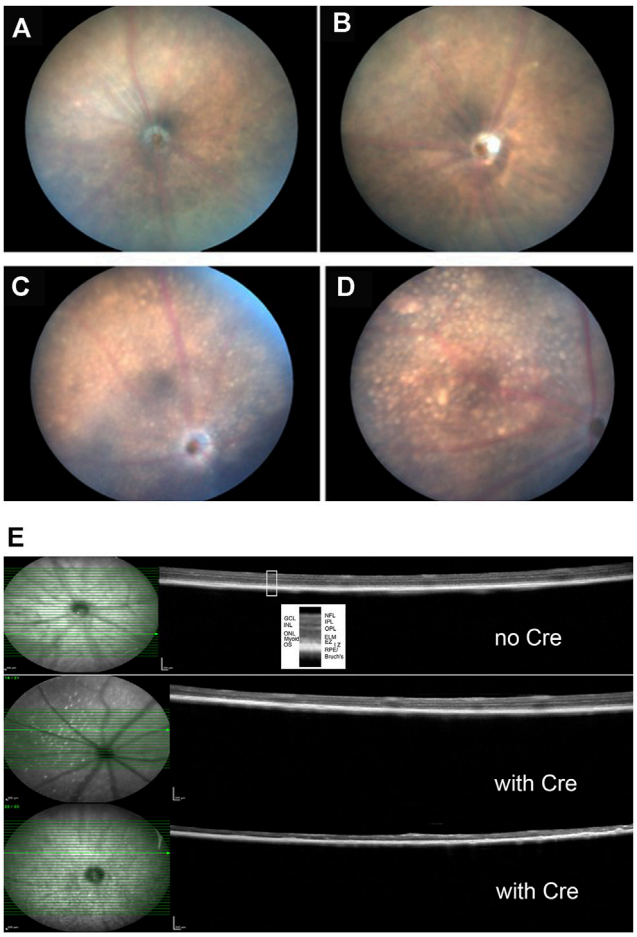

FIGURE 6 | Clinical and histological findings of Kcnj13 ko mice. **(A)** representative fundus photo of 9-month-old KCNJ13CKO ko/ko, VMD2-Cre –/– mouse OD **(B)** Representative fundus photo of KCNJ13CKO ko/ko, VMD2-Cre –/– mouse OS **(C)** Representative fundus photo of 9-month-old KCNJ13CKO ko/ko, VMD2-Cre +/+ mouse OD **(D)** Typical fundus photo of KCNJ13CKO ko/ko, VMD2-Cre +/+ mouse OS **(E)** OCT results showing loss of outer retinal layers in the KCNJ13CKO ko/ko, VMD2-Cre +/+ mice. Top: month old KCNJ13CKO ko/ko, VMD2-Cre –/– mouse retinal OCT shown as a control with all retinal layers visible. Middle: moderately affected 9-month-old KCNJ13CKO ko/ko, VMD2-Cre +/+ mouse retina with an increased number of hyperreflective deposits in the NFL but with most of the retinal layers intact on the right and center but showing successive loss of the photoreceptor layers followed by the OPL in the left part of the retina. Bottom: Severely affected 9-month-old KCNJ13CKO ko/ko, VMD2-Cre +/+ retina showing loss of the outer retinal layers throughout but with preservation of the inner retinal layers including the NFL, GCL, IPL, and INL as well as the RPE and Bruch's membrane. Increased hyperreflective deposits are also seen. Abbreviations: NFL, nerve fiber layer; GCL, ganglion cell layer; IPL, inner plexiform layer; INL, inner nuclear layer; OPL, outer plexiform layer; ONL, outer nuclear layer; ELM, external limiting membrane; Myoid, myoid component of the inner segment; EZ, ellipsoid zone of the inner segment; IZ, interdigitation zone of the outer segments and apical processes of the RPE; RPE, retinal pigmented epithelium; Bruch's, Bruch's membrane.

some places, two rows of the inner nuclear layer, with dendritic processes extending into the outer plexiform layer and their axons extending to the inner part of the inner plexiform layer with thick club-like branches abutting the outer layer of ganglion cells. Retinas in KCNJ13CKO ko/ko, VMD2-Cre +/+ mice show much less PKCα staining (**Figure 5C**, bottom row). As shown in the H&E-stained sections (**Figures 4E,F**), the OCT (**Figure 6E**), and retinal confocal sections (**Figure 5B**), the entire photoreceptor is absent, so that the inner nuclear layer abuts the RPE, which is seen as a single row of nuclei in the DAPI stained middle panel with some PKCα positivity, possibly background, in the choroid. There are only scattered cell bodies showing PKCα reactivity in the top row of cells of the inner nuclear layer, which as in **Figure 5B**, has the suggestion of being thinned and contain fewer nuclei, although this is not statistically significant in this section (**Figure 5E**). However, there are significant decreases in the number and percentage of bipolar cells as well as their span. These cells show no dendritic processes, and their axons are attenuated, showing fewer terminal branches, which also appear thinned. In addition, as it has been reported that zebrafish with the obdtd15 Kcnj13 mutation shows alterations in phagosomal clearance and mitochondrial area (Toms et al., 2019), mitochondrial staining with ATP5a in wt and Kcnj13 conditional ko mice was compared (**Supplementary Figure S2**). While no difference was observed in the density of staining between the ko and wt mice, there was a significant loss of length of the photoreceptor inner segments, both in absolute length and relative to the outer segments, which were relatively well preserved until late in the degenerative process. In addition, even with intermediate levels of Cre expression, shortening of the photoreceptor inner segments was accompanied by loss of photoreceptor morphology as seen in the middle row of **Supplementary Figure S2A** and progressively decreased thickness of the outer nuclear layer as shown in **Supplementary Figure S2A** and presented graphically in **Supplementary Figure S2B**. Similarly, no obvious differences were noted in the density of RPE phagosomes or mitochondria on EM (data not shown). These results are consistent with those seen in human iPSC-RPE cells (Shahi et al., 2019). These findings were equally present in male and female mice.

The morphological signs of retinal degeneration were accompanied by loss of visual function as shown in **Figure 7A**, which shows the a- and b-wave amplitudes of scotopic and photopic ERGs from Kcnj13 cKO Cre^{+} and Cre^{-} mice as they vary with flash energy. Both the scotopic and photopic Kcnj13 cKO Cre^{+} ERG a- and b-waves are extinguished, consistent with the loss of the entire photoreceptor layer shown in **Figures 4F**,G, **5B**,C, as well as the retinitis pigmentosa phenotype seen in humans with loss of function KCNJ13 mutations, or in some cases highly attenuated, consistent with the patchy degeneration seen in a relatively small group or mice (**Supplementary Figure S1**). Furthermore, when scotopic ERG was performed on Kcnj13 cKO Cre + mice, the amplitude of the c-waves that originate from the RPE cells was severely reduced (**Figure 7C** preinjected). When gene replacement therapy is carried out by subretinal delivery of lentivirus carrying the GFP-tagged Kir7.1 gene driven by either the EF1a or VMD2 promoters, GFP expression was

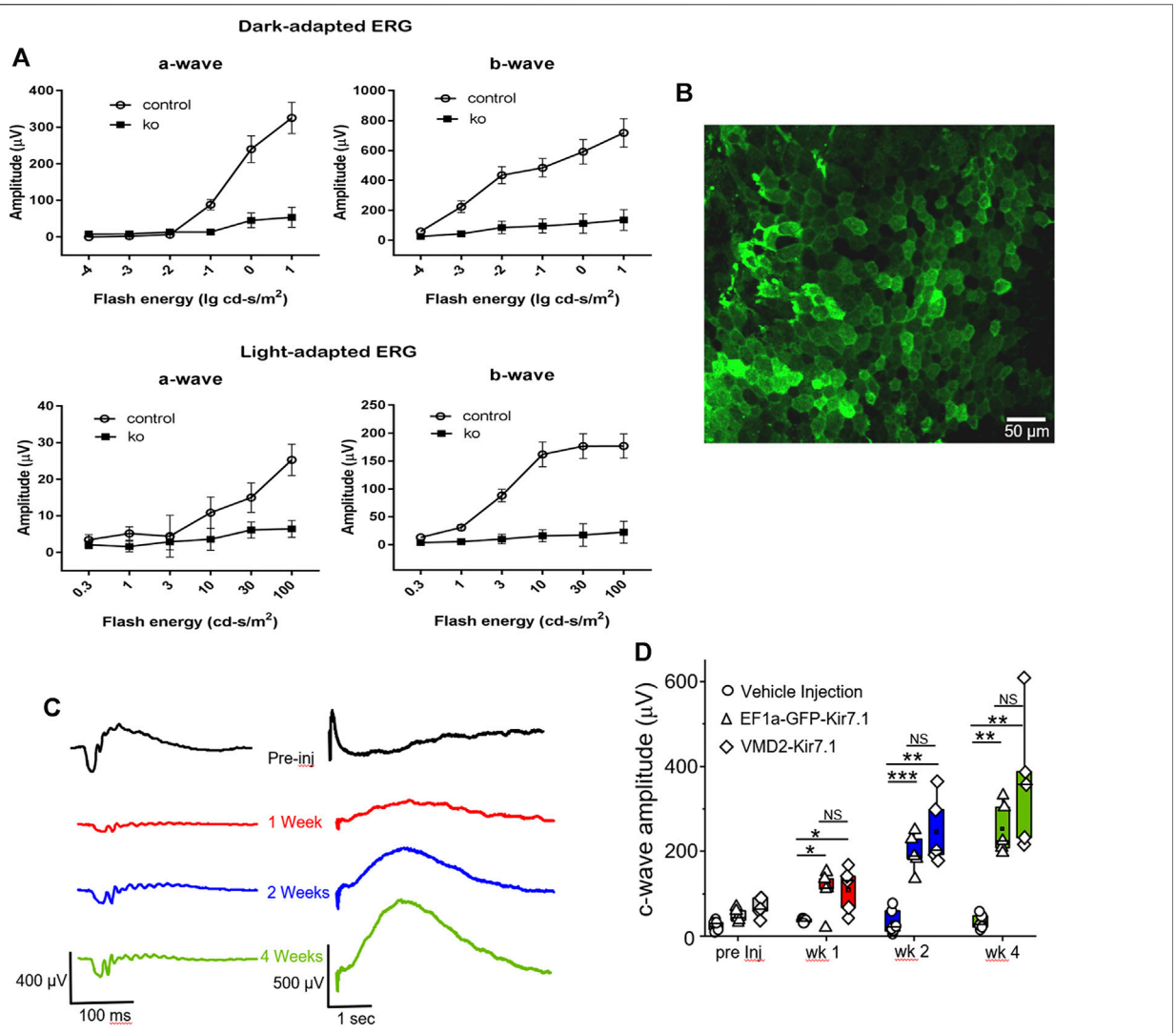

FIGURE 7 | Functional assessment and gene therapy of Kcnj13 ko mice. **(A)** Scotopic (top) and photopic (bottom) a-wave (left) and b-wave (right) ERG amplitudes of 6-month-old KCNJ13CKO ko/ko, VMD2-Cre +/+ (10 mice) and KCNJ13CKO ko/ko, VMD2-Cre +/+ (10 mice) mice. **(B)** Lentiviral transduction of RPE cells rescues the c-wave in the KCNJ13CKO ko/ko, VMD2-Cre +/+ knock out mice. Representative image of the RPE flat mount showing membrane localization of the Kir7.1 protein tagged with GFP 4 weeks after lentiviral transduction. **(C)** Representative ERG traces from KCNJ13CKO ko/ko, VMD2-Cre +/+ mice showing a-, b- and c-wave during pre-injection, week 1, week 2, and week 4 after lentiviral gene augmentation.**(D)** Comparison of the average plots of c-wave amplitude during the course of lentiviral transduction of RPE cells expressing Kir7.1 driven by either EF1a or VMD2 promoters or vehicle. NS: Not Significant; *$p < 0.05$; **$p < 0.005$; ***$p < 0.0005$.

observed in the RPE cells at 4 weeks after surgery (**Figure 7B**). The morphology of the RPE cells was preserved, and strong GFP fluorescence was observed with the Kir7.1 protein being trafficked to the membrane. The amplitude of the c-wave in mice transduced with lentivirus containing the KCNJ13 gene increased significantly after 2 weeks (**Figures 7C,D**), reaching roughly 5 times the pre-injection level by 4 weeks after injection, driven by either the EF1a ($p < 0.005$) or VMD2 ($p < 0.005$) promoters. Unlike the eyes injected with the virus, the eyes injected with the vehicle, as a control, had no change in the c-wave during any of the tested time points. (**Figures 7C,D**). Throughout this time period, the a- and b-waves show little increase, consistent with the complete degeneration of the photoreceptors seen in the histology and confocal microscopy results.

DISCUSSION

Here we investigated the implications of a lack of Kir7.1 function on the retina in a mouse conditional knockout model. Initially an unconditional knockout in which β-galactosidase was expressed from the Kcnj13 promoter was used, but no live embryos were detected after embryonic day 15, strongly suggesting that absence of Kir7.1 is an embryonic lethal in this strain, although other Kcnj13 knockout mice have been reported to survive to birth (Zhong et al., 2015; Yin et al., 2018). The importance of Kir7.1 for embryonic development is also emphasized by the smaller size of the homozygous Kcnj13 KO relative to heterozygous or wild type embryos. However, the relative importance of Kcnj13 expression for the eye is

demonstrated by the dense β-galactosidase staining in the embryonic eye relative to the remainder of the embryo. Embryonic expression of Kcnj13 is restricted to the anterior parts of both the neural retina and RPE, while it is expressed not only in the RPE, but also in the inner nuclear layer, nerve fiber layer, inner plexiform layer intensely in the internal limiting membrane in human adults (Hejtmancik et al., 2008). It is interesting that the region of high embryonic Kcnj13 expression will later form the ciliary body, which might explain the vitreal degeneration seen in snowflake vitreoretinal degeneration patients. Similarly, expression in the embryonic lens might also correlate with all SVD and KCNJ13 related arRP patients developing cataracts by early adulthood. The higher level of staining in central lens fiber cells relative to the anterior epithelial cells of the lens might reflect the amount of time over which the β-galactosidase protein has been accumulating as the epithelia differentiate into fiber cells, as Kcnj13 mRNA levels are higher in the epithelia than fibers in both the mouse and chick (Hawse et al., 2005; Hoang et al., 2014).

In conditional knockout mouse retinas, Kcnj13 expression in the RPE is expected to be eliminated by Cre expression. However, this correlation is not perfect, and in some retinas a few RPE cells expressing Cre also show residual Kcnj13 expression, presumably due to lower than threshold level of Cre expression in these cells. This is consistent with preservation of reduced ERG expression in a subset of KCNJ13CKO ko/ko, VMD2-Cre +/+ mice. In addition, it has been shown recently that Cre expression with this model shows some leakiness with expression in other retinal cells than the RPE (Chen et al., 2021; Choi et al., 2021). This is also apparent in **Figure 5B**, in which Cre expression is seen not only in the RPE but also the GCL and INL. However, as Kcnj13 is not expressed in those cells, as also shown in **Figure 5B**, this should not affect the results seen in this mouse model.

Overall, however, lack of Kcnj13 expression in the overlying RPE caused degeneration of the subjacent photoreceptors. This was accompanied by loss not only of the outer nuclear layer, but also the outer plexiform layer as shown by the loss of dendritic processes of rod bipolar cells. This loss of the outer retinal structures with relative preservation of the inner retina is seen on OCT and recapitulates, to some degree, that seen in human LCA resulting from a homozygous c.722T > C p.(Leu241-Pro]) KCNJ13 mutation (Sergouniotis et al., 2011). The inner nuclear layer also is thinned and shows loss of most of the bipolar cell bodies. Those rod bipolar cells that remain not only have lost their dendritic processes, but their axons also appear to be degenerating, with loss of their normal morphology. While the original insult to the photoreceptors certainly results from the failure to maintain potassium homeostasis in the subretinal space (Shahi et al., 2017), the damage is probably compounded by the general degeneration of the outer retina resulting in toxic debris secondary to the photoreceptor death. That this is the case is also suggested by the toxic changes evident in the RPE cells themselves. Given the extensive damage done to the outer retina, it is not surprising that rescue of Kcnj13 expression in the RPE is not accompanied by complete recovery of the a- and b-wave amplitudes, but does show recovery of the c-wave, which is generated by the RPE, at least in rodents (Perlman et al., 1995).

A comparable retinal degeneration model is the RCS rat, in which the RPE is unable to phagocytize rod outer segments as they are shed, due to a mutant Mertk causes photoreceptor degeneration with preservation of the gross structure of the inner retina (Ball et al., 2003). However, the inner retina does show reactive changes in Müller cells and altered branching patterns in bipolar and horizontal cells. However, cone bipolar cells in this model show increased expression of recoverin with an overall normal organization but atrophy of rod bipolar cell terminals but preservation of cell numbers and axonal projections. These differences might relate to the more chronic and progressive nature of retinal degeneration in the RCS rat relative to that in the Kcn13 cKO mouse and expression of PKCα in rod but not cone bipolar cells (Pan, 2000).

Thus, these results show that while the inwardly rectifying potassium channel Kcnj13 is responsible for maintaining potassium and ionic balance across the RPE, the importance of this goes well beyond facilitating light stimulated discharge of the photoreceptors and is necessary for their survival. In this sense, the downstream pathophysiology of Kcnj13 based retinal degenerations is similar to those of other causes of retinitis pigmentosa, causing photoreceptor or RPE cellular damage and death more directly. While this conditional knockout mouse as a loss of function mutation models autosomal recessive retinitis pigmentosa (Sergouniotis et al., 2011; Pattnaik et al., 2015), it seems likely that the downstream pathophysiology of the c.484C > T, p.(R162W) mutation implicated in snowflake vitreoretinal degeneration might be similar (Hejtmancik et al., 2008). However, that mutation results in depolarization of the resting membrane potential (Hejtmancik et al., 2008; Pattnaik et al., 2015) and might also act in a dominant-negative fashion to inhibit normal Kir7.1 channel function at least partially, either or both of which could explain the dominant inheritance pattern of snowflake vitreoretinal dystrophy (Zhang et al., 2013; Pattnaik et al., 2015). While it will require additional detailed future studies, it seems possible that partial preservation of the inwardly rectifying potassium channel activity in heterozygotes with the R162W change might contribute to the somewhat milder retinal changes in SVD, while depolarization of the resting membrane potential might be responsible for the vitreous changes, which are not seen to this degree in the arRP and LCA cases (Lee et al., 2003; Sergouniotis et al., 2011; Perez-Roustit et al., 2017).

In conclusion, we have used a conditional Kcnj13 knockout mouse model to explore the retinal pathophysiology of KCNJ13 based retinal degenerations, confirming and extending previous observations. Early embryonic expression patterns of Kcnj13 fit well with the characteristics of SVD, LCA, and arRP resulting from mutations in KCNJ13. While the initial insult of these mutations is the documented loss of inwardly rectifying potassium channel activity, coupled in the case of SVD with the leakiness of the mutant Kir7.1 channel, the final pathology

appears to be the death of the retinal photoreceptors with attendant degeneration of the entire outer retina, similar to that of other many retinal degenerations.

DATA AVAILABILITY STATEMENT

The original contributions presented in the study are included in the article/**Supplementary Material**, further inquiries can be directed to the corresponding author.

ETHICS STATEMENT

The animal study was reviewed and approved by the Institutional Animal Care and Use Committee (IACUC) of the National Eye Institute and the University of Wisconsin- Madison.

AUTHOR CONTRIBUTIONS

XDJ, BRP, and LD and JFH conceived and planned this project. XDJ, ZM, JL, PL, XC, PKS, C-CC, RF, LD and BRP carried out genotyping and haplotyping, generation of the mouse models, histological and confocal microscopy, fundus photography, ERG and OCT analysis, and gene therapy experiments. JFH, XDJ, C-CC, RF, BRP, and LD wrote and edited the manuscript and composed figures.

FUNDING

This work was supported in part by National Eye Institute Project EY000272-29.

SUPPLEMENTARY MATERIAL

The Supplementary Material for this article can be found online at: https://www.frontiersin.org/articles/10.3389/fcell.2021.810020/full#supplementary-material

Supplementary Figure S1 | Inverse relationship between Cre and Kcnj13 expression. **(A)** RPE flatmounts of 9-month-old KCNJ13CKO ko/ko, VMD2-Cre –/– (top row) and KCNJ13CKO ko/ko, VMD2-Cre +/+ mice with spotty intermediate expression of Cre (bottom row). The left column shows phalloidin stained flatmounts delineating the RPE cells, the second column shows Kcnj13 expression by immunofluorescence to Kir7.1, the third column shows Cre expression by immunofluorescence, and the right column shows an overlay of the first three images. Note that Kcnj13 expression occurs in some RPE cells expressing Cre, but it tends to be at lower levels than those in KCNJ13CKO ko/ko, VMD2-Cre –/– mice. **(B)** Confocal microscopy of retinal sections from 9-month-old KCNJ13CKO ko/ko, VMD2-Cre –/– (top row), KCNJ13CKO ko/ko, VMD2-Cre +/+ mice with high levels of Cre expression (middle row), and KCNJ13CKO ko/ko, VMD2-Cre +/+ mice with spotty Cre expression. Note the absence of Kcnj13 staining in the basal surface of the RPE (above the nuclei) in the middle row absence of Kcnj13 staining in the basal surface of the RPE (above the nuclei) in the middle row and the presence of Kcnj13 staining above the middle nucleus (DAPI but not Cre positive) and the absence of Kcnj13 staining at the base of both flanking cells with Cre stained nuclei. Arrows point to RPE basal surfaces above nuclei while *indicates the basal surface of the RPE and + indicates the choroid.

Supplementary Figure S2 | Confocal microscopy of mitochondrial density in retinal sections from 9-month-old KCNJ13CKO ko/ko, VMD2-Cre –/– mice (top row), KCNJ13CKO ko/ko, VMD2-Cre +/+ mice with intermediate Cre expression (middle row), and KCNJ13CKO ko/ko, VMD2-Cre +/+ mice with high levels of Cre expression (bottom row). The first column shows ATP5A expression by immunofluorescence, the second column shows DAPI staining of nuclei, and the third column shows an overlay of the first 2 images. White lines indicate measurements of the thickness of the inner segment of the photoreceptor layer as indicated by the presence of mitochondria and purple lines indicate the thickness of the ONL. Measurements were taken from similar regions of the retina from 5 KCNJ13CKO ko/ko, VMD2-Cre –/– mice, 5 KCNJ13CKO ko/ko, 5 VMD2-Cre +/+ mice with intermediate Cre expression (middle row), and 5 KCNJ13CKO ko/ko, VMD2-Cre +/+ mice with high levels of Cre expression. **(B)** Length of the photoreceptor inner segment (left) and outer nuclear layer (right). The ANOVA f-ratio value is 53.3 ($p < 10^{-6}$). Pairwise comparisons are by Tukey's HSD test.

REFERENCES

Ball, S., Hanzlicek, B., Blum, M., and Pardue, M. (2003). Evaluation of Inner Retinal Structure in the Aged RCS Rat. *Adv. Exp. Med. Biol.* 533, 181–188. doi:10.1007/978-1-4615-0067-4_23

Caminos, E., Velasco, A., Jarrín, M., Lillo, C., Jimeno, D., Aijón, J., et al. (2000). A Comparative Study of Protein Kinase C-like Immunoreactive Cells in the Retina. *Brain Behav. Evol.* 56, 330–339. doi:10.1159/000047217

Chen, M., Kim, L., Lu, C. W., Zeng, H., and Vollrath, D. (2021). An Efficient Inducible RPE-Selective Cre Transgenic Mouse Line. *Exp. Eye Res.* 202, 108370. doi:10.1016/j.exer.2020.108370

Choi, E. H., Suh, S., Einstein, D. E., Leinonen, H., Dong, Z., Rao, S. R., et al. (2021). An Inducible Cre Mouse for Studying Roles of the RPE in Retinal Physiology and Disease. *JCI Insight* 6. doi:10.1172/jci.insight.146604

Cornejo, I., Villanueva, S., Burgos, J., López-Cayuqueo, K. I., Chambrey, R., Julio-Kalajzić, F., et al. (2018). Tissue Distribution of Kir7.1 Inwardly Rectifying K+ Channel Probed in a Knock-In Mouse Expressing a Haemagglutinin-Tagged Protein. *Front. Physiol.* 9, 428. doi:10.3389/fphys.2018.00428

Döring, F., Derst, C., Wischmeyer, E., Karschin, C., Schneggenburger, R., Daut, J., et al. (1998). The Epithelial Inward Rectifier Channel Kir7.1 Displays Unusual K+Permeation Properties. *J. Neurosci.* 18, 8625–8636. doi:10.1523/jneurosci.18-21-08625.1998

Ghamari-Langroudi, M., Digby, G. J., Sebag, J. A., Millhauser, G. L., Palomino, R., Matthews, R., et al. (2015). G-protein-independent Coupling of MC4R to Kir7.1 in Hypothalamic Neurons. *Nature* 520, 94–98. doi:10.1038/nature14051

Hawse, J. R., DeAmicis-Tress, C., Cowell, T. L., and Kantorow, M. (2005). Identification of Global Gene Expression Differences between Human Lens Epithelial and Cortical Fiber Cells Reveals Specific Genes and Their Associated Pathways Important for Specialized Lens Cell Functions. *Mol. Vis.* 11, 274–283.

Hejtmancik, J. F., Jiao, X., Li, A., Sergeev, Y. V., Ding, X., Sharma, A. K., et al. (2008). Mutations in KCNJ13 Cause Autosomal-Dominant snowflake Vitreoretinal Degeneration. *Am. J. Hum. Genet.* 82, 174–180. doi:10.1016/j.ajhg.2007.08.002

Hirose, T., Lee, K. Y., and Schepens, C. L. (1974). Snowflake Degeneration in Hereditary Vitreoretinal Degeneration. *Am. J. Ophthalmol.* 77, 143–153. doi:10.1016/0002-9394(74)90665-5

Hoang, T. V., Kumar, P. K., Sutharzan, S., Tsonis, P. A., Liang, C., and Robinson, M. L. (2014). Comparative Transcriptome Analysis of Epithelial and Fiber Cells in Newborn Mouse Lenses with RNA Sequencing. *Mol. Vis.* 20, 1491–1517.

Hughes, B. A., and Takahira, M. (1996). Inwardly Rectifying K+ Currents in Isolated Human Retinal Pigment Epithelial Cells. *Invest. Ophthalmol. Vis. Sci.* 37, 1125–1139.

Iacovelli, J., Zhao, C., Wolkow, N., Veldman, P., Gollomp, K., Ojha, P., et al. (2011). Generation ofCreTransgenic Mice with Postnatal RPE-specific Ocular Expression. *Invest. Ophthalmol. Vis. Sci.* 52, 1378–1383. doi:10.1167/iovs.10-6347

Keeling, E., Chatelet, D. S., Tan, N. Y. T., Khan, F., Richards, R., Thisainathan, T., et al. (2020). 3D-Reconstructed Retinal Pigment Epithelial Cells Provide Insights into the Anatomy of the Outer Retina. *Int. J. Mol. Sci.* 21. doi:10.3390/ijms21218408

Krapivinsky, G., Medina, I., Eng, L., Krapivinsky, L., Yang, Y., and Clapham, D. E. (1998). A Novel Inward Rectifier K+ Channel with Unique Pore Properties. *Neuron* 20, 995–1005. doi:10.1016/s0896-6273(00)80480-8

Lee, M. M., Ritter, R., III, Hirose, T., Vu, C. D., and Edwards, A. O. (2003). Snowflake Vitreoretinal Degeneration. *Ophthalmology* 110, 2418–2426. doi:10.1016/s0161-6420(03)00828-5

Ookata, K., Tojo, A., Suzuki, Y., Nakamura, N., Kimura, K., Wilcox, C. S., et al. (2000). Localization of Inward Rectifier Potassium Channel Kir7.1 in the Basolateral Membrane of Distal Nephron and Collecting Duct. *Jasn* 11, 1987–1994. doi:10.1681/asn.v11111987

Pan, Z.-H. (2000). Differential Expression of High- and Two Types of Low-Voltage-Activated Calcium Currents in Rod and Cone Bipolar Cells of the Rat Retina. *J. Neurophysiol.* 83, 513–527. doi:10.1152/jn.2000.83.1.513

Pattnaik, B. R., and Hughes, B. A. (2009). Regulation of Kir Channels in Bovine Retinal Pigment Epithelial Cells by Phosphatidylinositol 4,5-bisphosphate. *Am. J. Physiology-Cell Physiol.* 297, C1001–C1011. doi:10.1152/ajpcell.00250.2009

Pattnaik, B. R., Shahi, P. K., Marino, M. J., Liu, X., York, N., Brar, S., et al. (2015). A NovelKCNJ13Nonsense Mutation and Loss of Kir7.1 Channel Function Causes Leber Congenital Amaurosis (LCA16). *Hum. Mutat.* 36, 720–727. doi:10.1002/humu.22807

Pattnaik, B. R., Tokarz, S., Asuma, M. P., Schroeder, T., Sharma, A., Mitchell, J. C., et al. (2013). Snowflake Vitreoretinal Degeneration (SVD) Mutation R162W Provides New Insights into Kir7.1 Ion Channel Structure and Function. *PLoS One* 8, e71744. doi:10.1371/journal.pone.0071744

Perez-Roustit, S., Marquette, V., Bocquet, B., Kaplan, J., Perrault, I., Meunier, I., et al. (2017). Leber Congenital Amaurosis with Large Retinal Pigment Clumps Caused by Compound Heterozygous Mutations in Kcnj13. *Retin. Cases Brief. Rep.* 11, 221–226. doi:10.1097/icb.0000000000000326

Perlman, I. (1995). "The Electroretinogram: ERG," in *Webvision: The Organization of the Retina and Visual System*. Editors H. Kolb, E. Fernandez, and R. Nelson (Salt Lake City (UT).

Roman, D., Zhong, H., Yaklichkin, S., Chen, R., and Mardon, G. (2018). Conditional Loss of Kcnj13 in the Retinal Pigment Epithelium Causes Photoreceptor Degeneration. *Exp. Eye Res.* 176, 219–226. doi:10.1016/j.exer.2018.07.014

Sergouniotis, P. I., Davidson, A. E., Mackay, D. S., Li, Z., Yang, X., Plagnol, V., et al. (2011). Recessive Mutations in KCNJ13, Encoding an Inwardly Rectifying Potassium Channel Subunit, Cause Leber Congenital Amaurosis. *Am. J. Hum. Genet.* 89, 183–190. doi:10.1016/j.ajhg.2011.06.002

Shahi, P. K., Hermans, D., Sinha, D., Brar, S., Moulton, H., Stulo, S., et al. (2019). Gene Augmentation and Readthrough Rescue Channelopathy in an iPSC-RPE Model of Congenital Blindness. *Am. J. Hum. Genet.* 104, 310–318. doi:10.1016/j.ajhg.2018.12.019

Shahi, P. K., Liu, X., Aul, B., Moyer, A., Pattnaik, A., Denton, J., et al. (2017). Abnormal Electroretinogram after Kir7.1 Channel Suppression Suggests Role in Retinal Electrophysiology. *Sci. Rep.* 7, 10651. doi:10.1038/s41598-017-11034-1

Shimura, M., Yuan, Y., Chang, J. T., Zhang, S., Campochiaro, P. A., Zack, D. J., et al. (2001). Expression and Permeation Properties of the K+channel Kir7.1 in the Retinal Pigment Epithelium. *J. Physiol.* 531, 329–346. doi:10.1111/j.1469-7793.2001.0329i.x

Toms, M., Burgoyne, T., Tracey-White, D., Richardson, R., Dubis, A. M., Webster, A. R., et al. (2019). Phagosomal and Mitochondrial Alterations in RPE May Contribute to KCNJ13 Retinopathy. *Sci. Rep.* 9, 3793. doi:10.1038/s41598-019-40507-8

Valenzuela, D. M., Murphy, A. J., Frendewey, D., Gale, N. W., Economides, A. N., Auerbach, W., et al. (2003). High-throughput Engineering of the Mouse Genome Coupled with High-Resolution Expression Analysis. *Nat. Biotechnol.* 21, 652–659. doi:10.1038/nbt822

Villanueva, S., Burgos, J., López-Cayuqueo, K. I., Lai, K.-M. V., Valenzuela, D. M., Cid, L. P., et al. (2015). Cleft Palate, Moderate Lung Developmental Retardation and Early Postnatal Lethality in Mice Deficient in the Kir7.1 Inwardly Rectifying K+ Channel. *PLoS One* 10, e0139284. doi:10.1371/journal.pone.0139284

Yin, W., Kim, H.-T., Wang, S., Gunawan, F., Wang, L., Kishimoto, K., et al. (2018). The Potassium Channel KCNJ13 Is Essential for Smooth Muscle Cytoskeletal Organization during Mouse Tracheal Tubulogenesis. *Nat. Commun.* 9, 2815. doi:10.1038/s41467-018-05043-5

York, N., Halbach, P., Chiu, M. A., Bird, I. M., Pillers, D.-A. M., and Pattnaik, B. R. (2017). Oxytocin (OXT)-stimulated Inhibition of Kir7.1 Activity Is through PIP 2 -dependent Ca 2+ Response of the Oxytocin Receptor in the Retinal Pigment Epithelium *In Vitro*. *Cell Signal.* 37, 93–102. doi:10.1016/j.cellsig.2017.06.005

Zhang, W., Zhang, X., Wang, H., Sharma, A. K., Edwards, A. O., and Hughes, B. A. (2013). Characterization of the R162W Kir7.1 Mutation Associated with snowflake Vitreoretinopathy. *Am. J. Physiology-Cell Physiol.* 304, C440–C449. doi:10.1152/ajpcell.00363.2012

Zhong, H., Chen, Y., Li, Y., Chen, R., and Mardon, G. (2015). CRISPR-engineered Mosaicism Rapidly Reveals that Loss of Kcnj13 Function in Mice Mimics Human Disease Phenotypes. *Sci. Rep.* 5, 8366. doi:10.1038/srep08366

Conflict of Interest: The authors declare that the research was conducted in the absence of any commercial or financial relationships that could be construed as a potential conflict of interest.

Publisher's Note: All claims expressed in this article are solely those of the authors and do not necessarily represent those of their affiliated organizations, or those of the publisher, the editors and the reviewers. Any product that may be evaluated in this article, or claim that may be made by its manufacturer, is not guaranteed or endorsed by the publisher.

Copyright © 2022 Jiao, Ma, Lei, Liu, Cai, Shahi, Chan, Fariss, Pattnaik, Dong and Hejtmancik. This is an open-access article distributed under the terms of the Creative Commons Attribution License (CC BY). The use, distribution or reproduction in other forums is permitted, provided the original author(s) and the copyright owner(s) are credited and that the original publication in this journal is cited, in accordance with accepted academic practice. No use, distribution or reproduction is permitted which does not comply with these terms.

frontiers in Cell and Developmental Biology

ORIGINAL RESEARCH
published: 18 January 2022
doi: 10.3389/fcell.2021.783547

Deletion of *Asrgl1* Leads to Photoreceptor Degeneration in Mice

Yu Zhou[1,2*†], *Wanli Tian*[1,2†], *Xiaoyan Jiang*[1,2], *Huining Yang*[1,2], *Zhilin Jiang*[1,2], *Xiao Li*[1,2], *Dan Jiang*[1,2], *Kuanxiang Sun*[1,2], *Yeming Yang*[1,2], *Wenjing Liu*[1,2*] *and Xianjun Zhu*[1,2,3*]

[1]*Sichuan Provincial Key Laboratory for Human Disease Gene Study, Department of Laboratory Medicine, Center for Medical Genetics, Sichuan Provincial People's Hospital, School of Medicine, University of Electronic Science and Technology of China, Chengdu, China,* [2]*Research Unit for Blindness Prevention of the Chinese Academy of Medical Sciences (2019RU026), Sichuan Academy of Medical Sciences and Sichuan Provincial People's Hospital, Chengdu, China,* [3]*Department of Ophthalmology, First People's Hospital of Shangqiu, Shangqiu, China*

OPEN ACCESS

Edited by:
Qingjiong Zhang,
Sun Yat-sen University, China

Reviewed by:
Ruifang Sui,
Peking Union Medical College Hospital (CAMS), China
Mallika Valapala,
Indiana University, United States
Wenmin Sun,
Sun Yat-sen University, China

***Correspondence:**
Yu Zhou
zhouyu422@yahoo.com
Wenjing Liu
nicolewjliu@163.com
Xianjun Zhu
xjzhu@uestc.edu.cn

[†]*These authors have contributed equally to this work*

Specialty section:
This article was submitted to Molecular and Cellular Pathology, a section of the journal Frontiers in Cell and Developmental Biology

Received: *26 September 2021*
Accepted: *23 November 2021*
Published: *18 January 2022*

Citation:
Zhou Y, Tian W, Jiang X, Yang H, Jiang Z, Li X, Jiang D, Sun K, Yang Y, Liu W and Zhu X (2022) Deletion of Asrgl1 *Leads to Photoreceptor Degeneration in Mice. Front. Cell Dev. Biol. 9:783547. doi: 10.3389/fcell.2021.783547*

The asparaginase and isoaspartyl peptidase 1 (ASRGL1) is an L-asparaginase and beta-aspartyl peptidase enzyme that may be involved in the formation of L-aspartate, a neurotransmitter that can operate as an excitatory neurotransmitter in some brain regions. Although variants in *ASRGL*1 have been reported in retinitis pigmentosa (RP) patients, the *in vivo* functions and mechanisms of *ASRGL* in RP remains unknown due to the lack of suitable disease models. To explore the role of *ASRGL* in RP, we generated an *Asrgl1* knockout mouse model (*Asrgl1* KO) using the CRISPR/Cas9 technique. *Asrgl1* ablation in mice led to an attenuated electroretinogram (ERG) response around 8 months. The thickness of the outer nuclei layer (ONL) started to decrease around 9 months in *Asrgl1* KO mice and gradually intensified at 12 and 15 months. Immunostaining revealed thinner inner segment (IS) and thinner outer segment (OS) as well as the progressive degeneration of rod and cone cells in *Asrgl1* KO mice. One hundred forty-nine transcriptional differentially expressed genes (DEGs) were found by RNA-seq in *Asrgl1* KO retina. These DEGs were linked to a number of biological processes that were considerably enriched, including gastrointestinal disease and organismal injury and abnormalities. By analysis of canonical pathways, glucocorticoid receptor signaling was the most significant canonical pathway altered in *Asrgl1* KO retina. Several molecules, including NFE2L2, IL-4, Foxp3, and Fos, were in the central nodes of the interaction network in *Asrgl1* KO retina. In summary, our study provided a knockout mouse model for a better understanding of the molecular mechanism for *ASRGL1*-related RP.

Keywords: retinitis pigmentosa, asparaginase and isoaspartyl peptidase 1, knockout mouse model, RNA-seq, photoreceptor degeneration

INTRODUCTION

Retinitis pigmentosa is one of the most common causes of visual impairment around the world, including symptoms such as night blindness and progressive loss of peripheral vision in the early stage, and no complete yet effective treatment exists up to date (Ferrari et al., 2011). The prevalence of this disorder is approximately 1:4,000 (Hartong et al., 2006). As an inherited retinal degeneration disease, it can be inherited in three ways: autosomal recessive (50%–60%), autosomal dominant (30%–40%), or X-linked (5%–15%). The phenotype of non-syndromic retinitis pigmentosa (RP) in RP patients might be limited to the eye or it can be part of a syndrome that includes extraocular

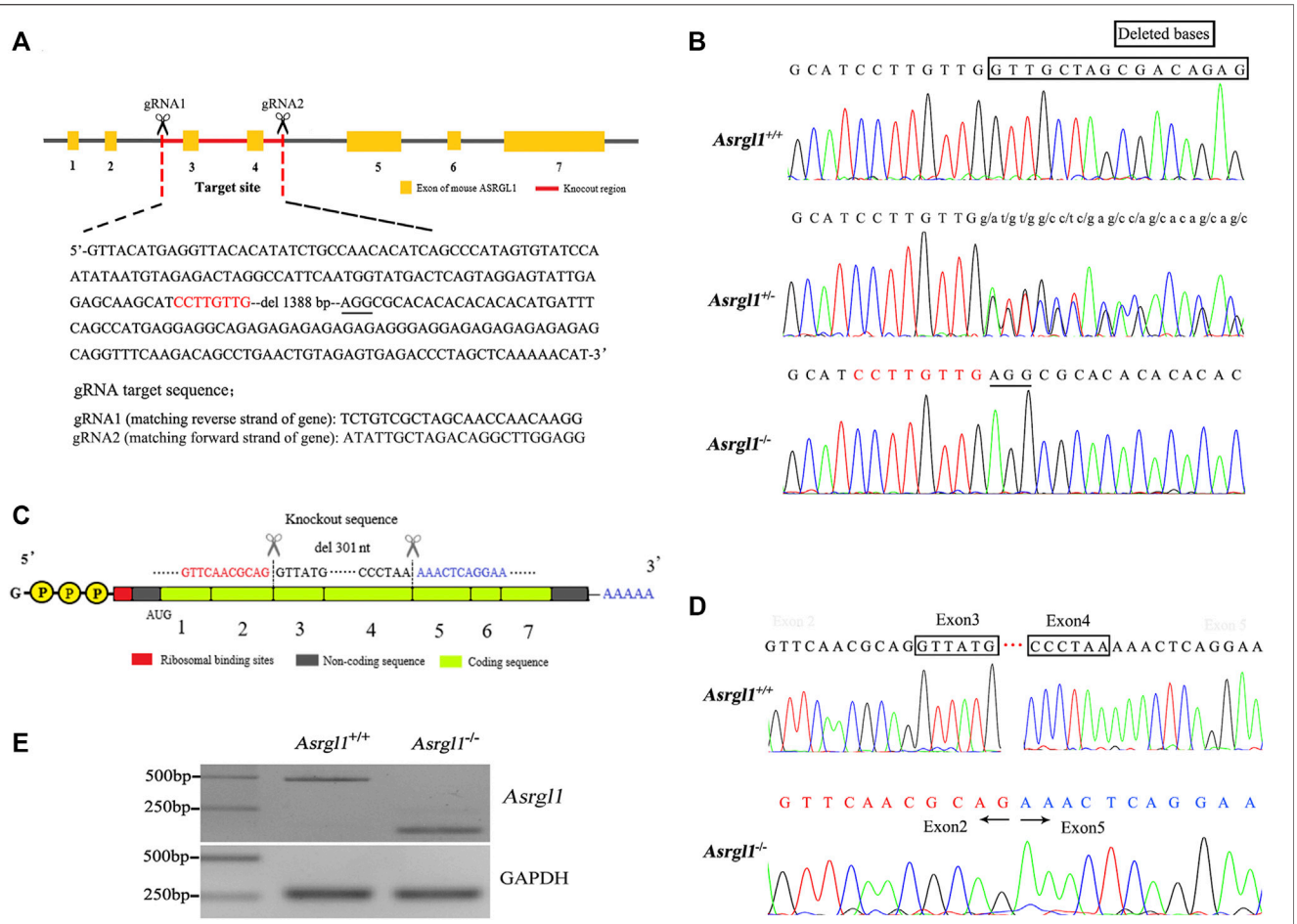

FIGURE 1 | Generation of *Asrgl1* knockout (KO) mice. **(A)** The partial genomic sequence of *Asrgl1* exons was shown. The 1,388-bp genomic deletion was indicated in red. **(B)** Sanger sequencing of *Asrgl1* genome in the wild-type (WT), *Asrgl1*$^{+/-}$ and *Asrgl1*$^{-/-}$ mice. **(C)** Schematic illustration of cDNA deletion in *Asrgl1* KO mice. **(D)** Sanger sequencing of *Asrgl1* cDNA in WT and Asrgl1$^{-/-}$ mice. A 301-bp fragment consisting of exon 3 and 4 is deleted in *Asrgl1* KO allele. **(E)** Reverse transcription PCR analysis of *Asrgl1* expression in WT and *Asrgl1*$^{-/-}$ mouse retinas at 3 months of age. Gapdh was used as a loading control.

illnesses such hearing loss, obesity, and neurologic diseases (Bhatti, 2006). Over 90 genes have been associated with non-syndromic RP according to the RetNet database (https://sph.uth.edu/retnet/; date last accessed Jul 30, 2021). However, only about 50%–60% of RP cases can be explained by these mutations, and the pathological and molecular mechanisms of some of the genes remain unknown (Daiger et al., 2013; Huang et al., 2015).

Asparaginase and isoaspartyl peptidase 1 (*ASRGL1*) has been reported as a RP disease gene in 2016 (Biswas et al., 2016). The p.G178R mutation, which causes photoreceptor degeneration and progressive vision loss, was discovered in a large five-generation pedigree with early-onset recessive retinal degeneration utilizing linkage analysis and homozygosity mapping combined with exome sequencing. *ASRGL1* encodes an enzyme L-asparaginase, has both L-asparaginase and beta-aspartyl peptidase activity, and may be involved in the production of L-aspartate (Cantor et al., 2009). However, the pathological and molecular mechanisms of *ASRGL1* in causing of RP remains unknown.

To investigate the function of *Asrgl1* in the mammalian retina and explore the molecular mechanism how *Asrgl1* affect photoreceptors or RPE cells, we developed a novel mouse model of RP with the *Asrgl1* gene knockout on a C57BL/6J genetic background by CRISPR/CAS9 technology. *Asrgl1* ablation in mice resulted in a typical retinal degeneration phenotype with decreased electroretinogram (ERG) response; thinner outer nuclei layer (ONL), inner segment (IS), and outer segment (OS); and decreased rod and cone proteins. A high-throughput transcriptional sequencing analysis found 149 transcriptional differentially expressed genes (DEGs) between *Asrgl1* knockout (KO) mouse retina and the normal controls. Glucocorticoid receptor signaling was the most changed pathway and might play key roles in the pathological process of *ASRGL1*-related RP. Our studies provide an *Asrgl1* KO mouse model for improving our understanding of RP disease mechanisms.

MATERIALS AND METHODS

Generation of *Asrgl1* Knockout Mice

The Animal Care and Use Committee of the Sichuan Provincial People's Hospital authorized all animal experiments, which

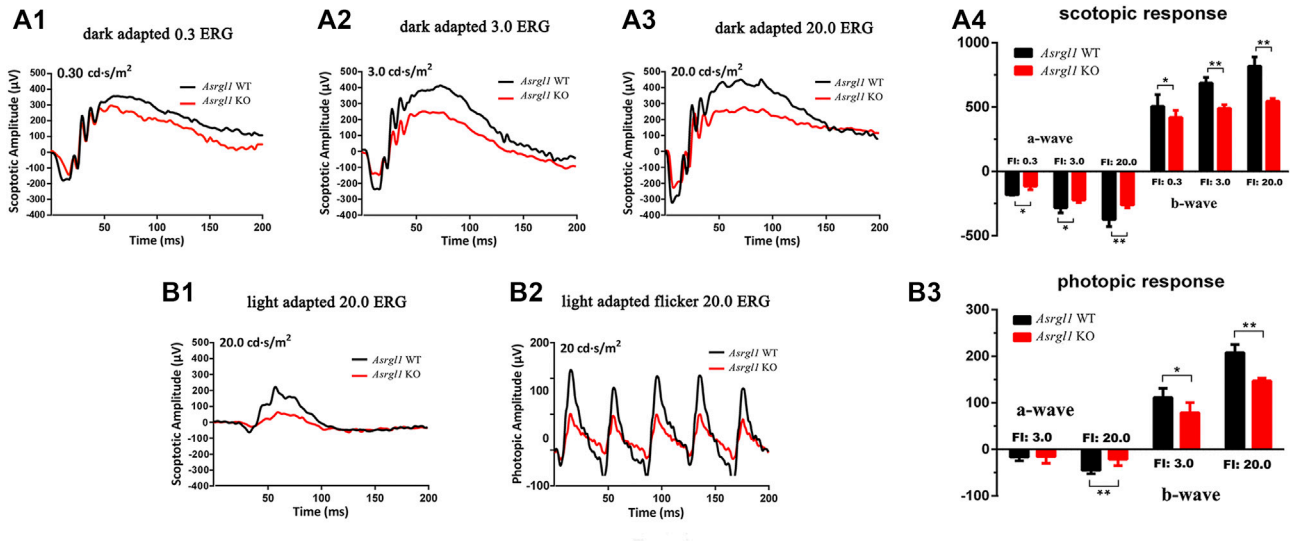

FIGURE 2 | ElectroretinogramERG) examinations of *Asrgl1* KO mice. **(A1–A4)** Asrgl1 KO mice at 8 months of age exhibited a reduced ERG scotopic response. Reduced amplitude peaks were observed for both the *a*-wave and the *b*-wave at light intensities of 0.3, 3.0, and 20.0 cds/m^2 in *Asrgl1* KO mice; two-tailed Student's *t*-test was used. $^{**}p < 0.01$; $^{***}p < 0.001$. **(B1–B3)** Compared with WT mice, 8-month-old KO mice exhibited a reduced photopic response at 20.0 cds/m^2; sample size $n = 4$. A two-tailed Student's *t*-test was used. $^{**}p < 0.01$; $^{***}p < 0.001$.

followed the ARVO guidelines for the use of animals in ophthalmology and vision research.

Asrgl1 KO mice were generated by using the CRISPR/Cas9 system on C57BL/6J genetic background. The Cas9 mRNA and two single guide RNAs targeting a region upstream of exon 3 and downstream of exon 4 of *Asrgl1* exon 3 were microinjected into mouse zygotes (**Figure 1**). gRNA1 sequence (matching reverse strand of gene) was as follows: TCTGTCGCTAGCAACCAA CAAGG. gRNA2 sequence (matching forward strand of gene) was as follows: ATATTGCTAGACAGGCTTGGAGG. As confirmed by Sanger sequencing and PCR genotyping analysis, the conventional translation start site was successfully eliminated.

Electroretinograms in Mice

Mouse ERG detection was performed on an Espion Visual Electrophysiology System (Diagnosys, Lowell, MA, United States). Briefly, female *Asrgl1* KO mice and female controls were dark-adapted overnight 1 day before detection. In the next morning, before ERG, animals were anesthetized and the eyes were dilated with a drop of tropicamide and phenylephrine, as well as tetracaine (0.5%). Throughout the experiment, a heating platform was used to keep the body temperature at 37°C. Gold wire loops were used to record dark-adapted ERGs in response to flashes with intensities ranging from 0.003 to 20 cds/m^2. After 20 min of complete light adaptation, cone-mediated ERGs were recorded with white flashes.

Retinal Hematoxylin and Eosin Staining

The eyes with the whole retina and optic nerve were chosen for imaging by hematoxylin and eosin (H&E) staining. Female wild-type (WT) and female KO mice's eyes were enucleated, marked for orientation on the nasal side, fixed overnight in 1.22% glutaraldehyde and 0.8% paraformaldehyde in 0.08 M phosphate buffer, embedded in paraffin, and cut into 5-μm slices. H&E staining was used on sections taken from five places around the optic nerve. The rows of photoreceptors in the outer nuclear layer were counted using H&E-stained slices. Every 200 μm from the optic nerve, three measurements of the outer nuclear layer were recorded and averaged. The optic nerve was given the number 0 mm.

Immunohistochemistry Analysis

Enucleated eyeballs were removed from female WT and female *Asrgl1* KO mice for immunohistochemistry, marked on the nasal side for orientation, fixed for 1 h in 4% paraformaldehyde in 100 mM phosphate buffer (pH 7.4), and cryoprotected in 30% sucrose. For sectioning, tissues were immersed in an optimal cutting temperature (OCT) solution and frozen on dry ice. For 30 min, sections were blocked and permeabilized in phosphate buffer with 10% normal goat serum and 0.2% Triton X-100, then labeled with different primary antibodies overnight at 4°C. Then, the slides were washed and incubated with secondary antibodies for 2 h. Finally, the slides were washed and covered with coverslips. The primary antibodies used in our study were as follows: rhodopsin (1D4, cat. #MA1-722, Thermo Fisher, Waltham, MA, United States), Na-K pump (cat. #MA3928, Thermo Fisher, Waltham, MA, United States), opsin (red/green, cat. #AB5405, Millipore, Burlington, MA, United States), and 594-conjugated peanut agglutinin (PNA) (cat. #RL1072, Vector laboratories, Burlingame, CA, United States). Secondary antibodies (Alexa Fluor 488 and Alexa Fluor 594) and DAPI (cat. #D8417, Sigma, St Louis, MO, United States, 1:2,000 dilution) were also used in the experiments. Confocal microscopy was used to image eye sections (LSM800, Carl Zeiss, Jena, Germany).

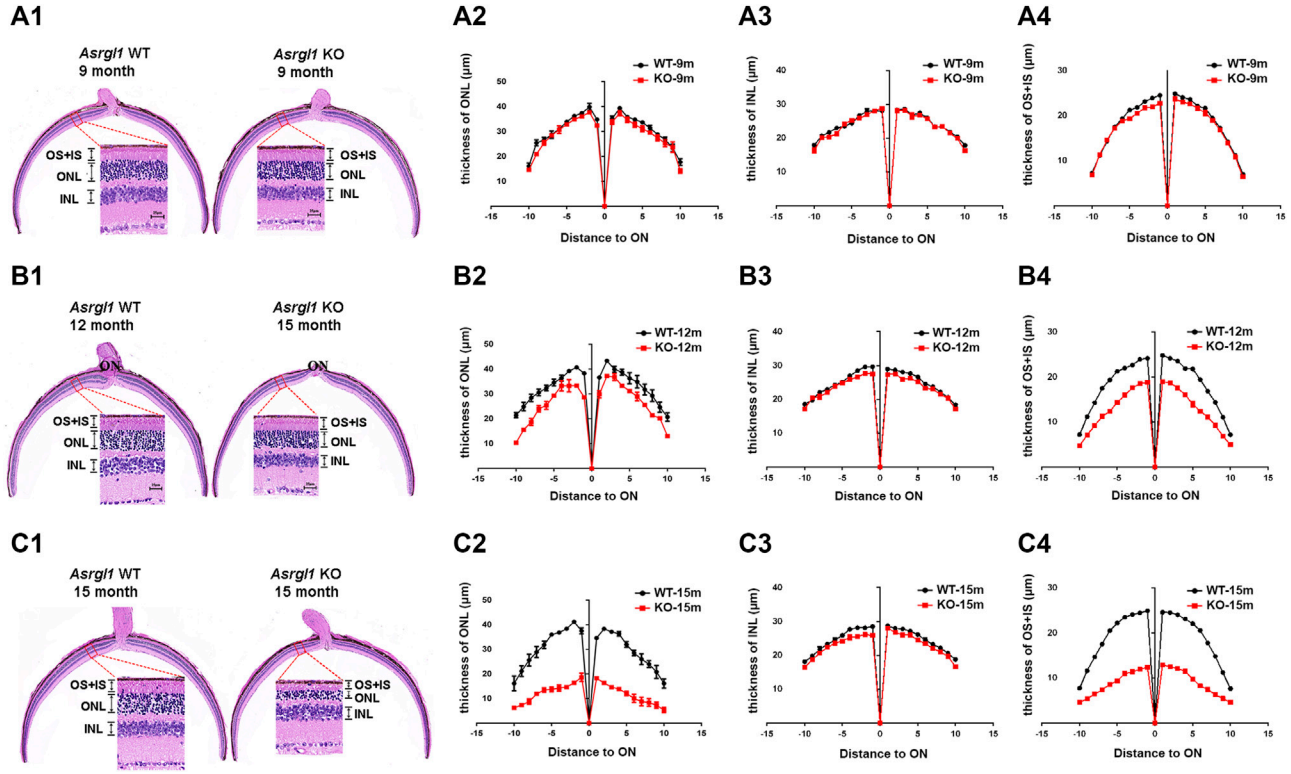

FIGURE 3 | Degeneration of the outer retina in *Asrgl1* KO mice. **(A1,B1,C1)** Hematoxylin and eosin (H&E) staining of paraffin sections of the *Asrgl1* KO and corresponding control retinas at the ages of 9, 12, and 15 months. Scale bar: 25 μm. **(A2,B2,C2)** Quantification analysis of the outer nuclei layer (ONL) thickness of the KO (n = 6) and WT (n = 6) retinas from mice at 9, 12, and 15 months old. **(A3,B3,C3)** Quantification analysis of the inner nuclei layer (INL) thickness of the KO (n = 6) and WT (n = 6) retinas from mice at 9, 12, and 15 months old. **(A4,B4,C4)** Quantification analysis of the outer segment (OS) plus inner segment (IS) thickness of the KO (n = 6) and WT (n = 6) retinas from mice at 9, 12, and 15 months old. The *Asrgl1* KO mouse retinas showed a drastically gradual degeneration of the photoreceptor cells at 15 months old.

RNA Isolation and RT-PCR

TRIzol (Invitrogen, Austin, TX, United States) was used to extract total RNA from the retinas of female *Asrgl1* KO mice and female normal controls, according to the manufacturer's protocol. cDNA was made as previously described. An Eppendorf Mastercycler personal PCR equipment (Eppendorf, Germany) was used to amplify *Asrgl1* genotyping products, which were then analyzed on a 1.5% agarose gel electrophoresis. Using the SYBR PCR Master Mix kit (Applied Biosystems, Foster City, CA) and the 7500 Fast Real-Time PCR detection machine, equal amounts of cDNA from the retinas of *Asrgl1* KO mice and normal controls were submitted to PCR. Specific primers used in our study were listed in **Supplementary Data S1**.

RNA-Seq and Differential Expression Analysis

RNA was isolated from the retinas of female *Asrgl1* KO mice and female normal controls, and the integrity of the RNA was determined using the Bioanalyzer 2100 system's RNA Nano 6000 Assay Kit (Agilent Technologies, CA, United States). The library was then produced and tested for transcriptome sequencing using the Agilent Bioanalyzer 2100 instrument. The index-coded samples were clustered using the TruSeq PE Cluster Kit v3-cBot-HS (Illumina) on a cBot Cluster Generation System according to the manufacturer's instructions. The library preparations were sequenced on an Illumina Novaseq device after cluster creation, yielding 150-bp paired-end reads. Raw data (raw readings) in fastq format were processed using in-house perl scripts, resulting in clean, high-quality data. The level of gene expression was measured after reads were mapped to the reference genome. All of the downstream analyses were based on clean, high-quality data. Prior to differential gene expression analysis, the read counts for each sequenced library were modified by one scaling normalization factor using the edgeR tool package. The edgeR R package was used to perform differential expression analysis of two situations. The P values were adjusted using the Benjamini and Hochberg method. The criterion for significant differential expression was set at 0.05 corrected P-value and log2 fold change. The raw data have been uploaded to the Genome Sequence Archive (https://ngdc.cncb.ac.cn/gsa/browse/CRA005193), and the assigned accession number was CRA005193.

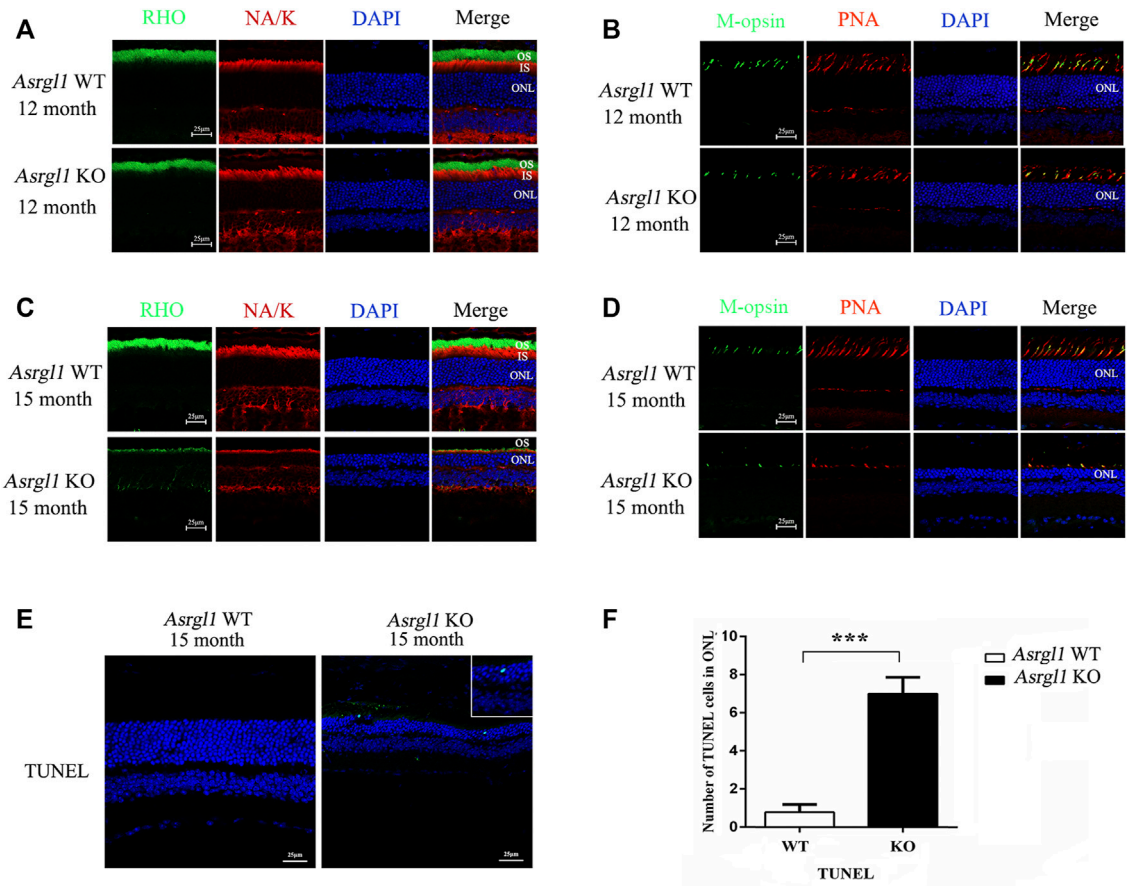

FIGURE 4 | Immunofluorescence staining analysis of the *Asrgl1* KO retinas. **(A,C)** Retinal cryosections from 12- and 15-month-old mice (n = 6) were labelled with rod-specific markers rhodopsin (outer segment) and Na-K ATPase (inner segment). **(B,D)** M-opsin and peanut agglutinin (PNA) was used as the cone markers in 12- and 15-month-old mice (n = 6). DAPI was used to counterstain the nuclei; scale bars: 25 μm. The data shown are representative of three independent tests. At least three slides of each retina were stained. **(E)** TUNEL assays in 15-month-old WT and KO mice revealed increased apoptosis. The magnified square indicated TUNEL-positive cells in the retinas. This experiment was performed three times. Sample size n = 6. **(F)** Quantification of TUNEL-positive cells in WT and KO retinas; sample size n = 6; ***p < 0.001. Statistical significance was determined by a two-tailed unpaired t-test.

Functional Analysis, Canonical Pathway Analysis, and Generation of Networks

Top biological functions as well as canonical pathways associated with DEGs generated from the RNA-seq between the *Asrgl1* KO retina and normal controls were identified by Ingenuity pathway analysis (IPA) (Qiagen). Fisher's exact test was used to determine the likelihood of any biological function or canonical pathway being explained only by chance. Algorithmically, molecular interaction networks are created based on the connectivity of the molecules. Fisher's exact test was used to determine network scores, which corresponded to −log 10 (p value).

Statistical Analysis

Statistical significance was established using Prism 7.0 software and the Student's t-test or one-way ANOVA (GraphPad Software, La Jolla, CA, United States). The data are presented as the mean SEM unless otherwise noted in the text and figure legends. The ERG datasets in **Figure 2** and the ONL thickness measurement dataset in **Figure 3** were subjected to ANOVA tests. The number of animals used in each experiment is indicated by n. In the figure legends, the total number of animals used in each experiment is also listed. The following p values are indicated by asterisks in the figures: *≤0.05, **≤0.01, and ***≤0.001.

RESULTS

Generation of *Asrgl1* Knockout Mice

ASRGL1 is widely expressed in all human tissues studied, with the highest levels of expression in the brain, female tissues including the uterine cervix and fallopian tube, and male tissues like the testis (Edqvist et al., 2015). To investigate the functions of *AsrgL1*

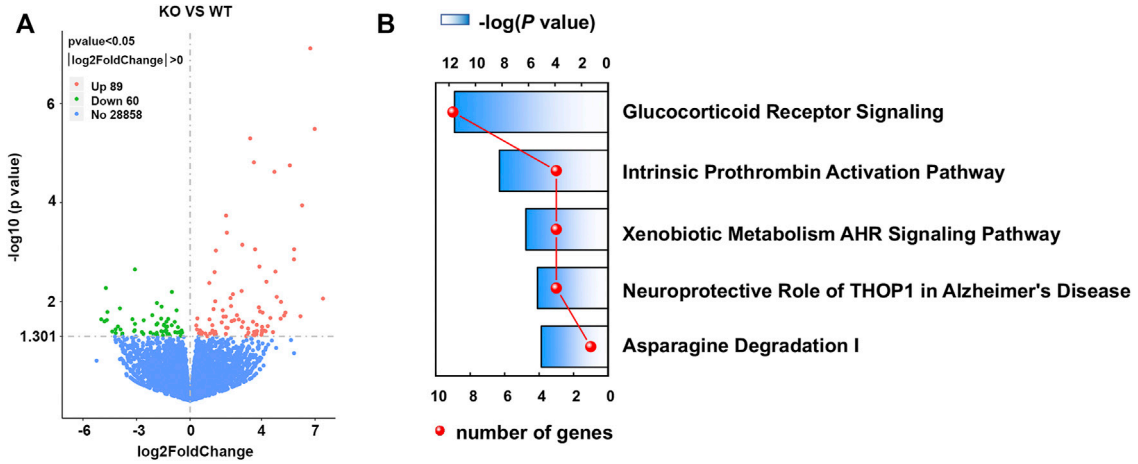

FIGURE 5 | Volcano plots of differentially expressed genes (DEGs) and top canonical pathways involved in *Asrgl1* KO mice. **(A)** Volcano plots of DEG profile. The vertical lines correspond to 2.0 FC up and down, and the horizontal line represents –log 10 (*P*-value). **(B)** Ingenuity pathway was used to analyze the total significantly differentially expressed genes and identify the canonical pathways involved in *Asrgl1* KO mice. The top five significant pathways identified were displayed (blue bar). The red curve shows the total number of genes in each of these pathways.

TABLE 1 | Functional analysis for the DEGs in the retina between *Asrgl1* knockout mice and normal controls.

Top diseases and bio functions	*p*-value range	# of molecules
Diseases and disorders		
Gastrointestinal disease	4.79E–02–2.61E–05	13
Organismal injury and abnormalities	4.94E–02–2.61E–05	31
Cancer	4.79E–02–3.23E–04	18
Dermatological diseases and conditions	4.48E–02–1.07E–03	8
Reproductive system disease	3.85E–02–1.32E–03	8
Molecular and cellular functions		
Cellular development	4.16E–02–3.14E–05	7
Cell morphology	4.79E–02–1.07E–03	6
Cell death and survival	4.94E–02–1.22E–03	7
Cellular growth and proliferation	4.16E–02–1.22E–03	5
Amino acid metabolism	19.76E–03–3.26E–03	1
Physiological system development and function		
Digestive system development and function	3.38E–02–2.61E–05	7
Organ morphology	4.48E–02–2.61E–05	13
Hematological system development and function	4.60E–02–3.14E–05	7
Lymphoid tissue structure and development	1.94E–02–3.14E–05	2
Hair and skin development and function	4.48E–02–1.07E–03	3

[a]*Range of p-values indicate higher-level functions that contained multiple lower-level functions.*

in vivo, *Asrgl1* KO were generated using CRISPR/Cas9 technology. The target sites were selected as exon 3 and exon 4 (**Figure 1A**). Genotyping analysis using PCR primers flanking the deletion site revealed the successful generation of *Asrgl1* knockout mice (**Supplementary Figure S1**). To validate the genomic *Asrgl1* ablation, mouse DNA samples were subjected to Sanger sequencing analysis, and results showed genomic deletion of 1,388 bp in *Asrgl1* KO mice (**Figure 1B**). Both Sanger sequencing and electrophoresis analysis of cDNA product from *Asrgl1* KO retinas revealed a 301-bp deletion of exon 3 and exon 4 in *Asrgl1* KO (**Figure 1C–E**). All the above data showed the successful generation of *Asrgl1* KO by CRISPR/Cas9 technology.

Asrgl1 Knockout Mice Exhibited Impaired Visual Function

ERG examination was first performed to test the *in vivo* function of *Asrgl1* in the retina. In three 6-month-old *Asrgl1* KO mice and littermate controls, no abnormal ERG response was observed (data not shown). However, all *Asrgl1* KO mice exhibited reduced scotopic and photopic responses at 8 months of age. The mean

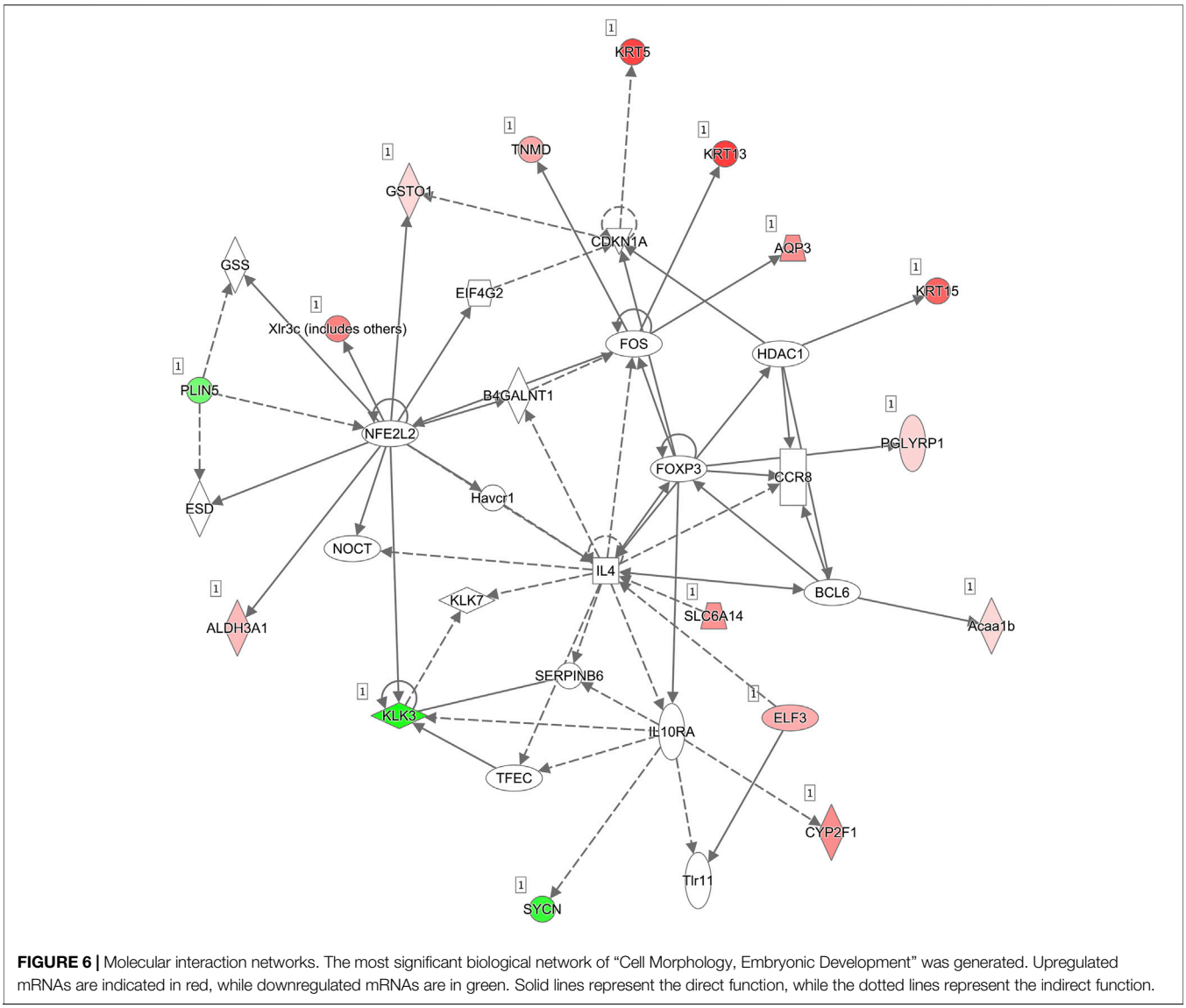

FIGURE 6 | Molecular interaction networks. The most significant biological network of "Cell Morphology, Embryonic Development" was generated. Upregulated mRNAs are indicated in red, while downregulated mRNAs are in green. Solid lines represent the direct function, while the dotted lines represent the indirect function.

a- and *b*-wave amplitudes of *Asrgl1* KO were reduced by approximately 15% and 30%, respectively, in scotopic response tests (**Figure 2A1–A4**), which indicated altered rod cell function. When compared to WT mice, *Asrgl1* KO had a somewhat flat wave under light-adapted conditions, showing that cone cell function was also impaired in *Asrgl1* KO (**Figure 2B1–B3**). Although, by H&E staining, the retinas from *Asrgl1* KO mice revealed no difference in the retinal ONL thickness at 6 months of age (**Supplementary Figure S2**), the thickness of the ONL started to decrease around 9 months of age (**Figure 3A1, A2**) and gradually intensified at 12 months (**Figure 3B1, B2**) and 15 months of age (**Figure 3C1, C2**). The photoreceptor layer including the inner segment and outer segment decreased around 9 months (**Figure 3A1, A4**) and intensified at 12 months (**Figure 3B1, B4**) and 15 months of age (**Figure 3C1, C4**). There was no obvious change in the inner nuclei layer (INL) of *Asrgl1* KO at 9 months of age (**Figure 3A1, A3**), and the thickness of the INL in *Asrgl1* KO was slightly decreased at 15 months of age (**Figure 3C1, C3**).

Loss of *Asrgl1* Leads to Degeneration and Apoptosis of Photoreceptor Cells

To investigate the pathological changes underlying the *Asrgl1* knockout mice's retinal degeneration phenotype, immunostaining was performed with retinal cryosections in *Asrgl1* KO and WT mice. There were no changes in rhodopsin and M-opsin expression in *Asrgl1* KO at 8 months of age (**Supplementary Figure S3A, B**). However, decreased rhodopsin protein was observed in the photoreceptor of 12- and 15-month-old *Asrgl1* KO mice, respectively (**Figure 4A, C**), compared to WT mice, which indicated a shortened outer segment of 12- and 15-month-old *Asrgl1* KO mice. Rhodopsin is a key outer segment protein that is required for adequate vision,

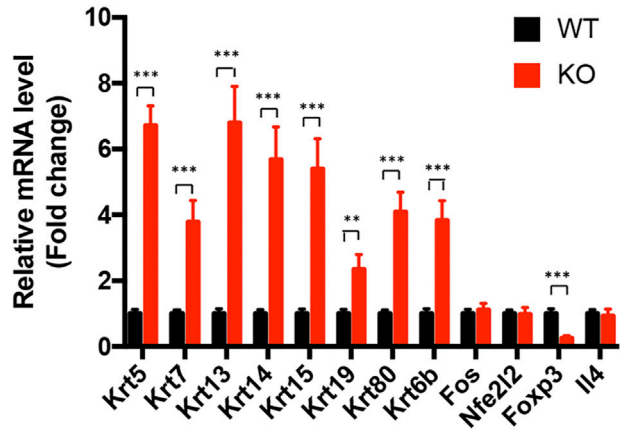

FIGURE 7 | Transcriptional validation of the differentially expressed genes in *Asrgl1* KO mice. The expression of Krt5, Krt7, Krt13, Krt14, Krt15, Krt19, and Krt80 in glucocorticoid receptor signaling pathway and the "central node" genes, NFE2L2, IL-4, Foxp3, and Fos, in the interaction network between WT and *Asrgl1* KO mice ($n = 6$) was validated by real-time PCR. A two-tailed Student's *t*-test was used; $^{**}p < 0.01$; $^{***}p < 0.001$. Data were from an average of four samples per group. Each test was repeated at least three times.

and its manufacture and transit are tightly regulated (Palczewski, 2006). Decreased rhodopsin is cytotoxic and leads to rod death. Decreased Na-K ATP staining in 15-month-old *Asrgl1* KO mice indicated shortened inner segment. M-opsin, a cone cell marker, and PNA (which binds to the sheaths of the cone matrix in all three types of cones) were also used to stain retinal sections. The number of cone cells was reduced in 12-month-old *Asrgl1* KO mice and drastically decreased in 15-month-old *Asrgl1* KO mice (**Figure 4B,D**). A TUNEL assay was utilized to determine whether the retinal degeneration was caused by apoptosis. There were no changes in TUNEL-positive cells in 8-month-old *Asrgl1* KO mice (**Supplementary Figure S3C**). TUNEL-positive cells were substantially more abundant at 15 months of age in *Asrgl1* KO retinas than in WT retinas (**Figure 4E,F**), and TUNEL-labeled nuclei were mostly found in the ONL, indicating continuous photoreceptor cell death in Asrgl1 KO retinas.

Differentially Expressed Genes in the Retinas Between *Asrgl1* KO and Normal Controls

To investigate the transcriptional effect of *Asrgl1* ablation, mouse retinal tissues from 8-month-old *Asrgl1* KO ($n = 3$) and WT mice ($n = 4$) were subjected to RNA-seq analysis. There were 149 DEGs identified in *Asrgl1* mice (**Supplementary Table S2**), among which 89 were upregulated ($p \leq 0.01$ and log2 ratio ≥ 1) and 60 ($p \leq 0.01$ and log2 ratio ≤ -1) were downregulated. Volcano plots of differentially expressed genes are shown in **Figure 5A**. IPA was used to identify numerous highly enriched biological processes related with DEGs in order to investigate the biological functions enriched in DEGs (**Table 1**). Gastrointestinal disease (p value: 4.79E−02 to 2.61E−05, 13 genes assigned), organismal injury and abnormalities (p value: 4.94E−02 to 2.61E−05, 31 genes assigned), and cancer (p value: 4.79E−02 to 3.23E−04, 18 genes assigned) were discovered as the top three highly enriched terms in the perspective of diseases and disorders. Cellular development (p value: 4.16E−02 to 3.14E−05, seven genes assigned), cell morphology (p value: 4.79E−02 to 1.07E−03, six genes assigned), and cell death and survival (p value: 4.94E−02 to 1.22E−03, seven genes assigned) were found as the top three highly enriched terms in the perspective of molecular and cellular functions. Digestive system development and function (p value: 3.38E−02 to 2.61E−05, seven genes assigned), organ morphology (p value: 4.48E−02 to 2.61E−05, 13 genes assigned), and hematological system development and function (p value: 4.60E−02 to 3.14E−05, seven genes assigned) were shown as the top three enriched terms in the perspective of physiological system development and functions.

Glucocorticoid Receptor Signaling Pathway Is Involved in *Asrgl1* Knockout Mice

Canonical pathway analysis could inform the key metabolism and signaling pathways in which the DEGs may be involved. The main metabolism and signaling pathways in which DEGs may be engaged could be informed *via* canonical pathway analysis. In this study, canonical molecular pathways enriched by DEGs were explored by bioinformation analysis of IPA software. **Figure 5B** shows the top five canonical pathways in the retina of *Asrgl1* KO mice that are significantly associated with DEGs. The glucocorticoid receptor signaling (p value = 9.36E−06), intrinsic prothrombin activation pathway (p value = 2.78E−04), and xenobiotic metabolism AHR signaling pathway (p value = 2.04E−03) were the top three major pathways altered in retinal tissues in *Asrgl1* KO mouse. The molecules that were changed in the glucocorticoid receptor signaling were IL1β, KRT5, KRT7, KRT13, KRT14, KRT15, KRT19, KRT80, and KRT6B. Our results firstly suggested an association of *Asrgl1* with GR signaling in the pathological process of retinitis pigmentosa.

Influenced Interaction Network by Ablation of *Asrgl1* in Mouse Retina

The molecular interaction networks were then created and ranked based on the connectivity of the detected DEGs. The network of "Cell Morphology, Embryonic Development" (score = 49) (**Figure 6**) was the most enriched network alerted in retinal tissues of *Asrgl1* KO mice. Notably, several genes including NFE2L2, IL-4, Foxp3, and Fos were the core "nodes" with the most connections in the network. To validate the expression levels of the main altered genes in glucocorticoid receptor signaling pathway and network of "Cell Morphology, Embryonic Development," real-time PCR was performed. As **Figure 7** shows, the expression of KRT5, KRT7, KRT13, KRT14, KRT15, KRT19, and KRT80 in glucocorticoid receptor signaling pathway all increased in *Asrgl1* knockout mice compared to the normal controls. Interestingly, only the expression of

Foxp3 was decreased among the selected "central node" genes, namely, NFE2L2, IL-4, Foxp3, and Fos. As Foxp3 is a transcriptional regulator that is required for regulatory T-cell development and inhibitory activity (Treg) (Li et al., 2015), its function in *Arsgl1*-related RP needs to be explored further in follow-up studies.

DISCUSSION

RP is the leading cause of inherited blindness in the developed world. Although more than 90 genes have been found associated to RP, some of the gene functions remain unknown (Dias et al., 2018). There are numerous RP animal models available, which have contributed to a better understanding of the disease's pathogenesis and the development of therapeutic strategies targeted at curing or delaying the hereditary illness (Petersen-Jones, 1998). In this study, we generated a novel *Asrgl1* knockout mouse model to investigate the *in vivo* roles of *ASRGL1*, a new RP gene reported in 2016.

We found *Asrgl1* ablation led to an attenuated ERG response around 8 months. The thickness of the ONL started to decrease at around 9 months in *Asrgl1* KO mice and gradually intensified at 12 and 15 months. Thinner IS and OS as well as the diminished expression of functional markers in the rod and cone were revealed by immunostaining in *Asrgl1* KO mice. Although the patients exhibited an early-onset retinal dystrophy, late-onset retinal dystrophy was observed in *Asrgl1* KO mice. It is not uncommon for the phenotypes of people with *Asrgl1* mutations and those of knockout mice to differ. One example is the difference between patients with CRB1 mutations and retinal degeneration-8 (rd8) mice phenotypes. CRB1 mutations led to retinitis pigmentosa 12, LCA8, or childhood- and juvenile-onset cone–rod dystrophy (den Hollander et al., 2004; Bujakowska et al., 2012). The majority of the patients exhibited severe vision loss. However, Mehalow et al. (2003) described a new mouse model, rd8, with a single-base loss in the Crb1 gene in mice. rd8 mutation resulted in a frameshift and premature stop codon. The truncated protein lost the transmembrane and cytoplasmic domains of CRB1. However, rd8 homozygous mutant mice only exhibited mild retinal degeneration. Photoreceptor degeneration was observed only within spotted regions of the retina. Furthermore, the severity of retinal pathology is influenced by genetic backgrounds (Aleman et al., 2011; Luhmann et al., 2015). Thus, our *Asrgl1* knockout mouse model showed a late-onset photoreceptor degeneration phenotype, which is valuable to investigate the pathogenesis in *ASRGL1*-related RP and further assess the *in vivo* function of *Asrgl1* in the retina.

The 308-amino-acid ASRGL1 protein is activated by autocleavage at amino acid 168, forming an alpha- and beta-chain that can dimerize into a heterodimer (Cantor et al., 2009; Li et al., 2012). In some brain regions, the ASRGL1 enzyme is involved in the synthesis of L-aspartate, which can operate as an excitatory neurotransmitter. In endometrioid endometrial carcinoma, loss of *ASRGL1* expression was an independent biomarker for disease-specific survival, and combined *ASRGL1* and p53 could be used as an independent predictor of survival (Edqvist et al., 2015; Huvila et al., 2018). *Asrgl1* was reported to be trafficked by neural stem/progenitor cell (NSC)-derived extracellular vesicles (EVs) and thus enables NSC EVs as independent metabolic units with asparaginase activity (Iraci et al., 2017). Biswas et al. (2016) showed that the p.G178R mutation in *ASRGL1* impaired the autocatalytic processing of ASRGL1 and resulted in the function loss of *ASRGL1*, which caused early-onset recessive retinal degeneration in a five-generation pedigree. Although the authors observed retinal abnormalities and loss of cone photoreceptors in a zebrafish model, the *in vivo* function of *ASRGL1* in mammalian animals remains unknown. In our study, we firstly observed the photoreceptor degeneration in *Asrgl1* knockout mouse models as well as the transcriptional molecular changes in the *Asrgl1* knockout mouse retina.

Deletion of genomic fragments in *Asrgl1* knockout mice was performed by CRISPR/Cas9 technology. Several available antibodies against ASRGL1 were subjected to immunoblotting and immunostaining analysis. Unfortunately, none of them worked well. Since *Asrgl1* is consist of seven exons and encodes a 326-amino-acid protein in *Mus musculus*, the deletion of a 301-bp fragment spanning exon 3 and exon 4 in *Asrgl1* knockout mice most likely led to generation of shortened proteins lacking majority of the downstream domains after exon 2 and resulted in impaired formation of heterodimer comprising an alpha- and beta-chain by autocleavage.

To further reveal the molecular mechanism of *ASRGL1* in mouse retinas, we explored differentially expressed genes, pathways, and interaction network in *Asrgl1* knockout mouse retinas by transcriptional analysis. Our results suggested an important role of glucocorticoid receptor signaling in the physiology of *Asrgl1*-related retinal degeneration. Although glucocorticoid receptor (GR) has been found in various cell types of the eye, including the retina, little is known yet about the mechanism of glucocorticoid signaling in distinct layers of the eye (Kadmiel and Cidlowski, 2013; Gallina et al., 2014; Sulaiman et al., 2018). As GR signaling is commonly associated with anti-inflammatory responses, GR agonists are widely used to treat inflammatory diseases of the eye. Further investigation is warranted to explore how *ASRG1L* influence the glucocorticoid receptor signaling pathway and its role in the pathological process of RP. Interestingly, glucocorticoids have been reported to suppress the expression of a subset of the keratin family genes K5-K14, K6-K16, and K17 (Radoja et al., 2000). However, in the present study, several genes in the keratin gene family, such as Krt5, Krt7, Krt13, Krt14, Krt15, Krt19, and Krt80, were found to have increased transcriptional expression in the *Asrgl1* knockout mice. The keratin gene family consists the highest number of members in humans with 54 distinct functional genes (Moll et al., 2008). The functions of several keratins in the eye have been reported. Krt8/keratin 8 was shown to protect against degeneration of retinal pigment epithelium under oxidative stress (Baek et al., 2017), and KRT3 and KRT12 gene mutations

associated with Meesmann corneal dystrophy (Chen et al., 2015). However, the function of keratin family genes in the retinas still needs to be further investigated. Several molecular interaction networks were generated using the identified DEGs. In the most enriched network, "Cell Morphology, Embryonic Development," NFE2L2, IL-4, Foxp3, and Fos were the network's central "nodes" with the greatest number of connections, which indicated the important roles of these molecules in the *Asrgl1* knockout retina. NFE2L2 (NRF2) is a transcription factor involved in the oxidative stress response, which has been linked to several ocular diseases (Ildefonso et al., 2016; Naguib et al., 2021). An anti-inflammatory cytokine, IL-4, has been reported to inhibit the proliferation of retinal cells (Silva et al., 2008). Foxp3 is a transcriptional regulator that is required for regulatory T-cell development and inhibitory activity (Treg). Foxp3+ Tregs can be recruited to the retina to repair abnormal angiogenesis (Deliyanti et al., 2017). C-fos has been linked to cell death and regeneration in retinal ganglion cells (Oshitari et al., 2002). Through c-Fos, inflammatory signals from photoreceptors influenced pathological retinal angiogenesis (Sun et al., 2017). Except the most enriched network "Cell Morphology, Embryonic Development," several other interaction networks with lower scores were identified (not shown). Although, we revealed the transcriptional regulation of glucocorticoid receptor signaling pathway and several molecules in *Asrgl1* KO mice, the intrinsic mechanism will be further explored in our future work.

In conclusion, our study firstly explored the function of *Asrgl1* using a novel knockout mouse model and confirm its role in the pathological process of RP. Studies utilizing mouse models have been proven important not only in recapitulation of the disease phenotype in humans but also in improving our understanding of disease mechanisms, and this knockout model is valuable for further development of translational therapeutic approaches.

DATA AVAILABILITY STATEMENT

The data presented in the study are deposited in the Genome Sequence Archive (https://ngdc.cncb.ac.cn/gsa/browse/CRA005193), accession number was CRA005193.

ETHICS STATEMENT

The animal study was reviewed and approved by the Animal Care and Use Committee of the Sichuan Provincial People's Hospital.

AUTHOR CONTRIBUTIONS

XZ and YZ designed the study. WT, WL, XJ, HY, ZJ, XL, DJ, KS, and YY performed the experiments and plotted the data. YZ and WT validated the data and drafted the manuscript. YZ and XZ reviewed and edited the manuscript. XZ funded the experiments for the study. All authors contributed to the article and approved the submitted version.

FUNDING

This work was supported by the National Natural Science Foundation of China (81970825, 81970841, and 81221003), the Department of Science and Technology of Sichuan Province (22JCQN0028 and 2021YFS0386), the CAMS Innovation Fund for Medical Sciences (2019-12M-5-032), the Department of Chengdu Science and Technology (nos. 2018-YF05-01080-SN and 2021-YF05-01316-SN), and the National University Basic funding (ZYGX2021J026).

ACKNOWLEDGMENTS

The authors would like to thank Chengdu LiLai Biotechnology Co., Ltd for providing technical assistance with histology analysis.

SUPPLEMENTARY MATERIAL

The Supplementary Material for this article can be found online at: https://www.frontiersin.org/articles/10.3389/fcell.2021.783547/full#supplementary-material

REFERENCES

Aleman, T. S., Cideciyan, A. V., Aguirre, G. K., Huang, W. C., Mullins, C. L., Roman, A. J., et al. (2011). HumanCRB1-Associated Retinal Degeneration: Comparison with Therd8 Crb1-Mutant Mouse Model. *Invest. Ophthalmol. Vis. Sci.* 52, 6898–6910. doi:10.1167/iovs.11-7701

Baek, A., Yoon, S., Kim, J., Baek, Y. M., Park, H., Lim, D., et al. (2017). Autophagy and KRT8/keratin 8 Protect Degeneration of Retinal Pigment Epithelium under Oxidative Stress. *Autophagy* 13, 248–263. doi:10.1080/15548627.2016.1256932

Bhatti, M. T. (2006). Retinitis Pigmentosa, Pigmentary Retinopathies, and Neurologic Diseases. *Curr. Neurol. Neurosci. Rep.* 6, 403–413. doi:10.1007/s11910-996-0021-z

Biswas, P., Chavali, V. R., Agnello, G., Stone, E., Chakarova, C., Duncan, J. L., et al. (2016). A Missense Mutation in ASRGL1 Is Involved in Causing Autosomal Recessive Retinal Degeneration. *Hum. Mol. Genet.* 25, 2483–2497. doi:10.1093/hmg/ddw113

Bujakowska, K., Audo, I., Mohand-Saïd, S., Lancelot, M.-E., Antonio, A., Germain, A., et al. (2012). CRB1 Mutations in Inherited Retinal Dystrophies. *Hum. Mutat.* 33, 306–315. doi:10.1002/humu.21653

Cantor, J. R., Stone, E. M., Chantranupong, L., and Georgiou, G. (2009). The Human Asparaginase-like Protein 1 hASRGL1 Is an Ntn Hydrolase with β-Aspartyl Peptidase Activity. *Biochemistry* 48, 11026–11031. doi:10.1021/bi901397h

Chen, J. L., Lin, B. R., Gee, K. M., Gee, J. A., Chung, D. W., Frausto, R. F., et al. (2015). Identification of Presumed Pathogenic KRT3 and KRT12 Gene Mutations Associated with Meesmann Corneal Dystrophy. *Mol. Vis.* 21, 1378–1386.

Daiger, S. P., Sullivan, L. S., and Bowne, S. J. (2013). Genes and Mutations Causing Retinitis Pigmentosa. *Clin. Genet.* 84, 132–141. doi:10.1111/cge.12203

Deliyanti, D., Talia, D. M., Zhu, T., Maxwell, M. J., Agrotis, A., Jerome, J. R., et al. (2017). Foxp3+ Tregs Are Recruited to the Retina to Repair Pathological Angiogenesis. *Nat. Commun.* 8, 748. doi:10.1038/s41467-017-00751-w

den Hollander, A. I., Davis, J., van der Velde-Visser, S. D., Zonneveld, M. N., Pierrottet, C. O., Koenekoop, R. K., et al. (2004). CRB1 Mutation Spectrum in

Inherited Retinal Dystrophies. *Hum. Mutat.* 24, 355–369. doi:10.1002/humu.20093

Dias, M. F., Joo, K., Kemp, J. A., Fialho, S. L., Cunha, A. D. S., Jr., Woo, S. J., et al. (2018). Molecular Genetics and Emerging Therapies for Retinitis Pigmentosa: Basic Research and Clinical Perspectives. *Prog. Retin. Eye Res.* 63, 107–131. doi:10.1016/j.preteyeres.2017.10.004

Edqvist, P.-H. D., Huvila, J., Forsström, B., Talve, L., Carpén, O., Salvesen, H. B., et al. (2015). Loss of ASRGL1 Expression Is an Independent Biomarker for Disease-specific Survival in Endometrioid Endometrial Carcinoma. *Gynecol. Oncol.* 137, 529–537. doi:10.1016/j.ygyno.2015.03.055

Ferrari, S., Di Iorio, E., Barbaro, V., Ponzin, D., Sorrentino, F. S., and Parmeggiani, F. (2011). Retinitis Pigmentosa: Genes and Disease Mechanisms. *Curr. Genomics* 12, 238–249. doi:10.2174/138920211795860107

Gallina, D., Zelinka, C., and Fischer, A. J. (2014). Glucocorticoid Receptors in the Retina, Müller Glia and the Formation of Müller Glia-Derived Progenitors. *Development* 141, 3340–3351. doi:10.1242/dev.109835

Hartong, D. T., Berson, E. L., and Dryja, T. P. (2006). Retinitis Pigmentosa. *The Lancet* 368, 1795–1809. doi:10.1016/s0140-6736(06)69740-7

Huang, X.-F., Huang, F., Wu, K.-C., Wu, J., Chen, J., Pang, C.-P., et al. (2015). Genotype-phenotype Correlation and Mutation Spectrum in a Large Cohort of Patients with Inherited Retinal Dystrophy Revealed by Next-Generation Sequencing. *Genet. Med.* 17, 271–278. doi:10.1038/gim.2014.138

Huvila, J., Laajala, T. D., Edqvist, P.-H., Mardinoglu, A., Talve, L., Pontén, F., et al. (2018). Combined ASRGL1 and P53 Immunohistochemistry as an Independent Predictor of Survival in Endometrioid Endometrial Carcinoma. *Gynecol. Oncol.* 149, 173–180. doi:10.1016/j.ygyno.2018.02.016

Ildefonso, C. J., Jaime, H., Brown, E. E., Iwata, R. L., Ahmed, C. M., Massengill, M. T., et al. (2016). Targeting the Nrf2 Signaling Pathway in the Retina with a Gene-Delivered Secretable and Cell-Penetrating Peptide. *Invest. Ophthalmol. Vis. Sci.* 57, 372–386. doi:10.1167/iovs.15-17703

Iraci, N., Gaude, E., Leonardi, T., Costa, A. S. H., Cossetti, C., Peruzzotti-Jametti, L., et al. (2017). Extracellular Vesicles Are Independent Metabolic Units with Asparaginase Activity. *Nat. Chem. Biol.* 13, 951–955. doi:10.1038/nchembio.2422

Kadmiel, M., and Cidlowski, J. A. (2013). Glucocorticoid Receptor Signaling in Health and Disease. *Trends Pharmacol. Sci.* 34, 518–530. doi:10.1016/j.tips.2013.07.003

Li, W., Cantor, J. R., Yogesha, S. D., Yang, S., Chantranupong, L., Liu, J. Q., et al. (2012). Uncoupling Intramolecular Processing and Substrate Hydrolysis in the N-Terminal Nucleophile Hydrolase hASRGL1 by Circular Permutation. *ACS Chem. Biol.* 7, 1840–1847. doi:10.1021/cb300232n

Li, Z., Li, D., Tsun, A., and Li, B. (2015). FOXP3+ Regulatory T Cells and Their Functional Regulation. *Cell Mol Immunol* 12, 558–565. doi:10.1038/cmi.2015.10

Luhmann, U. F. O., Carvalho, L. S., Holthaus, S.-M. k., Cowing, J. A., Greenaway, S., Chu, C. J., et al. (2015). The Severity of Retinal Pathology in Homozygous Crb1rd8/rd8 Mice Is Dependent on Additional Genetic Factors. *Hum. Mol. Genet.* 24, 128–141. doi:10.1093/hmg/ddu424

Mehalow, A. K., Kameya, S., Smith, R. S., Hawes, N. L., Denegre, J. M., Young, J. A., et al. (2003). CRB1 Is Essential for External Limiting Membrane Integrity and Photoreceptor Morphogenesis in the Mammalian Retina. *Hum. Mol. Genet.* 12, 2179–2189. doi:10.1093/hmg/ddg232

Moll, R., Divo, M., and Langbein, L. (2008). The Human Keratins: Biology and Pathology. *Histochem. Cel Biol* 129, 705–733. doi:10.1007/s00418-008-0435-6

Naguib, S., Backstrom, J. R., Gil, M., Calkins, D. J., and Rex, T. S. (2021). Retinal Oxidative Stress Activates the NRF2/ARE Pathway: An Early Endogenous Protective Response to Ocular Hypertension. *Redox Biol.* 42, 101883. doi:10.1016/j.redox.2021.101883

Oshitari, T., Dezawa, M., Okada, S., Takano, M., Negishi, H., Horie, H., et al. (2002). The Role of C-Fos in Cell Death and Regeneration of Retinal Ganglion Cells. *Invest. Ophthalmol. Vis. Sci.* 43, 2442–2449.

Palczewski, K. (2006). G Protein-Coupled Receptor Rhodopsin. *Annu. Rev. Biochem.* 75, 743–767. doi:10.1146/annurev.biochem.75.103004.142743

Petersen-Jones, S. M. (1998). Animal Models of Human Retinal Dystrophies. *Eye (Lond)* 12, 566–570. doi:10.1038/eye.1998.146

Radoja, N., Komine, M., Jho, S. H., Blumenberg, M., and Tomic-Canic, M. (2000). Novel Mechanism of Steroid Action in Skin through Glucocorticoid Receptor Monomers. *Mol. Cel Biol* 20, 4328–4339. doi:10.1128/mcb.20.12.4328-4339.2000

Silva, A., Campellocosta, P., Linden, R., and Shollfranco, A. (2008). Interleukin-4 Blocks Proliferation of Retinal Progenitor Cells and Increases Rod Photoreceptor Differentiation through Distinct Signaling Pathways. *J. Neuroimmunology* 196, 82–93. doi:10.1016/j.jneuroim.2008.03.003

Sulaiman, R. S., Kadmiel, M., and Cidlowski, J. A. (2018). Glucocorticoid Receptor Signaling in the Eye. *Steroids* 133, 60–66. doi:10.1016/j.steroids.2017.11.002

Sun, Y., Lin, Z., Liu, C.-H., Gong, Y., Liegl, R., Fredrick, T. W., et al. (2017). Inflammatory Signals from Photoreceptor Modulate Pathological Retinal Angiogenesis via C-Fos. *J. Exp. Med.* 214, 1753–1767. doi:10.1084/jem.20161645

Conflict of Interest: The authors declare that the research was conducted in the absence of any commercial or financial relationships that could be construed as a potential conflict of interest.

Publisher's Note: All claims expressed in this article are solely those of the authors and do not necessarily represent those of their affiliated organizations, or those of the publisher, the editors, and the reviewers. Any product that may be evaluated in this article, or claim that may be made by its manufacturer, is not guaranteed or endorsed by the publisher.

Copyright © 2022 Zhou, Tian, Jiang, Yang, Jiang, Li, Jiang, Sun, Yang, Liu and Zhu. This is an open-access article distributed under the terms of the Creative Commons Attribution License (CC BY). The use, distribution or reproduction in other forums is permitted, provided the original author(s) and the copyright owner(s) are credited and that the original publication in this journal is cited, in accordance with accepted academic practice. No use, distribution or reproduction is permitted which does not comply with these terms.

frontiers in Cell and Developmental Biology

ORIGINAL RESEARCH
published: 14 February 2022
doi: 10.3389/fcell.2021.816397

Cysteine Substitution and Calcium-Binding Mutations in *FBN1* cbEGF-Like Domains Are Associated With Severe Ocular Involvement in Patients With Congenital Ectopia Lentis

OPEN ACCESS

Min Zhang[1,2,3†], *Zexu Chen*[1,2†], *Tianhui Chen*[1,2], *Xiaodong Sun*[3] *and Yongxiang Jiang*[1,2*]

[1]Department of Ophthalmology and Vision Science, Eye and ENT Hospital of Fudan University, Shanghai, China, [2]NHC Key Laboratory of Myopia (Fudan University), Key Laboratory of Myopia, Chinese Academy of Medical Sciences, and Key Laboratory of Visual Impairment and Restoration of Shanghai, Shanghai, China, [3]Department of Ophthalmology, Shanghai General Hospital, Shanghai Jiao Tong University School of Medicine, Shanghai, China

Edited by:
Qingjiong Zhang,
Sun Yat-sen University, China

Reviewed by:
Wenmin Sun,
Sun Yat-sen University, China
James Hejtmancik,
National Eye Institute (NEI),
United States
Xiaodong Jiao,
National Institutes of Health (NIH),
United States

***Correspondence:**
Yongxiang Jiang
yongxiang_jiang@163.com

†These authors have contributed equally to this work and share first authorship

Specialty section:
This article was submitted to Molecular and Cellular Pathology, a section of the journal Frontiers in Cell and Developmental Biology

Received: 16 November 2021
Accepted: 13 December 2021
Published: 14 February 2022

Citation:
Zhang M, Chen Z, Chen T, Sun X and Jiang Y (2022) Cysteine Substitution and Calcium-Binding Mutations in FBN1 cbEGF-Like Domains Are Associated With Severe Ocular Involvement in Patients With Congenital Ectopia Lentis. Front. Cell Dev. Biol. 9:816397. doi: 10.3389/fcell.2021.816397

Purpose: To investigate the clinical manifestations of congenital ectopia lentis (CEL) in patients with fibrillin (*FBN1*) calcium-binding epidermal growth factor (cbEGF)-like mutations.

Design: Retrospective cohort study.

Methods: Consecutive 68 CEL probands with *FBN1* cbEGF-like mutations were recruited, mostly comprising Marfan syndrome (MFS) patients. Patients were classified into the cysteine group ($n = 43$), calcium (Ca^{2+})-binding group ($n = 13$) or the others ($n = 12$) according to their genotypes. Ocular biometrics, morbidities and visual performance were compared among different mutation groups. Linear regression was used to evaluate the risk factors for axial length (AL) elongation.

Results: With age-adjustment, cysteine substitution and Ca^{2+}-binding mutations positively contributed to AL elongation (standardized coefficient: 0.410 and 0.367, $p = 0.008$ and 0.017, respectively). In addition, cataract formation was more frequently detected in patients with Ca^{2+}-binding mutations (observed $n = 3$, expected n = 1.0; $p = 0.036$). Patients with cysteine substitutions had the poorest preoperative visual acuity among the three groups ($p = 0.012$) and did not recover as well as other patients. More MFS diagnoses were made in patients with cysteine substitutions (observed $n = 16$, expected $n = 12.6$), while ectopia lentis syndrome was detected more often in patients with cbEGF-like mutations out of the functional regions (observed n = 6, expected n = 2.5; $p = 0.023$).

Conclusion: Compared with patients with cbEGF-like mutations out of functional regions, patients with cysteine substitutions or Ca^{2+}-binding mutations had longer ALs with age adjustment, poorer ocular involvement, visual performance, and systematic manifestations.

Keywords: cbEGF-like, FBN1, cysteine, congenital ectopia lentis, marfan syndrome

INTRODUCTION

Congenital ectopia lentis (CEL), or congenital lens subluxation, is a result of inheritable zonular dysplasia, and is the second leading cause of pediatric lens surgery after congenital cataracts. CEL can be an isolated ocular disease known as ectopia lentis syndrome (ELS) or be secondary to systematic disorders, such as Marfan syndrome (MFS), and both pathologies can be caused by fibrillin-1 (*FBN1*) mutations (Faivre et al., 2008).

FBN1 is a cysteine-rich glycoprotein that serves as the principal structural component of microfibrils, contributing to the force-bearing capacity of zonules in the eyes and other connective tissue throughout the body. Calcium-binding epidermal growth factor (cbEGF)-like domains are the most common domains of FBN1 (**Figure 1A**). This consensus sequence is especially important for FBN1-to-microfibril assembly (Schrijver et al., 1999; Smallridge et al., 1999; Hilhorst-Hofstee et al., 2010; Schrenk et al., 2018). It relies on two special functional regions, the conserved cysteines and calcium-binding (Ca^{2+}-binding) sequences, to construct a characteristic rigid rod-like shape (Haller et al., 2020). Disulfide bonds are formed among the six cysteine residues in a C1-C3, C2-C4, and C5-C6 pattern, which uniquely orchestrates protein folding. The Ca^{2+}-binding sequence includes a N-terminal loop and a C-terminal β-hairpin. They contribute to mechanosensitive calcium-binding

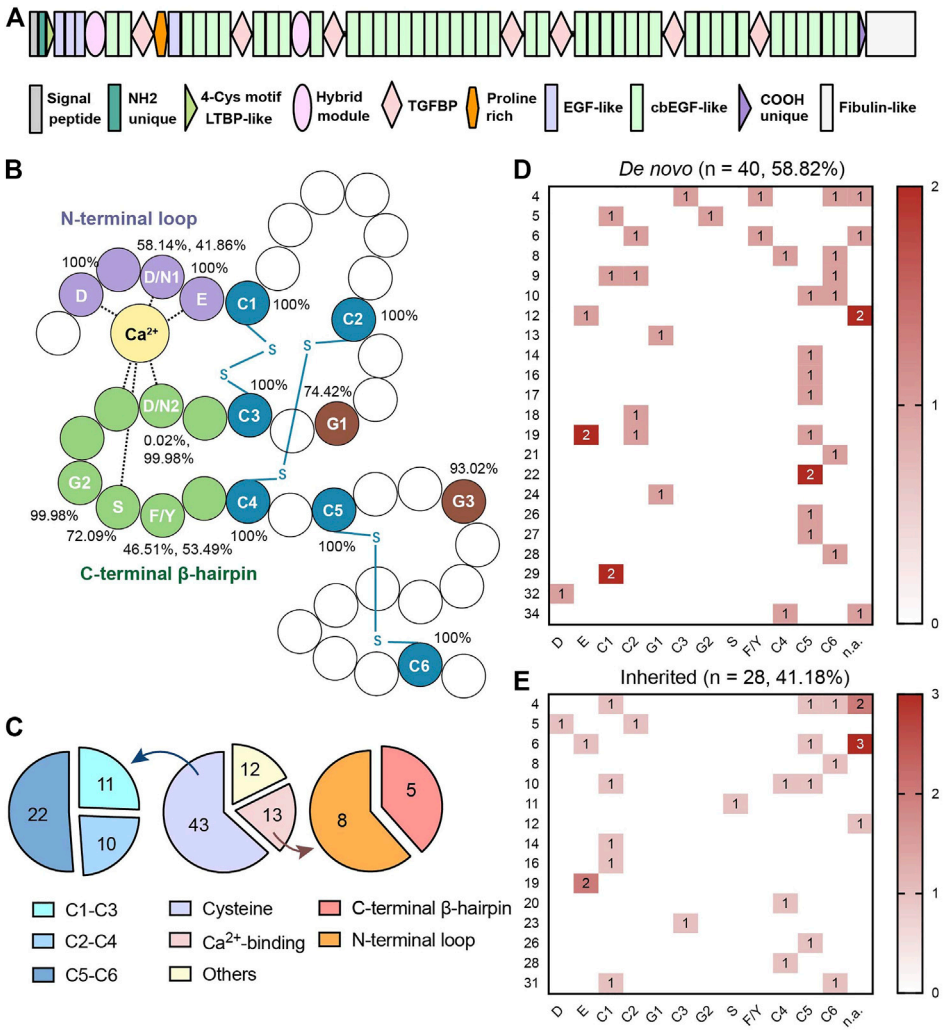

FIGURE 1 | (A) Schematic diagram of FBN1 with forty-three cbEGF-like domains. **(B)** Schematic diagram of cbEGF-like domain. The N-terminal loop, C-terminal β-harpin and cysteine residues were remarked in purple, green and blue, respectively. All the conservative amino acid residues were annotated with abbreviations in white. Disulfide bonds (-S-S-) are annotated in blue. Percentages of conservative amino acid residues in different cbEGF-like domains in FBN1 peptides are also listed. The same conservative amino acids are numbered according to the sequence. **(C)** Distribution of mutations in different regions in cbEGF-like domains. Both cysteine pairs and Ca^{2+}-binding regions were termed as functional regions. Cysteine substitutions and Ca^{2+}-binding mutations were further divided into 3 pairs and 2 terminals, respectively. **(D,E)** are heatmaps of conservative amino acids mutations in patients with *de novo* mutations and with inherited mutations, respectively. Each line indicates one cbEGF-like domain in FBN1 and each column indicates one conservative amino acid. Each line indicates one cbEGF-like domain in FBN1 and each column indicates one conservative amino acid. cbEGF-like 11–18 fall into the neonatal region of FBN1. D = aspartic acid, N = asparagine, E = glutamic acid, C = cysteine, G = glycine, S = serine, F = phenylalanine, Y = tyrosine. The numbers following the amino acid indicated its order.

dynamics and the further stabilization of FBN1 (Schrenk et al., 2018). These two evolutionarily conserved functional regions extend alongside the cbEGF-like repeats for microfibril integrity and provide protection against proteolysis (Schrenk et al., 2018; Haller et al., 2020). Both of them are key functional regions in cbEGF-like domains (**Figure 1B**).

Around 60% of *FBN1* missense mutations occur in cbEGF-like domains (Haller et al., 2020; Chen et al., 2021a). These mutations are predicted to disrupt disulfide bonds or reduce calcium binding by removing cysteines or a side-chain ligand for calcium (McGettrick et al., 2000). Clinical manifestations, including cardiovascular (Wu et al., 2020), skeletal, and ophthalmic (Chen et al., 2021b) disorders, of patients with general *FBN1* mutations were widely analyzed. Cardiovascular problems have often been reported to be associated with cysteine substitutions in cbEGF-like domains (Kühne et al., 2013), but there is a lack of targeted research on the correlations between genotype and phenotype for cbEGF-like mutations and ocular lesions.

In addition, mutations in cbEGF-like domains 11–18, i.e., eight cbEGF-like domains in the neonatal region [exons 24–32, according to next-generation sequencing (NGS)], generally accounted for about 17% of missense mutations (Kühne et al., 2013; Haller et al., 2020; Wu et al., 2020). This region is named after its severity to frequently cause death before 2 years of age (Child, 2017). Severe cardiovascular involvement is reported to be associated with neonatal forms (Wu et al., 2020), especially those with cysteine substitution (Child, 2017). These cbEGF-like mutations in the neonatal region are systematic and are probably responsible for ocular microfibril disorganization and ophthalmic pathologies. Clinical observation is needed on this topic.

In this study, we reviewed the pathology of CEL patients with missense cbEGF-like mutations in *FBN1*. Most of them received surgical treatment and were followed up. We wished to address the following questions: 1) What are the ocular characteristics of CEL patients with cbEGF-like mutations? 2) Do patients with mutations in cysteine residues, Ca^{2+}-binding sequences, and other sequences have different ocular biometrics and different distributions of ocular comorbidities, and do they have similar ocular involvement and systematic manifestation? 3) Do patients with cbEGF-like mutations in neonatal regions have ocular involvement earlier than patients with other cbEGF-like mutations?

METHODS

Consecutive CEL probands, mostly MFS patients, that visited our Department of Ophthalmology from March 2017 to March 2021 were initially recruited to this retrospective clinical observational case series (N = 170). The general inclusion and exclusion criteria were as described in published works (Chen et al., 2021a; Chen et al., 2021b). Briefly, CEL probands with a medical history of ocular trauma or surgeries were excluded.

The study was approved by the Human Research Ethics Committee of the Eye and ENT Hospital of Fudan University (no. 2020126–1) and performed with adherence to the tenets of the Declaration of Helsinki. It was also registered with the Chinese Clinical Trial Registry (ChiCTR2000039132). Written informed consent was obtained from all participants or their guardians before peripheral blood samples were collected.

Ophthalmic Examination

Full ophthalmic examinations were performed on all CEL probands, and their medical histories were evaluated. The classification of lens subluxation directions is shown in **Supplementary Figure S1A.** The severity of lens subluxation was measured as described before (Chen et al., 2021c; Zhang et al., 2021) (**Supplementary Figure S1B**). Briefly, the curvature degree of the ring (pupil)-ring (lens) cross was measured with the pupil dilated to an 8-mm-diameter under slit-lamp examination. Curvature less than 180-, 180- to 270- and over 270-degrees were defined as mild, moderate and severe lens subluxation, respectively. Anterior segmental biometrics and axial length (AL) were measured using a partial coherence interferometry (iolmaster 700, Carl Zeiss Meditec AG, Jena, Germany) and a rotating Scheimpflug camera (Pentacam AXL, Oculus GmbH, Wetzlar, Germany). Ocular comorbidities were also detected by B-scan ultrasound and ultrasound biomicroscopy (MD-300L, 50-MHz probe transducer; Meda Co., Ltd., Tianjin, China).

Genetic Screening

Peripheral blood samples underwent panel-based NGS (Amplicon Gene, Shanghai, China) for the exon sequences of 289 genes of common inherited anterior eye diseases (**Supplementary Table S1**). For patients with undetected pathogenic mutations but suspected *FBN1* mutations, multiplex ligation-dependent probe amplification (MLPA) of this gene was performed using SALSA MLPA Probemix Kits (P065-C1/P066-C1, MRC-Holland, Amsterdam, Netherlands).

The frequencies of identified variants were annotated through the Genome Aggregation Database (https://gnomad.broadinstitute.org/). Pathogenicity was also predicted by in silico predictive algorithms (SIFT, PolyPhen and Condel) using an integrated online software, the Ensembl Variant Effect Predictor (http://uswest.ensembl.org/info/docs/tools/vep/index.html).

Genotype Classification

The causality nature of each *FBN1* mutation was evaluated using Ghent-2 criteria (Loeys et al., 2010). All mutations were classified following the American College of Medical Genetics and Genomics guidelines (Richards et al., 2015). All *FBN1* missense mutations were reviewed, and splicing variants and premature termination codons were excluded. Missense mutations were further classified based on the amino acid changes, location, and protein domains. The UMD-FBN1 database (http://umd.be/FBN1/) was referred to for the mapping of 43 cbEGF-like domains. Some special regions were annotated, such as the Ca^{2+}-binding regions in the cbEGF-like domain (including N-terminal loop and C-terminal β-hairpin) (Smallridge et al., 1999; McGettrick et al., 2000; Haller et al., 2020) and the six conservative cysteine residues (C1-C6) (Suk et al., 2004).

Patients Selection and Diagnoses

Probands with heterozygous pathogenic or likely pathogenic *FBN1* mutations were selected as shown in the flow chart

(Supplementary Figure S2). Only the probands of pedigrees were recruited in this study. Considering high binocular correlation in these patients, as was shown in our previous study (Chen et al., 2021b), only one random eye from each proband were studied to avoid selection bias.

The systematic diagnosis of MFS was based on Ghent-2 nosology (Loeys et al., 2010). ELS was diagnosed in CEL adults with no history of cardiovascular disorders to avoid confounding. Otherwise, the patients were annotated as potential MFS cases.

Surgical Treatment and Postoperative Follow-Ups

CEL patients underwent modified capsular tension ring (MCTR) and intraocular lens (IOL) in-the-bag implantation, as previously described (Chen et al., 2021c). Generally, the lens was aspired, but the capsular bag was preserved. The MCTR was sutured to the sclera through a sulcus by 9–0 polypropylene with the modified knotless Z-suture technique.

These patients were followed up in our out-patient department; surgical complications, such as retinal detachment, were reviewed, and visual records were obtained. The best corrected visual acuity (BCVA) was only recorded if posterior capsular opacification was not detected or was treated with Nd:YAG laser.

Statistical Analyses

The distributions of ocular biometric parameters were tested for normality with the Shapiro-Wilk test. The Kruskal-Wallis test with Bonferroni correction was applied to compare the parameters among different mutation groups, and patients with and without neonatal mutations were compared with the Wilcoxon Mann-Whitney test. Spearman's correlation test was used to explore the relationships among ocular biometrics and ages. The related-samples Wilcoxon signed-rank test was utilized to test BCVA changes before and after surgical treatment. BCVA records of patients with a medical history of retinal detachment were excluded in this analysis. Chi-square test or Fisher's exact test was employed to compare the direction and severity of lens subluxation and the incidence of ocular comorbidities, as appropriate. Unmeasurable or unreliable values due to incoordination or incorporation were annotated as missing. Linear regression was used to identify the risk factors for AL elongation. $p < 0.05$ was considered statistically significant, and statistical analyses were performed using SPSS for Mac (version 26, 64-bit edition, IBM Corp, Armonk, NY, United States).

RESULTS

Cohort Characteristics and Phenotypic Summaries

A total of 68 (44.12%) probands were included in the genotype-phenotype analyses of the cbEGF-like mutations. The mean age of our cohort of 39 boys/men and 29 girls/women was 12.47 ± 12.63 (median: 7, range: 2–58) years old. **Table 1** presents the demographics and clinical characteristics of the enrolled eyes. Among these probands, 28 (41.18%) patients had cbEGF-like mutations inherited from their parents, while 40 (58.82%) had *de novo* mutations. Our spontaneous mutation rate was much higher than that previously reported (Madar et al., 2019).

Nearly all the patients had bilateral lens subluxation ($n = 67$, 98.53%) rather than unilateral lens subluxation. Almost half of the patients had lenses subluxated into the superior-nasal quadrant ($n = 32$, 47.06%) or nasal side ($n = 9$, 13.24%). Most patients had lens subluxation within three quadrants (≤270°), including 24 (35.29%) mild cases and 34 (50.00%) moderate cases. The most common ocular comorbidity was posterior staphyloma ($n = 20$, 29.41%). **Table 1** also presents the ocular manifestations of all enrolled patients, including long AL (25.06 ± 3.03 mm), flat cornea (total corneal Km = 40.26 ± 1.79 D), and reduced corneal spherical aberration (SA; 0.096 ± 0.133 μm).

There were 66 patients who received surgical treatment (**Table 1**). Of the remaining two treatment-naïve patients, one had a case of lens subluxation that was not severe enough to warrant intervention, and the other was poorly cooperative. During the maximum 24-months follow-up period, three cases (4.55%) were complicated with postoperative retinal detachment. In patients with no severe postoperative complications, the median LogMAR BCVA recovered from 0.52 to 0.15 ($p < 0.001$).

The genotypes, phenotypes and segregation of all enrolled patients are summarized in **Supplementary Tables S2–4**.

Distribution of Mutation Sites in cbEGF-like Domains

Out of the 47 EGF modules in *FBN1*, 43 contained the cbEGF consensus sequence (Schrenk et al., 2018). This study showed that all missense mutations were distributed over 27 cbEGF-like domains (27/43 = 62.79%). Fifty-six (82.35%) patients had mutations in functional regions **(Figure 1C)**, and a comparative percentage of conservative amino acid mutations was also detected in patients with *de novo* mutations (35/40 = 87.50%; **Figure 1D**). There were 43 patients (43/68 = 63.24%) with cysteine substitutions in cbEGF-like domains, and nearly half of them (22/43, 51.16%) had mutations in the C5-C6 pair. The C5-C6 pair was also the top *de novo* and the top inherited mutation hotspot (15/40 = 37.5%, **Figures 1D,E**). Specifically, the most prevalent mutation was c.4096G > A/p.E1366K in cbEGF 19 (4/68 = 5.88%).

Ocular Biometrics and Age-Related Changes With cbEGF-like Mutations

To better evaluate the ocular biometrics of patients with different cbEGF-like mutations and determine the potential role of the *FBN1* genotypes, the age-related effects on ocular biometrics first had to be determined and removed.

Five ocular biometrics were found to be significantly correlated with age: corneal endothelial cell counts ($r_s = -0.489$, $p < 0.001$, $n = 59$), AL ($r_s = 0.407$, $p = 0.001$, $n = 64$), total corneal K1 ($r_s = 0.294$, $p = 0.038$, $n = 50$), SA ($r_s = 0.364$, $p = 0.006$, $n = 56$), and higher-order aberrations ($r_s = -0.277$, $p = 0.039$, $n = 56$, **Supplementary Figure S3**). Furthermore, age-adjusted linear regression showed that cysteine

TABLE 1 | Demographics and clinical characteristics of patients with enrolled eyes.

Characteristics				Counts (%) or mean ± SD (median, range)
Demographics	Male/female			39 (57.35)/29 (42.65)
	Age (years old)	≤20		53 (77.94)
		>20		12.47 ± 12.63 (2 to 58, 7) 15 (22.06)
	Neonatal/others			13 (19.12)/55 (80.88)
Ocular phenotypes	Bilateral/unilateral subluxation			67 (98.53)/1 (1.47)
	Right/left			32 (47.06)/36 (52.94)
	Comorbidity	MSP		8 (11.76)
		Cataract		5 (7.35)
		Strabismus		6 (8.82)
		Staphyloma		20 (29.41)
		Glaucoma		3 (4.41)
		Ciliary body cyst		4 (5.88)
		Megalocornea		4 (5.88)
	AL (mm), n = 64)			25.06 ± 3.03 (24.27, 21.11 to 33.62)
	ACD (mm), n = 43			3.21 ± 0.45 (3.24, 1.80 to 4.46)
	LT (mm), n = 30			3.83 ± 0.98 (3.83, 1.36 to 5.90)
	WTW (mm), n = 37			12.21 ± 0.56 (12.20, 11.2 to 13.5)
	Corneal biometrics	Anterior K1 (D), n = 52		39.71 ± 1.64 (39.85, 36.3 to 43.7)
		Anterior K2 (D), n = 52		41.45 ± 1.74 (41.40, 38.2 to 46.5)
		Anterior Km (D), n = 59		40.60 ± 1.72 (40.60, 37.7 to 46.0)
		Total K1 (D), n = 50		39.34 ± 1.88 (39.50, 35.9 to 45.4)
		Total K2 (D), n = 50		41.22 ± 1.99 (40.90, 37.6 to 46.5)
		Total Km (D), n = 56		40.26 ± 1.79 (40.10, 36.9 to 45.9)
		TCRP (D), n = 55		39.89 ± 1.59 (40.10, 36.7 to 45.1)
		SA (μm), n = 56		0.096 ± 0.133 (0.091, -0.415 to 0.584)
		HOA (μm), n = 56		0.233 ± 0.281 (0.171, 0.082 to 1.650)
		CCT (μm), n = 59		542.86 ± 41.25 (541, 458 to 640)
		Endothelial cell count (/mm^2), n = 59		3273.05 ± 437.61 (3307, 2013 to 4365)
Surgical treatment	Treatment/naïve			66 (97.06)/2 (2.94)
	Postoperative RD[a]			3 (4.55)
	Follow-up of visual outcomes[b], n = 47	Duration (months)		13.91 ± 9.38, 12 (1 to 24)
		BCVA (LogMAR)	Baseline	0.71 ± 0.48, 0.52 (0.10 to 2.00)
			Postoperative	0.19 ± 0.22, 0.15 (0.00 to 1.30)
			P value[c]	<0.001

Others refer to lens tremor or anterior or posterior subluxation.

SA, spherical aberration; HOA, high-order aberrations; MSP, microspherophakia; AL, axial length; ACD, anterior chamber depth; LT, lens thickness; WTW, white-to-white, K1 = minimal corneal power, K2 = maximal corneal power, Km = mean corneal power, TCRP, total corneal refractive power (centered at corneal apex), BCVA, best corrected visual acuity; RD, retinal detachment.

[a]*With or without postoperative RD, complications were recorded in all 66 patients.*

[b]*Complete visual outcomes were obtained in 49 patients. Records of 2 patients with medical history of retinal detachment were excluded and visual outcomes of 47 patients were presented here.*

[c]*p value was reported by related-samples Wilcoxon signed-rank test.*

substitution ($p = 0.008$) and Ca^{2+}-binding mutations ($p = 0.017$) were significantly and positively associated with AL elongation, even if no differences in age or AL distribution were detected among the three mutation groups (**Table 2**).

The only ocular parameter found to be significantly different among the mutation groups was SA ($p = 0.009$, **Supplementary Figure S4A**). Patients with cysteine substitutions, in particular, had a lower SA than those with cbEGF-like mutations out of the functional regions ($p = 0.007$). Though there was no significant age difference among the three mutation groups ($p = 0.771$, **Supplementary Figure S4B**), linear regression showed that for SA reduction, age was a significant factor ($p < 0.001$) but not cysteine substitution ($p = 0.174$). The reduced SA in the cysteine substitution group could be explained by lower age of patients with cysteine substitutions rather than effects of cysteine substitutions themselves.

Lens Subluxation and Ocular Comorbidities With cbEGF-like Mutations

Figures 2A–C provides examples of lens subluxation with and without ocular comorbidities. No significant differences in subluxation direction ($p = 0.590$) or subluxation severity ($p = 0.911$) were detected among the three mutation groups (**Supplementary Table S5**).

Among CEL patients with ocular comorbidities, one 6-year-old boy with a cataract was noted (c.3921T > G/p.Cys1307Trp). Advanced analysis showed that there was an increase in cataract formation in patients with Ca^{2+}-binding mutations ($p = 0.036$, **Figure 2D**). However, the three cataract patients with Ca^{2+}-binding mutations were 22, 31, and 58 years old, and they all had quite long AL (28.73, 29.61, and 30.09 mm, respectively). Therefore, whether cataract formation can be directly attributed

TABLE 2 | Mutations in Cysteine or Calcium-binding related regions contributed to AL-elongation.

Mean ± SD (median, range) or observed counts (expected counts)		**Functional regions (*n* = 53)**		**Others (*n* = 11)**	***p* values**
		Cysteine (*n* = 41)	**Ca^{2+}-binding (*n* = 12)**		
Age (years old)		11.60 ± 9.81 (8, 2–41)	12.77 ± 15.92 (6, 3–58)	15.25 ± 17.78 (6.5, 3–54)	0.771[a]
AL (mm)	≤26 (*n* = 43)	26 (27.6)	6 (8.1)	11 (7.3)	0.091[b]
	26–28 (*n* = 6)	4 (3.8)	2 (1.1)	0 (1.0)	
	>28 (*n* = 15)	11 (9.6)	4 (2.8)	0 (2.6)	

Linear regression: AL (mm)	**Standardized coefficient**	***t***	***p* values[c]**
Constant	—	23.146	<0.001
Age (years old)	0.354	3.066	0.003
Cysteine	0.410	2.721	0.008
Ca^{2+}-binding	0.367	2.453	0.017

AL, axial length. There were 4 AL values missing, n = *64.*

[a]p *value was reported by Kruskal-Wallis test.*

[b]p *value was reported by Fisher exact test.*

[c]p *values were reported by linear regression and the dependent variable was AL (mm).*

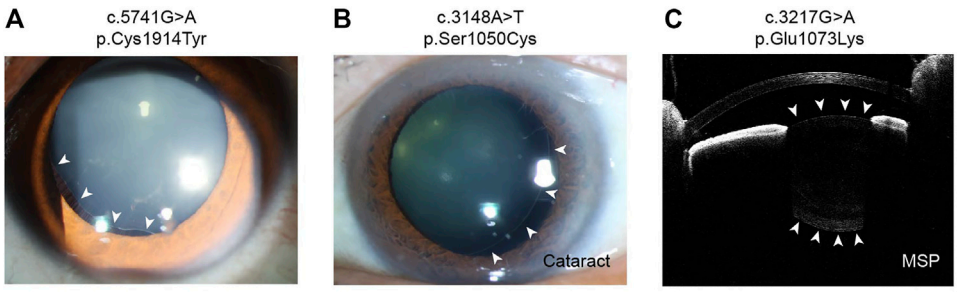

D

Counts (expected)	Cysteine (n = 43)	Ca^{2+}-binding (n = 13)	Others (n = 12)	*P* value
Cataract (n = 5)	1 (3.2)	3 (1.0)	1 (0.9)	0.036
n.a. (n = 63)	42 (39.8)	10 (12.0)	11 (11.1)	

E

		Glaucoma		OR (95% CI)	*P* value
		Yes (n = 3)	No (n = 65)		
MSP	Yes (n = 8)	2	6	19.67 (1.55 to 250.15)	0.035
	No (n = 60)	1	59		

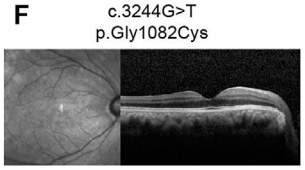

FIGURE 2 | Photos of CEL in patients with *FBN1* cbEGF-like mutations and their ocular comorbidities. **(A)** Right eye of patient no. 7 with mild lens subluxation into the superior-temporal quadrant. **(B)** Left eye of patient no. 20 with moderate lens subluxation and cataract. **(C)** Right eye of patient no. 47 with severe lens subluxation and MSP. White arrowhead in **(A,C)** indicate the border of lens. **(D)** Inclination of cataract formation was detected in patients with Ca^{2+}-binding mutations. *p* values were reported by Fisher's exact test. **(E)** Consistency of MSP and glaucoma in CEL patients. MSP = microspherophakia. OR = odds ratio, CI = confidence interval. *p* value was reported by Fisher's exact test. **(F)** Optical coherence tomography of patient no. 2 with normal macular structure. MSP = microspherophakia.

to mutations or secondarily to the patients' relatively advanced age or high myopia is uncertain. Although no inclination of other ocular comorbidities was detected in patients with functional region mutations (**Supplementary Table S5**), MSP and glaucoma were often observed consistently (**Figure 2E**), indicating the high susceptibility of MSP cases to glaucoma.

Incidentally, no retinal abnormalities were detected in any patient on optical coherence tomography (OCT) (**Figure 2F**), except for postoperative retinal detachment in three cases.

Visual Performance and Systematic Diagnoses of Patients With cbEGF-like Mutations

Patients with cysteine substitutions had the poorest BCVA among the different mutation groups (p = 0.012 at baseline,

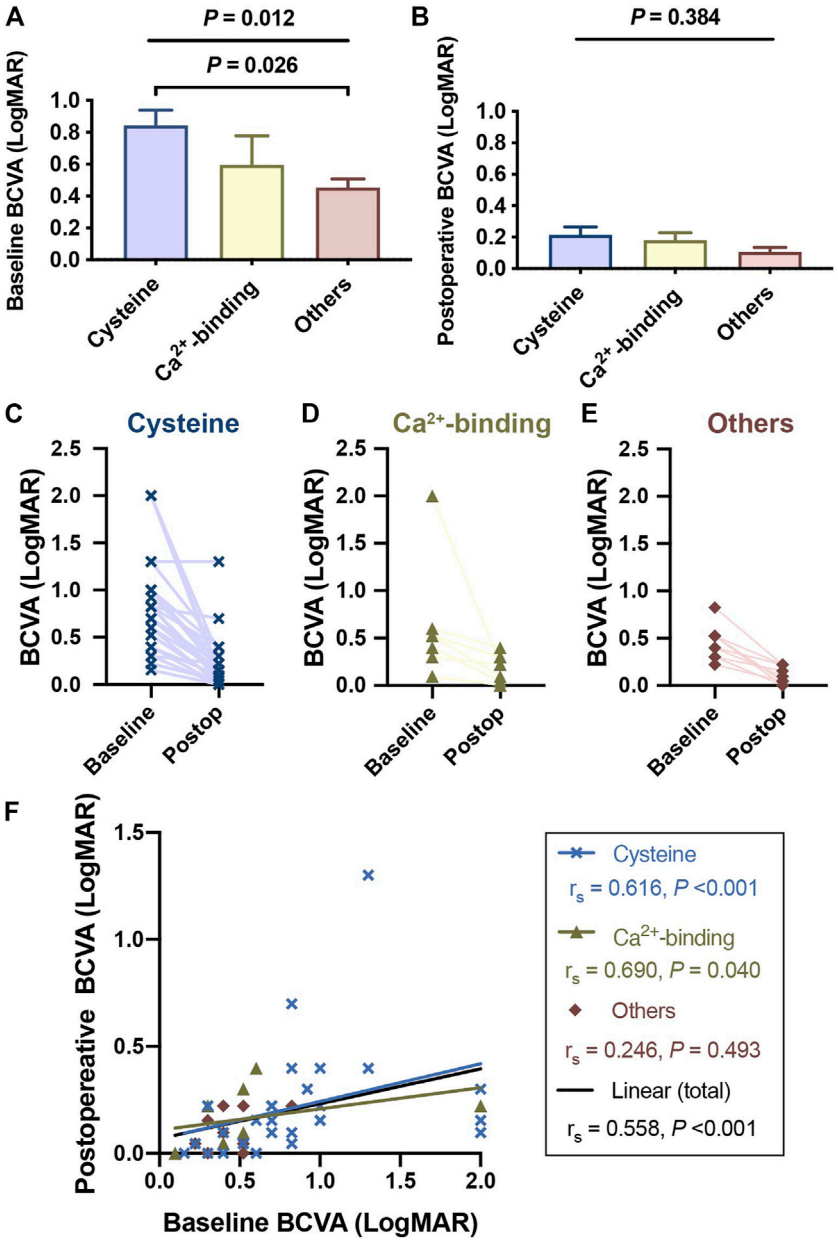

FIGURE 3 | Patients with cysteine substitutions had the poorest visual performance among different functional region groups. Complete visual outcomes before and after surgical treatments were obtained in 49 patients. Records of 2 patients with the medical history of retinal detachment were excluded and visual outcomes of 47 patients were presented here. **(A)** Patients with cysteine substitutions had the poorest visual performance among different functional region groups, reported by Kruskal-Wallis test (with Bonferroni correction) at the baseline. **(B)** Though this difference was not significant anymore after the surgical treatment, patients who had cbEGF-like mutations out of functional regions still tended to have better visual outcomes. **(C,E)** showed the BCVA changes of each patient with different cbEGF-like mutations before and after the surgical treatment. Postop = postoperative. **(F)** Linear correlation between the baseline BCVA and postoperative BCVA. The blue line and the black line indicated the linear correlations of these two variables in the patients with cysteine substitution and in all study populations, respectively. r_s and p values were reported by Spearman's correlation test.

Figure 3A; p = 0.384 postoperatively, **Figure 3B**), and there was obvious visual improvement before and after surgical treatment (p < 0.001). The median LogMAR BCVA recovered from 0.76 to 0.15 (p < 0.001) in the cysteine group, from 0.52 to 0.22 in the Ca^{2+}-binding group (p = 0.008), and from 0.46 to 0.07 in the remaining patients (p = 0.005). Patients in the different groups were followed up over similar durations (p = 0.926, **Supplementary Table S6**). Although the postoperative BCVA was not significantly different among the different mutation groups (p = 0.330), the values showed a decreasing trend in the order of cysteine group, Ca^{2+}-binding group, and others.

TABLE 3 | Patients with cbEGF-like mutations in functional regions were more vulnerable to systematic disorders.

Observed counts (expected counts)		Diagnoses (*N* = 68)			*p* value
		potential MFS (*n* = 34)	MFS (*n* = 20)	ELS (*n* = 14)	
Functional regions (*n* = 56)	Cysteine (*n* = 43)	23 (21.5)	16 (12.6)	4 (8.9)	0.023
	Ca^{2+}-binding (*n* = 13)	7 (6.5)	2 (3.8)	4 (2.7)	
Others (*n* = 12)		4 (6.0)	2 (3.5)	6 (2.5)	

p value was reported by Fisher's exact test. MFS, Marfan syndrome; ELS, Ectopia lens syndrome. Others refer to cbEGF-like mutations out of cbEGF-like functional regions.

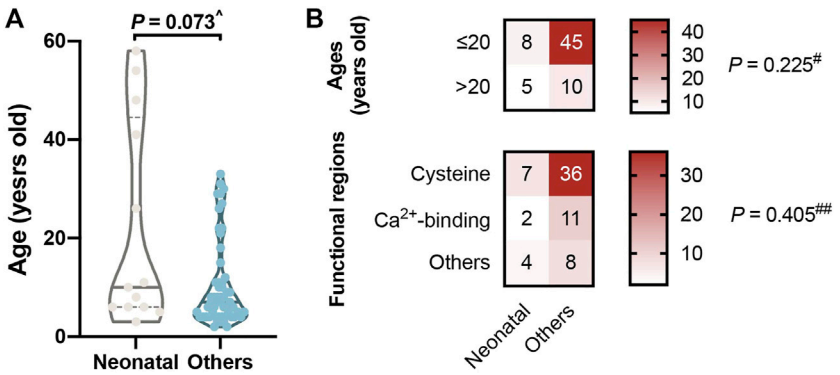

FIGURE 4 | Mutations in neonatal regions (cbEGF like 11–18). **(A)** No significant difference in ages between the neonatal group and the others. It was surprising to find that our four oldest patients all had mutations in the neonatal group. **(B)** Neonatal mutations are distributed adequately among different age strata and functional regions. ^*p* value reported by Wilcoxon Mann-Whitney test, #*p* value reported by Pearson Chi-square test with continuity correction and ##*p* value reported by Fisher's exact test.

Similar results were detected in the systematic diagnoses. More MFS diagnoses were found in the cysteine group (observed n = 16, expected n = 12.6), while ELS was more often detected in patients with cbEGF-like mutations out of the functional regions (observed n = 6, expected n = 2.5; p = 0.023, **Table 3**). Patients with Ca^{2+}-binding mutations tended to have similar diagnosis distributions to the overall study populations. These results indicate that patients with cysteine substitutions have the worst overall systematic manifestations in all patients with cbEGF-like mutations.

cbEGF-like Mutations in the Neonatal Region

A total of 13 (19.12%) patients had mutations that fell within the neonatal region (**Table 1**), comparable to the reported 17% percent of neonatal missense mutations in all *FBN1* missense mutations (Kühne et al., 2013). We were surprised to find that patients in the neonatal group were generally older than the others, although not significantly (p = 0.073; **Figure 4A**). One patient with lens subluxation was even diagnosed at 58 years of age (c.3148A > T, p. Ser1050Cys); he had lens subluxation combined with cataract but was only diagnosed as ELS. In addition, neonatal mutations are distributed adequately among different age strata and functional regions (p = 0.225 and 405, respectively; **Figure 4B**).

Detailed differences were further detected in cbEGF-like mutations in the neonatal region. A hotspot of cbEGF-like mutations in the neonatal region was cbEGF-like 12 (n = 4), but no patient's carried cysteine substitutions. Instead, cysteines eliminations were found in all cbEGF-like 14 mutations (n = 3), which was the second hotspot in the neonatal region. Considering the other domains' long-range cooperative dependence on cbEGF-like 12[19], the importance of cysteines was again suggested. Furthermore, there were no mutations in cbEGF-like 13 detected in our patients, which may have contributed to its highest Ca^{2+}-binding affinity and high-malignancy of the corresponding mutations.

DISCUSSION

In this study, we reviewed the ocular biometrics and medical histories of 68 CEL patients with cbEGF-like mutations in *FBN1*. The involvement of cysteine substitutions or Ca^{2+}-binding mutations, along with the patients' age, contributed to AL elongation. More severe ocular involvement and systematic manifestations were also found in these patients with mutations in functional regions. We showed that cysteine

substitutions in cbEGF-like domains, along with Ca^{2+}-binding mutations, were of great clinical significance in CEL patients.

We observed long AL (25.03 ± 3.04 mm), flat cornea (Km = 40.58 ± 1.71 D), reduced corneal SA (0.096 ± 0.133 μm), and frequent lens subluxation into the superior-nasal quadrant (n = 31, 45.59%) in CEL patients. These were consistent with our previous findings (Chen et al., 2018a; Chen et al., 2018b; Chen et al., 2021a; Chen et al., 2021b; Chen et al., 2021d) and reports of other MFS patients (Sandvik et al., 2019; Vanhonsebrouck et al., 2021). AL was found to be reasonably increased with aging (r_s = 0.407, p = 0.001, **Supplementary Figure S3**). The positive correlations between the corneal SA and ages in our patients (r_s = 0.364, p = 0.006) were also consistent with a study of a normal population (Navarro et al., 2013). However, we found that in patients with cbEGF-like mutations, the total corneal K1 increased with aging (r_s = 0.294, p = 0.038). This differs from the overall findings for MFS patients with lens subluxation (Chen et al., 2018a) or healthy children (He et al., 2021; Liu et al., 2021), indicating the specific role of cbEGF-like mutations, rather than general *FBN1* mutations, in age-related corneal changes.

Therefore, statistical comparisons of ocular biometrics among the different mutation groups should first be weighted for age. After age-adjustment, linear regression showed that both cysteine substitutions and Ca^{2+}-binding mutations contributed to AL elongation (**Table 2**). The cysteine substitution even contributed to AL elongation more than Ca^{2+}-binding mutations (standardized coefficient: 0.410 vs. 0.367). We also found that no patients with mutations out of the functional regions had ALs longer than 26 mm (**Table 2**). Hence, the findings re-confirmed the involvement of functional region mutations in ocular development.

In addition to the ocular biometrics, functional mutations in cbEGF-like domains also contributed to ocular comorbidities, such as cataracts, MSP, and glaucoma (**Figure 2**). In this study, patients with Ca^{2+}-binding mutations, but not cysteine substitutions, tended to develop cataracts (p = 0.036, **Figure 2D**). The comorbidities of MSP and glaucoma were also detected. Glaucoma is considered to be secondary to MSP (Yu et al., 2020) and to lens subluxation (Zhou et al., 2021). We detected a significantly increased incidence of glaucoma development with MSP [odds ratio (OR): 19.67, p = 0.035; **Figure 2E**]. However, the incidence of glaucoma in MSP patients was reported to be 44–51% (Yu et al., 2020), much higher than those detected in our cohort (2/8 = 25%). This might be due to the posterior dislocation of MSP in these patients, as vitreous liquefaction at the base was often observed in those patients (Remulla and Tolentino, 2001). Interestingly, only one CEL patient with glaucoma but without MSP, had cysteine substitutions (c.2810G > A/p.Cys937Tyr). Once again, the functional region mutations caught our attention. More work is needed to clarify the underlying mechanisms of cbEGF-like mutations in zonular weakness and the lens subluxation-MSP-glaucoma axis.

We also found that patients with cysteine substitutions had poor visual performance. Previous 10-years reinvestigation reported that the visual potential of MFS patients was relatively good (Sandvik et al., 2019). Our results are consistent with this interpretation, as 41 (87.22%) patients had postoperative LogMAR BCVA of better than 0.3 (**Figure 3**). However, those with cysteine substitutions had the poorest preoperative LogMAR BCVA among the three groups and did not recover as well as those in the other two mutation groups (**Figures 3C–F**). This was difficult to explain, as no retinal abnormalities were detected in any patient given OCT (**Figure 2F**), except for three with postoperative retinal detachment (not included in the statistical analyses of visual performance). The fundus blood flow density of patients with cysteine substitutions might be affected, leading to defects in visual function. Amblyopia might also contribute to this situation. Advanced visual analyses of these patients' data are needed to clarify the underlying mechanism.

Long-term follow-up also showed that the risk of developing vision-threatening complications, such as retinal detachment in MFS patients, was still much higher than in the normal population (Sandvik et al., 2019). In this study, three retinal detachment cases were detected (Sandvik et al., 2019). Though all three retinal detachment cases had cysteine substitutions, the surgical complications were rarely seen in general study populations, and it was difficult for us to investigate the correlation between functional region mutations and retinal detachment. All these patients had posterior staphyloma and had almost the longest ALs in our cohort. Thus, pathological myopia may take the responsibility for myopic rhegmatogenous retinal detachment (Ruiz-Medrano et al., 2019).

When we focused on cbEGF-like mutations in the neonatal regions, they were all found to occur in patients older than 2 years. This came from the recruitment methods of our study, as neonatal MFS with severe cardiovascular and skeletal abnormalities tend to be treated in the Department of Pediatrics rather than the Department of Ophthalmology. But it was surprising to find that our four oldest patients all had mutations in the neonatal group (**Figure 4**). The involvement of different functional region mutations and changes in cbEGF-like domain rigidity might contribute to this phenomenon. For example, the cbEGF-like 12/13 pair is located within the longest contiguous section of cbEGF-like domains, and a number of mutations in this pair are associated with the most severe neonatal MFS (Whiteman et al., 2007). In addition, cbEGF-like 13 possesses the highest Ca^{2+} affinity in any cbEGF-like investigated from FBN1 (Smallridge et al., 1999). Because cbEGF-Ca^{2+} affinity can be modulated by the domain that is linked to its N-terminus, the affinities of the cbEGF-like 13/14 pair are also substantially higher than those of the C-terminal region of FBN1 (Smallridge et al., 1999). Our observation was in accordance with these biomechanical characteristics, as no mutation was detected in cbEGF-like 13. Additionally, mutations other than cysteine substitutions in cbEGF-like 12 and cysteine substitutions in cbEGF-like 14 were the most prevalent in the neonatal regions. Combined with the report that cardiovascular disorders correlated with cysteine substitutions (Kühne et al., 2013), we propose that mutations of cbEGF-like 13 and cysteine substitutions in

cbEGF-like 12, followed by cysteine substitutions in cbEGF-like 14, were the top three hazardous neonatal mutations.

There were some limitations in our study. 1) The postoperative visual outcomes of some patients were not rigorously or regularly recorded. This was due, to some extent, to the retrospective nature and dramatically increased postoperative BCVA. There were 22 patients (46.81%) who had near-term postoperative LogMAR BCAV <0.10 (fraction >32/40), some of whom were satisfied with the surgical outcomes and were lost in long-term follow-ups. 2) We still had some patients diagnosed with potential MFS, and the final confirmation was not achieved. This came from the fact that some of our patients were too young to fully exclude the cardiovascular disorders. The diagnoses of these patients can only be determined until adulthood. 3) Although Ca^{2+}-binding regions and cysteine residues work together in maintaining cbEGF-like domain rigidity, they play different roles in binding calcium ions and forming disulfide bonds. It is reasonable for us to consider both of them as functional regions and compare the clinical manifestation of the patients between these two groups.

Overall, CEL patients with *FBN1* cbEGF-like mutations also had ocular characteristics of long AL, flat cornea, and reduced corneal SA. Compared with patients with cbEGF-like mutations out of functional regions, patients with cysteine substitutions and Ca^{2+}-binding mutations had longer AL after age adjustment. They also had poorer ocular involvement, visual performance, and systematic manifestations. In our series, those with cbEGF-like mutations in the neonatal regions did not show earlier ocular involvement compared with patients with cbEGF-like mutations out of the neonatal regions.

DATA AVAILABILITY STATEMENT

The raw data supporting the conclusion of this article will be made available by the authors, without undue reservation.

ETHICS STATEMENT

The study was approved by the Human Research Ethics Committee of the Eye and ENT Hospital of Fudan University (no. 2020126-1) and performed with adhering to the tenets of the Declaration of Helsinki. Signed consent was obtained from all patients, or the patients' guardians for those under 18 years old.

AUTHOR CONTRIBUTIONS

MZ and ZC was responsible for the research design of this article. TC collected the clinical data congenital EL patients. MZ and ZC was responsible for statistical analyses. XS provided critical suggestions. YJ supervised the whole project. All authors in this study reviewed and revised the final manuscript.

FUNDING

This study was supported by the National Key the Shanghai Science and Technology Commission (Scientific Innovation Action Plan, Grant no. 20Y119110), and the Natural Science Foundation of China (Grant no. 82070943 and 81770908).

ACKNOWLEDGMENTS

We thank Ang Li, Lina Cheng, Ying Yang, Xin Liu and Lin Wang for their kind help in assisting collecting data.

SUPPLEMENTARY MATERIAL

The Supplementary Material for this article can be found online at: https://www.frontiersin.org/articles/10.3389/fcell.2021.816397/full#supplementary-material

REFERENCES

Chen, J., Jing, Q., Tang, Y., Qian, D., Lu, Y., and Jiang, Y. (2018). Age Differences in Axial Length, Corneal Curvature, and Corneal Astigmatism in Marfan Syndrome with Ectopia Lentis. *J. Ophthalmol.* 2018, 1436834. doi:10.1155/2018/1436834

Chen, J., Jing, Q., Tang, Y., Qian, D., Lu, Y., and Jiang, Y. (2018). Corneal Curvature, Astigmatism, and Aberrations in Marfan Syndrome with Lens Subluxation: Evaluation by Pentacam HR System. *Sci. Rep.* 8, 4079. doi:10.1038/s41598-018-22358-x

Chen, T., Chen, J., Jin, G., Zhang, M., Chen, Z., Zheng, D., et al. (2021). Clinical Ocular Diagnostic Model of Marfan Syndrome in Patients with Congenital Ectopia Lentis by Pentacam AXL System. *Trans. Vis. Sci. Tech.* 10, 3. doi:10.1167/tvst.10.7.3

Chen, Z., Chen, T., Zhang, M., Chen, J., Deng, M., Zheng, J., et al. (2021). Fibrillin-1 Gene Mutations in a Chinese Cohort with Congenital Ectopia Lentis: Spectrum and Genotype-Phenotype Analysis. *Br. J. Ophthalmol.*. doi:10.1136/bjophthalmol-2021-319084

Chen, Z., Zhang, M., Deng, M., Chen, T., Chen, J., Zheng, J., et al. (2021). Surgical Outcomes of Modified Capsular Tension Ring and Intraocular Lens Implantation in Marfan Syndrome with Ectopia Lentis. *Eur. J. Ophthalmol.*. doi:10.1177/11206721211012868

Chen, Z.-X., Chen, T.-H., Zhang, M., Chen, J.-H., Lan, L.-N., Deng, M., Zheng, J.-L., and Jiang, Y.-X. (2021). Correlation Between *FBN1* Mutations and Ocular Features with Ectopia Lentis in the Setting of Marfan Syndrome and Related Fibrillinopathies. *Hum. Mutat.* 42, 1637–1647. doi:10.1002/humu.24283

Child, A. H. (2017). Non-cardiac Manifestations of Marfan Syndrome. *Ann. Cardiothorac. Surg.* 6, 599–609. doi:10.21037/acs.2017.10.02

Faivre, L., Collod-Beroud, G., Child, A., Callewaert, B., Loeys, B. L., Binquet, C., et al. (2008). Contribution of Molecular Analyses in Diagnosing Marfan Syndrome and Type I Fibrillinopathies: an International Study of 1009 Probands. *J. Med. Genet.* 45, 384–390. doi:10.1136/jmg.2007.056382

Haller, S. J., Roitberg, A. E., and Dudley, A. T. (2020). Steered Molecular Dynamic Simulations Reveal Marfan Syndrome Mutations Disrupt Fibrillin-1 cbEGF Domain Mechanosensitive Calcium Binding. *Sci. Rep.* 10, 16844. doi:10.1038/s41598-020-73969-2

He, X., Sankaridurg, P., Naduvilath, T., Wang, J., Xiong, S., Weng, R., et al. (2021). Normative Data and Percentile Curves for Axial Length and Axial Length/corneal Curvature in Chinese Children and Adolescents Aged 4-18 Years. *Br. J. Ophthalmol.*. doi:10.1136/bjophthalmol-2021-319431

Hilhorst-Hofstee, Y., Rijlaarsdam, M. E., Scholte, A. J., Swart-van den Berg, M., Versteegh, M. I., van der Schoot-van Velzen, I., et al. (2010). The Clinical

Spectrum of Missense Mutations of the First Aspartic Acid of cbEGF-like Domains in Fibrillin-1 Including a Recessive Family. *Hum. Mutat.* 31, E1915–E1927. doi:10.1002/humu.21372

Kühne, K., Keyser, B., Groene, E. F., Sheikhzadeh, S., Detter, C., Lorenzen, V., et al. (2013). FBN1 Gene Mutation Characteristics and Clinical Features for the Prediction of Mitral Valve Disease Progression. *Int. J. Cardiol.* 168, 953–959. doi:10.1016/j.ijcard.2012.10.044

Liu, L., Li, R., Huang, D., Lin, X., Zhu, H., Wang, Y., et al. (2021). Prediction of Premyopia and Myopia in Chinese Preschool Children: a Longitudinal Cohort. *BMC Ophthalmol.* 21, 283. doi:10.1186/s12886-021-02045-8

Loeys, B. L., Dietz, H. C., Braverman, A. C., Callewaert, B. L., De Backer, J., Devereux, R. B., et al. (2010). The Revised Ghent Nosology for the Marfan Syndrome. *J. Med. Genet.* 47, 476–485. doi:10.1136/jmg.2009.072785

Madar, L., Szakszon, K., Pfliegler, G., Szabó, G. P., Brúgós, B., Ronen, N., et al. (2019). FBN1 Gene Mutations in 26 Hungarian Patients with Suspected Marfan Syndrome or Related Fibrillinopathies. *J. Biotechnol.* 301, 105–111. doi:10.1016/j.jbiotec.2019.05.012

McGettrick, A. J., Knott, V., Willis, A., and Handford, P. A. (2000). Molecular Effects of Calcium Binding Mutations in Marfan Syndrome Depend on Domain Context. *Hum. Mol. Genet.* 9, 1987–1994. doi:10.1093/hmg/9.13.1987

Navarro, R., Rozema, J. J., and Tassignon, M.-J. (2013). Optical Changes of the Human Cornea as a Function of Age. *Optom. Vis. Sci.* 90, 587–598. doi:10.1097/opx.0b013e3182928bc6

Remulla, J. F., and Tolentino, F. I. (2001). Retinal Detachment in Marfan's Syndrome. *Int. Ophthalmol. Clin.* 41, 235–240. doi:10.1097/00004397-200110000-00021

Richards, S., Aziz, N., Bale, S., Bick, D., Das, S., Gastier-Foster, J., et al. (2015). Standards and Guidelines for the Interpretation of Sequence Variants: a Joint Consensus Recommendation of the American College of Medical Genetics and Genomics and the Association for Molecular Pathology. *Genet. Med.* 17, 405–424. doi:10.1038/gim.2015.30

Ruiz-Medrano, J., Montero, J. A., Flores-Moreno, I., Arias, L., García-Layana, A., and Ruiz-Moreno, J. M. (2019). Myopic Maculopathy: Current Status and Proposal for a New Classification and Grading System (ATN). *Prog. Retin. Eye Res.* 69, 80–115. doi:10.1016/j.preteyeres.2018.10.005

Sandvik, G. F., Vanem, T. T., Rand-Hendriksen, S., Cholidis, S., Sæthre, M., and Drolsum, L. (2019). Ten-year Reinvestigation of Ocular Manifestations in Marfan Syndrome. *Clin. Exp. Ophthalmol.* 47, 212–218. doi:10.1111/ceo.13408

Schrenk, S., Cenzi, C., Bertalot, T., Conconi, M. T., and Di Liddo, R. (2018). Structural and Functional Failure of Fibrillin-1 in H-uman D-iseases (Review). *Int. J. Mol. Med.* 41, 1213–1223. doi:10.3892/ijmm.2017.3343

Schrijver, I., Liu, W., Brenn, T., Furthmayr, H., and Francke, U. (1999). Cysteine Substitutions in Epidermal Growth Factor-like Domains of Fibrillin-1: Distinct Effects on Biochemical and Clinical Phenotypes. *Am. J. Hum. Genet.* 65, 1007–1020. doi:10.1086/302582

Smallridge, R. S., Whiteman, P., Doering, K., Handford, P. A., and Downing, A. K. (1999). EGF-like Domain Calcium Affinity Modulated by N-Terminal Domain Linkage in Human Fibrillin-1 1 1Edited by J. Karn. *J. Mol. Biol.* 286, 661–668. doi:10.1006/jmbi.1998.2536

Suk, J. Y., Jensen, S., McGettrick, A., Willis, A. C., Whiteman, P., Redfield, C., et al. (2004). Structural Consequences of Cysteine Substitutions C1977Y and C1977R in Calcium-Binding Epidermal Growth Factor-like Domain 30 of Human Fibrillin-1. *J. Biol. Chem.* 279, 51258–51265. doi:10.1074/jbc.m408156200

Vanhonsebrouck, E., Consejo, A., Coucke, P. J., Leroy, B. P., and Kreps, E. O. (2021). The Corneoscleral Shape in Marfan Syndrome. *Acta Ophthalmol.* 99, 405–410. doi:10.1111/aos.14636

Whiteman, P., Willis, A. C., Warner, A., Brown, J., Redfield, C., and Handford, P. A. (2007). Cellular and Molecular Studies of Marfan Syndrome Mutations Identify Co-operative Protein Folding in the cbEGF12-13 Region of Fibrillin-1. *Hum. Mol. Genet.* 16, 907–918. doi:10.1093/hmg/ddm035

Wu, Y., Sun, H., Wang, J., Wang, X., Gong, M., Han, L., et al. (2020). Marfan Syndrome: Whole-Exome Sequencing Reveals De Novo Mutations, Second Gene and Genotype-Phenotype Correlations in the Chinese Population. *Biosci. Rep.* 40, BSR20203356. doi:10.1042/BSR20203356

Yu, X., Chen, W., and Xu, W. (2020). Diagnosis and Treatment of Microspherophakia. *J. Cataract Refract. Surg.* 46, 1674–1679. doi:10.1097/j.jcrs.0000000000000334

Zhang, M., Chen, T., Deng, M., Chen, Z., and Jiang, Y. (2021). Accuracy of IOL Power Calculation Formulas in Marfan Lens Subluxation Patients with In-The-Bag IOLs and Implantation of Scleral-Sutured Single-Eyelet Modified Capsular Tension Rings. *J. Cataract Refract. Surg.* 47, 1423–1429. doi:10.1097/j.jcrs.0000000000000649

Zhou, Y., Guo, D., Cao, Q., Zhang, X., Jin, G., and Zheng, D. (2021). Genotype Variant Screening and Phenotypic Analysis of FBN1 in Chinese Patients with Isolated Ectopia Lentis. *Mol. Med. Rep.* 23, 275. doi:10.3892/mmr.2021.11914

Conflict of Interest: The authors declare that the research was conducted in the absence of any commercial or financial relationships that could be construed as a potential conflict of interest.

Publisher's Note: All claims expressed in this article are solely those of the authors and do not necessarily represent those of their affiliated organizations, or those of the publisher, the editors and the reviewers. Any product that may be evaluated in this article, or claim that may be made by its manufacturer, is not guaranteed or endorsed by the publisher.

Copyright © 2022 Zhang, Chen, Chen, Sun and Jiang. This is an open-access article distributed under the terms of the Creative Commons Attribution License (CC BY). The use, distribution or reproduction in other forums is permitted, provided the original author(s) and the copyright owner(s) are credited and that the original publication in this journal is cited, in accordance with accepted academic practice. No use, distribution or reproduction is permitted which does not comply with these terms.

frontiers in Cell and Developmental Biology

ORIGINAL RESEARCH
published: 14 March 2022
doi: 10.3389/fcell.2022.841660

The *MDM2* Single-Nucleotide Polymorphism T309G Is Associated With the Development of Epimacular Membranes

Heng Jiang[1], *Bin Yan*[1], *Zhishang Meng*[1], *Lusi Zhang*[1], *Hetian Lei*[2]* *and Jing Luo*[1]*

[1]Department of Ophthalmology, The Second Xiangya Hospital, Central South University, Changsha, China, [2]Shenzhen Eye Institute, Shenzhen Eye Hospital, Jinan University, Shenzhen, China

Purpose: To investigate the role of the *mouse double minute 2* (*MDM2*) gene single-nucleotide polymorphism (SNP) T309G in the development of epimacular membranes (EMMs) by analyzing the genotype distribution and consistency of the polymorphism in paired membrane-blood samples.

Methods: This was a cross–sectional genetic association study of patients with proliferative vitreoretinopathy (PVR) or EMMs. PVR membranes (PVRMs), internal limiting membranes (ILMs) (PVR-ILMs) and blood samples (PVR-blood) from patients with PVR, and EMMs, EMM-ILMs and EMM-blood from patients with EMMs were collected. The genotype of all samples was determined by Sanger sequencing. Sex composition, mean age, the genotype distribution of *MDM2* T309G, the allelic frequency of the *MDM2* SNP309 G allele (% G) and the somatic mutation rate at the *MDM2* T309G locus (% M) were analyzed and compared. The PVR and healthy Chinese donor groups were used as controls for different comparisons.

Results: The EMM group of 62 patients was older than the PVR group of 61 patients by an average of 8.87 years ($p < 0.0001$), but the two groups were statistically similar in the sex composition ($p = 0.1754$). Importantly, G allele carriers were at a higher risk of developing EMMs than non-G allele carriers ($p = 0.0479$; OR = 2.047). Moreover, EMM-blood exhibited a significantly higher % G than blood samples from healthy Chinese donors (EMM-blood: 56.78%, donors: 45.61%; $p = 0.0256$; OR = 1.567). Regarding membrane-blood consistency, % M was significantly different between PVRMs and EMMs (PVRMs: 2.63%, EMMs: 21.57%; $p = 0.0097$; OR = 10.18) but not between different types of ILMs (PVR-ILMs: 18.18%, EMM-ILMs: 29.17%; $p = 0.6855$). Furthermore, EMMs ($p = 0.0053$; OR = 8.250) and EMM-ILMs ($p = 0.0233$; OR = 14.40) from patients with preoperative

OPEN ACCESS

Edited by:
Ling Zhao,
Sun Yat-sen University, China

Reviewed by:
Ling Yuan,
The First Affiliated Hospital of Kunming Medical University, China
Xiaoqing Guo,
Schepens Eye Research Institute, United States

***Correspondence:**
Hetian Lei
leihetian18@hotmail.com,
Jing Luo
luojing001@csu.edu.cn

Specialty section:
This article was submitted to Molecular and Cellular Pathology, a section of the journal Frontiers in Cell and Developmental Biology

Received: *22 December 2021*
Accepted: *15 February 2022*
Published: *14 March 2022*

Citation:
Jiang H, Yan B, Meng Z, Zhang L, Lei H and Luo J (2022) The MDM2 Single-Nucleotide Polymorphism T309G Is Associated With the Development of Epimacular Membranes. Front. Cell Dev. Biol. 10:841660. doi: 10.3389/fcell.2022.841660

Abbreviations: 95% CI, 95% confidence interval; 2-OH-dATP, 2-hydroxy-2′-deoxyadenosine 5′-triphosphate; 8-OH-dGTP, 8-hydroxy-2′-deoxyguanosine 5′-triphosphate; ECM, extracellular matrix; EMM, epimacular membrane; EMT, epithelial to mesenchymal transition; ILM, internal limiting membrane; MDM2, mouse double minute 2 gene; MC, Müller cell; ns, not significant; OCT, optical coherence tomography; OR, odds ratio; PCR, polymerase chain reaction; PDGFR-α, platelet-derived growth factor receptor α; PVD, posterior vitreous detachment; PVR, proliferative vitreoretinopathy; PVRM, proliferative vitreoretinopathy membrane; RPE, retinal pigment epithelium; RD, retinal detachment; SEM, standard error of mean; SNP, single-nucleotide polymorphism.

macular holes were more predisposed toward somatic mutations at the *MDM2* T309G locus than those from patients without preoperative macular holes.

Conclusions: *MDM2* T309G is associated with the development of EMMs. Herein, the *MDM2* SNP309 G allele is first reported as an associated factor of EMMs in a Chinese population. In addition, EMMs and ILMs are genetically unstable at the *MDM2* T309G locus, especially when complicated with preoperative macular holes.

Keywords: *MDM2* SNP T309G, rs2279744, sanger sequencing, epimacular membrane, proliferative vitreoretinopathy, internal limiting membrane, macular hole

INTRODUCTION

The tumor suppressor p53 is a pivotal component of cells that monitors and controls the most important cellular events, including cell cycle arrest, apoptosis, senescence, metabolism, DNA repair and malignant transformation. p53 acts as a switch between life (cell cycle arrest and attendant DNA repair) and death (apoptosis) and thus determines the fate of cells in response to cellular stress (Carvajal and Manfredi, 2013). The mouse double minute 2 (MDM2) homolog oncoprotein, an E3 ubiquitin ligase encoded by the proto-oncogene *MDM2*, is the primary negative regulator of p53. MDM2 represses p53-dependent transcription via a triple mechanism: nuclear or cytoplasmic ubiquitin-dependent proteasomal degradation of p53, reversible cytoplasmic p53 translocation and direct abrogation of p53-dependent transactivation. MDM2 deficiency leads to p53-driven embryonic lethality, which can be fully rescued by simultaneous deletion of p53 (Jones et al., 1995). In contrast, overexpression of MDM2 impairs p53-mediated regulation of cell growth, with the substantial accumulation of DNA damage, which supports tumorigenesis. Wade et al. (2013) reported that amplification of the *MDM2* gene or altered expression of the MDM2 protein is a feature of many tumors. In general, the expression of MDM2 is dependent on two promoters: the upstream P1 promoter in the first exon of the *MDM2* gene, which controls basal constitutive expression in normal living cells, and the downstream P2 promoter in the first intron, which initiates inducible expression in response to stimuli such as p53, RAS and estrogen receptor α under stress conditions (Barak et al., 1994). Transcripts derived from the P2 promoter exhibit enhanced translational efficiency that is approximately eight times that of transcripts derived from the P1 promoter (Landers et al., 1997). A naturally occurring single-nucleotide polymorphism (SNP) in the P2 promoter, *MDM2* T309G (rs2279744, a thymine-to-guanine change at the 309th nucleotide in the first intron), enhances binding of the transcriptional activator Sp1 to the P2 promoter and stimulates P2-driven inducible expression of MDM2 under stress, with subsequent attenuation of p53 signaling (Bond et al., 2004). Several clinical investigations have indicated that *MDM2* T309G is related to increased risk, early onset, high malignancy and poor prognosis in cancers (Boersma et al., 2006; Bougeard et al., 2006; Lind et al., 2006; Ohmiya et al., 2006; Gryshchenko et al., 2008). Moreover, Post et al. (2010) corroborated the correlation between *MDM2* T309G and increased tumor risk using two cohorts of genetically engineered mice carrying either the humanized *MDM2* SNP309 G allele or T allele.

Proliferative vitreoretinopathy (PVR) is the major cause of failure after rhegmatogenous retinal detachment (RD) surgery and is responsible for 5–10% of all RD cases (Machemer et al., 1991; de la Rua et al., 2008). PVR is generally characterized by postoperative growth and contraction of fibrocellular membranes within the vitreous cavity and on both retinal surfaces and, in many cases, a fibrotic process of the retina itself (Pastor et al., 2002). These periretinal membranes create tangential traction force on the retina, and the distorted retina develops into fixed retinal folds, causing vision-compromising RD (**Figure 1**). Therefore, identifying and following individuals at high risk of developing PVR after RD surgery for early intervention have great practical significance. SNPs are important to genetic susceptibility and can serve as risk factors for multifactorial diseases in humans. For example, a case–control study by Pastor-Idoate et al. (2013a); Pastor-Idoate et al. (2013b) showed that the Pro variant of the *p53* codon 72 polymorphism (rs1042522) and the *MDM2* SNP309 G allele are associated with a higher risk of PVR among European subjects undergoing RD surgery. Given that rs1042522 and *MDM2* T309G synergistically attenuate the proapoptotic

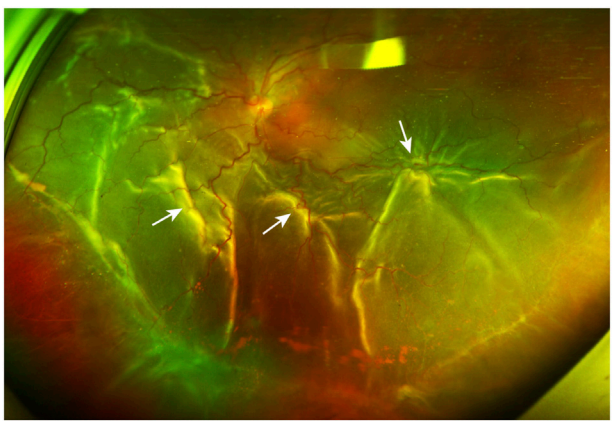

FIGURE 1 | A PVR patient with retinal detachment. The ultra-widefield retinal image shows inferior vitreous hemorrhage and extensive retinal folds (white arrows) caused by PVRMs. *PVR, proliferative vitreoretinopathy; PVRM, proliferative vitreoretinopathy membrane.*

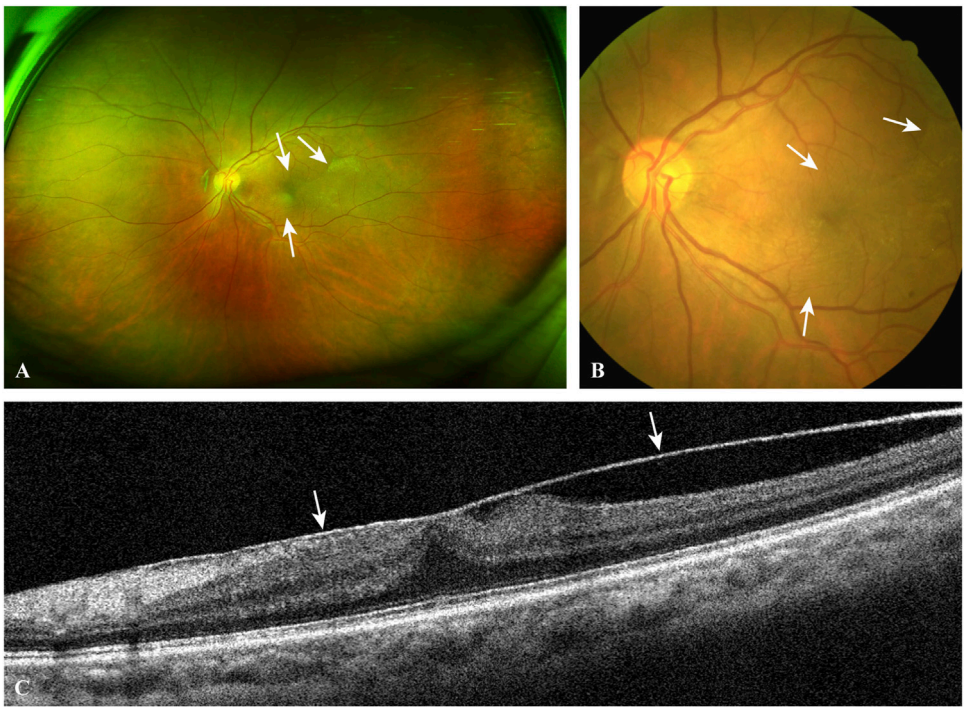

FIGURE 2 | A typical case of EMM. The ultra-widefield retinal image **(A)** and the fundus photograph **(B)** show macular puckers (white arrows) caused by contracted EMMs. OCT scan **(C)** through the central fovea of **(A,B)** demonstrates a contracted EMM (white arrows) causing significant macular wrinkling and thickening. *EMM, epimacular membrane; OCT, optical coherence tomography.*

function of p53 in direct and indirect ways, respectively, they produce an additional effect on the risk of PVR in carriers harboring both SNPs (Pastor-Idoate et al., 2013b). This finding highlights the association of *MDM2* T309G and individual genetic susceptibility to PVR.

Epimacular membranes (EMMs) are relatively common sight-threatening conditions featuring fibrocellular proliferation along the surface of the internal limiting membrane (ILM) of the retina. These membranes preferentially grow in the macular region. Primary/idiopathic EMMs are strongly associated with the development of posterior vitreous detachment (PVD) and vitreomacular traction induced by age-related changes in the extracellular matrix (ECM) of the vitreoretinal interface (Bu et al., 2014). Other EMMs are secondary to various predisposing conditions, including diabetic retinopathy, retinal vein occlusion, rhegmatogenous RD, high myopia, ocular trauma, vitreous hemorrhage, retinal photocoagulation or cryotherapy, uveitis and cataract surgery. In the initial stage of EMM development, which is termed cellophane maculopathy, thin, translucent membranes increase the foveal light reflex under ophthalmoscopy, although patients are usually asymptomatic. In the progressive stage, known as macular puckers or preretinal macular fibrosis, the membranes become thickened and semitranslucent with incremental degrees of inflammation and fibrosis. Contractile EMMs generate retinal wrinkling and distort the macula, causing macular edema, ischemia or even macular holes (**Figure 2**). Typical manifestations are decreased visual acuity, central scotoma, metamorphopsia, micropsia/macropsia and monocular diplopia. According to previous histological studies, cellular components in EMMs include hyalocytes, retinal pigment epithelium (RPE) cells, Müller cells (MCs), astrocytes, microglia, macrophages, fibroblasts and myofibroblasts (Smiddy et al., 1989; Zhao et al., 2013; Vishwakarma et al. (2020) demonstrated that retinal glial cells are activated under oxidative stress and interact with other cells to cause neuroinflammation and neurodegeneration, which underlie the formation of EMMs under different pathological conditions. As the activation of oxidative stress and proinflammatory signaling as well as fibrocellular proliferation are, to some extent, modulated by the MDM2-p53 axis in these cells, we sought to determine whether *MDM2* T309G is related to EMMs. To the best of our knowledge, no studies have yet examined this issue. In this study, we aimed to investigate the role of *MDM2* T309G in EMM formation by comparing the genotype distribution and consistency of the polymorphism in paired membrane-blood samples between the PVR, EMM and healthy Chinese donor groups.

MATERIALS AND METHODS

Design and Study Population

This was a cross–sectional study of patients who underwent pars plana vitrectomy for PVR or EMMs at the Second Xiangya

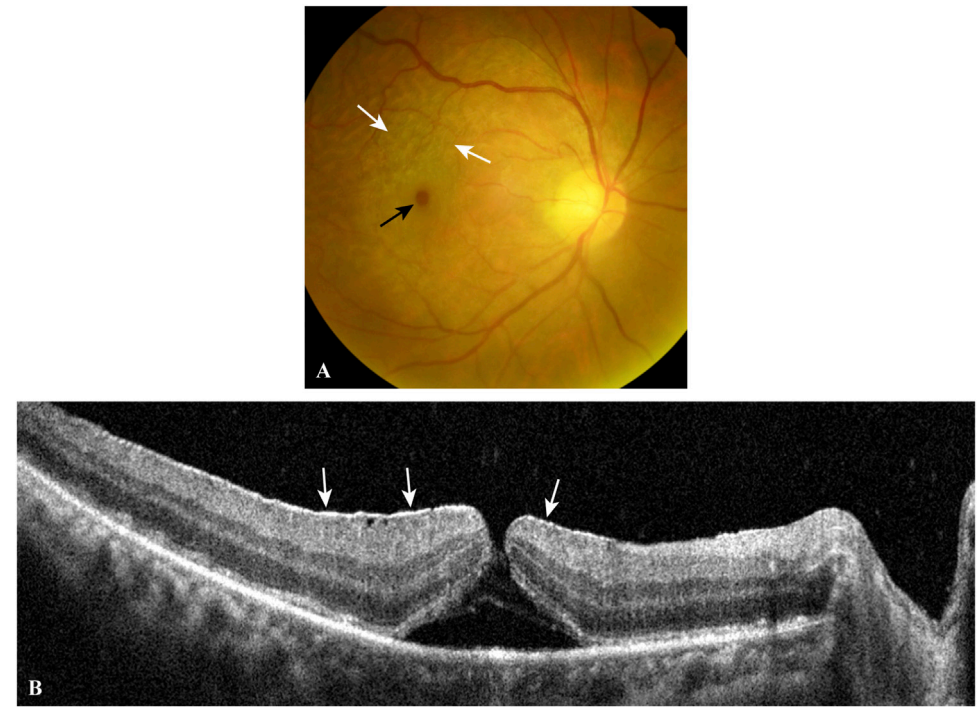

FIGURE 3 | A typical case of EMM complicated by a macular hole. The fundus photograph **(A)** shows a macular hole (black arrow) and surrounding macular puckers (white arrows) caused by contracted EMMs. OCT scan **(B)** through the central fovea of **(A)** demonstrates a contracted EMM (white arrows) causing a macular hole with significant macular wrinkling and thickening. *EMM, epimacular membrane; OCT, optical coherence tomography.*

Hospital of Central South University between 2020 and 2021. PVR membranes (PVRMs), ILMs removed along with PVRMs (PVR-ILMs) and peripheral venous blood samples from the same patients (PVR-blood) were collected from patients with PVR, and EMMs, EMM-ILMs and EMM-blood were collected from patients with EMMs. Membranes that were too small in size or compound membranes consisting of fibrocellular membranes and ILMs were first excluded.

For the PVR group, the inclusion criteria were an age older than 18 years, a diagnosis of rhegmatogenous RD by preoperative ocular examination (slit-lamp microscopy, optical coherence tomography (OCT), B-scan, fundus photography), and Machemer grade C1 PVR (Machemer et al., 1991) or higher, and the exclusion criterion was traumatic, tractional, exudative or iatrogenic RD. For the EMM group, the inclusion criteria were an age older than 18 years, Gass grade 2 EMMs diagnosed by preoperative ocular examination, complaint of decreased visual acuity, metamorphopsia or other visual defects, and the exclusion criterion was RD of any kind.

To investigate the association between macular holes and genomic stability at the *MDM2* T309G locus in EMMs and EMM-ILMs, we subdivided the EMM group into a macular hole subgroup and a control subgroup based on preoperative ocular examination. A patient belonged to the macular hole subgroup if signs of macular holes were found (**Figure 3**). Those without any signs of preoperative macular holes were included in the control subgroup.

Genotyping

Genomic DNA was isolated from 300 µl of peripheral blood using the Wizard® Genomic DNA Purification Kit (Promega, Madison, WI, United States) following the standard protocol. Membranes were ground by a KZ-II High-Speed Tissue Homogenizer (Servicebio, Wuhan, Hubei, PRC) in a clean, sterilized 1.8-ml tube with 150 µl of QuickExtract™ DNA Extraction Solution (Lucigen, Madison, WI, United States). The time and frequency were usually 120 s and 70 Hz, respectively, but varied from case to case. The homogenate was transferred to a 200-µl polymerase chain reaction (PCR) tube and boiled at 99°C for 40 min in a T100™ Thermal Cycler (Bio–Rad, Hercules, CA, United States). After centrifugation at 13,000 ×g for 5 min, the supernatant was retained and contained the genomic DNA of membrane cells.

The genomic DNA was subjected to PCR with the forward primer 5′-GGCACGTGGCTTTGCGGAGG-3′ and reverse primer 5′-GCCCCAGCTGGAGACAAGTC-3′ to obtain a 359-base pair DNA fragment. The 30-µl reaction mixture was composed of 2 µl of genomic DNA template, 2 µl of each primer at 10 µM, 9 µl of ddH_2O and 15 µl of 2× Taq PCR Master Mix with Dye (Biosune, Shanghai, PRC; the mix contains dNTPs at 200 µM, $MgCl_2$ at 1.5 mM and 0.5–0.7 U of Taq DNA polymerase). The PCR steps were an initial 4-min denaturation step at 95°C, followed by 35 cycles of 95°C for 40 s, 58°C for 40 s, 72°C for 40 s and a final elongation step at 72°C for 5 min. The amplified DNA fragments were separated on a 1.58% agarose gel and purified with a Gel/PCR DNA

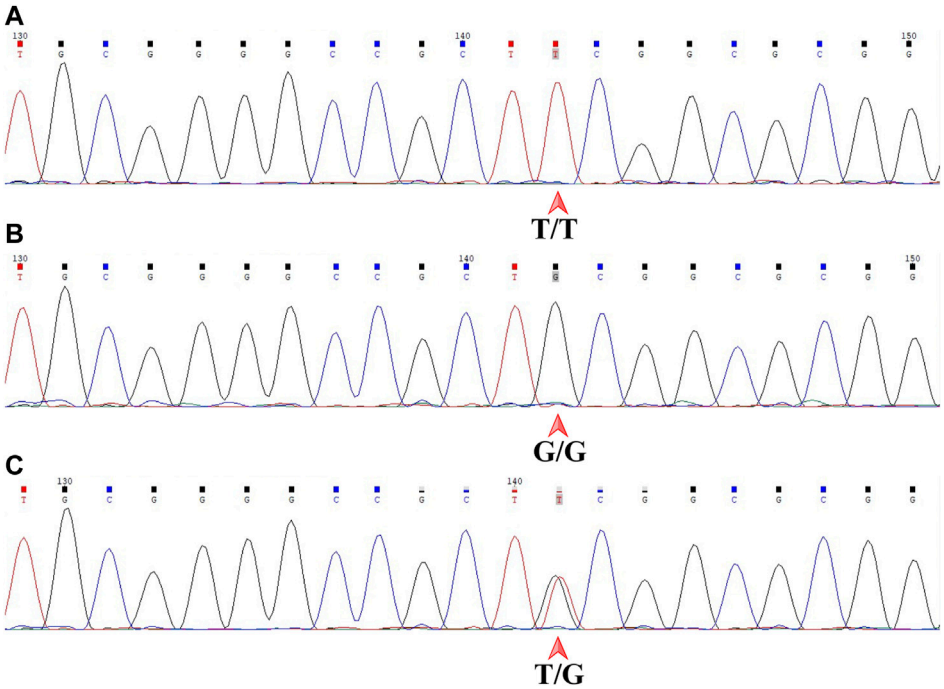

FIGURE 4 | Sanger DNA sequencing of the 359-base pair DNA fragment in a forward read. *MDM2* SNP309 is downstream of 5′-CCGCT-3′. **(A)** T/T shown by a single red peak. **(B)** G/G shown by a single black peak. **(C)** T/G shown by overlapping red and black peaks. *MDM2, mouse double minute 2 gene; SNP, single-nucleotide polymorphism.*

Purification Kit (Biosune, Shanghai, PRC) for bidirectional Sanger DNA sequencing performed by Shanghai Biosune Biotechnology Co., Ltd.

The genotype of each sample was independently determined by two senior experts in a blinded fashion. Chromas software (version 2.6.6, Technelysium, Brisbane, QLD, AUS) was used to display the sequencing files. *MDM2* T309G is just downstream of 5′-CCGCT-3′ by forward sequencing and just upstream of 5′-AGCGG-3′ by reverse sequencing. The genotype of a sample was T/T, G/G or T/G, as indicated by a single red peak, a single black peak or overlapping red and black peaks by forward sequencing (**Figure 4**), which corresponded to A/A with a single green peak, C/C with a single blue peak or A/C with overlapping green and blue peaks by reverse sequencing. All samples included gave consistent results by forward and reverse sequencing.

TABLE 1 | Basic characteristics of the study population.

Characteristic	PVR group	EMM group
Sex		
Male, N	34	26
Female, N	28	35
Total, N	62	61
p Value	0.1754 (ns)	
Age		
Mean ± SEM (years)	52.03 ± 1.65	60.90 ± 1.39
95% CI	48.73–55.33	58.13–63.68
p Value	<0.0001 (****)	

*95% CI, 95% confidence interval; EMM, epimacular membrane; ns, not significant; PVR, proliferative vitreoretinopathy; SEM, standard error of mean. Asterisks indicate statistical significance upon comparison: ****p < 0.0001.*

Statistical Analysis

Statistical analyses were conducted using GraphPad Prism software (version 9.0.0.121, GraphPad, San Diego, CA, United States). The sex composition and mean age of the study population were analyzed by the chi-square and unpaired t tests. The genotype distribution of *MDM2* T309G and the frequency of the *MDM2* SNP309 G allele in all samples were compared by the chi-square test. The somatic mutation rate at the *MDM2* T309G locus in all membrane samples was compared by the chi-square and Fisher's exact tests, as in some cases, one or more theoretical frequencies were less than five, or the total number was less than 40. Two-sided *p* values with a significance level of 0.05 were obtained for all comparisons. Odds ratios (ORs) and 95% confidence intervals (95% CIs) were calculated using the Baptista-Pike and Wilson/Brown methods, respectively.

TABLE 2 | Genotype Distribution of *MDM2* T309G and frequency of the *MDM2* SNP309 G allele in all samples.

	PVR group			EMM group			Healthy donors[1]
	PVRM	ILM	Blood	EMM	ILM	Blood	Blood
Genotype							
G/G, N	12	4	14	10	3	18	66
T/G, N	31	8	26	35	19	31	159
T/T, N	9	2	7	8	2	10	94
p Value		0.9585 (ns)			0.1996 (ns)		
T/G + G/G, N			40			49	225
T/T, N			7			10	94
p Value (compared to donors)			0.0369 (*)			0.0479 (*)	
OR			2.387			2.047	
95% CI			1.065–5.740			1.027–4.149	
Frequency of the G allele							
G allele, N			54			67	291
T allele, N			40			51	347
p Value (compared to donors)			0.0319 (*)			0.0256 (*)	
OR			1.610			1.567	
95% CI			1.034–2.499			1.046–2.335	
% G^2			57.45%			56.78%	45.61%
95% CI			47.35–66.96%			47.77–65.36%	41.78–49.49%

*95% CI, 95% confidence interval; EMM, epimacular membrane; ILM, internal limiting membrane; MDM2, mouse double minute 2 gene; ns, not significant; OR, odds ratio; PVR, proliferative vitreoretinopathy; PVRM, proliferative vitreoretinopathy membrane; SNP, single-nucleotide polymorphism. Asterisks indicate statistical significance upon comparison: *p < 0.05.1. The distribution of MDM2 T309G in blood from healthy Chinese donors was derived from Knappskog et al. (2011) 2. % G is the frequency of the MDM2 SNP309 G allele calculated by G allele N/total allele N×100%.*

RESULTS

Study Characteristics

According to diagnosis, the study population was divided into a PVR group and an EMM group. The final analysis included 123 subjects, consisting of 62 patients with PVR and 61 with EMMs. **Table 1** summarizes the basic characteristics of all subjects. The two groups were statistically similar in sex composition based on the chi-square test (p = 0.1754). The mean age significantly differed between the two groups, as revealed by the unpaired t test (p < 0.0001). The EMM group (60.90 years, 95% CI, 58.13–63.68 years) was older on average than the PVR group (52.03 years, 95% CI, 48.73–55.33 years).

Genotype Distribution and Allelic Frequency of *MDM2* T309G

All samples were classified into three categories, each of which was composed of subsamples from the PVR group and the EMM group: fibrocellular membranes (PVRMs or EMMs), ILMs peeled together with fibrocellular membranes during surgery (PVR-ILMs or EMM-ILMs) and peripheral venous blood samples. The distribution of *MDM2* T309G in blood from healthy Chinese donors was derived from Knappskog et al. (2011). Fibrocellular membranes, ILMs and blood samples from both groups were genotyped by Sanger DNA sequencing. The statistics for the genotype distribution of *MDM2* T309G and the frequency of the *MDM2* SNP309 G allele (% G) are presented with details in **Table 2**. The proportion of the G allele number to the total allele number in each subsample is represented by % G, whereby a higher percentage indicates a greater impact of the G allele on disease pathogenesis. The genotype distribution was not significantly different within the PVR group (PVRMs, PVR-ILMs and PVR-blood; p = 0.9585) or EMM group (EMMs, EMM-ILMs and EMM-blood; p = 0.1996) (**Table 2**).

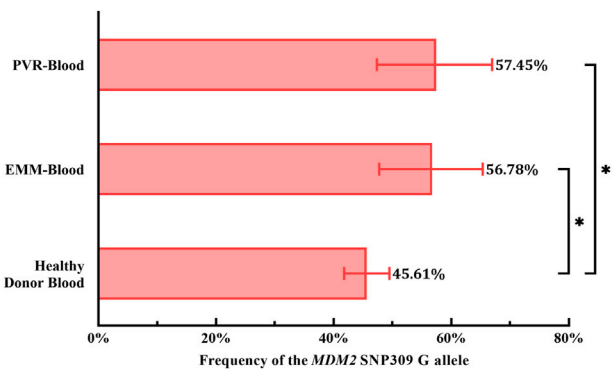

FIGURE 5 | Comparison of the frequency of the *MDM2* SNP309 G allele in blood samples. Overall, both cohorts of patients exhibited a higher frequency of the G allele than healthy Chinese donors. *95% CI, 95% confidence interval; EMM, epimacular membrane; MDM2, mouse double minute 2 gene; PVR, proliferative vitreoretinopathy; SNP, single nucleotide polymorphism.* Asterisks indicate statistical significance upon comparison: *p < 0.05. Data are presented as the frequency of the *MDM2* SNP309 G allele ±95% CI.

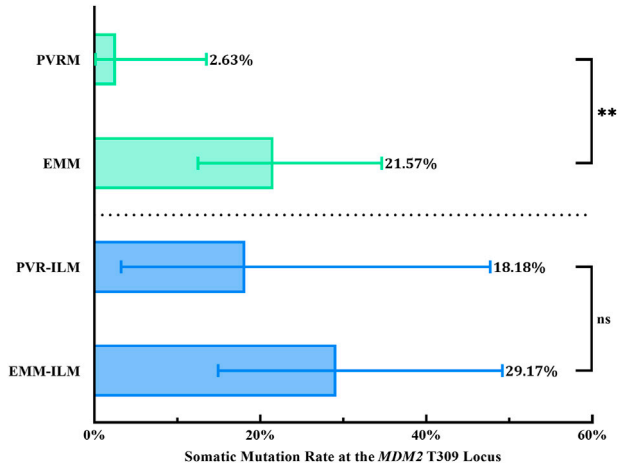

FIGURE 6 | Somatic mutation at the *MDM2* T309G locus in membranes. EMMs were prone toward somatic mutation at the *MDM2* T309G locus, in contrast to PVRMs. PVR-ILMs and EMM-ILMs showed comparable mutation rates. *95% CI, 95% confidence interval; EMM, epimacular membrane; ILM, internal limiting membrane; MDM2, mouse double minute 2 gene; ns, not significant; PVRM, proliferative vitreoretinopathy membrane.* Asterisks indicate statistical significance upon comparison: $^{**}p < 0.01$. Data are presented as the somatic mutation rate at the *MDM2* T309G locus ±95% CI.

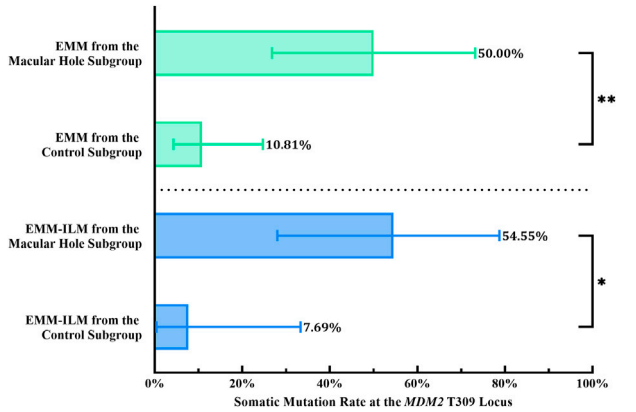

FIGURE 7 | EMMs and ILMs from EMM cases with preoperative macular holes tended toward somatic mutation at the *MDM2* T309G locus. *EMM, epimacular membrane; ILM, internal limiting membrane; MDM2, mouse double minute 2 gene.* Asterisks indicate statistical significance upon comparison: $^{*}p < 0.05$, $^{**}p < 0.01$. Data are presented as the somatic mutation rate at the *MDM2* T309G locus ±95% CI.

To evaluate the role of the G allele in the pathogenesis of PVR and EMMs, we used the genotype distribution of *MDM2* T309G in blood from healthy Chinese donors in a study by Knappskog et al. (2011) because the genotype distribution varies by race. Based on chi-square tests, significant differences in the proportion of *MDM2* SNP309 G allele carriers (T/G + G/G) were observed between PVR-blood ($p = 0.0369$; OR = 2.387, 95% CI, 1.065–5.740) or EMM-blood ($p = 0.0479$; OR = 2.047, 95% CI, 1.027–4.149) and blood from healthy Chinese donors (**Table 2**). Additionally, the % G of PVR-blood (% G = 57.45%, 95% CI, 47.35–66.96%; $p = 0.0319$; OR = 1.610, 95% CI, 1.034–2.499) and EMM-blood (% G = 56.78%, 95% CI, 47.77–65.36%; $p = 0.0256$; OR = 1.567, 95% CI, 1.046–2.335) was significantly higher than that of blood from healthy donors (% G = 45.61%, 95% CI, 41.78–49.49%) (**Figure 5**; **Table 2**). Thus, the *MDM2* SNP309 G allele is associated with higher risks of both PVR and EMMs.

Somatic Mutation at the *MDM2* T309G Locus

We found that the genotypes of the membranes were not always consistent with those of the matched blood samples. These membranes were considered somatically mutated. Genotype determined by Sanger DNA sequencing varied between mutated membranes and matched blood samples. In contrast, the results for unmutated membranes were consistent with those for matched blood samples. All pairs of mutated samples were examined *de novo* twice to exclude errors. The somatic mutation rate at the *MDM2* T309G locus (% M) was obtained by dividing

TABLE 3 | Somatic mutation at the *MDM2* T309G locus in all membrane samples.

	Fibrocellular membrane		ILM	
	PVRM	**EMM**	**PVR-ILM**	**EMM-ILM**
Somatic mutation in membranes				
Mutated Membrane, N	1	11	2	7
Unmutated Membrane, N	37	40	9	17
p Value	0.0097 (**)		0.6855 (ns)	
OR	10.18		1.853	
95% CI	1.594–112.4		0.3435–10.12	
% M[1]	2.63%	21.57%	18.18%	29.17%
95% CI	0.13–13.49%	12.49–34.63%	3.23–47.70%	14.91–49.17%

*95% CI, 95% confidence interval; EMM, epimacular membrane; ILM, internal limiting membrane; MDM2, mouse double minute 2 gene; ns, not significant; OR, odds ratio; PVR, proliferative vitreoretinopathy; PVRM, proliferative vitreoretinopathy membrane. Asterisks indicate statistical significance upon comparison: **p < 0.01.1. % M is the somatic mutation rate at the MDM2 T309G locus in a subset of membranes.*

TABLE 4 | Association of somatic mutation at the *MDM2* T309G locus and macular holes in EMM cases.

	EMM		EMM-ILM	
	Macular hole subgroup	**Control subgroup**	**Macular hole subgroup**	**Control subgroup**
Somatic mutation in membranes				
Mutated Membrane, N	7	4	6	1
Unmutated Membrane, N	7	33	5	12
p Value	0.0053 (**)		0.0233 (*)	
OR	8.250		14.40	
95% CI	1.668–29.20		1.560–175.8	
% M[1]	50.00%	10.81%	54.55%	7.69%
95% CI	26.80–73.20%	4.29–24.71%	28.01–78.73%	0.39–33.31%

*95% CI, 95% confidence interval; EMM, epimacular membrane; ILM, internal limiting membrane; MDM2, mouse double minute 2 gene; OR, odds ratio. Asterisks indicate statistical significance upon comparison: *p < 0.05, **p < 0.01.1. % M is the somatic mutation rate at the MDM2 T309G locus in a subset of membranes.*

the mutated membrane number by the paired membrane number times 100%.

Interestingly, the chi-square test revealed a significantly higher % M for EMMs than for PVRMs (% M of PVRMs = 2.63%, 95% CI, 0.13–13.49%; % M of EMMs = 21.57%, 95% CI, 12.49–34.63%; p = 0.0097; OR = 10.18, 95% CI, 1.594–112.4) (**Figure 6**; **Table 3**). To our surprise, ILMs in both groups showed a considerable % M by Fisher's exact test (% M of PVR-ILMs: 18.18%, 95% CI, 3.23–47.70%; % M of EMM-ILMs: 29.17%, 95% CI, 14.91–49.17%; p = 0.6855; OR = 1.853, 95% CI, 0.3435–10.12) (**Figure 6**; **Table 3**). These results suggest that in the ILMs from both sources and EMMs, but not in the PVRMs, proliferating cells tended to incur somatic mutation at the *MDM2* T309G locus.

Mechanical retinal damage, disruption of the outer blood–retinal barrier and exposure of the vitreous body are crucial steps in PVR pathogenesis. To investigate whether these factors are involved in somatic mutation at the *MDM2* T309G locus in EMMs and EMM-ILMs, the EMM group was subdivided into a macular hole subgroup and a control subgroup according to preoperative ocular examination. The % M of EMMs was higher for the macular hole subgroup than for the control subgroup, as demonstrated by Fisher's exact test (% M of the macular hole subgroup = 50.00%, 95% CI, 26.80–73.20%; % M of the control subgroup: 10.81%, 95% CI, 4.29–24.71%; p = 0.0053; OR = 8.250, 95% CI, 1.668–29.20) (**Figure 7**; **Table 4**). Furthermore, EMM-ILMs from the macular hole subgroup were more likely to be mutated than EMM-ILMs from the control subgroup (% M of the macular hole subgroup: 54.55%, 95% CI, 28.01–78.73%; % M of the control subgroup: 7.69%, 95% CI, 0.39–33.31%; p = 0.0233; OR = 14.40, 95% CI, 1.560–175.8) (**Figure 7**; **Table 4**). In brief, EMMs and ILMs from EMM cases with preoperative macular holes tended to exhibit somatic mutation at the *MDM2* T309G locus.

DISCUSSION

In the present study, we investigated the genotype distribution of *MDM2* T309G in fibrocellular membranes, ILMs and blood samples from PVR and EMM patients. For both groups, the proportion of *MDM2* SNP309 G allele carriers and the frequency of the G allele (% G) in blood samples were significantly higher than those in blood samples from the healthy donor group. Furthermore, between-group comparisons of *MDM2* T309G consistency in paired membrane-blood samples revealed that EMMs are predisposed toward somatic mutation at the *MDM2* T309G locus but that PVRMs are not, in contrast to PVR-ILMs and EMM-ILMs, which undergo mutation at similar ratios. Another notable finding was that EMMs and ILMs from EMM patients with preoperative macular holes had a greater mutation rate (% M) than those from patients without preoperative macular holes. Hence, we propose for the first time that *MDM2* T309G is associated with the development of EMMs in the Chinese population. That is, carriers of the *MDM2* SNP309 G allele are at a higher risk for developing EMMs. Moreover, EMMs and ILMs, especially those complicated with macular holes, are genetically unstable at the *MDM2* T309G locus. We hypothesize that MCs, which participate in reactive gliosis against various retinal stresses, or retinal progenitor/stem cells derived from dedifferentiated MCs are susceptible to oxygen free radical-induced single-base substitutions at the *MDM2* T309G locus. These cells may be responsible for the genomic instability in EMMs and ILMs, although this hypothesis needs to be further confirmed.

Our results are consistent with a previous report showing that age is a risk factor for EMMs but do not support female sex as a risk factor (Xiao et al., 2017). The average age of the EMM group was 8.87 years older than that of the PVR group, possibly due to the rapid worsening of visual function in PVR patients or the prolonged development of EMMs. Nevertheless, this study is not a large-scale epidemiological survey, and the above results are for reference only. We believe that the difference in average age is mainly attributed to the intrinsic properties of the two diseases and hardly affects our results, as such a difference is far from enough to have a statistically significant impact on overall genomic stability.

PVR is a pathological vitreoretinal fibrosis condition induced by vitreal growth factors, cytokines and inflammatory mediators produced by RPE cells, MCs, microglial cells and macrophages,

including platelet-derived growth factor (PDGF), TGF-β2, EGF, FGF2, and TNF-α. Stimulated by these vitreal factors, detached RPE cells undergo epithelial to mesenchymal transition (EMT), acquiring enhanced proliferation and migration capacities, resistance to apoptosis and the ability to produce ECM (Chiba, 2014). The transformed cells then migrate into the subretinal space or, through retinal breaks, the vitreous cavity. They proliferate and transdifferentiate into fibroblasts and myofibroblasts together with other cells to form subretinal or epiretinal PVRMs (Agrawal et al., 2007; Pastor et al., 2016). Therefore, researchers employ PVR vitreous from patients or animals to induce EMT in RPE cells for experiments. In recent years, multiple studies have confirmed that MDM2 is involved in PVR. Initially, chronic activation of Akt and suppression of p53 were identified by Lei et al. (2011) as a signature pathway downstream of the PDGF receptor α (PDGFR-α) signaling cascade in PVR. However, stabilizing intracellular p53 levels by Nutlin-3, a small-molecule antagonist of the MDM2-p53 interaction, abrogated the Akt-p53 pathway and prevented human PVR vitreous-induced contraction of cells isolated from a PVRM (Lei et al., 2012). In fact, PVR vitreous induces ERK/Sp1-dependent MDM2 upregulation and subsequent p53 downregulation in RPE cells. The resultant enhanced abilities of RPE cells to proliferate, survive, contract and migrate are intrinsic to PVR. Inspired by previous works by Pastor-Idoate et al. (2013b), Lei's team introduced *MDM2* T309G into RPE cells to create RPE cells with *MDM2* SNP309 T/T and *MDM2* SNP309 T/G. Importantly, PVR vitreous-induced cellular responses were enhanced in T/G RPE cells compared with T/T RPE cells, but this was abrogated by genetic silencing of aberrant P2-driven expression of MDM2 caused by *MDM2* T309G (Duan et al., 2016; Zhou et al., 2017; Chen et al., 2019). *MDM2* T309G also promoted the development of experimental PVR in an *in vivo* rabbit model (Zhou et al., 2017). Our results show a larger proportion of G allele carriers in the PVR group than in healthy donors and a higher % G in blood samples from PVR patients than from healthy donors. This finding is consistent with the established notion that *MDM2* T309G promotes PVR. It has been proposed that aberrant P2-driven inducible expression of MDM2 facilitates EMT in RPE cells by targeting E-cadherin, a cell adhesion protein and a key regulator of EMT, among others, for ubiquitin-dependent proteasomal degradation (Yang et al., 2006; Liu et al., 2019). Thus, carriers of the *MDM2* SNP309 G allele exhibit a greater increase in MDM2 levels in response to RD-induced stress. Such an overabundance of MDM2 induces RPE cells to undergo EMT, thereby contributing to PVRM formation. Most importantly, we show that G allele carriers were at a higher risk of developing EMMs than non-G allele carriers (p = 0.0479; OR = 2.047, 95% CI, 1.027–4.149) and that EMM patients exhibited a significantly higher % G than healthy donors (p = 0.0256; OR = 1.567, 95% CI, 1.046–2.335), indicating the role of the *MDM2* SNP309 G allele in promoting EMMs (**Figure 5**; **Table 2**).

Surprisingly, of all 124 pairs of matched membrane-blood samples, 21 pairs were inconsistent in genotype. Moreover, possible operational errors were excluded by duplicate examination of both forward and reverse sequencing. Since peripheral blood leukocytes are typically genetically stable, such inconsistency arises from somatic mutations in membrane cells under pathological conditions. A likely explanation for this finding is that mutation is a consequence of overproduced reactive oxygen species in the vitreal inflammatory response. Reactive oxygen species are constantly produced through normal cellular oxygen respiration or stress responses to various environmental mutagens and carcinogens, such as ionizing radiation, chemicals and ultraviolet light. Excessive oxygen free radicals attack DNA and its precursor deoxyribonucleotides, leading to DNA damage and mutations. The most studied oxidative DNA lesion, 8-oxo-7,8-dihydro-2′-deoxyguanosine (8-oxo-dG)/8-hydroxy-2′-deoxyguanosine (8-OH-dG, an enol tautomer of 8-oxo-dG), has been strongly implicated in cancers due to its capacity to induce the G/C → T/A transversion (Moriya, 1993; Valko et al., 2006). Furthermore, free nucleotides are oxidized more efficiently than DNA, and oxidized dNTPs cause potent genomic instability when they are incorporated into daughter strands during DNA replication (Maki, 2002). 8-Hydroxy-2′-deoxyguanosine 5′-triphosphate (8-OH-dGTP, an equivalent of 8-oxo-dGTP) and 2-hydroxy-2′-deoxyadenosine 5′-triphosphate (2-OH-dATP, an equivalent of 2-oxo-dATP), the oxidized forms of dGTP and dATP, respectively, induce A/T → C/G and G/C → T/A transversions, respectively, in newly synthesized DNA (Inoue et al., 1998). These single-base substitutions are elicited by human DNA polymerase η-, ζ- or REV1-mediated misincorporation of 8-OH-dGTP opposite template adenine and 2-OH-dATP opposite template guanine (Maki and Sekiguchi, 1992; Inoue et al., 1998; Hidaka et al., 2008; Satou et al., 2009). Correspondingly, of the 21 membrane samples with heterozygous mutations in this study, 6 and 15 harbored an A/T → C/G transversion and a G/C → T/A transversion at the *MDM2* T309G locus, respectively.

An interesting finding is that % M varied between PVRMs and EMMs (p = 0.0097; OR = 10.18, 95% CI, 1.594–112.4) but not between PVR-ILMs and EMM-ILMs (p = 0.6855; OR = 1.853, 95% CI, 0.3435–10.12), suggesting that EMMs and ILMs are intrinsically connected in terms of genomic instability at the *MDM2* T309G locus (**Figure 6**; **Table 3**). Histologically, Müller glial cells are a major cellular component of EMMs (Zhao et al., 2013). These cells are a major type of macroglia that maintain retinal homeostasis and provide structural, metabolic and trophic support. Their radial processes extend across the entire neurosensory retina, serving as living optical fibers. Above all, MCs also play a pivotal role in retinal gliosis. Reactive MC gliosis is a protective process against retinal injury that insulates the retina from vitreal pathogenic factors, promotes retinal tissue regeneration and limits tissue remodeling (Bringmann and Wiedemann, 2012). Under diverse pathological conditions, MCs in the mature retina rapidly proliferate and dedifferentiate to pluripotent retinal progenitor/stem cells, which migrate along MC processes to the damaged retinal layer and redifferentiate to replenish lost neurons (Reichenbach and Bringmann, 2013). Any retinal or vitreal insult might trigger this reparative reaction, and common initiating factors are RD, retinal ischemia, PVD, vitreous hemorrhage, endophthalmitis and trauma. However, excessive gliosis leads to glial scars, which are aberrant tissue repairs in response to retinal stress. In particular, various EMMs (primary and secondary) are a distinct type of glial scar attached to the retina by hypertrophied MC fibers (Bringmann and

Wiedemann, 2012). In response to stress, retinal glial cells, notably MCs, migrate to the vitreoretinal interface through an intact or defective ILM, proliferating and transdifferentiating, along with hyalocytes, RPE cells, macrophages, fibroblasts and myofibroblasts, on the scaffold of the ILM (collagen IV) to form early EMMs. In brief, EMMs essentially constitute progressive fibrocellular proliferation on the vitreal side of the ILM and are inextricably linked to the ILM. As routine clinical procedures, vitrectomy and the removal of EMMs along with ILM peeling clear the hazardous local microenvironment and relieve macular traction, thus favoring postoperative anatomic and visual recovery of the retina. The ILM is the innermost layer of the neurosensory retina that adheres the vitreous to the retina. It is a thin basement membrane formed by MC endfeet. ECM proteins that make up the ILM, including collagen IV, laminins, nidogens and heparan sulfate proteoglycans, are believed to be produced and secreted by MCs (Peynshaert et al., 2019; Zhang and Johnson, 2021). Based on the above facts, it is reasonable to speculate that MCs are responsible for the propensity of EMMs and ILMs toward somatic mutation at the *MDM2* T309G locus.

Last but not least, the heightened % M observed in EMMs ($p = 0.0053$; OR = 8.250, 95% CI, 1.668–29.20) and ILMs ($p = 0.0233$; OR = 14.40, 95% CI, 1.560–175.8) from EMM patients with preoperative macular holes compared with those without holes (**Figure 7**; **Table 4**) further corroborates this speculation, as oxidative stress and aberrant preretinal gliosis intensify with retinal injury, giving rise to genomic instability at the *MDM2* T309G locus in highly proliferating MCs. We hypothesize that the blood–retinal barrier adjacent to macular holes is disrupted and that leukocytes emigrate to the preretinal space or vitreous cavity, releasing cytokines and inflammatory mediators. Inflammatory infiltration produces vast amounts of oxygen free radicals that attack proliferating MCs in EMMs and ILMs and cause somatic mutation at the *MDM2* T309G locus. Admittedly, further research is needed to confirm our conjecture.

The major limitations of this study include the following: 1) An insufficient sample size. A substantial number of compound membranes consisting of fibrocellular membranes and ILMs and their matched blood samples were unqualified for this study and excluded from the cohorts. The association between *MDM2* T309G and EMMs may need to be further validated with a larger sample size. 2) A lack of blood samples from healthy donors. The genotype distribution of *MDM2* T309G varies with race (Wilkening et al., 2007; Knappskog et al., 2011). Therefore, the statistics of genotype distribution for healthy Chinese donors (Knappskog et al., 2011) were selected for comparison to minimize racial/ethnic bias. 3) This study was conducted in only the Chinese population, and it is unclear whether these conclusions can be extended to other ethnicities. Hence, replication studies in larger independent cohorts of different ethnicities are required.

In summary, this study highlights the role of the *MDM2* SNP T309G in the development of EMMs. Herein, we report for the first time that the *MDM2* SNP309 G allele is an associated factor for EMMs in a Chinese population. This observation provides new insights into the molecular mechanism of these pathologies, which may be beneficial for developing novel approaches and enabling early intervention for high-risk populations to improve visual prognosis.

DATA AVAILABILITY STATEMENT

The original contributions presented in the study are included in the article/Supplementary Material, further inquiries can be directed to the corresponding authors.

ETHICS STATEMENT

The studies involving human participants were reviewed and approved by The Ethics Committee of The Second Xiangya Hospital, Central South University. The patients/participants provided their written informed consent to participate in this study.

AUTHOR CONTRIBUTIONS

HJ, HL, and JL conceived of and designed this study. HJ, BY, ZM, and JL were responsible for sample collection. HJ and BY conducted most experiments. LZ and JL determined the genotype of each sample. Data analysis and interpretation were performed by HJ, LZ, HL, and JL. The manuscript was written and edited by HJ and revised by HL and JL. All authors have read and approved the final manuscript.

FUNDING

This work was supported by the National Natural Science Foundation of China (81570847) and the Hunan Traditional Chinese Medicine Scientific Research Program (C2022009) to JL, the National Natural Science Foundation of China (82070989) and the Sanming Project of Medicine in Shenzhen (SZSM202011015) to HL. No funding bodies had any role in the study design, data collection and analysis, decision to publish or preparation of the manuscript.

ACKNOWLEDGMENTS

We thank Jing Deng (Department of Epidemiology and Health Statistics, Xiangya School of Public Health, Central South University, Changsha, China) for her assistance with statistical analysis. We also thank Jun Zeng and Xiaojian Guo (Department of Ophthalmology, The Second Xiangya Hospital, Central South University, Changsha, China) for offering membranes and blood samples.

REFERENCES

Agrawal, R. N., He, S., Spee, C., Cui, J. Z., Ryan, S. J., and Hinton, D. R. (2007). *In Vivo* models of Proliferative Vitreoretinopathy. *Nat. Protoc.* 2 (1), 67–77. doi:10.1038/nprot.2007.4

Barak, Y., Gottlieb, E., Juven-Gershon, T., and Oren, M. (1994). Regulation of Mdm2 Expression by P53: Alternative Promoters Produce Transcripts with Nonidentical Translation Potential. *Genes Dev.* 8 (15), 1739–1749. doi:10.1101/gad.8.15.1739

Boersma, B. J., Howe, T. M., Goodman, J. E., Yfantis, H. G., Lee, D. H., Chanock, S. J., et al. (2006). Association of Breast Cancer Outcome with Status of P53 and MDM2 SNP309. *J. Natl. Cancer Inst.* 98 (13), 911–919. doi:10.1093/jnci/djj245

Bond, G. L., Hu, W., Bond, E. E., Robins, H., Lutzker, S. G., Arva, N. C., et al. (2004). A Single Nucleotide Polymorphism in the MDM2 Promoter Attenuates the P53 Tumor Suppressor Pathway and Accelerates Tumor Formation in Humans. *Cell* 119 (5), 591–602. doi:10.1016/j.cell.2004.11.022

Bougeard, G., Baert-Desurmont, S., Tournier, I., Vasseur, S., Martin, C., Brugieres, L., et al. (2006). Impact of the MDM2 SNP309 and P53 Arg72Pro Polymorphism on Age of Tumour Onset in Li-Fraumeni Syndrome. *J. Med. Genet.* 43 (6), 531–533. doi:10.1136/jmg.2005.037952

Bringmann, A., and Wiedemann, P. (2012). Müller Glial Cells in Retinal Disease. *Ophthalmologica* 227 (1), 1–19. doi:10.1159/000328979

Bu, S.-C., Kuijer, R., Li, X.-R., Hooymans, J. M. M., and Los, L. I. (2014). Idiopathic Epiretinal Membrane. *Retina* 34 (12), 2317–2335. doi:10.1097/iae.0000000000000349

Carvajal, L. A., and Manfredi, J. J. (2013). Another fork in the Road-Life or Death Decisions by the Tumour Suppressor P53. *EMBO Rep.* 14 (5), 414–421. doi:10.1038/embor.2013.25

Chen, N., Hu, Z., Yang, Y., Han, H., and Lei, H. (2019). Inactive Cas9 Blocks Vitreous-Induced Expression of Mdm2 and Proliferation and Survival of Retinal Pigment Epithelial Cells. *Exp. Eye Res.* 186, 107716. doi:10.1016/j.exer.2019.107716

Chiba, C. (2014). The Retinal Pigment Epithelium: an Important Player of Retinal Disorders and Regeneration. *Exp. Eye Res.* 123, 107–114. doi:10.1016/j.exer.2013.07.009

de la Rua, E. R., Pastor, J. C., Fernandez, I., Sanabria, M. R., Garcia-Arumi, J., Martinez-Castillo, V., et al. (2008). Non-complicated Retinal Detachment Management: Variations in 4 years. Retina 1 Project; Report 1. *Br. J. Ophthalmol.* 92 (4), 523–525. doi:10.1136/bjo.2007.127688

Duan, Y., Ma, G., Huang, X., D'Amore, P. A., Zhang, F., and Lei, H. (2016). The Clustered, Regularly Interspaced, Short Palindromic Repeats-Associated Endonuclease 9 (CRISPR/Cas9)-created MDM2 T309G Mutation Enhances Vitreous-Induced Expression of MDM2 and Proliferation and Survival of Cells. *J. Biol. Chem.* 291 (31), 16339–16347. doi:10.1074/jbc.M116.729467

Gryshchenko, I., Hofbauer, S., Stoecher, M., Daniel, P. T., Steurer, M., Gaiger, A., et al. (2008). MDM2 SNP309 Is Associated with Poor Outcome in B-Cell Chronic Lymphocytic Leukemia. *Jco* 26 (14), 2252–2257. doi:10.1200/jco.2007.11.5212

Hidaka, K., Yamada, M., Kamiya, H., Masutani, C., Harashima, H., Hanaoka, F., et al. (2008). Specificity of Mutations Induced by Incorporation of Oxidized dNTPs into DNA by Human DNA Polymerase η. *DNA Repair* 7 (3), 497–506. doi:10.1016/j.dnarep.2007.12.005

Inoue, M., Kamiya, H., Fujikawa, K., Ootsuyama, Y., Murata-Kamiya, N., Osaki, T., et al. (1998). Induction of Chromosomal Gene Mutations in *Escherichia coli* by Direct Incorporation of Oxidatively Damaged Nucleotides. *J. Biol. Chem.* 273 (18), 11069–11074. doi:10.1074/jbc.273.18.11069

Jones, S. N., Roe, A. E., Donehower, L. A., and Bradley, A. (1995). Rescue of Embryonic Lethality in Mdm2-Deficient Mice by Absence of P53. *Nature* 378 (6553), 206–208. doi:10.1038/378206a0

Knappskog, S., Bjørnslett, M., Myklebust, L. M., Huijts, P. E. A., Vreeswijk, M. P., Edvardsen, H., et al. (2011). The MDM2 Promoter SNP285C/309G Haplotype Diminishes Sp1 Transcription Factor Binding and Reduces Risk for Breast and Ovarian Cancer in Caucasians. *Cancer Cell* 19 (2), 273–282. doi:10.1016/j.ccr.2010.12.019

Landers, J. E., Cassel, S. L., and George, D. L. (1997). Translational Enhancement of Mdm2 Oncogene Expression in Human Tumor Cells Containing a Stabilized Wild-type P53 Protein. *Cancer Res.* 57 (16), 3562–3568.

Lei, H., Rheaume, M.-A., Cui, J., Mukai, S., Maberley, D., Samad, A., et al. (2012). A Novel Function of P53: A Gatekeeper Of Retinal Detachment. *Am. J. Pathol.* 181 (3), 866–874. doi:10.1016/j.ajpath.2012.05.036

Lei, H., Velez, G., and Kazlauskas, A. (2011). Pathological Signaling via Platelet-Derived Growth Factor Receptor Involves Chronic Activation of Akt and Suppression of P53. *Mol. Cell Biol.* 31 (9), 1788–1799. doi:10.1128/MCB.01321-10

Lind, H., Zienolddiny, S., Ekstrøm, P. O., Skaug, V., and Haugen, A. (2006). Association of a Functional Polymorphism in the Promoter of theMDM2 Gene with Risk of Nonsmall Cell Lung Cancer. *Int. J. Cancer* 119 (3), 718–721. doi:10.1002/ijc.21872

Liu, B., Song, J., Han, H., Hu, Z., Chen, N., Cui, J., et al. (2019). Blockade of MDM2 with Inactive Cas9 Prevents Epithelial to Mesenchymal Transition in Retinal Pigment Epithelial Cells. *Lab. Invest.* 99 (12), 1874–1886. doi:10.1038/s41374-019-0307-9

Machemer, R., Aaberg, T. m., Freeman, H. M., Alexander, R. I., John, S. L., and Ronald, M. M. (1991). An Updated Classification of Retinal Detachment with Proliferative Vitreoretinopathy. *Am. J. Ophthalmol.* 112 (2), 159–165. doi:10.1016/s0002-9394(14)76695-4

Maki, H. (2002). Origins of Spontaneous Mutations: Specificity and Directionality of Base-Substitution, Frameshift, and Sequence-Substitution Mutageneses. *Annu. Rev. Genet.* 36, 279–303. doi:10.1146/annurev.genet.36.042602.094806

Maki, H., and Sekiguchi, M. (1992). MutT Protein Specifically Hydrolyses a Potent Mutagenic Substrate for DNA Synthesis. *Nature* 355 (6357), 273–275. doi:10.1038/355273a0

Moriya, M. (1993). Single-stranded Shuttle Phagemid for Mutagenesis Studies in Mammalian Cells: 8-oxoguanine in DNA Induces Targeted G.C-->T.A Transversions in Simian Kidney Cells. *Proc. Natl. Acad. Sci.* 90 (3), 1122–1126. doi:10.1073/pnas.90.3.1122

Ohmiya, N., Taguchi, A., Mabuchi, N., Itoh, A., Hirooka, Y., Niwa, Y., et al. (2006). MDM2Promoter Polymorphism Is Associated with Both an Increased Susceptibility to Gastric Carcinoma and Poor Prognosis. *Jco* 24 (27), 4434–4440. doi:10.1200/jco.2005.04.1459

Pastor, J. C., de la Rúa, E. R., and Martín, F. (2002). Proliferative Vitreoretinopathy: Risk Factors and Pathobiology. *Prog. Retin. Eye Res.* 21 (1), 127–144. doi:10.1016/s1350-9462(01)00023-4

Pastor, J. C., Rojas, J., Pastor-Idoate, S., Di Lauro, S., Gonzalez-Buendia, L., and Delgado-Tirado, S. (2016). Proliferative Vitreoretinopathy: A New Concept of Disease Pathogenesis and Practical Consequences. *Prog. Retin. Eye Res.* 51, 125–155. doi:10.1016/j.preteyeres.2015.07.005

Pastor-Idoate, S., Rodriguez-Hernández, I., Rojas, J., Fernández, I., García-Gutierrez, M. T., Ruiz-Moreno, J. M., et al. (2013a). The P53 Codon 72 Polymorphism (Rs1042522) Is Associated with Proliferative Vitreoretinopathy. *Ophthalmology* 120 (3), 623–628. doi:10.1016/j.ophtha.2012.08.019

Pastor-Idoate, S., Rodríguez-Hernández, I., Rojas, J., Fernández, I., García-Gutiérrez, M. T., Ruiz-Moreno, J. M., et al. (2013b). The T309G MDM2 Gene Polymorphism Is a Novel Risk Factor for Proliferative Vitreoretinopathy. *PLoS One* 8 (12), e82283. doi:10.1371/journal.pone.0082283

Peynshaert, K., Devoldere, J., Minnaert, A.-K., De Smedt, S. C., and Remaut, K. (2019). Morphology and Composition of the Inner Limiting Membrane: Species-specific Variations and Relevance toward Drug Delivery Research. *Curr. Eye Res.* 44 (5), 465–475. doi:10.1080/02713683.2019.1565890

Post, S. M., Quintás-Cardama, A., Pant, V., Iwakuma, T., Hamir, A., Jackson, J. G., et al. (2010). A High-Frequency Regulatory Polymorphism in the P53 Pathway Accelerates Tumor Development. *Cancer Cell* 18 (3), 220–230. doi:10.1016/j.ccr.2010.07.010

Reichenbach, A., and Bringmann, A. (2013). New Functions of Müller Cells. *Glia* 61 (5), 651–678. doi:10.1002/glia.22477

Satou, K., Hori, M., Kawai, K., Kasai, H., Harashima, H., and Kamiya, H. (2009). Involvement of Specialized DNA Polymerases in Mutagenesis by 8-Hydroxy-dGTP in Human Cells. *DNA Repair* 8 (5), 637–642. doi:10.1016/j.dnarep.2008.12.009

Smiddy, W. E., Maguire, A. M., Green, W. R., Michels, R. G., de la Cruz, Z., Enger, C., et al. (1989). Idiopathic Epiretinal Membranes. *Ophthalmology* 96 (6), 811. doi:10.1016/s0161-6420(89)32811-9

Valko, M., Rhodes, C. J., Moncol, J., Izakovic, M., and Mazur, M. (2006). Free Radicals, Metals and Antioxidants in Oxidative Stress-Induced Cancer. *Chemico-Biological Interactions* 160 (1), 1–40. doi:10.1016/j.cbi.2005.12.009

Vishwakarma, S., Gupta, R. K., Jakati, S., Tyagi, M., Pappuru, R. R., Reddig, K., et al. (2020). Molecular Assessment of Epiretinal Membrane: Activated Microglia, Oxidative Stress and Inflammation. *Antioxidants (Basel)* 9 (8), 654. doi:10.3390/antiox9080654

Wade, M., Li, Y.-C., and Wahl, G. M. (2013). MDM2, MDMX and P53 in Oncogenesis and Cancer Therapy. *Nat. Rev. Cancer* 13 (2), 83–96. doi:10.1038/nrc3430

Wilkening, S., Bermejo, J. L., and Hemminki, K. (2007). MDM2 SNP309 and Cancer Risk: a Combined Analysis. *Carcinogenesis* 28 (11), 2262–2267. doi:10.1093/carcin/bgm191

Xiao, W., Chen, X., Yan, W., Zhu, Z., and He, M. (2017). Prevalence and Risk Factors of Epiretinal Membranes: a Systematic Review and Meta-Analysis of Population-Based Studies. *BMJ Open* 7, e014644. doi:10.1136/bmjopen-2016-014644

Yang, J.-Y., Zong, C. S., Xia, W., Wei, Y., Ali-Seyed, M., Li, Z., et al. (2006). MDM2 Promotes Cell Motility and Invasiveness by Regulating E-Cadherin Degradation. *Mol. Cel Biol* 26 (19), 7269–7282. doi:10.1128/MCB.00172-06

Zhang, K. Y., and Johnson, T. V. (2021). The Internal Limiting Membrane: Roles in Retinal Development and Implications for Emerging Ocular Therapies. *Exp. Eye Res.* 206, 108545. doi:10.1016/j.exer.2021.108545

Zhao, F., Gandorfer, A., Haritoglou, C., Scheler, R., Schaumberger, M. M., Kampik, A., et al. (2013). Epiretinal Cell Proliferation in Macular Pucker and Vitreomacular Traction Syndrome. *Retina* 33 (1), 77–88. doi:10.1097/IAE.0b013e3182602087

Zhou, G., Duan, Y., Ma, G., Wu, W., Hu, Z., Chen, N., et al. (2017). Introduction of the MDM2 T309G Mutation in Primary Human Retinal Epithelial Cells Enhances Experimental Proliferative Vitreoretinopathy. *Invest. Ophthalmol. Vis. Sci.* 58 (12), 5361–5367. doi:10.1167/iovs.17-22045

Conflict of Interest: The authors declare that the research was conducted in the absence of any commercial or financial relationships that could be construed as a potential conflict of interest.

Publisher's Note: All claims expressed in this article are solely those of the authors and do not necessarily represent those of their affiliated organizations, or those of the publisher, the editors and the reviewers. Any product that may be evaluated in this article, or claim that may be made by its manufacturer, is not guaranteed or endorsed by the publisher.

Copyright © 2022 Jiang, Yan, Meng, Zhang, Lei and Luo. This is an open-access article distributed under the terms of the Creative Commons Attribution License (CC BY). The use, distribution or reproduction in other forums is permitted, provided the original author(s) and the copyright owner(s) are credited and that the original publication in this journal is cited, in accordance with accepted academic practice. No use, distribution or reproduction is permitted which does not comply with these terms.

frontiers | Frontiers in Cell and Developmental Biology

ORIGINAL RESEARCH
published: 21 April 2022
doi: 10.3389/fcell.2022.794837

Identification of a New Mutation p.P88L in Connexin 50 Associated with Dominant Congenital Cataract

Aixia Jin[1†], Qingqing Zhao[1†], Shuting Liu[1], Zi-bing Jin[2], Shuyan Li[3], Mengqing Xiang[1], Mingbing Zeng[1,4]* and Kangxin Jin[1,2]**

[1]State Key Laboratory of Ophthalmology, Zhongshan Ophthalmic Center, Sun Yat-Sen University, Guangdong Provincial Key Laboratory of Ophthalmology and Visual Science, Guangzhou, China, [2]Beijing Institute of Ophthalmology, Beijing Tongren Eye Center, Beijing Tongren Hospital, Capital Medical University, Beijing Ophthalmology and Visual Science Key Laboratory, Beijing, China, [3]Department of Biochemistry and Biophysics, Peking University Health Science Center, Beijing, China, [4]Hainan Eye Hospital, Hainan Key Laboratory of Ophthalmology, Zhongshan Ophthalmic Center, Sun Yat-sen University, Haikou, China

Congenital hereditary cataract is genetically heterogeneous and the leading cause of visual impairment in children. Identification of hereditary causes is critical to genetic counselling and family planning. Here, we examined a four-generation Chinese pedigree with congenital dominant cataract and identified a new mutation in *GJA8* via targeted exome sequencing. A heterozygous missense mutation c.263C > T, leading to a proline-to-Leucine conversion at the conserved residue 88 in the second transmembrane domain of human connexin 50 (Cx50), was identified in all patients but not in unaffected family members. Functional analyses of the mutation revealed that it disrupted the stability of Cx50 and had a deleterious effect on protein function. Indeed, the mutation compromised normal membrane permeability and gating of ions, and impeded cell migration when overexpressed. Together, our results expand the pathogenic mutation spectrum of Cx50 underlying congenital cataract and lend more support to clinical diagnosis and genetic counseling.

Keywords: congenital cataract, genetic mutation, exome sequencing, connexin, gap junction, hemichannel

OPEN ACCESS

Edited by:
Youjin Hu,
Sun Yat-sen University, China

Reviewed by:
Núria Comes,
University of Barcelona, Spain
Songlin Zhou,
Nantong University, China

****Correspondence:***
Kangxin Jin
jinkx@mail.sysu.edu.cn
Mengqing Xiang
xiangmq3@mail.sysu.edu.cn
Mingbing Zeng
zengmingbing@gzzoc.com

[†]These authors have contributed equally to this work

Specialty section:
This article was submitted to Molecular and Cellular Pathology, a section of the journal Frontiers in Cell and Developmental Biology

Received: *14 October 2021*
Accepted: *29 March 2022*
Published: *21 April 2022*

Citation:
Jin A, Zhao Q, Liu S, Jin Z-b, Li S, Xiang M, Zeng M and Jin K (2022) Identification of a New Mutation p.P88L in Connexin 50 Associated with Dominant Congenital Cataract. Front. Cell Dev. Biol. 10:794837. doi: 10.3389/fcell.2022.794837

INTRODUCTION

The mammalian lens is a transparent organ whose main function is to transmit and focus light onto the retina. During development, the lens is originated from invaginated surface ectoderm that reciprocally induces primordium optic cup (Cvekl and Zhang, 2017). Three cell types, the lens epithelial cells (LECs) and the differentiating and mature fiber cells, compose the lens. The LECs form a monolayer covering the anterior surface and the fiber cells build the bulk of the organ. Fiber cells are differentiated from LECs through a process involving cell proliferation, migration and elongation, and loss of nuclei and cytoplasmic organelles (Cvekl and Ashery-Padan, 2014; Cvekl and Zhang, 2017).

Lens growth occurs almost throughout the lifetime, though extremely slow in adulthood. Genetic or environmental factors interfering with the process could lead to congenital or developmental cataracts, characterized by cloudiness and opacity of the lens. For genetic cataracts, nearly half of them are caused by mutations in the main structural protein crystallins, and surprisingly, about a quarter by abnormalities in gap junction protein connexins (Shiels et al., 2010). With the advances of next generation sequencing technologies, more and more new genetic mutations are identified. For example, some new mutations in Cx46, Cx50 and other genes were recently found to be associated

with cataract and other visual impairments (Berry et al., 2020; Fan et al., 2020). Despite all the mutations identified thus far, the known mutations can explain only a small fraction of hereditary diseases.

Three major connexins, Cx50, Cx46 and Cx43, are dynamically expressed in mammalian lens cells (Bassnett and Šikić, 2017; Cvekl and Zhang, 2017; Donaldson et al., 2017). In LECs, connexins are predominantly Cx50 and Cx43, and include some Cx46. Cx43 is diminishing in the differentiating fiber cells and almost disappears from mature fiber cells. On the contrary, Cx46 gradually increases in the differentiating and mature fiber cells (Mathias et al., 2010; Berthoud and Ngezahayo, 2017). Though the structure and function of the three connexins are similar, there is only partial redundancy in their function. For example, the phenotype of smaller lens in *Cx50* knockout mice could not be rescued by replacement with *Cx46* knockin (Sellitto et al., 2004). The nature of the dynamic and differential expression patterns of the connexins is still not understood.

Recently, near-atomic level structure of sheep lens Cx46/50 has been resolved with electron cryo-microscopy (CryoEM) (Myers et al., 2018; Flores et al., 2020), providing us clues to how the architectural stability, structure and function of gap junction communication channels are maintained. Given that mammalian connexins are highly conserved, especially in functional domains, the native structural details are very helpful for understanding how human Cx50 works *in vivo*. Despite this, the importance of individual amino acid residue and its contribution to protein structure and function have largely been gained from patients and causative mutational studies. In this study, we identified a new mutation c.263C > T in *GJA8* gene, corresponding to p.P88L in Cx50, from a four-generation pedigree with dominant congenital cataract in Hainan province of China. This finding adds a new mutation to the mutation spectrum and expands our understanding of the structural base and function of human Cx50.

MATERIALS AND METHODS

Patients and Deoxyribonucleic Acid Collection

A four-generation Chinese family with hereditary dominant congenital cataract was recruited at Hainan Eye Hospital, Zhongshan Ophthalmic Center. We obtained the medical histories of 24 family members, among which 11 members were available in this study, including 9 affected and 2 unaffected individuals. The diagnosis of cataract was confirmed by a series of ophthalmologic examinations. Genomic DNA was extracted from peripheral blood cells using the QIAamp DNA Blood Mini Kit (Qiagen, China).

The medical protocol was approved by the Committee of Human Ethics in Medical Research in Zhongshan Ophthalmic Center and consistent with the Declaration of Helsinki. The written informed consent was obtained from each participant or their legal custodians.

Targeted Exome Sequencing

A minimum of 3 ug DNA was used for the indexed Illumina libraries according to manufacturer's protocol (MyGenostics Inc., Beijing, China). DNA fragments with sizes ranging from 350 to 450 bp and those including the adapter sequences were selected for the DNA libraries. Next, targeted exome sequencing was selected by a gene capture strategy, using the GenCap Exome Enrichment Kit V4.0 (MyGenostics Inc., Beijing, China). The biotinylated capture probes (80–120-mer) were designed to tile the targeted exons with non-repeated regions. The kit was designed to detect exome of 3,086 genes whose mutations are known to be pathogenic. The captured DNA was amplified and purified with SPRI beads (Beckman Coulter, Brea, CA, United States). The enriched libraries were sequenced with an Illumina NextSeq 500 sequencer for paired-end reads of 150 bp with an average depth of 120X. The data was deposited to GSA-Human with accession number HRA001484 (https://bigd.big.ac.cn/gsa-human/browse/HRA001484).

Mutation and Bioinformatics Analysis

Following sequencing, raw image files were processed using Bcl2Fastq software (Bcl2Fastq 2.18.0.12, Illumina, Inc.) for base calling and raw data generation. Low-quality variations were filtered out using a quality score ≥20. Short Oligonucleotide Analysis Package (SOAP) aligner software (SOAP2.21; soap.genomics.org.cn/soapsnp.html) was then used to align the clean reads to the reference human genome (hg19). Polymerase chain reaction (PCR) duplicates were removed using the Picard program. Subsequently, single nucleotide polymorphisms (SNPs) were determined using the SOAPsnp program, reads were realigned using Burrows-Wheeler Aligner software 0.7.15, and the deletions and insertions (InDels) were detected using Genome Analysis Toolkit software 3.7. The identified SNPs and InDels were annotated using the Exome-assistant program (http://122.228.158.106/exomeassistant). The MagicViewer was used to view the short-read alignment, and confirm the candidate SNPs and InDels.

To determine pathogenicity, non-synonymous variants were evaluated using the following programs: PolyPhen2 (http://genetics.bwh.harvard.edu/pph2/), PROVEAN (Protein Variation Effect Analyzer V1.1.3, http://provean.jcvi.org/), PANTHER (Protein Analysis Through Evolutionary Relationships, www.pantherdb.org), SDM2 (Site Directed Mutator, http://marid.bioc.cam.ac.uk/sdm2/), PMut (http://mmb.irbbarcelona.org/PMut) and MutationTaster (http://doro.charite.de/MutationTaster/index.html). The calculation of hydrophobicity score was determined by ProtScale (https://web.expasy.org/protscale/), and image was redrawn with GraphPad Prism (GraphPad Software, La Jolla, CA). The prediction of mutational protein structure was obtained from RoseTTAFold (Baek et al., 2021) (https://robetta.bakerlab.org/), a fast and accurate deep learning-based modeling method comparable to AlphaFold2. Wild type and mutational protein structures and amino acid interactions were captured with Pymol Molecular Graphics System (v2.6.0a0).

Sanger Sequencing

All mutations identified by the Illumina NextSeq 500 sequencer were confirmed by Sanger sequencing. To validate the mutation in *GJA8* gene, a 262bp PCR product was amplified from each patient genome DNA. The following PCR primers were used: 5′-ATGAGCAATCCGACTTCG -3' (forward), and 5′- TTCTTA GTGCCTTTGCTGC -3' (reverse). High fidelity PrimeSTAR Max DNA Polymerase (Takara, Beijing, China) was used to avoid amplification errors. The amplified DNA fragments were purified and sequenced with an ABI PRISM 3730 genetic analyzer (Applied Biosystems; Thermo Fisher Scientific, Inc.). The sequence reading was carefully examined and confirmed manually.

Plasmid Construction and Cell Scratch Wound Analysis

The human *GJA8* open reading frame (ORF) sequence (NM_005,267.5) and ORF with the point mutation (*P88L*, c.263C > T) were cloned into the pCIG plasmid, a mammalian expression vector containing a sequence of the CMV enhancer, chicken *ß*-actin promoter, multiple cloning sites (MCS), internal ribosome entry site (IRES), *eGFP,* and rabbit *ß*-globin polyA sequences, as described previously (Jin et al., 2015).

The human LECs were purchased from ATCC (Cat# CRL-11421)). Cells were cultured in 10 cm dishes following the manufacture's protocol. They were then transfected with 40 μg of each plasmid using Hieff Trans™ Liposomal Transfection Reagent (Yeasen, Cat# 40802ES03). After reaching a confluent monolayer, cells were scraped with a 10 μL pipette tip to create scratches of similar sizes. Images were captured from the marked region every 12 h (hours) and were analyzed quantitatively with the software ImageJ. The wound closure ratio was calculated as one minus the ratio of the blank area at each timepoint with the initial blank area (1 - blank area/initial blank area). The statistical analyses and line charts were processed and generated with Graphpad Prism. The non-parametric method Friedman test was used to determine the statistical difference and a value of $p < 0.05$ is considered to be significantly different.

EdU Labeling

Human LECs transfected with 3 μg of pCIG-vector, -hGJA8 or -P88L were cultured in 6-well plate for 48 h. Then 1×10^5 cells were plated in each well (12-well plate) containing a glass coverslip pre-coated with poly-L-Lysine and laminin. One day following plating, EdU (5-ethynyl-2′-deoxyuridine) was added into the culture medium to a final concentration of 10 μM, and cells were cultivated for 24 h or 48 h. They were fixed with 4% formaldehyde for 15 min, washed with PBS and blocked with 10% donkey serum in PBS for 1h under room temperature. GFP antibody (1:1,000 dilution, Abcam, cat# ab6673) was added and incubated at 4 °C overnight. Cells were washed with PBS and incubated with secondary antibodies conjugated with Alexa-488 for 1 h. EdU staining was carried out according to the manufacturer's instruction (Click-iT EdU Cell Proliferation Kit, Thermofisher Scientific, Cat# C10338). Images were captured with Zeiss confocal 700 system. GFP^+, EdU^+, and GFP^+Edu^+ double-positive cells were counted and analyzed.

Patch Clamp Analysis of Membranal Voltage Gating and Ion Permeability

Human LECs were transfected with pCIG-vector, -*GJA8*, or -*P88L*. To obtain the whole-cell recording, GFP-positive cells were bathed in external solution which contained 135 mM NaCl, 5 mM KCl, 2 mM CsCl, 2 mM CaCl2, 1 mM MgCl2, 5 mM HEPES, 5 mM dextrose, 2 mM pyruvate, and 1 mM BaCl2, pH 7.4. The patch pipette solution (internal solution) contained 125 mM CsCl, 10 mM EGTA, 0.5 mM CaCl2, and 10 mM HEPES and its pH value was adjusted to 7.2. Recordings were performed with the Axon 700B amplifier and Clampfit software (v11). The glass patch pipette had a resistance of 3–5 MΩ in bath solution. Data were sampled at minimal start intervals and low-pass was filtered at 1 kHz. Leak subtraction was not employed.

Antibodies and Cell Immunofluorescence

Human LECs transfected with pCIG-vector, -hGJA8 or -P88L were cultured for 72 h and fixed in 4% paraformaldehyde in PBS (pH7.4) for 5 min. They were then washed with 1x PBS 3 times and blocked with 5% normal sheep serum in PBS for 1 h. Primary antibodies against Cx50 (1:200 dilution, Santa Cruz, cat# sc-3738,011) and GFP (1:500 dilution, Abcam, cat# ab6673) were added and incubated at 4°C overnight. Cells were washed with PBS 3 times to remove free primary antibodies and secondary antibodies conjugated with Alexa-488 or Alexa-594 were added and incubated for 1 h at room temperature. Extra antibodies were washed away with PBS. Images were captured with Zeiss confocal 700 system.

RESULTS

Clinical Data and Findings

Due to the island and mountainous landscape, Hainan province has relatively more undiagnosed families with hereditary diseases. We recently found a four-generation pedigree with congenital dominant cataract in the province (**Figure 1A**). There were a total of 11 affected and 13 unaffected members in the pedigree. Eight members (II:3, III:5, 6, 9, 11, IV:3, 4, 5) had sought treatment in our hospital, all with bilateral cataract (**Figure 1B**), 4 with bilateral nystagmus (III:5, 6, 11, IV:3), 3 with bilateral or unilateral strabismus (III:6, 9, 11). The nystagmus and strabismus were secondary diseases following cataract. The category of cataract types and severity varied among patients (**Figure 1B**); however, upon inquiry of patients and family members, all affected members in the pedigree were confirmed to have congenital bilateral cataracts.

Mutation Identification and Analyses

To identify the causative mutation(s), we sent 3 patient genomic DNA samples (II:3, III:11, IV:5) for targeted exome sequencing, which was designed to specifically focus on the exome of a panel of 3,086 genes known to be pathogenic when mutated. A total of 8 mutations, c.2010 + 10G > A (splicing) in *ACTN4*, c.1697A > G

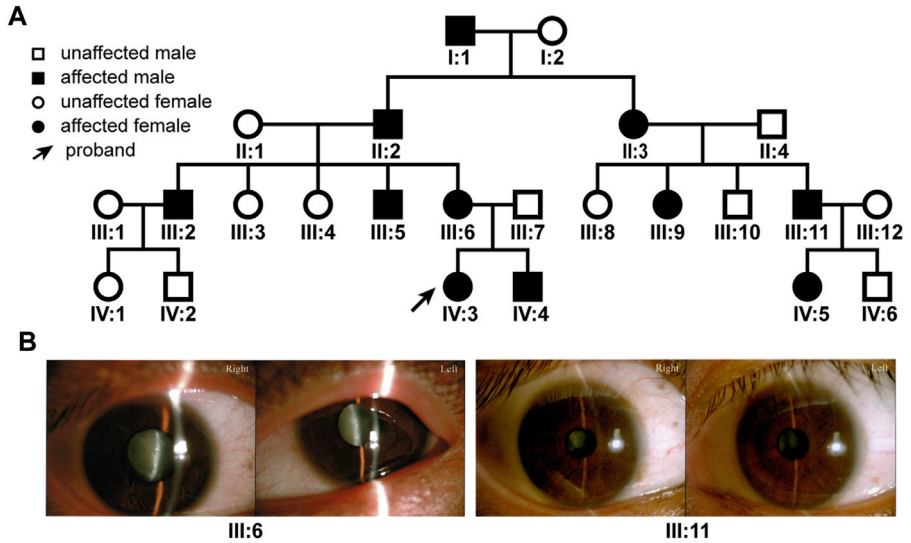

FIGURE 1 | The family tree of the patient pedigree and cataract phenotype. **(A)** The four-generation 24-member pedigree with dominant congenital cataract. **(B)** Varied cataract types and severity in patients. Photographs of eyes of two patients were shown. Patient III:6 has bilateral total cataracts. Patient III: 11 has a nuclear cataract in the right eye and a zonular cataract in the left eye.

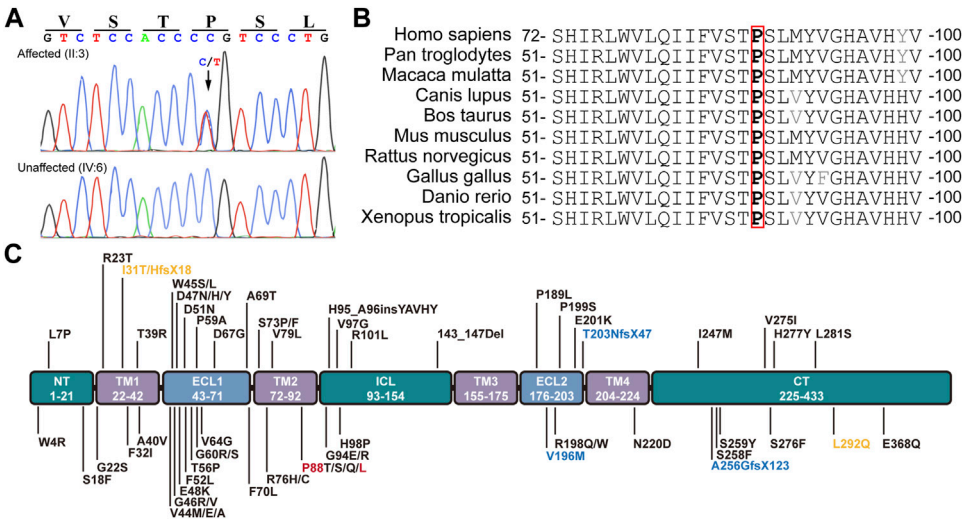

FIGURE 2 | Mutation identification and analyses. **(A)** The c.262C > T heterozygous mutation in GJA8 was confirmed in all affected but not in unaffected family members by the Sanger sequencing. This mutation results in a p.P88L amino acid change in the second transmembrane domain in Cx50. **(B)** The P88 (highlighted in red box) and neighbor amino acid residues were conserved in the indicated vertebrates. **(C)** Known pathogenic mutations in human Cx50 are listed according to their positions in the functional domains. Dominant mutations are listed in black, recessive mutations in blue, and uncertain mutations in orange. Letters in red denote the mutation in this study. NT (N-terminus), ICL (intracellular loop), and CT (C-terminus) are intracellular regions (in green boxes). TM1-4 indicate the four transmembrane regions (in purple boxes). ECL1-2 are extracellular loops (in light blue boxes).

(p.H566R) in *ATP2A2*, c.242C > T (p.P81L) in *CFHR5*, c.263C > T (p.P88L) in *GJA8*, c.4475A > C (p.Q1492P) in *MED13*, c.1021G > T (p.G341C) in *PRX*, c.3634C > T (p.P1212S) in *SHANK3*, and c.697G > C (p.V233L) in *SLC26A4*, were present in all 3 patients. Except for the *GJA8* mutation, the other 7 gene mutations were autosomal-recessive or predicted to be benign or uncertain to be pathogenic, and more importantly, no correlated diseases or symptoms were previously diagnosed in patients with these mutations. The c.263C > T mutation in *GJA8* was verified in all 3 patients by Sanger sequencing. We further examined genomic DNA from the other 8 inpatient and outpatient individuals (I:1, III:5, 6, 9, 12, IV:3, 4, 6) in the pedigree by Sanger sequencing. The c.263C > T mutation was co-segregated with all affected but not with unaffected individuals.

TABLE 1 | Reported human GJA8 mutations and related diseases.

Nucleotide Change	Amino Acid Change	Mutation Type	Hetero-/ Homozygous	AR or AD	Related Diseases	Reference
c.10T > A	p.W4R	missense	Het	AD	congenital cataract	Zhang et al. (2018a)
c.20T > C	p.L7P	missense	Het	AD	congenital cataract	Mackay et al. (2014)
c.53C > T	p.S18F	missense	Het	AD	congenital cataract	Micheal et al. (2018)
c.64G > A	p.G22S	missense	Het	AD	congenital pulverulent cataract	Ye et al. (2019)
c.68G > C	p.R23T	missense	Het	AD	congenital nuclear cataract	Willoughby et al. (2003)
c.89dupT	p.I31HfsX18	Insertion, frameshift	*Homo*	AR (AD?)	congenital cataract	Ma et al. (2016)
c.92T > C	p.I31T	missense	Het	AD	congenital nuclear cataract	Wang et al. (2009)
c.94T > C	p.F32I	missense	Het	AD	congenital cataract	Dang et al. (2016)
c.116C > G	p.T39R	missense	Het	AD	congenital cataract with microcornea	Sun et al. (2011); Ceroni et al. (2019)
c.119C > T	p.A40V	missense	Het	AD	congenital cataract	Ma et al. (2016)
c.130G > A	p.V44M	missense	Het	AD	congenital cataract	Mohebi et al. (2017); Zhang et al. (2018b)
c.131T > A	p.V44E	missense	Het	AD	congenital cataract with microcornea	Devi and Vijayalakshmi, (2006)
c.131T > C	p.V44A	missense	Het	AD	congenital nuclear cataract	Zhu et al. (2014)
c.134G > C	p.W45S	missense	Het	AD	congenital cataract with microcornea	Vanita et al. (2008b); Ma et al. (2016)
c.134G > T	p.W45L	missense	Het	AD	congenital cataract, w/o microcornea	Mohebi et al. (2017); Ceroni et al. (2019)
c.136G > A	p.G46R	missense	Het	AD	congenital cataract with microcornea	Sun et al. (2011); Fan et al. (2020)
c.137G > T	p.G46V	missense	Het	AD	congenital cataract	Minogue et al. (2009)
c.139G > A	p.D47N	missense	Het	AD	congenital nuclear/zonular/ pulverulent cataract	Arora et al. (2008); He et al. (2011); Wang et al. (2011); Liang et al. (2015); Shen et al. (2017); Gunda et al. (2018)
c.139G > C	p.D47H	missense	Het	AD	congenital nuclear/zonular/ pulverulent cataract	Li et al. (2013)
c.139G > T	p.D47Y	missense	Het	AD	congenital cataract	Lin et al. (2008)
c.142G > A	p.E48K	missense	Het	AD	Congenital zonular/nuclear/ pulverulent cataract	Berry et al. (1999)
c.151G > A	p.D51N	missense	Het	AD	congenital cataract, sclerocornea, microphthalmia	Ma et al. (2016); Ceroni et al. (2019)
c.154T > C	p.F52 L	missense	Het	AD	congenital cataract	Li et al. (2019a)
c.166A > C	p.T56P	missense	Het	AD	congenital nuclear cataract	Hadrami et al. (2019)
c.175C > G	p.P59A	missense	Het	AD	congenital cataract	Yu et al. (2016); Micheal et al. (2018)
c.178G > C	p.G60R	missense	Het	AD	congenital zonular cataract	Berry et al. (2020)
c.178G > A	p.G60S	missense	Het	AD	congenital cataract	Ding et al. (2020)
c.191T > G	p.V64G	missense	Het	AD	congenital cataract	Zheng et al. (2005)
c.200A > G	p.D67G	missense	Het	AD	congenital cataract	Reis et al. (2013)
c.205G > A	p.A69T	missense	Het	AD	congenital cataract	Li et al. (2020)
c.208T > C	p.F70L	missense	Het	AD	congenital cataract with microphthalmia	Ceroni et al. (2019)
c.217T > C	p.S73P	missense	Het	AD	congenital cataract	Li et al. (2019b)
c.218C > T	p.S73F	missense	Het	AD	congenital nuclear cataract	Yang et al. (2015)
c.226C > T	p.R76C	missense	Het	AD	congenital cataract	Reis et al. (2013)
c.227G > A	p.R76H	missense	Het	AD	congenital cataract	Yu et al. (2016); Wang et al. (2020)
c.235G > C	p.V79L	missense	Het	AD	congenital cataract	Vanita et al. (2006)
c.262C > A[#1]	p.P88T	missense	Het	AD	congenital cataract	Ge et al. (2014)
c.262C > T	p.P88S	missense	Het	AD	congenital zonular/ pulverulent cataract	Shiels et al. (1998); Berry et al. (2020)
c.263C > A[#2]	p.P88Q	missense	Het	AD	congenital cataract	Arora et al. (2006); Vanita et al. (2008a)
c.263C > T	p.P88L	missense	Het	AD	congenital cataract	this study
c.280G > C	p.G94R	missense	Het	AD	congenital cataract	Ma et al. (2018)
c.280G > A	p.G94R	missense	Het[#9]	AD[#9]	no lens, microphthalmia, coloboma, etc.	Ceroni et al. (2019)
c.281G > A	p.G94E	missense	Het	AD	congenital cataract, sclerocornea	Ma et al. (2018)
c.285ins	p.H95_A96insYAVHY	insertion	Het	AD	congenital cataract	Cui et al. (2018)
c.290T > G	p.V97G	missense	Het[#10]	AD[#10]		Ceroni et al. (2019)

(Continued on following page)

TABLE 1 | (*Continued*) Reported human GJA8 mutations and related diseases.

Nucleotide Change	Amino Acid Change	Mutation Type	Hetero-/ Homozygous	AR or AD	Related Diseases	Reference
					congenital cataract, microphthalmia, glaucoma, etc.	
c.293A > C	p.H98P	missense	Het	AD	congenital cataract	Mackay et al. (2014)
c.301G > T	p.R101L	missense	Het	AD	congenital cataract	Mohebi et al. (2017)
c.426_440del	p.143_147del	deletion	Het	AD	congenital cataract	Min et al. (2016)
c.433G > T	p.G145W	missense	Het	AD	congenital cataract	Ren et al. (2017)
c.565C > T	p.P189L	missense	Het	AD	congenital cataract with microcornea	Hansen et al. (2007)
c.586G > A[#3]	p.V196M	missense	*Homo*	AR	congenital cataract	Ponnam et al. (2013)
c.592C > T	p.R198W	missense	Het	AD	congenital cataract with microcornea	Hu et al. (2010)
c.593G > A	p.R198Q	missense	Het	AD	developmental cataract	Devi and Vijayalakshmi, (2006)
c.595C > T[#4]	p.P199S	missense	Het	AD	congenital cataract	Ponnam et al. (2013)
c.601G > A	p.E201K	missense	Het	AD	congenital perinuclear cataract	Su et al. (2013)
c.607insA[#5]	p.T203NfsX47	insertion, frameshift	*Homo*	AR	congenital cataract	Ponnam et al. (2007)
c.658A > G	p.N220D	missense	Het	AD	congenital cataract (or unaffected)	Kuo et al. (2017)
c.741T > G	p.I247M	missense	Het	AD	congenital zonular pulverulent cataract	Polyakov et al. (2001); Reis et al. (2013)[#12]
c.766insG[#6]	p.A256GfsX123[#11]	insertion, frameshift	*Homo*	AR	congenital cataract	Schmidt et al. (2008)
c.773C > T	p.S258F	missense	Het	AD	congenital nuclear cataract	Gao et al. (2010)
c.776C > A[#7]	p.S259Y	missense	Het	AD	congenital cataract	Hansen et al. (2009)
c.823G > A	p.V275I	missense	Het	AD	developmental cataract	Zhou et al. (2011)
c.827C > T	p.S276F	missense	Het	AD	congenital nuclear pulverulent cataract	Yan et al. (2008)
c.829C > T	p.H277Y	missense	Het	AD	congenital nuclear pulverulent cataract	Chen et al. (2015)
c.842T > C[#8]	p.L281S[#8]	missense	Het	AD	congenital zonular cataract	Kumar et al. (2011)
c.875T > A	p.L292Q	missense	n/a	n/a	congenital cataract, coloboma, etc.	Ceroni et al. (2019)
c.1102G > C	p.E368Q	missense	Het	AD	congenital cataract	Senthil Kumar et al. (2016)

Notes, #1–8: They were listed as c.264C > A, c.262C > A, c.649G > A, c.658C > T, c,670insA, c.776insG, c.836C > A, c.905T > C (p.L281C) in the original publications, respectively, but were re-numbered with the common standard (39). #9–10: The mutations were justified as heterozygous and dominant according to the Sanger sequencing results in the original publication. #11: The amino acid changes were not described in the original publication. Here it shows the inferred sequence from nucleotide changes. #12: It is present in 0.7% of the European American population and is most likely a polymorphism.

The conversion of c.263C > T leads to the substitution of Leucine (L) for Proline (P) at the 88th residue (p.P88L) in the 2nd transmembrane domain of Cx50 (**Figure 2A**). The P88 residue is extremely conserved in all examined homologues from the *Xenopus*, zebrafish, chicken, rat, mouse, cow, dog, mulatta, chimpanzee, and human (**Figure 2B**), as well as in counterparts of other connexins (Arora et al., 2006; Ge et al., 2014; Myers et al., 2018), indicating an indispensable role for it in maintaining connexin structure and function (Shiels et al., 1998; Arora et al., 2006; Vanita et al., 2008a; Ge et al., 2014). The mutation is an unreported mutation (**Figure 2C** and **Table 1**). It is not present in databases including Ensembl, 1,000 Genomes, dbSNP, HapMap, ClinVar, or gnomAD.

P88L Mutation Disrupts Cx50 Structure and Function

To evaluate the damaging effects of P88L mutation in Cx50, we used well-endorsed programs for *in silico* predictions. PolyPhen2, PANTHER, PMut, SDM2, PROVEAN, and MutationTaster output the results of 'Probably damaging', 'Probably damaging', 'Disease', 'Increased stability', 'Deleterious' and 'Disease causing', respectively (**Table 2**). These results are in agreement with the increased hydrophobicity score around the mutation site (**Figure 3A**).

The native channel structure of the 12 subunits of Cx50 and/or Cx46 has recently been elucidated with cryo-EM (Flores et al., 2020; Myers et al., 2018). P88 sits at the homo/heteromeric interface but not homo/heterotypic interface (**Figures 3B,C**) (Myers et al., 2018), and therefore the P88L mutation likely interrupts the Cx50 conformation or homo/heteromeric interface interactions. In the wildtype Cx50 protein, P88 maintains the transmembrane α-helix structure by establishing a hydrogen bond with Y92 (Tyr92, **Figure 3D**). In the mutant, even though L88 reestablishes a hydrogen bond with Y92, it also interacts with F84 and M91 through hydrogen bonds, resulting in regional and global protein conformational changes (**Figure 3E**). The changes might directly or indirectly disrupt the physiological function of the channels or hemi-channels.

TABLE 2 | In silico predictions of functional effects for Cx50-P88L mutation.

	PolyPhen2	PANTHER	PMut	SDM2	PROVEAN	MutationTaster
Score	1.000	Preservation time: 797 million years	0.93	ΔΔG = 1.56	−9.963	Probability = 0.999 Score = 98
Result	Probably damaging	Probably damaging	Disease	Increased stability	Deleterious	Disease causing

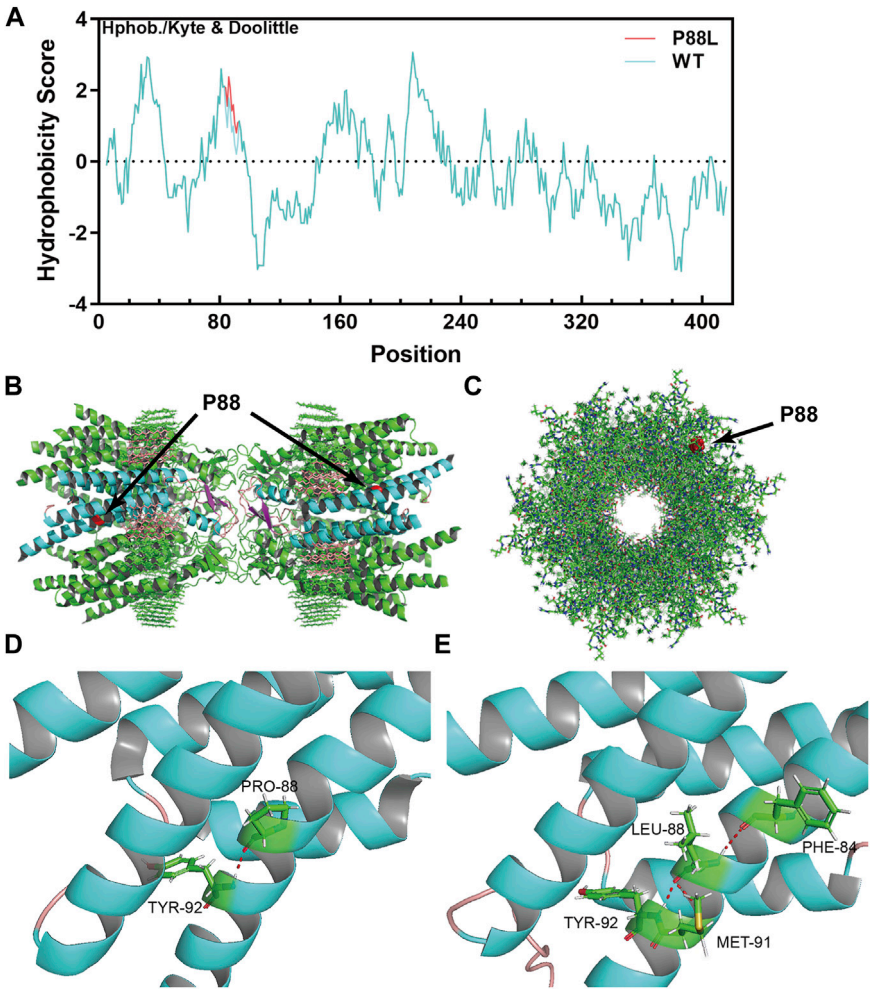

FIGURE 3 | The P88L mutation increases local hydrophobicity and transforms 3-dimentional conformation of Cx50. **(A)** The hydrophobicity score was calculated with the Kphob/Kyle & Doolittle method on ProtScale. It is obvious that the local hydrophobicity score is increased around position 88 in the P88L mutant. **(B)** The horizontal view of the two P88 positions (labeled in red) in the gap junction channel made of a dodecamer of sheep Cx50. **(C)** The vertical view of one P88 position (labeled in red) in the gap junction channel made of a dodecamer of sheep Cx50. **(D, E)** Even though the Pro88-to-Leu88 substitute keeps a hydrogen bond (in red) interaction with Tyr92, Leu88 establishes extra hydrogen bonds with Met91 and Phe84, which drastically transforms the three-dimensional conformation as shown. The structures in **(B–D)** were generated based on the protein structure file 7jjp.pdb downloaded from PDB. The mutant structure in E was predicted with RoseTTAFold. The pictures in **(B–E)** were visualized and captured with Pymol (V2.6.0a0).

P88L Mutation Impedes the Migration but Not Proliferation of Lens Epithelial Cells

It has been shown that connexins including Cx50 could directly or indirectly affect cell proliferation and migration (Sellitto et al., 2004; White et al., 2007; Machtaler et al., 2014; Polusani et al., 2016; Tjahjono et al., 2020). To examine if P88L mutation could interfere with LECs proliferation and/or migration, we cloned the human wildtype *GJA8* and *P88L* into a plasmid vector that could overexpress them by a ubiquitously active promoter CAG (consisting of the cytomegalovirus enhancer fused to the chicken beta-actin promoter) (**Figure 4A**).

Comparable amounts of wildtype Cx50 or P88L were expressed in GFP^+ cells as determined by cellular immunofluorescence staining (**Supplementary Figure S1**).

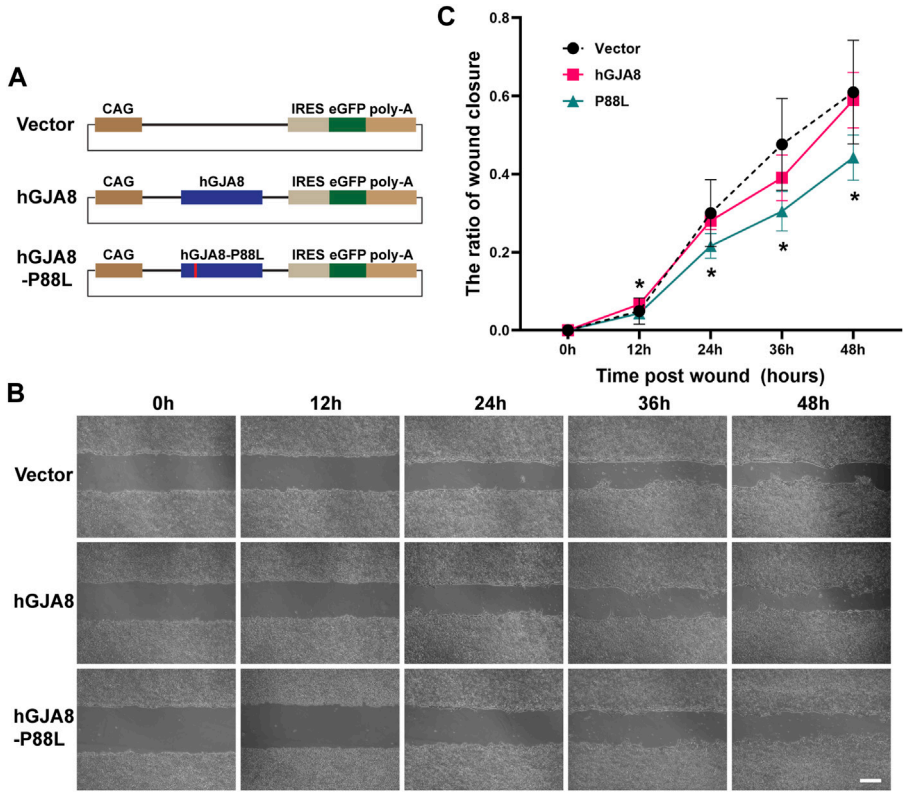

FIGURE 4 | Overexpression of P88L inhibits human LECs migration. **(A)** Illustration of pCIG-vector, pCIG-hGJA8 and pCIG-hGJA8-P88L plasmids used for transfection. **(B)** Human LECs were transfected with the indicated plasmids. Cells were scraped to create wounds of similar sizes. Representative images were captured at timepoints 0 h (hour), 12, 24, 36 and 48 h after cell scratches. Scale bar: 200 μm. **(C)** The wound closure ratios were calculated at each timepoint by ImageJ. The asterisk '*' represents a significant difference ($p < 0.05$; $N = 6$ for GJA8 and vector, $N = 8$ for P88L) between P88L and wildtype GJA8 or vector at the timepoint.

GFP^+, EdU^+, and GFP^+EdU^+ double-positive cells were counted after 24 and 48 h. There was no difference in the ratios of GFP^+EdU^+/GFP^+ cells among groups (**Supplementary Figure S2**), implying that overexpression of *P88L* does not affect LECs proliferation, which probably explains why the patients do not have a phenotype of microphthalmia.

On the other hand, cell scratch wound assay showed that overexpression of human *GJA8* had a similar effect as vector (GFP), but overexpression of *P88L* caused a significantly slower rate of wound closure than those of wildtype and vector (**Figures 4B,C**), indicating that cells with P88L have a slower migration rate.

P88L Inhibits Voltage Gating of Cx50 and Decreases the Membranal Ion Permeability of Human LECs

To examine if P88L mutation compromises membranal voltage gating, human LECs were transfected with pCIG-vector, *-hGJA8* or *-P88L* mutant. To selectively evaluate the hemichannel conductance, isolated GFP^+ cells were chosen (**Figures 5A–C**). Membrane currents were recorded while cells were clamped to different membrane voltages. We found that LECs expressing pCIG-vector, -hGJA8 or -P88L all displayed bigger currents at positive membrane voltages compared to the negative ones, particularly LECs with hGJA8 (1,263 ± 155 pA at 90 mV versus -546 ± 154 pA at −100 mV), indicating that Cx50 hemichannel is voltage-dependent. The LECs showed outward currents at positive potentials in a voltage-dependent manner (**Figure 5D**), consistent with low expression of GJA8 in these cells. Upon overexpression of GJA8, the outward currents were amplified significantly (107 ± 26 pA/pF versus 32 ± 6 pA/pF) (**Figures 5E,G**), and the inward current at negative membrane potential showed much lower than pCIG-vector (−51 ± 22 pA/pF versus −24 ± 11 pA/pF); however, both the inward and outward currents were dampened in cells expressing P88L (31 ± 4 pA/pF versus 107 ± 26 pA/pF) (**Figures 5F,G**). These results thus indicated that the P88L mutant protein inhibited the ionic currents in a voltage-dependent manner in human LECs.

DISCUSSION

There are four subclasses (GJA, GJB, GJC and GJD), around 20 members of connexins in human, sharing a topology of 4 transmembrane domains, 2 extracellular loops, and 3 intracellular regions (N-terminus, intracellular loop and C-terminus) (Beyer and Berthoud, 2018). Each hemichannel is

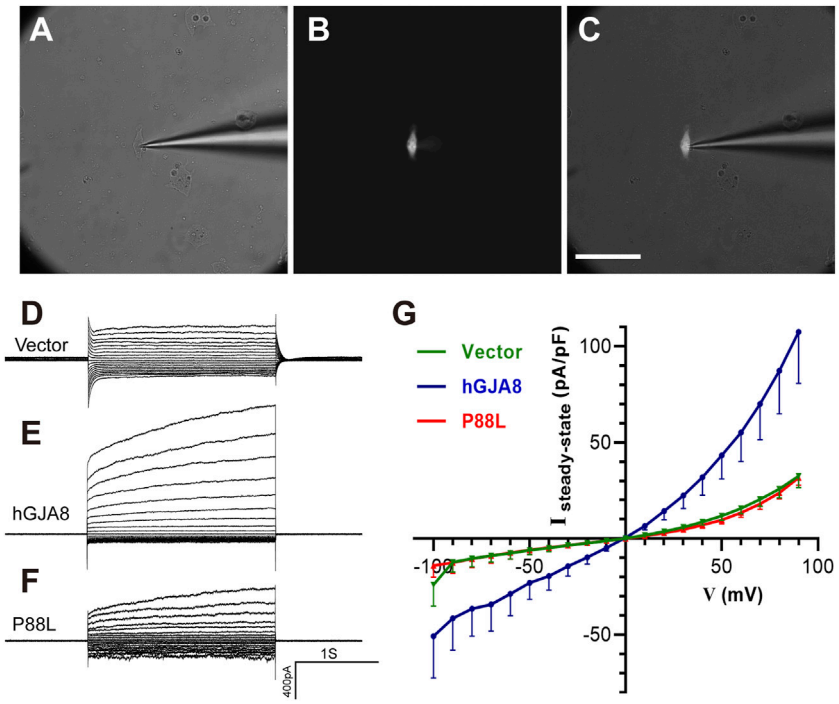

FIGURE 5 | The P88L mutation inhibits hemichannel currents of Cx50 in human LECs. **(A–C)** Representative images show patch-clamp recordings of isolated GFP-positive cells under white light only **(A)**, blue light only **(B)**, and both white and blue lights **(C)**. Scale bar: 80 μm. **(D–F)** Steady-state currents from pulses were plotted as a function of membrane voltage. Representative voltage-dependent transmembrane current traces of LECs transfected with pCIG-vector **(D)**, *-hGJA8* **(E)** or *-P88L* **(F)** were measured at a holding potential of 0 mV and subjected to voltage pulses ranging from -100 to 90 mV in 10 mV steps. **(G)** Population steady-state current density–voltage relationships from human LECs expressing pCIG-vector, -hGJA8 or -P88L. Data is represented as mean ± SEM. Sample sizes: $N = 12$ for vector and P88L, $N = 11$ for hGJA8. $p < 0.0001$ for interaction and row factor, $p = 0.0061$ for column factor, with two-way ANOVA analysis.

assembled by the oligomerization of six homomeric or heteromeric subunits of Cxs, and two hemichannels dock end-to-end to form a gap junction channel. Hemichannels and channels allow the exchange of ions, metabolites and small molecules such as second messengers between a cell and its extracellular environment or between neighbor cells, respectively (Esseltine and Laird, 2016; García et al., 2016; Aasen et al., 2018; Jindal et al., 2021). However, how the differential tissue-specific expression of each connexin and the ratio of hemichannel-to-channel are controlled is not well understood.

There is no direct blood supply to mature lenses, and fiber cells depend on hemichannels to exchange ions and metabolites with extracellular aqueous humor while relying on gap junction channels for intercellular material swaps (Mathias et al., 2007; Mathias et al., 2010; Berthoud et al., 2020; Totland et al., 2020). Given that Cx50 is highly expressed in mature fiber cells and exists predominantly in the hemichannels rather than channels, we surmise that Cx50 may be the major player for exchanging ions and metabolites between the cells and the environmental humor (Mathias et al., 2010), and hence critical for maintaining lens homeostasis and physiology, which could be the primary reason to induce cataract when mutated.

Accumulating evidence from genetic sources and biochemical, cellular and physiological data indicates that the molecular mechanisms of connexin mutation-induced cataracts can attribute to four major causes, including disruption of lens development, impairment of lens transparency, alteration of channel and hemichannel electrical properties, disturbance of protein trafficking to trigger stress responses, or combinations of these causes (Mathias et al., 2010). The majority of the disease-causing mutations in Cx50 are dominant, indicating that these are either dominant-negative or gain-of-function mutations. The mutations are scattered across all the domains from C- to N-terminus (**Figure 2C**), demonstrating the integral requirement of all regions. One of the most frequently mutated regions in Cx50 is located between amino acid residues 40–60th, which directly influence the pore and channel and their mutations may result in significant perturbation to gating properties, conductance and free energy of the open-closed state (Myers et al., 2018).

The four transmembrane domains of Cx50 form the central channel and pore. The new mutation P88L is located in the second transmembrane domain. The P88 residue does not form the channel wall directly; however, it is highly conserved evolutionarily and most likely plays an essential role in the protein structure and function. A few mutations of the residue, P88T, P88S and P88Q, have been reported previously to cause various types of congenital cataracts (Shiels et al., 1998; Arora et al., 2006; Vanita et al., 2008a; Ge et al., 2014; Berry et al.,

2020). Consistent with these reports, there was no microphthalmia or microcornea symptom associated with the P88L mutation, implying that P88 mutations probably do not perturb the LECs proliferation *in vivo*. Cell culture and other *in vitro* experiments showed that the membrane distribution of gap junction plaques and membrane-floating proteins were substantially different in the mutants, indicating a disruption of normal function by P88 mutations.

The mechanism of how Cx50 is involved in LECs proliferation and differentiation is unclear. Shi et al. showed that Cx50 C-terminus directly interacts with E3 ubiquitin ligase Skp2 and regulates lens cell-cycle progression and differentiation by modulating expression of Skp2 (Shi et al., 2015). However, there should be other mechanisms since this discovery cannot reconcile all the genetic findings. For example, a much higher ratio of microcornea/microphthalmia symptoms were associated with mutations in the first transmembrane domain and extracellular loop, which are known to participate in the structure and function of the central pore and channel. As another example, frameshift mutations causing loss of C-terminus or C-terminus point mutations have been found not to be associated with microcornea/microphthalmia. We speculate that intercellular material exchanges, such as cAMP and ions, may also be important for LECs proliferation and differentiation.

It is well known that precursor cell migration is crucial for the cell fate commitment and/or maturation during development. As an example, loss of Lhx1 causes mislocation of the differentiating migratory horizontal precursors and these displaced cells finally commit apoptosis (Poche et al., 2007). It is very complicated that how LECs migration and differentiation are regulated. Surface LECs at different positions are exposed to unique microenvironment defined by neighbor tissues such as cornea, iris and retina. As a result, the BMP, FGF, Notch, Wnt signaling molecules play crucial roles controlling LECs migration and differentiation (Bassnett and Šikić, 2017; Cvekl and Zhang, 2017; McAvoy et al., 2017). The *in vitro* data showed that P88L mutant deterred LECs migration to some extent that it is probably insufficient to interrupt LECs differentiation *in vivo*. However, proper cell migration is essential for the delicate assembly of lens structure as evidenced in the post-operative capsular opacification (PCO) (Raj et al., 2007).

Whole exome sequencing has greatly expedited the discovery of causative genetic mutations of Mendelian diseases, in which a high percentage of mutations occur in the exon regions. Targeted exome sequencing enables rapid identification of common and rare genetic variants at a much affordable cost. In China, its cost still continues to drop and it is being gradually adapted in more and more hospitals and institutes. We anticipate that it will soon become a common procedure in genetic counselling and clinical practice.

DATA AVAILABILITY STATEMENT

The datasets presented in this study can be found in online repositories. The names of the repository/repositories and accession number(s) can be found below: https://ngdc.cncb.ac.cn/gsa-human/HRA001484.

ETHICS STATEMENT

The studies involving human participants were reviewed and approved by The medical protocol was approved by the Committee of Human Ethics in Medical Research in Zhongshan Ophthalmic Center and consistent with the Declaration of Helsinki. Written informed consent to participate in this study was provided by the participants' legal guardian/next of kin.

AUTHOR CONTRIBUTIONS

MZ, MX and KJ designed and supervised the project; AJ, QZ, SL, MZ and KJ collected data; AJ, QZ, SLi and KJ analyzed the data; MZ, MX, ZJ, SL and KJ wrote the manuscript. MZ, MX and KJ provided funding support of the project. All authors have read the manuscript and agree with the submission.

FUNDING

We thank the patients and family for participating in this study. This work was partially supported by the National Natural Science Foundation of China (82060176, 31871497, 82171470, 31900584, 81970794), National Key R&D Program of China (2017YFA0104100), Local Innovative and Research Teams Project of Guangdong Pearl River Talents Program, Science and Technology Planning Projects of Guangzhou City (201904020036, 201904010358), Natural Science Foundation of Guangdong Province of China (2020A1515010328), "Technology Innovation 2030-Major Projects" on Brain Science and Brain-Like Computing of the Ministry of Science and Technology of China (2021ZD0202603) and the Fundamental Research Funds of the State Key Laboratory of Ophthalmology, Sun Yat-sen University.

SUPPLEMENTARY MATERIAL

The Supplementary Material for this article can be found online at: https://www.frontiersin.org/articles/10.3389/fcell.2022.794837/full#supplementary-material

REFERENCES

Aasen, T., Johnstone, S., Vidal-Brime, L., Lynn, K. S., and Koval, M. (2018). Connexins: Synthesis, Post-Translational Modifications, and Trafficking in Health and Disease. *Int. J. Mol. Sci.* 19 (5). doi:10.3390/ijms19051296

Arora, A., Minogue, P. J., Liu, X., Addison, P. K., Russel-Eggitt, I., Webster, A. R., et al. (2008). A Novel Connexin50 Mutation Associated with Congenital Nuclear Pulverulent Cataracts. *J. Med. Genet.* 45 (3), 155–160. doi:10.1136/jmg.2007.051029

Arora, A., Minogue, P. J., Liu, X., Reddy, M. A., Ainsworth, J. R., Bhattacharya, S. S., et al. (2006). A Novel GJA8 Mutation Is Associated with Autosomal Dominant Lamellar Pulverulent Cataract: Further Evidence for gap junction Dysfunction in Human Cataract. *J. Med. Genet.* 43 (1), e2. doi:10.1136/jmg.2005.034108

Baek, M., DiMaio, F., Anishchenko, I., Dauparas, J., Ovchinnikov, S., Lee, G. R., et al. (2021). Accurate Prediction of Protein Structures and Interactions Using a Three-Track Neural Network. *Science* 2021, eabj8754. doi:10.1126/science.abj8754

Bassnett, S., and Šikić, H. (2017). The Lens Growth Process. *Prog. Retin. Eye Res.* 60, 181–200. doi:10.1016/j.preteyeres.2017.04.001

Berry, V., Ionides, A., Pontikos, N., Moghul, I., Moore, A. T., Quinlan, R. A., et al. (2020). Whole Exome Sequencing Reveals Novel and Recurrent Disease-Causing Variants in Lens Specific Gap Junctional Protein Encoding Genes Causing Congenital Cataract. *Genes (Basel)* 11 (5). doi:10.3390/genes11050512

Berry, V., Mackay, D., Khaliq, S., Francis, P. J., Hameed, A., Anwar, K., et al. (1999). Connexin 50 Mutation in a Family with Congenital "zonular Nuclear" Pulverulent Cataract of Pakistani Origin. *Hum. Genet.* 105 (1-2), 168–170. doi:10.1007/s004399900094

Berthoud, V. M., Gao, J., Minogue, P. J., Jara, O., Mathias, R. T., and Beyer, E. C. (2020). Connexin Mutants Compromise the Lens Circulation and Cause Cataracts through Biomineralization. *Int. J. Mol. Sci.* 21 (16). doi:10.3390/ijms21165822

Berthoud, V. M., and Ngezahayo, A. (2017). Focus on Lens Connexins. *BMC Cell Biol* 18 (Suppl. 1), 6. doi:10.1186/s12860-016-0116-6

Beyer, E. C., and Berthoud, V. M. (2018). Gap junction Gene and Protein Families: Connexins, Innexins, and Pannexins. *Biochim. Biophys. Acta (Bba) - Biomembranes* 1860 (1), 5–8. doi:10.1016/j.bbamem.2017.05.016

Ceroni, F., Aguilera-Garcia, D., Chassaing, N., Bax, D. A., Blanco-Kelly, F., Ramos, P., et al. (2019). New GJA8 Variants and Phenotypes Highlight its Critical Role in a Broad Spectrum of Eye Anomalies. *Hum. Genet.* 138 (8-9), 1027–1042. doi:10.1007/s00439-018-1875-2

Chen, C., Sun, Q., Gu, M., Liu, K., Sun, Y., and Xu, X. (2015). A Novel Cx50 (GJA8) p.H277Y Mutation Associated with Autosomal Dominant Congenital Cataract Identified with Targeted Next-Generation Sequencing. *Graefes Arch. Clin. Exp. Ophthalmol.* 253 (6), 915–924. doi:10.1007/s00417-015-3019-x

Cui, X., Zhou, Z., Zhu, K., Feng, R., Han, J., Li, M., et al. (2018). A Novel Cx50 Insert Mutation from a Chinese Congenital Cataract Family Impairs its Cellular Membrane Localization and Function. *DNA Cell Biol.* 37 (5), 449–456. doi:10.1089/dna.2017.4051

Cvekl, A., and Ashery-Padan, R. (2014). The Cellular and Molecular Mechanisms of Vertebrate Lens Development. *Development* 141 (23), 4432–4447. doi:10.1242/dev.107953

Cvekl, A., and Zhang, X. (2017). Signaling and Gene Regulatory Networks in Mammalian Lens Development. *Trends Genet.* 33 (10), 677–702. doi:10.1016/j.tig.2017.08.001

Dang, F. T., Yang, F. Y., Yang, Y. Q., Ge, X. L., Chen, D., Zhang, L., et al. (2016). A Novel Mutation of p.F32I in GJA8 in Human Dominant Congenital Cataracts. *Int. J. Ophthalmol.* 9 (11), 1561–1567. doi:10.18240/ijo.2016.11.05

Devi, R. R., and Vijayalakshmi, P. (2006). Novel Mutations in GJA8 Associated with Autosomal Dominant Congenital Cataract and Microcornea. *Mol. Vis.* 12, 190–195.

Ding, N., Chen, Z., Song, X., and Tang, X. (2020). Novel Mutation of GJA8 in Autosomal Dominant Congenital Cataracts. *Ann. Transl Med.* 8 (18), 1127. doi:10.21037/atm-20-4663

Donaldson, P. J., Grey, A. C., Maceo Heilman, B., Lim, J. C., and Vaghefi, E. (2017). The Physiological Optics of the Lens. *Prog. Retin. Eye Res.* 56, e1–e24. doi:10.1016/j.preteyeres.2016.09.002

Esseltine, J. L., and Laird, D. W. (2016). Next-Generation Connexin and Pannexin Cell Biology. *Trends Cell Biol.* 26 (12), 944–955. doi:10.1016/j.tcb.2016.06.003

Fan, F., Luo, Y., Wu, J., Gao, C., Liu, X., Mei, H., et al. (2020). The Mutation Spectrum in Familial versus Sporadic Congenital Cataract Based on Next-Generation Sequencing. *BMC Ophthalmol.* 20 (1), 361. doi:10.1186/s12886-020-01567-x

Flores, J. A., Haddad, B. G., Dolan, K. A., Myers, J. B., Yoshioka, C. C., Copperman, J., et al. (2020). Connexin-46/50 in a Dynamic Lipid Environment Resolved by CryoEM at 1.9 Å. *Nat. Commun.* 11 (1), 4331. doi:10.1038/s41467-020-18120-5

Gao, X., Cheng, J., Lu, C., Li, X., Li, F., Liu, C., et al. (2010). A Novel Mutation in the Connexin 50 Gene (GJA8) Associated with Autosomal Dominant Congenital Nuclear Cataract in a Chinese Family. *Curr. Eye Res.* 35 (7), 597–604. doi:10.3109/02713681003725831

García, I. E., Prado, P., Pupo, A., Jara, O., Rojas-Gómez, D., Mujica, P., et al. (2016). Connexinopathies: a Structural and Functional Glimpse. *BMC Cell Biol* 17 (Suppl. 1), 17. doi:10.1186/s12860-016-0092-x

Ge, X.-L., Zhang, Y., Wu, Y., Lv, J., Zhang, W., Jin, Z.-B., et al. (2014). Identification of a Novel GJA8 (Cx50) point Mutation Causes Human Dominant Congenital Cataracts. *Sci. Rep.* 4, 4121. doi:10.1038/srep04121

Gunda, P., Manne, M., Adeel, S. S., Kondareddy, R. K. R., and Tirunilai, P. (2018). Detection of c.139G>A (D47N) Mutation in GJA8 Gene in an Extended Family with Inheritance of Autosomal Dominant Zonular Cataract without Pulverulent Opacities by Exome Sequencing. *J. Genet.* 97 (4), 879–885. doi:10.1007/s12041-018-0971-3

Hadrami, M., Bonnet, C., Veten, F., Zeitz, C., Condroyer, C., Wang, P., et al. (2019). A Novel Missense Mutation of GJA8 Causes Congenital Cataract in a Large Mauritanian Family. *Eur. J. Ophthalmol.* 29 (6), 621–628. doi:10.1177/1120672118804757

Hansen, L., Mikkelsen, A., Nüirnberg, P., Nüirnberg, G., Anjum, I., Eiberg, H., et al. (2009). Comprehensive Mutational Screening in a Cohort of Danish Families with Hereditary Congenital Cataract. *Invest. Ophthalmol. Vis. Sci.* 50 (7), 3291–3303. doi:10.1167/iovs.08-3149

Hansen, L., Yao, W., Eiberg, H., Kjaer, K. W., Baggesen, K., Hejtmancik, J. F., et al. (2007). Genetic Heterogeneity in Microcornea-Cataract: Five Novel Mutations inCRYAA,CRYGD, andGJA8. *Invest. Ophthalmol. Vis. Sci.* 48 (9), 3937–3944. doi:10.1167/iovs.07-0013

He, W., Li, X., Chen, J., Xu, L., Zhang, F., Dai, Q., et al. (2011). Genetic Linkage Analyses andCx50mutation Detection in a Large Multiplex Chinese Family with Hereditary Nuclear Cataract. *Ophthalmic Genet.* 32 (1), 48–53. doi:10.3109/13816810.2010.535886

Hu, S., Wang, B., Zhou, Z., Zhou, G., Wang, J., Ma, X., et al. (2010). A Novel Mutation in GJA8 Causing Congenital Cataract-Microcornea Syndrome in a Chinese Pedigree. *Mol. Vis.* 16, 1585–1592.

Jin, K., Jiang, H., Xiao, D., Zou, M., Zhu, J., and Xiang, M. (2015). Tfap2a and 2b Act Downstream of Ptf1a to Promote Amacrine Cell Differentiation during Retinogenesis. *Mol. Brain* 8 (1), 28. doi:10.1186/s13041-015-0118-x

Jindal, S., Chockalingam, S., Ghosh, S. S., and Packirisamy, G. (2021). Connexin and gap Junctions: Perspectives from Biology to Nanotechnology Based Therapeutics. *Translational Res.* 235, 144–167. doi:10.1016/j.trsl.2021.02.008

Kumar, M., Agarwal, T., Khokhar, S., Kumar, M., Kaur, P., Roy, T. S., et al. (2011). Mutation Screening and Genotype Phenotype Correlation of Alpha-Crystallin, Gamma-Crystallin and GJA8 Gene in Congenital Cataract. *Mol. Vis.* 17, 693–707.

Kuo, D. S., Sokol, J. T., Minogue, P. J., Berthoud, V. M., Slavotinek, A. M., Beyer, E. C., et al. (2017). Characterization of a Variant of gap junction Protein α8 Identified in a Family with Hereditary Cataract. *PLoS One* 12 (8), e0183438. doi:10.1371/journal.pone.0183438

Li, D., Xu, C., Huang, D., Guo, R., Ji, J., and Liu, W. (2020). Identification and Functional Analysis of a Novel Missense Mutation in GJA8, p.Ala69Thr. *BMC Ophthalmol.* 20 (1), 461. doi:10.1186/s12886-020-01725-1

Li, J., Wang, Q., Fu, Q., Zhu, Y., Zhai, Y., Yu, Y., et al. (2013). A Novel Connexin 50 Gene (gap junction Protein, Alpha 8) Mutation Associated with Congenital Nuclear and Zonular Pulverulent Cataract. *Mol. Vis.* 19, 767–774.

Li, L., Fan, D.-B., Zhao, Y.-T., Li, Y., Yang, Z.-B., and Zheng, G.-Y. (2019). GJA8 Missense Mutation Disrupts Hemichannels and Induces Cell Apoptosis in Human Lens Epithelial Cells. *Sci. Rep.* 9 (1), 19157. doi:10.1038/s41598-019-55549-1

Li, S., Zhang, J., Cao, Y., You, Y., and Zhao, X. (2019). Novel Mutations Identified in Chinese Families with Autosomal Dominant Congenital Cataracts by Targeted Next-Generation Sequencing. *BMC Med. Genet.* 20 (1), 196. doi:10.1186/s12881-019-0933-5

Liang, C., Liang, H., Yang, Y., Ping, L., and Jie, Q. (2015). Mutation Analysis of Two Families with Inherited Congenital Cataracts. *Mol. Med. Rep.* 12 (3), 3469–3475. doi:10.3892/mmr.2015.3819

Lin, Y., Liu, N. N., Lei, C. T., Fan, Y. C., Liu, X. Q., Yang, Y., et al. (2008). A Novel GJA8 Mutation in a Chinese Family with Autosomal Dominant Congenital Cataract. *Zhonghua Yi Xue Yi Chuan Xue Za Zhi* 25 (1), 59–62.

Ma, A. S., Grigg, J. R., Ho, G., Prokudin, I., Farnsworth, E., Holman, K., et al. (2016). Sporadic and Familial Congenital Cataracts: Mutational Spectrum and New Diagnoses Using Next-Generation Sequencing. *Hum. Mutat.* 37 (4), 371–384. doi:10.1002/humu.22948

Ma, A. S., Grigg, J. R., Prokudin, I., Flaherty, M., Bennetts, B., and Jamieson, R. V. (2018). New Mutations in GJA8 Expand the Phenotype to Include Total Sclerocornea. *Clin. Genet.* 93 (1), 155–159. doi:10.1111/cge.13045

Machtaler, S., Choi, K., Dang-Lawson, M., Falk, L., Pournia, F., Naus, C. C., et al. (2014). The Role of the gap junction Protein Connexin43 in B Lymphocyte Motility and Migration. *FEBS Lett.* 588 (8), 1249–1258. doi:10.1016/j.febslet.2014.01.027

Mackay, D. S., Bennett, T. M., Culican, S. M., and Shiels, A. (2014). Exome Sequencing Identifies Novel and Recurrent Mutations in GJA8 and CRYGDassociated with Inherited Cataract. *Hum. Genomics* 8 (1), 19. doi:10.1186/s40246-014-0019-6

Mathias, R. T., Kistler, J., and Donaldson, P. (2007). The Lens Circulation. *J. Membr. Biol* 216 (1), 1–16. doi:10.1007/s00232-007-9019-y

Mathias, R. T., White, T. W., and Gong, X. (2010). Lens gap Junctions in Growth, Differentiation, and Homeostasis. *Physiol. Rev.* 90 (1), 179–206. doi:10.1152/physrev.00034.2009

McAvoy, J. W., Dawes, L. J., Sugiyama, Y., and Lovicu, F. J. (2017). Intrinsic and Extrinsic Regulatory Mechanisms Are Required to Form and Maintain a Lens of the Correct Size and Shape. *Exp. Eye Res.* 156, 34–40. doi:10.1016/j.exer.2016.04.009

Micheal, S., Niewold, I. T. G., Siddiqui, S. N., Zafar, S. N., Khan, M. I., and Bergen, A. A. B. (2018). Delineation of Novel Autosomal Recessive Mutation in GJA3 and Autosomal Dominant Mutations in GJA8 in Pakistani Congenital Cataract Families. *Genes (Basel)* 9 (2). doi:10.3390/genes9020112

Min, H.-Y., Qiao, P.-P., Asan, Z. H., Yan, Z.-H., Jiang, H.-F., Zhu, Y.-P., et al. (2016). Targeted Genes Sequencing Identified a Novel 15 Bp Deletion on GJA8 in a Chinese Family with Autosomal Dominant Congenital Cataracts. *Chin. Med. J. (Engl).* 129 (7), 860–867. doi:10.4103/0366-6999.178966

Minogue, P. J., Tong, J.-J., Arora, A., Russell-Eggitt, I., Hunt, D. M., Moore, A. T., et al. (2009). A Mutant Connexin50 with Enhanced Hemichannel Function Leads to Cell Death. *Invest. Ophthalmol. Vis. Sci.* 50 (12), 5837–5845. doi:10.1167/iovs.09-3759

Mohebi, M., Chenari, S., Akbari, A., Ghassemi, F., Zarei-Ghanavati, M., Fakhraie, G., et al. (2017). Mutation Analysis of Connexin 50 Gene Among Iranian Families with Autosomal Dominant Cataracts. *Iran J. Basic Med. Sci.* 20 (3), 288–293. doi:10.22038/IJBMS.2017.8358

Myers, J. B., Haddad, B. G., O'Neill, S. E., Chorev, D. S., Yoshioka, C. C., Robinson, C. V., et al. (2018). Structure of Native Lens Connexin 46/50 Intercellular Channels by Cryo-EM. *Nature* 564 (7736), 372–377. doi:10.1038/s41586-018-0786-7

Poche, R. A., Kwan, K. M., Raven, M. A., Furuta, Y., Reese, B. E., and Behringer, R. R. (2007). Lim1 Is Essential for the Correct Laminar Positioning of Retinal Horizontal Cells. *J. Neurosci.* 27 (51), 14099–14107. doi:10.1523/jneurosci.4046-07.2007

Polusani, S. R., Kalmykov, E. A., Chandrasekhar, A., Zucker, S. N., and Nicholson, B. J. (2016). Cell Coupling Mediated by Connexin 26 Selectively Contributes to Reduced Adhesivity and Increased Migration. *J. Cell Sci* 129 (23), 4399–4410. doi:10.1242/jcs.185017

Polyakov, A. V., Shagina, I. A., Khlebnikova, O. V., and Evgrafov, O. V. (2001). Mutation in the Connexin 50 Gene (GJA8) in a Russian Family with Zonular Pulverulent Cataract. *Clin. Genet.* 60 (6), 476–478. doi:10.1034/j.1399-0004.2001.600614.x

Ponnam, S. P., Ramesha, K., Matalia, J., Tejwani, S., Ramamurthy, B., and Kannabiran, C. (2013). Mutational Screening of Indian Families with Hereditary Congenital Cataract. *Mol. Vis.* 19, 1141–1148.

Ponnam, S. P., Ramesha, K., Tejwani, S., Ramamurthy, B., and Kannabiran, C. (2007). Mutation of the gap junction Protein Alpha 8 (GJA8) Gene Causes Autosomal Recessive Cataract. *J. Med. Genet.* 44 (7), e85. doi:10.1136/jmg.2007.050138

Raj, S. M., Vasavada, A. R., Johar, S. R., Vasavada, V. A., and Vasavada, V. A. (2007). Post-operative Capsular Opacification: a Review. *Int. J. Biomed. Sci.* 3 (4), 237–250.

Reis, L. M., Tyler, R. C., Muheisen, S., Raggio, V., Salviati, L., Han, D. P., et al. (2013). Whole Exome Sequencing in Dominant Cataract Identifies a New Causative Factor, CRYBA2, and a Variety of Novel Alleles in Known Genes. *Hum. Genet.* 132 (7), 761–770. doi:10.1007/s00439-013-1289-0

Ren, M., Yang, X. G., Dang, X. J., and Xiao, J. A. (2017). Exome Sequencing Identifies a Novel Mutation in GJA8 Associated with Inherited Cataract in a Chinese Family. *Graefes Arch. Clin. Exp. Ophthalmol.* 255 (1), 141–151. doi:10.1007/s00417-016-3513-9

Schmidt, W., Klopp, N., Illig, T., and Graw, J. (2008). A Novel GJA8 Mutation Causing a Recessive Triangular Cataract. *Mol. Vis.* 14, 851–856.

Sellitto, C., Li, L., and White, T. W. (2004). Connexin50 Is Essential for normal Postnatal Lens Cell Proliferation. *Invest. Ophthalmol. Vis. Sci.* 45 (9), 3196–3202. doi:10.1167/iovs.04-0194

Senthil Kumar, G., Dinesh Kumar, K., Minogue, P. J., Berthoud, V. M., Kannan, R., Beyer, E. C., et al. (2016). The E368Q Mutant Allele of GJA8 Is Associated with Congenital Cataracts with Intrafamilial Variation in a South Indian Family. *Open Access J. Ophthalmol.* 1 (1).

Shen, C., Wang, J., Wu, X., Wang, F., Liu, Y., Guo, X., et al. (2017). Next-generation Sequencing for D47N Mutation in Cx50 Analysis Associated with Autosomal Dominant Congenital Cataract in a Six-Generation Chinese Family. *BMC Ophthalmol.* 17 (1), 73. doi:10.1186/s12886-017-0476-5

Shi, Q., Gu, S., Yu, X. S., White, T. W., Banks, E. A., and Jiang, J. X. (2015). Connexin Controls Cell-Cycle Exit and Cell Differentiation by Directly Promoting Cytosolic Localization and Degradation of E3 Ligase Skp2. *Dev. Cell* 35 (4), 483–496. doi:10.1016/j.devcel.2015.10.014

Shiels, A., Bennett, T. M., and Hejtmancik, J. F. (2010). Cat-Map: Putting Cataract on the Map. *Mol. Vis.* 16, 2007–2015.

Shiels, A., Mackay, D., Ionides, A., Berry, V., Moore, A., and Bhattacharya, S. (1998). A Missense Mutation in the Human Connexin50 Gene (GJA8) Underlies Autosomal Dominant "zonular Pulverulent" Cataract, on Chromosome 1q. *Am. J. Hum. Genet.* 62 (3), 526–532. doi:10.1086/301762

Su, D., Yang, Z., Li, Q., Guan, L., Zhang, H., and E, D. (2013). Identification and Functional Analysis of GJA8 Mutation in a Chinese Family with Autosomal Dominant Perinuclear Cataracts. *PLoS One* 8 (3), e59926. doi:10.1371/journal.pone.0059926

Sun, W., Xiao, X., Li, S., Guo, X., and Zhang, Q. (2011). Mutational Screening of Six Genes in Chinese Patients with Congenital Cataract and Microcornea. *Mol. Vis.* 17, 1508–1513.

Tjahjono, N., Xia, C.-h., Li, R., Chu, S., Wang, J., and Gong, X. (2020). Connexin 50-R205G Mutation Perturbs Lens Epithelial Cell Proliferation and Differentiation. *Invest. Ophthalmol. Vis. Sci.* 61 (3), 25. doi:10.1167/iovs.61.3.25

Totland, M. Z., Rasmussen, N. L., Knudsen, L. M., and Leithe, E. (2020). Regulation of gap junction Intercellular Communication by Connexin Ubiquitination: Physiological and Pathophysiological Implications. *Cell. Mol. Life Sci.* 77 (4), 573–591. doi:10.1007/s00018-019-03285-0

Vanita, V., Hennies, H. C., Singh, D., Nürnberg, P., Sperling, K., and Singh, J. R. (2006). A Novel Mutation in GJA8 Associated with Autosomal Dominant Congenital Cataract in a Family of Indian Origin. *Mol. Vis.* 12, 1217–1222.

Vanita, V., Singh, J. R., Singh, D., Varon, R., and Sperling, K. (2008). A Mutation in GJA8 (p.P88Q) Is Associated with "Balloon-like" Cataract with Y-Sutural Opacities in a Family of Indian Origin. *Mol. Vis.* 14, 1171–1175.

Vanita, V., Singh, J. R., Singh, D., Varon, R., and Sperling, K. (2008). A Novel Mutation in GJA8 Associated with Jellyfish-like Cataract in a Family of Indian Origin. *Mol. Vis.* 14, 323–326.

Wang, K., Wang, B., Wang, J., Zhou, S., Yun, B., Suo, P., et al. (2009). A Novel GJA8 Mutation (p.I31T) Causing Autosomal Dominant Congenital Cataract in a Chinese Family. *Mol. Vis.* 15, 2813–2820.

Wang, K. J., Da Wang, J., Chen, D. D., Wang, M. Y., Yun, B., and Zhu, S. Q. (2020). Characterization of a p.R76H Mutation in Cx50 Identified in a Chinese Family with Congenital Nuclear Cataract. *J. Formos. Med. Assoc.* 119 (1 Pt 1), 144–149. doi:10.1016/j.jfma.2019.02.015

Wang, L., Luo, Y., Wen, W., Zhang, S., and Lu, Y. (2011). Another Evidence for a D47N Mutation in GJA8 Associated with Autosomal Dominant Congenital Cataract. *Mol. Vis.* 17, 2380–2385.

White, T. W., Gao, Y., Li, L., Sellitto, C., and Srinivas, M. (2007). Optimal Lens Epithelial Cell Proliferation Is Dependent on the Connexin Isoform Providing gap Junctional Coupling. *Invest. Ophthalmol. Vis. Sci.* 48 (12), 5630–5637. doi:10.1167/iovs.06-1540

Willoughby, C. E., Arab, S., Gandhi, R., Zeinali, S., Arab, S., Luk, D., et al. (2003). A Novel GJA8 Mutation in an Iranian Family with Progressive Autosomal Dominant Congenital Nuclear Cataract. *J. Med. Genet.* 40 (11), e124. doi:10.1136/jmg.40.11.e124

Yan, M., Xiong, C., Ye, S. Q., Chen, Y., Ke, M., Zheng, F., et al. (2008). A Novel Connexin 50 (GJA8) Mutation in a Chinese Family with a Dominant Congenital Pulverulent Nuclear Cataract. *Mol. Vis.* 14, 418–424.

Yang, Z., Li, Q., Ma, X., and Zhu, S. Q. (2015). Mutation Analysis in Chinese Families with Autosomal Dominant Hereditary Cataracts. *Curr. Eye Res.* 40 (12), 1225–1231. doi:10.3109/02713683.2014.997885

Ye, Y., Wu, M., Qiao, Y., Xie, T., Yu, Y., and Yao, K. (2019). Identification and Preliminary Functional Analysis of Two Novel Congenital Cataract Associated Mutations of Cx46 and Cx50. *Ophthalmic Genet.* 40 (5), 428–435. doi:10.1080/13816810.2019.1675179

Yu, Y., Wu, M., Chen, X., Zhu, Y., Gong, X., and Yao, K. (2016). Identification and Functional Analysis of Two Novel Connexin 50 Mutations Associated with Autosome Dominant Congenital Cataracts. *Sci. Rep.* 6, 26551. doi:10.1038/srep26551

Zhang, L., Liang, Y., Zhou, Y., Zeng, H., Jia, S., and Shi, J. (2018). A Missense Mutation in GJA8 Encoding Connexin 50 in a Chinese Pedigree with Autosomal Dominant Congenital Cataract. *Tohoku J. Exp. Med.* 244 (2), 105–111. doi:10.1620/tjem.244.105

Zhang, X. H., Da Wang, J., Jia, H. Y., Zhang, J. S., Li, Y., Xiong, Y., et al. (2018). Mutation Profiles of Congenital Cataract Genes in 21 Northern Chinese Families. *Mol. Vis.* 24, 471–477.

Zheng, J. Q., Ma, Z. W., and Sun, H. M. (2005). A Heterozygous Transversion of Connexin 50 in a Family with Congenital Nuclear Cataract in the Northeast of China. *Zhonghua Yi Xue Yi Chuan Xue Za Zhi* 22 (1), 76–78.

Zhou, Z., Wang, B., Hu, S., Zhang, C., Ma, X., and Qi, Y. (2011). Genetic Variations in GJA3, GJA8, LIM2, and Age-Related Cataract in the Chinese Population: a Mutation Screening Study. *Mol. Vis.* 17, 621–626.

Zhu, Y., Yu, H., Wang, W., Gong, X., and Yao, K. (2014). A Novel GJA8 Mutation (p.V44A) Causing Autosomal Dominant Congenital Cataract. *PLoS One* 9 (12), e115406. doi:10.1371/journal.pone.0115406

Conflict of Interest: The authors declare that the research was conducted in the absence of any commercial or financial relationships that could be construed as a potential conflict of interest.

Publisher's Note: All claims expressed in this article are solely those of the authors and do not necessarily represent those of their affiliated organizations, or those of the publisher, the editors and the reviewers. Any product that may be evaluated in this article, or claim that may be made by its manufacturer, is not guaranteed or endorsed by the publisher.

Copyright © 2022 Jin, Zhao, Liu, Jin, Li, Xiang, Zeng and Jin. This is an open-access article distributed under the terms of the Creative Commons Attribution License (CC BY). The use, distribution or reproduction in other forums is permitted, provided the original author(s) and the copyright owner(s) are credited and that the original publication in this journal is cited, in accordance with accepted academic practice. No use, distribution or reproduction is permitted which does not comply with these terms.

Advantages of publishing in Frontiers

OPEN ACCESS
Articles are free to read for greatest visibility and readership

FAST PUBLICATION
Around 90 days from submission to decision

HIGH QUALITY PEER-REVIEW
Rigorous, collaborative, and constructive peer-review

TRANSPARENT PEER-REVIEW
Editors and reviewers acknowledged by name on published articles

Frontiers
Avenue du Tribunal-Fédéral 34
1005 Lausanne | Switzerland

Visit us: www.frontiersin.org
Contact us: frontiersin.org/about/contact

REPRODUCIBILITY OF RESEARCH
Support open data and methods to enhance research reproducibility

DIGITAL PUBLISHING
Articles designed for optimal readership across devices

FOLLOW US
@frontiersin

IMPACT METRICS
Advanced article metrics track visibility across digital media

EXTENSIVE PROMOTION
Marketing and promotion of impactful research

LOOP RESEARCH NETWORK
Our network increases your article's readership